Abstract

Phase Slips in Isolated Mesoscopic Superconducting Aluminum Rings

Anthony Lollo

2018

Phase slips result in many interesting properties of superconducting materials, such as the finite resistance of thin superconducting nanowires, the decay of current in superconducting rings, and the flux periodicity of the critical temperature T_c in hollow superconducting cylinders or rings [1, 2]. Though the first experiments were performed in 1961, the goal of observing coherent macroscopic quantum tunneling in uniform superconductors has sparked recent interest in the field.

In this dissertation, we present measurements of the supercurrent I in arrays of uniform isolated mesoscopic aluminum rings as a function of applied magnetic field B, measured through cantilever torque magnetometry. These measurements are taken over the full range of applied magnetic fields for which the rings are superconducting and for 400 mK $< T < T_c$. We fit the $I(B)$ data to Ginzburg-Landau (GL) theory for a 1-dimensional superconducting ring with the inclusion of finite width. This detailed analysis extends the range of both temperature and applied magnetic fields over which prior measurements were quantitatively analyzed. Further, we show that phase slips occur deterministically as the free energy barrier separating two metastable states vanishes. We also present measurements of the distribution of applied magnetic fields at which a phase slip occurs for two individual isolated superconducting rings each of different radius. We find that as temperature is increased the mean and standard deviation decrease, while the skewness is always close to -1 with respect to an applied magnetic field ramp that decreases the free energy barrier.

We provide a theoretical review of GL theory relevant to this work and we review key experimental works within the phase slip literature. We describe the cantilever torque magnetometry technique, as well as the details necessary for the inclusion of a small magnetic coil, which allowed us to precisely control the magnetic field we applied to the individual superconducting rings.

Phase Slips in Isolated Mesoscopic Superconducting Aluminum Rings

A Dissertation
Presented to the Faculty of the Graduate School
of
Yale University
in Candidacy for the Degree of
Doctor of Philosophy

by
Anthony Lollo

Dissertation Director: Jack Harris

May 2018

Contents

List of Figures

List of Tables

Acknowledgments

I would like to thank Jack Harris for being an excellent mentor and giving me the opportunity to work on such a fascinating project. Of course, I could not have done the research alone and I am extremely grateful for the help of Ivana Petković and the years we spent working together on this project. I also want to acknowledge the great level of collaboration I've had with other professors at Yale, including Leonid Glazman, Daniel Prober, and Michel Devoret. As well, I appreciate the awesome easy-going atmosphere that existed throughout the Harris Lab due to all of its members and useful casual science discussions that would come about over lunch. I also want to personally thank Michael Rooks, Michael Powers, Chris Tillinghast, and Vincent Bernardo. They have helped us immensely with fabrication, imaging, and machining and their expertise has been integral to the success of this experiment.

Personally, I appreciate the constant support from my family, especially my parents, who always gave me the opportunity to pursue what I was interested in. And finally, I would like to thank my husband Ryan, who supported me daily and was always there to get me through the tougher and most frustrating parts of my graduate research.

Chapter 1

Introduction

The main goals of my graduate research were to measure the superconducting persistent current in aluminum rings and to study phase slips, a process by which the rings' superconducting order parameter transitions between metastable states that enclose a different integer number of flux quanta. In this dissertation, I will mainly focus on the theoretical description of supercurrent in nm-scale aluminum rings, the implementation of a small superconducting coil to precisely control the magnetic field that is applied to the rings, and the analysis of measurements of arrays of aluminum rings and individual aluminum rings. As both the sample and most of the measurement setup were the same as those used by William Shanks, I will only provide a brief description of those aspects and will refer the reader to his thesis for a detailed description [3]. While our measurements of arrays of rings significantly improve our quantitative understanding of phase slips and persistent current in mesoscopic superconducting rings, our results for the single ring measurements go against the existing theoretical understanding and the simplest models.

I will use the term persistent current or supercurrent to refer to the dissipationless current that flows through a superconducting material without any resistance. A phase slip, fluxoid transition, or winding number change all refer to the same process by which the complex superconducting order parameter (which in one dimension for a ring geometry carrying constant current is of the form $\psi = |\psi|e^{in\theta}$, where θ is the polar coordinate along the circumference of the ring) transitions to one in which the total phase accumulation along the circumference of the ring is different by $2\pi n$ for $n \in \mathbb{Z}$.

Here, I provide a quantitative analysis of the measured persistent current over the full magnetic field range below the rings' critical field and over a temperature range as low as 450 mK and up to the rings' critical temperature ($\sim$1.3 K). For several different ring sizes we fit the persistent current data to a simple theoretical model with only 2 fitting parameters at each temperature (coherence length and penetration depth) and 3 global fitting parameters for each sample (ring width, ring radius, and cantilever spring constant). We find that the magnetic flux at which phase slips occur matches the theoretical prediction, which includes a small correction due to the rings' finite length. The remarkable level of agreement we find over this large parameter space with so few fitting parameters demonstrates a significant improvement in our quantitative understanding of phase slips and supercurrent.

For a single isolated aluminum ring, I present measurements of the distribution of the applied flux at which a phase slip occurs. These measurements are taken over the same expansive temperature range. Such distributions have been measured in Josephson junctions, rings shunted with Josephson junctions, in uniform superconducting rings (but only very close to their critical temperature), and in superconducting nanowires biased with current. The Josephson junction measurements and the measurement of uniform rings close to their critical temperature are all explained remarkably well by a simple theory of thermal activation; the results of the nanowire measurements and Josephson junction measurements taken at $T \ll T_c$ are reproduced by considering a combination of quantum phase slips and thermal activation. Our measurement is made on a uniform ring away from the critical temperature and disagrees with our current theoretical understanding in that the distribution width decreases with increased temperature, though the mean and skewness agree with the theoretical prediction.

My goal with this dissertation is to provide a complete and straightforward description of my work. Many of the theoretical derivations will appear longer than those in their references and this is because I will include all of the intermediate steps that I often struggled with when going through the calculation for the first time. I will reference equations rather heavily, and in doing so I hope to make it unambiguous to follow the logical progression of my arguments.

In Chapter 2, I present a very brief historical overview of superconductivity and then

a theoretical overview of superconductivity relevant to this work. Following Tinkham [4], I begin with the simplest case of a 1-dimensional superconductor in the absence of fields, gradients, and boundary conditions and build complexity piece by piece to our experimental realization of a 1-dimensional flux-biased ring with finite width [4]. Appendix A details the prerequisite mathematics and more laborious calculations needed to derive the physics of Chapter 2. To follow the same convention as the physics literature, I will use gaussian cgs units in Chapter 2. In Chapter 3, I review a portion of the experimental literature related to phase slips. I start with the first experimental observation of phase slips and finish the discussion with work on MoGe wires within the Bezryadin group.

In Chapter 4, I describe the cantilever torsional magnetometry technique, which allows us to measure the equilibrium current of a superconducting ring. I will cover the basic physics of how a persistent current manifests itself as a change in the cantilever's resonant frequency. In Chapter 5, I describe the experimental apparatus and measurement procedures common to both the array and single ring measurements. The sample and experimental apparatus were developed by William Shanks and Ania Jayich under the direction of Jack Harris. The MATLAB routines used in the array measurements were created by Dustin Ngo, and I programmed the single ring MATLAB routines.

In Chapter 6, I describe the measurement procedures unique to array measurements and present the data and analysis of array supercurrent, which were both performed by Ivana Petković and me. Ivana developed and performed the fitting routine for the full supercurrent fits. In Chapter 7, I focus on measurements of a single aluminum ring. For this we added a small magnetic coil to the experimental stage, which is described and characterized in detail. The measurements of the phase slip distributions were split between Ivana and me, and we both independently analyzed the data. The analysis presented here will be mostly my own, though the final result of the distribution mean and width will incorporate both of our analyses. Again, Ivana performed the fits to the full supercurrent measurements (i.e., covering all magnetic fields for which the rings are in their superconducting state) to extract the sample parameters for the single ring. Finally in Chapter 8, I summarize the main results of this research.

Chapter 2

Superconducting theory and background

2.1 Historical overview of superconductivity

Shortly after liquefying helium, H. Kamerlingh Onnes discovered that the resistance of certain metals (mercury, tin, and lead) abruptly disappears below 4.2 K [5]. He argued that, "[w]hen the specific resistance of a circuit becomes a million times smaller than that of the best conductors at ordinary temperatures it will, in the majority of cases, be just as if electrical resistance no longer existed," and thus, the field of superconductivity was born. The next major discovery came two decades later when Meissner and Ochsenfeld found that magnetic fields are not allowed to enter certain bulk superconducting materials [6]. Further, they found that when a material was placed in a magnetic field and then cooled through this superconducting transition, the field lines were still expelled from the sample instead of being trapped within the sample. Perfect conductivity would tend to trap flux inside the sample, and so this second observation indicated that superconductors were also perfect diamagnets.[1]

Two years later, the London brothers provided an explanation for both of these phenomena. They argued that in superconductors, perfect conductivity allows currents to be

1. Deep within the superconductor, many penetration depths away from a surface.

maintained without an electromagnetic field and so Ohm's law might be replaced by an "acceleration equation" between the electric field strength $\mathbf{E}$ and the current density $\mathbf{J}$

$$\mathbf{E} = \Lambda \frac{\partial}{\partial t}\mathbf{J}; \qquad \Lambda = \frac{m}{n_{\mathrm{s}} e^2} \tag{2.1}$$

where m is the mass of an electron, n_{s} is the number density of superconducting electrons and e is the electron charge [7]. Taking the curl of Eq. 2.1 and combing it with Maxwell's equation $\nabla \times \mathbf{B} = 4\pi\mathbf{J}/c$, where c is the speed of light, leads to an equation for the magnetic field $\mathbf{B}$ within a superconductor

$$\nabla^2 \mathbf{B} = \frac{\mathbf{B}}{\lambda^2} \tag{2.2}$$

where $\lambda = \sqrt{\frac{mc^2}{4\pi n_{\mathrm{s}} e^2}}$. This shows that the magnetic field exponentially decays within the interior of a superconductor over a length scale set by the penetration depth λ. Though the value of n_{s} remained an open question at the time, London used the total number of conduction electrons to set an upper bound on the penetration depth, $\lambda_L \approx 10\,\mathrm{nm}$, thus corroborating Meissner and Ochsenfeld's work.

A stronger motivation for Eq. 2.1 came 15 years later when F. London noted that the canonical momentum is given by

$$\mathbf{p}_{\mathrm{s}} = (m\mathbf{v}_{\mathrm{s}} + e\mathbf{A}/c) \tag{2.3}$$

where $\mathbf{A}$ is the magnetic vector potential given by $\mathbf{B} = \nabla \times \mathbf{A}$. Without an applied field the ground state of a superconductor has zero net momentum [8]; thus, the average local velocity is given by $\langle v_{\mathrm{s}} \rangle = -\frac{e\mathbf{A}}{mc}$ and so the current density is

$$\mathbf{J}_{\mathrm{s}} = n_{\mathrm{s}} e \langle v_{\mathrm{s}} \rangle = \frac{-n_{\mathrm{s}} e^2 \mathbf{A}}{mc} = \frac{c}{4\pi}\frac{\mathbf{A}}{\lambda^2} \tag{2.4}$$

Taking the time derivative of Eq. 2.4 in the London gauge, where the electric potential φ_{E} is constant so that $\mathbf{E} = -\frac{d\mathbf{A}}{dt}$, yields Eq. 2.1.

The next major advancement came in 1950 when Ginzburg and Landau formulated their theory of superconducting electrons. Building upon Landau's prior work on second-order

phase transitions, they proposed that the free energy density f of a superconductor could be expressed as a series expansion in powers of ψ and $\nabla\psi$, with ψ being a complex order parameter describing the superconducting electrons (of mass m^* and charge e^*) such that $n_\mathrm{s} = |\psi(\mathbf{r})|^2$. By minimizing this free energy density

$$f = f_\mathrm{n} + \alpha|\psi(\mathbf{r})|^2 + \frac{\beta}{2}|\psi(\mathbf{r})|^4 + \frac{1}{2m^*}|(-i\hbar\nabla - \frac{e^*}{c}\mathbf{A})\psi(\mathbf{r})|^2 + \frac{\mathbf{B}^2}{8\pi} \tag{2.5}$$

with respect to ψ and $\mathbf{A}$ (worked out in Appendix A.1), where f_n is the normal state free energy density, α and β are phenomenological parameters, and $\hbar$ is Plank's constant, they arrived at the famous Ginzburg-Landau (GL) equations [9]

$$\alpha\psi(\mathbf{r}) + \beta|\psi(\mathbf{r})|^2\psi(\mathbf{r}) + \frac{1}{2m^*}(-i\hbar\nabla - \frac{e^*}{c}\mathbf{A})^2\psi(\mathbf{r}) = 0 \tag{2.6}$$

$$\mathbf{J} = -\frac{ie^*\hbar}{2m^*}\Big(\psi^*(\mathbf{r})\nabla\psi(\mathbf{r}) - \psi(\mathbf{r})\nabla\psi^*(\mathbf{r})\Big) - \frac{e^{*2}}{m^*c}|\psi(\mathbf{r})|^2\mathbf{A} \tag{2.7}$$

Unlike in the London equations $n_\mathrm{s}(\mathbf{r}) = |\psi(\mathbf{r})|^2$ was no longer a constant and could be spatially inhomogeneous. Despite this success, it was largely ignored due to its phenomenological origin. However, once Gor'kov [10] proved that the GL equations could be obtained from the theory proposed by Bardeen, Cooper, and Schrieffer (BCS) in the limit that the temperature approaches the critical temperature T_c, it became a widely used theory to describe macroscopic superconductivity (i.e., superconducting properties where an understanding of the overall free energy of the superconductor is important, instead of detailed knowledge of the density of states).

In 1957, Bardeen, Cooper, and Schrieffer provided a microscopic explanation for the superconducting phenomenon. By allowing electrons to interact via a virtual exchange of phonons, they found an attractive electron-electron interaction that could dominate the repulsive screened Coulomb interaction. This attractive interaction comes about by including the motion of the positive ion cores of the superconductor; one electron polarizes the lattice and attracts the positive ion cores, which in turn attract a second electron. Having this effectively attractive electron-electron interaction allowed them to reproduce Onnes' original discovery of vanishing resistance, predict a Meissner effect, and predict a second-order

phase transition, which was in agreement with the observed jump in specific heat at the critical temperature found by previous experiments [11, 12].

In addition to this theoretical work, there has been a great deal of effort spent on practical applications of superconductivity with the ultimate goal of one day finding a room temperature superconductor. Shortly before BCS theory, Nb_3Sn was discovered to have $T_c = 18$ K, which was the highest T_c at the time [13]. Then in 1961 Kunzler, Buehler, Hsu, and Wernick showed that superconductivity in Nb_3Sn survived at current densities exceeding 1 GA/m^2 and at magnetic fields as high as 8.8 T [14]. These exceptional qualities, despite its brittleness, have made Nb_3Sn a staple material in superconducting magnet systems with the capability to generate fields as large as 20 T.

The quest to find materials with even higher T_c continued and in 1987 a Nobel prize was awarded to Bednorz and Müller for their work on high-T_c superconductors [15]. They discovered that certain ceramics in the BaLaCuO system could have T_c as high as 35 K, which intensified the search to find even higher T_c materials. Only one year later Wu *et al.* found that $Y_{1.2}Ba_{0.8}CuO_4$ began superconducting at 93 K [16]. Other ceramics like $Hg_8Ba_2Ca_2Cu_3O_8$ were later discovered with $T_c = 134$ K [17], but the highest T_c superconductor to date is hydrogen sulfide subject to extremely high pressure ($\sim$150 GPa), which has $T_c = 203$ K [18]. Though these high T_c superconductors exhibit many of the same phenomenological properties as the classic superconductors, we still lack a microscopic understanding of the underlying mechanism in these materials.

2.2 The Ginzburg-Landau theory

The superconducting persistent current studied in this dissertation is a property derived from the overall free energy of an aluminum ring. As a result, applying a microscopic theory, like BCS theory, is needlessly difficult and instead GL theory provides a more intuitive framework from which we can understand our results. We will first establish the temperature dependence of the GL parameters $\alpha(T)$ and $\beta(T)$ and the concept of the coherence length $\xi(T)$. Then we will solve the GL differential equations, Eqs. 2.6 and 2.7, starting from the simplest case of a 1-d superconductor in the absence of fields and building

up to our experimental case of a ring of finite width biased with flux.

2.2.1 Ginzburg-Landau parameters $\alpha(T)$ and $\beta(T)$

Without any fields, gradients, or boundary conditions we can write Eq. 2.5 as

$$f - f_{\mathrm{n}} = \alpha|\psi(\mathbf{r})|^2 + \frac{\beta}{2}|\psi(\mathbf{r})|^4 \tag{2.8}$$

which is nothing more than a series expansion in powers of $|\psi(\mathbf{r})|^2$ keeping only the first two terms. To prevent the free energy density from being minimized at arbitrarily large $|\psi(\mathbf{r})|^2$ we must demand $\beta > 0$. For $\alpha > 0$, Eq. 2.8 is always positive and is minimized at $|\psi(\mathbf{r})|^2 = 0$. In this case $f = f_{\mathrm{n}}$ and so the normal state minimizes the free energy density. For $\alpha < 0$, the minimum with respect to $|\psi(\mathbf{r})|^2$ is given by $|\psi(\mathbf{r})|^2 = |\psi_\infty|^2 = -\frac{\alpha}{\beta}$. Thus, the order parameter has a constant magnitude throughout the entire superconductor. Inserting this value back into Eq. 2.8 we find the minimum free energy density is lower than that of the normal state

$$f - f_{\mathrm{n}} = -\frac{\alpha^2}{2\beta} \tag{2.9}$$

The free energy density difference between the normal and superconducting states (condensation energy) in zero field defines the thermodynamic critical field B_{c}

$$\frac{B_{\mathrm{c}}^2}{8\pi} = f - f_{\mathrm{n}} \tag{2.10}$$

which comes about by equating the condensation energy with the energy associated with holding field out against magnetic pressure, that is, the Meissner effect.

It is useful to determine the temperature-dependence of $\alpha(T)$, $\beta(T)$, and $|\psi(T)|^2$ in terms of parameters whose temperature dependence can be empirically measured or determined microscopically, like $B_{\mathrm{c}}(T)$ and $\lambda(T)$. If we consider the gradient and field terms in the expansion of Eq. 2.5 and write $\psi(\mathbf{r}) = |\psi_{\mathrm{A}}(\mathbf{r})|e^{i\varphi(\mathbf{r})}$, we have

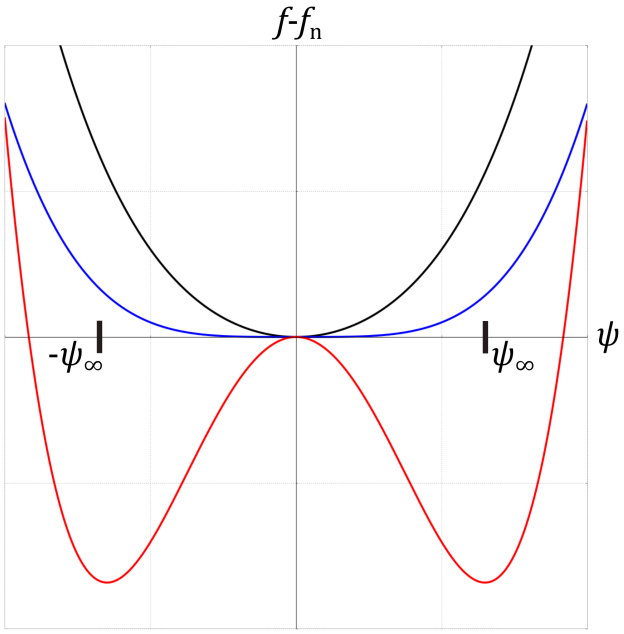

Figure 2.1: The Ginzburg-Landau free energy density, Eq. 2.8, in the absence of fields, gradients, and boundary conditions with $\beta > 0$ and either $\alpha > 0$ (black), $\alpha = 0$ (blue), or $\alpha < 0$ (red). ψ is assumed to be completely real for plotting purposes.

$$\begin{aligned}
\frac{1}{2m^*}\left|(-i\hbar\nabla - \frac{e^*}{c}\mathbf{A})\psi(\mathbf{r})\right|^2 &= \frac{1}{2m^*}|(-i\hbar\nabla - \frac{e^*}{c}\mathbf{A})|\psi_{\mathrm{A}}(\mathbf{r})|e^{i\varphi(\mathbf{r})}|^2 \\
&= \frac{1}{2m^*}\left| - i\hbar e^{i\varphi(\mathbf{r})}(\nabla|\psi_{\mathrm{A}}(\mathbf{r})| + i|\psi_{\mathrm{A}}(\mathbf{r})|\nabla\varphi(\mathbf{r})) - \frac{e^*}{c}\mathbf{A}|\psi_{\mathrm{A}}(\mathbf{r})|e^{i\varphi(\mathbf{r})}\right|^2 \\
&= \frac{1}{2m^*}|e^{i\varphi(\mathbf{r})}|^2\left| - i\hbar\nabla|\psi_{\mathrm{A}}(\mathbf{r})| + (\hbar\nabla\varphi(\mathbf{r}) - \frac{e^*}{c}\mathbf{A})|\psi_{\mathrm{A}}(\mathbf{r})|\right|^2 \\
&= \frac{1}{2m^*}\left[\hbar^2(\nabla|\psi_{\mathrm{A}}(\mathbf{r})|)^2 + \left(\hbar\nabla\varphi(\mathbf{r}) - \frac{e^*}{c}\mathbf{A}\right)^2|\psi_{\mathrm{A}}(\mathbf{r})|^2\right] \qquad (2.11)
\end{aligned}$$

The first term is the extra energy associated with gradients in the magnitude of the order parameter, while the second term deals with the kinetic energy of supercurrents. If we use the London gauge, where φ is constant, the kinetic energy term is just $e^{*2}\mathbf{A}^2|\psi_{\mathrm{A}}(\mathbf{r})|^2/2m^*c^2$. This is the same gauge used in Eq. 2.4 which tell us the kinetic energy density for a London superconductor is $\mathbf{A}^2/8\pi\lambda^2$. Equating these two we find

$$|\psi_{\mathrm{A}}(\mathbf{r})|^2 = |\psi_\infty|^2 = \frac{m^*c^2}{4\pi e^{*2}\lambda^2} = \frac{mc^2}{8\pi e^2\lambda^2} \qquad (2.12)$$

As we know that Cooper pairs are responsible for superconductivity, we have used $m^* = 2m$ and $e^* = 2e$ in the last equality, with m and e the mass and charge of a single electron, respectively. Using Eqs. 2.9 and 2.10 and $|\psi_\infty|^2 = -\frac{\alpha}{\beta}$, $\alpha(T)$ and $\beta(T)$ are given by

$$\alpha(T) = -\frac{2e^2}{mc^2} B_c^2(T)\lambda^2(T) \tag{2.13}$$

$$\beta(T) = \frac{16\pi e^4}{m^2c^4} B_c^2(T)\lambda^4(T) \tag{2.14}$$

As GL theory is only exact sufficiently close to T_c the above temperature-dependence is not universal. Further GL theory is a local theory, that is, the current of the superconductor at a point is determined by the electric field at that point. In general, the response of a superconductor can be non-local so that the current at a point is determined by the electric field averaged over a region of radius ℓ or ξ around that point as proposed by Pippard [19]. Here ℓ is the mean free path (average distance between elastic collisions of electrons with non-magnetic impurities in the superconductor) and ξ is the coherence length (characteristic length scale for variations of $\psi(\mathbf{r})$). GL theory will fail to treat nonlocal systems; however, in many important systems like dirty superconductors, in which $\xi(T) \approx \ell < \lambda(T)$, the impact of nonlocal effects is minimized and GL theory will still provide an accurate description. In cases where nonlocality is important, $\lambda(T)$ is not the London penetration depth we used to derive Eq. 2.12, and is instead should be replaced by an effective $\lambda_{\text{eff}}(T)$ which can lead to a different temperature dependence than that predicted by GL theory.

2.2.2 The Ginzburg-Landau coherence length

In the previous section we found that in the absence of fields, gradients, and boundary conditions the free energy F is minimized by taking $|\psi(\mathbf{r})|^2 = |\psi_\infty|^2 = -\frac{\alpha}{\beta}$ everywhere within the superconductor. However, once we relax those constraints the complex order parameter $\psi(\mathbf{r}) = |\psi_A(\mathbf{r})|e^{i\varphi(\mathbf{r})}$ adjusts itself to minimize the free energy F over the entire volume V of the superconductor

$$F[\psi(\mathbf{r})] = \int_V f dV = \int_V \left(\alpha|\psi(\mathbf{r})|^2 + \frac{\beta}{2}|\psi(\mathbf{r})|^4 + \frac{1}{2m^*}|(-i\hbar\nabla - \frac{e^*}{c}\mathbf{A})\psi(\mathbf{r})|^2 + \frac{|\mathbf{B}|^2}{8\pi} \right) dV \tag{2.15}$$

This variational problem is solved in Appendix A.1 and leads to the GL differential equations, Eqs. 2.6 and 2.7.

In the simplified case of no fields ($\mathbf{A} = 0$) and all of the coefficients of Eq. 2.6 being purely real, we can assume the order parameter is real without loss of generality. Further assuming that ψ depends on one spatial coordinate x we have

$$\alpha\psi(x) + \beta\psi^3(x) - \frac{\hbar^2}{2m^*}\frac{d^2\psi(x)}{dx^2} = 0 \tag{2.16}$$

By defining $f(x) = \psi(x)/\psi_\infty$ this equation becomes

$$\frac{\hbar^2}{2m^*|\alpha|}\frac{df^2(x)}{dx^2} + f(x) - f^3(x) = 0 \tag{2.17}$$

and we can see that

$$\xi(T) = \left(\frac{\hbar^2}{2m^*|\alpha(T)|}\right)^{1/2} \tag{2.18}$$

is a characteristic length for variations of $\psi(x)$. If we look at small deviations from ψ_∞ such that $f(x) = 1 + g(x)$ then to first order in $g(x)$ Eq. 2.17 is

$$\begin{aligned} \xi^2(T)\frac{d^2g(x)}{dx^2} + (1+g(x)) - (1 + 3g(x) + \cdots) &= 0 \\ \frac{d^2g(x)}{dx^2} &= \frac{2}{\xi^2(T)}g(x) \\ g(x) &\sim e^{\pm 2x/\xi(T)} \end{aligned} \tag{2.19}$$

Thus, any small deviation of $\psi(x)$ from ψ_∞ exponentially decays on a length scale set by $\xi(T)$. To complete the discussion of $\xi(T)$ we can determine its temperature dependence sufficiently close to T_c using Eq. 2.13

$$\xi(T) = \frac{hc}{2\sqrt{2}\pi e^* B_c(T)\lambda(T)} = \frac{\Phi_0}{2\sqrt{2}\pi B_c(T)\lambda(T)} \tag{2.20}$$

where $\Phi_0 = \frac{hc}{2e}$ is the superconducting flux quantum.[2]

2. In SI units, $\Phi_0 = \frac{h}{2e}$

2.2.3 The Ginzburg-Landau theory in 1 dimension for uniform current in the presence of flux bias

In this section, we will consider the effects of fields strong enough to cause $\psi(\mathbf{r})$ to depart from ψ_∞ within the superconductor. However, we will still restrict ourselves to 1 dimension, in which the superconductor thickness s and width w satisfy $s \ll \xi(T)$ and $w \ll \xi(T)$ while its length (i.e. its dimension along x) is unrestricted. In this case, any variations in ψ across these lateral dimensions will cause an excessive contribution to the free energy given the $(\nabla|\psi(\mathbf{r})|)^2$ term. Thus, we can approximate $\psi(\mathbf{r})$ by $|\psi(x)|e^{i\varphi(x)}$, where in the case of a wire or ring x is along the length or circumference respectively.

As this dissertation mainly focuses on equilibrium states that carry uniform current we will impose that restriction now. Substituting $\psi(x) = |\psi(x)|e^{i\varphi(x)}$ into Eq. 2.7 we obtain

$$\begin{aligned}\mathbf{J} = \frac{-ie^*\hbar}{2m^*}\Bigg(&|\psi(x)|e^{-i\varphi(x)}\Big(|\psi'(x)|e^{i\varphi(x)} + i\nabla\varphi(x)|\psi(x)|e^{i\varphi(x)}\Big) \\ &- |\psi(x)|e^{i\varphi(x)}\Big(|\psi'(x)|e^{-i\varphi(x)} - i\nabla\varphi(x)|\psi(x)|e^{-i\varphi(x)}\Big)\Bigg) - \frac{e^{*2}\mathbf{A}}{m^*c}|\psi(x)|^2 \\ \mathbf{J} = \frac{e^*}{m^*}|\psi(x)|^2&\Big(\hbar\nabla\varphi(x) - \frac{e^*\mathbf{A}}{c}\Big) \qquad (2.21)\end{aligned}$$

Eq. 2.21 has current proportional to $|\psi(x)|^2$ so the restriction of constant current throughout the superconductor further limits $\psi(x)$ to those with a constant amplitude, $\psi(x) = |\psi|e^{i\varphi(x)}$.[3] Using the momentum operator, Eq. 2.3 can be re-written in the form

$$m^*\mathbf{v}_\mathrm{s} = \mathbf{p}_\mathrm{s} - \frac{e^*\mathbf{A}}{c} = \hbar\nabla\varphi(x) - \frac{e^*\mathbf{A}}{c} \qquad (2.22)$$

Thus, the uniform current of an equilibrium state of a 1-dimensional system given by Eq. 2.21 is

$$\mathbf{J} = e^*|\psi|^2\mathbf{v}_\mathrm{s} \qquad (2.23)$$

Given this expression for current density, it is useful to calculate the maximum current

3. There are other possibilities for constant current order parameters, for example one where $|\psi(x)|$ varies, but the $\nabla\varphi(\mathbf{r})$ term exactly compensates for this variation to maintain constant $\mathbf{J}$. These states have higher free energy than the nearby uniform states $|\psi|e^{i\varphi(\mathbf{r})}$ and are discussed in detail in section 2.3.1.

density $\mathbf{J}_\mathrm{c}$ that a superconductor can support before superconductivity is destroyed, a phenomenon observed by Onnes in 1913 [20]. Using Eq. 2.22 in Eq. 2.5 we can find the $|\psi|^2$ that minimizes the free energy density for a given $\mathbf{v}_\mathrm{s}$

$$\begin{aligned} 0 = \frac{df}{d|\psi|^2} &= \alpha + \beta|\psi|^2 + \frac{m^*\mathbf{v}_\mathrm{s}^2}{2} \\ |\psi|^2 &= -\frac{\alpha}{\beta} - \frac{m^*\mathbf{v}_\mathrm{s}^2}{2\beta} \\ |\psi|^2 &= |\psi_\infty|^2\big(1 - \frac{m^*\mathbf{v}_\mathrm{s}^2}{2|\alpha|}\big) \end{aligned} \tag{2.24}$$

The current associated with this is thus

$$\mathbf{J} = e^*|\psi_\infty|^2\big(\mathbf{v}_\mathrm{s} - \frac{m^*\mathbf{v}_\mathrm{s}^3}{2|\alpha|}\big) \tag{2.25}$$

which is maximized at $\mathbf{v}_\mathrm{s} = \sqrt{\frac{2|\alpha|}{3m^*}}$, or equivalently $|\psi|^2 = \frac{2}{3}|\psi_\infty|^2$. With this, the critical current density[4] that the superconductor can support is

$$\mathbf{J}_\mathrm{c} = e^*|\psi_\infty|^2\frac{2}{3}\sqrt{\frac{2|\alpha|}{3m^*}} = \frac{cB_\mathrm{c}(T)}{3\sqrt{6}\pi\lambda(T)} \tag{2.26}$$

where in the last equality we used Eqs. 2.12 and 2.13 to obtain the temperature-dependence of the critical current density sufficiently close to T_c.

2.2.4 The fluxoid and fluxoid quantization

There are many ways to derive the concept of the fluxoid and quantization but one of the simplest is to demand that the complex order parameter is single-valued as it is physically related to the number density of superconducting electrons. As a result, the phase φ can only change by $2n\pi$, for $n \in \mathbb{Z}$, when going around any closed path $\mathbf{l}$, that is

$$\oint \nabla\varphi \cdot d\mathbf{l} = 2n\pi \tag{2.27}$$

4. As we assume no variations in the lateral dimensions of the sample, the current I is trivially related to the current density by $I = \sigma J$, where σ is the cross-sectional area of the superconductor.

Using Eq. 2.22 this is

$$\oint \left(\frac{m^*\mathbf{v}_\mathrm{s}}{\hbar} + \frac{e^*\mathbf{A}}{c\hbar}\right) \cdot d\mathbf{l} = 2n\pi$$
$$\frac{m^*c}{e^*} \oint \mathbf{v}_\mathrm{s} \cdot d\mathbf{l} + \oint \mathbf{A} \cdot d\mathbf{l} = \frac{nhc}{e^*} \tag{2.28}$$

where we have just multiplied by constants in the second line. Using Stokes' theorem we can write $\oint \mathbf{A} \cdot d\mathbf{l} = \int \mathbf{B} \cdot d\mathbf{S} = \Phi$ where $\mathbf{S}$ is the surface bounded by $\mathbf{l}$, and now we see that the requirement that $\psi(\mathbf{r})$ is single-valued is the same as fluxoid quantization as

$$\Phi + \frac{m^*c}{e^*} \oint \mathbf{v}_\mathrm{s} \cdot d\mathbf{l} = n\Phi_0 \tag{2.29}$$

A consequence of this fluxoid quantization is that certain properties of ring-like superconducting geometries will be flux periodic. If a hollow superconducting cylinder (or ring) of radius R is placed coaxial with a uniform magnetic field B, the flux enclosed by the ring is $\Phi = B\pi R^2$. The path integration of Eq. 2.29 is taken around the circumference of the superconductor which gives

$$n\Phi_0 = \Phi + \frac{m^*c}{e^*}\mathbf{v}_\mathrm{s} 2\pi R$$
$$\mathbf{v}_\mathrm{s} = \frac{\hbar}{m^*R}\left(n - \frac{\Phi}{\Phi_0}\right) \tag{2.30}$$

For a given applied flux, the system will reach equilibrium when its winding number n minimizes the free energy. We can neglect the self-field term generated by the supercurrent, $\frac{\mathbf{B}^2}{8\pi}$, in the free energy as it can be made arbitrarily small as long as the superconductor is thin enough compared to its cross-sectional area.[5] Therefore, combining Eq. 2.5 with

5. When the sample thickness s is smaller than λ we can have a uniform current throughout the entire superconductor, and not just restricted to the surface. As a result, the field term energy will be smaller than the kinetic energy term by a factor of order $\sigma/\lambda^2 \sim s^2/\lambda^2$, which allows us to neglect it for thin enough superconductors ($s < \lambda$).

Eq. 2.22 and Eq. 2.24 we can write

$$f - f_{\mathrm{n}} = \alpha|\psi|^2 + \frac{1}{2}\beta|\psi|^4 + \frac{1}{2}m^*\mathbf{v}_{\mathrm{s}}^2$$
$$f - f_{\mathrm{n}} = \frac{\alpha^2}{2\beta}\left(-1 + \frac{m^*\mathbf{v}_{\mathrm{s}}^2}{\alpha^2} + \frac{m^{*2}\mathbf{v}_{\mathrm{s}}^4}{4\alpha^4}\right) \tag{2.31}$$

As $\mathbf{v}_{\mathrm{s}}$ only appears in the free energy to even powers with positive coefficients, the superconducting free energy is minimized when $\mathbf{v}_{\mathrm{s}}$ takes on its smallest absolute value.

If there is no barrier for the system to change its winding number then the superconducting system will transition to a state of different winding number when that state has lower free energy than its current state.[6] States of adjacent winding number have equal free energy when

$$\frac{\alpha^2}{2\beta}\left(-1 + \frac{m^*\mathbf{v}_{\mathrm{s},n}^2}{\alpha^2} + \frac{m^{*2}\mathbf{v}_{\mathrm{s},n}^4}{4\alpha^4}\right) = \frac{\alpha^2}{2\beta}\left(-1 + \frac{m^*\mathbf{v}_{\mathrm{s},n+1}^2}{\alpha^2} + \frac{m^{*2}\mathbf{v}_{\mathrm{s},n+1}^4}{4\alpha^4}\right)$$
$$\frac{m^*\mathbf{v}_{\mathrm{s},n}^2}{\alpha^2} + \frac{m^{*2}\mathbf{v}_{\mathrm{s},n}^4}{4\alpha^4} = \frac{m^*\mathbf{v}_{\mathrm{s},n+1}^2}{\alpha^2} + \frac{m^{*2}\mathbf{v}_{\mathrm{s},n+1}^4}{4\alpha^4}$$
$$\left(n - \frac{\Phi}{\Phi_0}\right)^2 + \frac{\hbar}{4\alpha^2 R}\left(n - \frac{\Phi}{\Phi_0}\right)^4 = \left(n + 1 - \frac{\Phi}{\Phi_0}\right)^2 + \frac{\hbar}{4\alpha^2 R}\left(n + 1 - \frac{\Phi}{\Phi_0}\right)^4 \tag{2.32}$$

The only real solution to the above equation occurs when

$$\Phi = \Phi_0\left(n + \frac{1}{2}\right) \tag{2.33}$$

Thus, it becomes energetically favorable for the superconductor to change its winding number by 1 at every half-interger value of Φ_0, which leads to Φ_0-periodic oscillations of the superconducting free energy. As a result, all other quantities derived from the free energy (e.g. supercurrent and specific heat) will also display this same periodicity.

6. Practically, this situation can also be realized when there is still an energy barrier between transitions, but the system has sufficient thermal energy to easily overcome such a barrier. This typically occurs very close to T_{c}, a regime relevant to many experiments discussed later.

2.2.5 Finite width correction in a ring

Up until this point, we have succeeded in solving the GL equations for constant current states which minimize the superconducting free energy in the presence of fields and gradients, with and without boundary conditions, and in 1 dimension (or sufficiently close to T_c such that the thickness and width satisfy $s \ll \xi(T)$ and $w \ll \xi(T)$, respectively, in which case the system is effectively 1-dimensional). With these assumptions we were able to derive the temperature-dependence of all of the GL parameters and we also demonstrated the origin of flux-periodicity.

However, these arguments are not enough to explain the suppression of superconductivity at high fields. Together, Eqs. 2.24 and 2.30 indicate that when the superconductor increases or decreases its winding number, the maximum obtainable amplitude of the order parameter $|\psi|^2$ and $\mathbf{v}_s$ remain the same. Superconductivity will still be extinguished at fields where it is energetically unfavorable to expel flux from the superconductor compared with the normal state; however, from Eq. 2.23 we would expect measurable quantities like the supercurrent, which depends on $|\psi|^2$ and $\mathbf{v}_s$, to show no decay up until this point. Experimentally, this is not the case and it is our neglect of the sample's finite volume that causes this discrepancy.

We will remedy this by proceeding with the same assumptions that we are looking for constant current carrying states and that our lateral dimensions are small enough that the $(\nabla|\psi(\mathbf{r})|)^2$ term in the free energy prevents $|\psi(\mathbf{r})|$ from varying appreciably in these dimensions. However, we will now properly integrate the free energy density over the entire sample volume. In doing so, we fill find small corrections to the results of the previous sections. As this treatment corresponds to our experimental realization, we will also point out many of the qualitative and quantitative aspects of the free energy and superconducting current to compare against our measurements in Chapter 6.

2.2.5.1 Finite width corrections to the order parameter

We will consider a ring of mean radius R, width w and thickness s as shown in Fig. 2.2. A magnetic field is perpendicular to the plane of the ring, which allows us to express it in terms

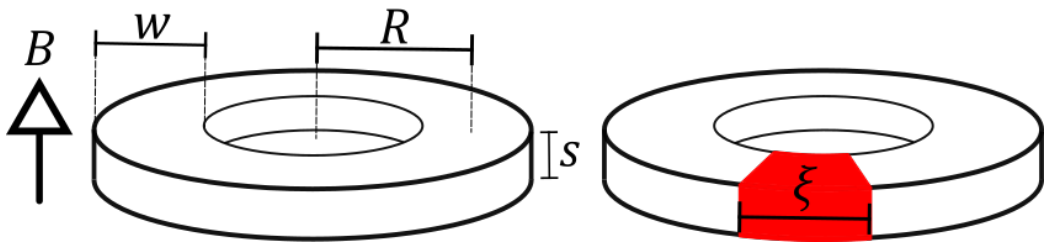

Figure 2.2: A superconducting ring of mean radius R, width w, and thickness s in a constant magnetic field B applied perpendicular to the plane of the ring. In the right panel, a region of the ring of size ξ illustrates a section of the ring that will become normal during a phase slip. At higher temperatures, this region becomes larger as ξ increases rapidly near T_c.

of the associated vector potential $\mathbf{A} = \frac{1}{2}rB\hat{\theta}$. As we are considering metastable constant current carrying states without considering radial variations of the order parameter we can write $\psi(\mathbf{r}) = \psi_0 e^{in\theta}$ where ψ_0 is a constant.[7] The free energy density of this configuration is

$$f - f_n = \alpha\psi_0^2 + \frac{1}{2}\beta\psi_0^4 + \frac{1}{2m^*V}\int\left(\left|\left(-i\hbar\nabla - \frac{e^*}{c}\mathbf{A}\right)\psi_0 e^{in\theta}\right|^2\right)dV \tag{2.34}$$

where $V = 2\pi Rws$ is the total sample volume. Again, we are looking for the value of ψ_0 that minimizes the free energy, which is solved in Appendix A.2 and leads to

$$\psi_0^2 = |\psi_\infty|^2\left(1 - \frac{\hbar^2}{2m^*|\alpha|R^2}\left[\left(n - \frac{\Phi}{\Phi_0}\right)^2 + \left(\frac{n^2}{3} + \left(\frac{\Phi}{\Phi_0}\right)^2\right)\left(\frac{w}{2R}\right)^2\right]\right) \tag{2.35}$$

Previously from Eq. 2.24 and Eq. 2.30 we found

$$\psi_0^2(w=0) = |\psi_\infty|^2\left(1 - \frac{\hbar^2}{2m^*|\alpha|R^2}\left(n - \frac{\Phi}{\Phi_0}\right)^2\right) \tag{2.36}$$

which is consistent with Eq. 2.35 and so our inclusion of finite width merely provides a small correction or order $\left(\frac{w}{2R}\right)^2$ to our previous results. Though small, this correction is enough to explain the gradual suppression of superconductivity at high fields since the $\frac{n^2}{3} + \left(\frac{\Phi}{\Phi_0}\right)^2$ term monotonically increases as flux and winding number are increased, which leads to a suppression of the order parameter amplitude ψ_0^2, and thus current, at finite magnetic fields.

7. This phase dependence, $\varphi(\theta) = n\theta$, takes care of the boundary condition that $\psi(\mathbf{r})$ must have the same value at $\theta = 0$ and $\theta = 2\pi$. Alternatively this phase can be expressed as $\varphi(x) = kx = \frac{2\pi}{L}x$ where x runs along the circumference, L, of the ring.

2.2.5.2 Finite width free energy

Even with the inclusion of finite width, the free energy density of the ring is constant over the ring's volume so the free energy is simply $F[\psi(\mathbf{r})] = f[\psi_0 e^{in\theta}]V$. Using Eq. 2.18 and defining

$$G(\Phi) = \left(n - \frac{\Phi}{\Phi_0}\right)^2 + \left(\frac{n^2}{3} + \left(\frac{\Phi}{\Phi_0}\right)^2\right)\left(\frac{w}{2R}\right)^2 \tag{2.37}$$

we can compactly express

$$\psi_0^2 = |\psi_\infty|^2\left(1 - \frac{\xi^2}{R^2}G(\Phi)\right) \tag{2.38}$$

$$f - f_\mathrm{n} = \alpha\psi_0^2 + \frac{1}{2}\beta\psi_0^4 - \alpha\psi_0^2\frac{\xi^2}{R^2}G(\Phi) \tag{2.39}$$

where we obtained f from Eq. A.27 with an expansion of the logarithm to third order in $\frac{w}{2R}$. The free energy is

$$F/V = \alpha\left(1 - \frac{\xi^2}{R^2}G(\Phi)\right)\psi_0^2 + \frac{1}{2}\beta\psi_0^4 \tag{2.40}$$

$$F/V = \alpha|\psi_\infty|^2\left(1 - \frac{\xi^2}{R^2}G(\Phi)\right)^2 + |\psi_\infty|^4\frac{\beta}{2}\left(1 - \frac{\xi^2}{R^2}G(\Phi)\right)^2$$

$$F/V = \left(1 - \frac{\xi^2}{R^2}G(\Phi)\right)^2\left(\alpha|\psi_\infty|^2 + \frac{\beta}{2}|\psi_\infty|^2\left(\frac{-\alpha}{\beta}\right)\right)$$

$$F = V\frac{\alpha|\psi_\infty|^2}{2}\left(1 - \frac{\xi^2}{R^2}G(\Phi)\right)^2 \tag{2.41}$$

From Eq. 2.40 we can see that the free energy is an expansion in powers of ψ_0^2, and that the inclusion of finite width only modifies the ψ_0^2 term. We still require the coefficient of the ψ_0^2 term to be negative for the superconducting state to have a lower free energy than the normal state and this coefficient is now flux-dependent. This leads to a restriction on the fields at which superconductivity can exist for each winding number. As α is already negative in our notation this condition is,

$$1 - \frac{\xi^2}{R^2}\left[\left(n - \frac{\Phi}{\Phi_0}\right)^2 + \left(\frac{n^2}{3} + \left(\frac{\Phi}{\Phi_0}\right)^2\right)\left(\frac{w}{2R}\right)^2\right] > 0 \tag{2.42}$$

To get a sense of the maximum allowed winding number for this ring, we will set Eq. 2.42

equal to zero and solve for n

$$n_{\max}(\Phi) = \frac{3\xi^2 \frac{\Phi}{\Phi_0} \pm \sqrt{3R^2\xi^2\left(3+\left(\frac{w}{2R}\right)^2\right) - 3\xi^4\left(\frac{\Phi}{\Phi_0}\right)^2\left(\frac{w}{2R}\right)^2\left(4+\left(\frac{w}{2R}\right)^2\right)}}{\xi^2\left(3+\left(\frac{w}{2R}\right)^2\right)} \tag{2.43}$$

This expression gives us the maximum winding number at a specified flux, but to find the overall maximum winding number we should find the flux Φ_* that maximizes $n_{\max}(\Phi)$, which is given by

$$\begin{aligned} \frac{dn_{\max}}{d\Phi} &= 0 \\ \Phi_* &= \pm\frac{\Phi_0\sqrt{3}R}{\xi\frac{w}{2R}\sqrt{4+5\left(\frac{w}{2R}\right)^2+\left(\frac{w}{2R}\right)^4}} \approx \pm\frac{\sqrt{3}R^2}{\xi w}\Phi_0 \end{aligned} \tag{2.44}$$

where in the last approximation we used $\frac{w}{2R} \ll 1$. The the overall maximum winding number is thus

$$n_{\max}(\Phi_*) = \frac{\sqrt{3}\left(\frac{3R\xi}{\frac{w}{2R}\sqrt{4+5\left(\frac{w}{2R}\right)^2+\left(\frac{w}{2R}\right)^4}} + \sqrt{\frac{R^2\xi^2\left(\frac{w}{2R}\right)^2\left(4+\left(\frac{w}{2R}\right)^2\right)}{1+\left(\frac{w}{2R}\right)^2}}\right)}{\xi^2\left(3+\left(\frac{w}{2R}\right)^2\right)} \approx \frac{\sqrt{3}R^2}{\xi w} \tag{2.45}$$

again using the approximation $\frac{w}{2R} \ll 1$ in the last step.

2.2.5.3 Finite width supercurrent

In this section, we will derive expressions for the experimentally relevant observable, the superconducting persistent current. The thermodynamic supercurrent is related to the free energy by

$$I = -\frac{\partial F}{\partial \Phi} \tag{2.46}$$

and from Eq. 2.41 we can write

$$\begin{aligned} I &= V\frac{\alpha\xi^2|\psi_\infty|^2}{R^2}\left(1-\frac{\xi^2}{R^2}G(\Phi)\right)\frac{dG(\Phi)}{d\Phi} \\ I &= \frac{-2V\alpha\xi^2|\psi_\infty|^2}{\Phi_0 R^2}\left(1-\frac{\xi^2}{R^2}G(\Phi)\right)\left(n-\left[1+\left(\frac{w}{2R}\right)^2\right]\frac{\Phi}{\Phi_0}\right) \end{aligned} \tag{2.47}$$

As before, we can find the maximum current I_c by maximizing this function with respect to Φ. A useful[8] quantity to determine is the flux at which I_c occurs, denoted by Φ_c, which for a given winding number is

$$\frac{\Phi_{c,n}}{\Phi_0} = \frac{n}{1+\left(\frac{w}{2R}\right)^2} \pm \frac{\sqrt{\xi^2\left(1+\left(\frac{w}{2R}\right)^2\right)\left[3R^2\left(1+\left(\frac{w}{2R}\right)^2\right) - \xi^2 n^2\left(\frac{w}{2R}\right)^2\left(4+\left(\frac{w}{2R}\right)^2\right)\right]}}{3\xi^2\left(1+\left(\frac{w}{2R}\right)^2\right)} \tag{2.48}$$

$$\frac{\Phi_{c,n}}{\Phi_0} = \frac{n}{1+\left(\frac{w}{2R}\right)^2} \pm \frac{R}{\sqrt{3}\xi} + \mathcal{O}\left(\left(\frac{w}{2R}\right)^2\right) \tag{2.49}$$

Since the current is the derivative of the free energy, the free energy is extremized when the current equals zero, and from Eq. 2.47 this occurs when either

$$n - \left[1+\left(\frac{w}{2R}\right)^2\right]\frac{\Phi}{\Phi_0} = 0 \qquad \text{or} \qquad 1 - \frac{\xi^2}{R^2}G(\Phi) = 0$$

The first equation, which yields

$$\Phi_{\min,n} = \frac{n\Phi_0}{1+\left(\frac{w}{2R}\right)^2} \tag{2.50}$$

gives the value of flux that minimizes the free energy for a given winding number. Our previous result, in the limit of zero width, had the free energy minimized[9] at $\Phi_{\min,n}(w = 0) = n\Phi_0$ and so again we see the inclusion of finite width is only a small correction of the order $\left(\frac{w}{2R}\right)^2$. The second condition also corresponds to $F = 0$, so its solution will lead to the depairing flux for a given winding number. This flux is

$$\frac{\Phi}{\Phi_0} = \frac{3n\xi^2 \pm \sqrt{3\xi^2\left[3R^2\left(1+\left(\frac{w}{2R}\right)^2\right) - n^2\xi^2\left(\frac{w}{2R}\right)^2\left(4+\left(\frac{w}{2R}\right)^2\right)\right]}}{3\xi^2\left(1+\left(\frac{w}{2R}\right)^2\right)} \tag{2.51}$$

$$\Phi \approx \Phi_{\min,n} \pm \frac{R}{\xi}\Phi_0 \tag{2.52}$$

8. In Appendix A.3 we show that at the critical current the energy barrier between fluxoid transitions disappears.

9. From Eq. 2.31 we can see that the superconducting free energy is minimized when $\mathbf{v}_s$ is zero, and from Eq. 2.30 this occurs when $\Phi = n\Phi_0$.

In going from Eq. 2.51 to Eq. 2.52 we have assumed that $\frac{w}{2R} \ll 1$ and also that n is small compared to $n_{\max}$ given by the approximation in Eq. 2.45. For comparisons with experimental data in Chapter 6 we will use the full form of Eq. 2.51; however, Eq. 2.52 is

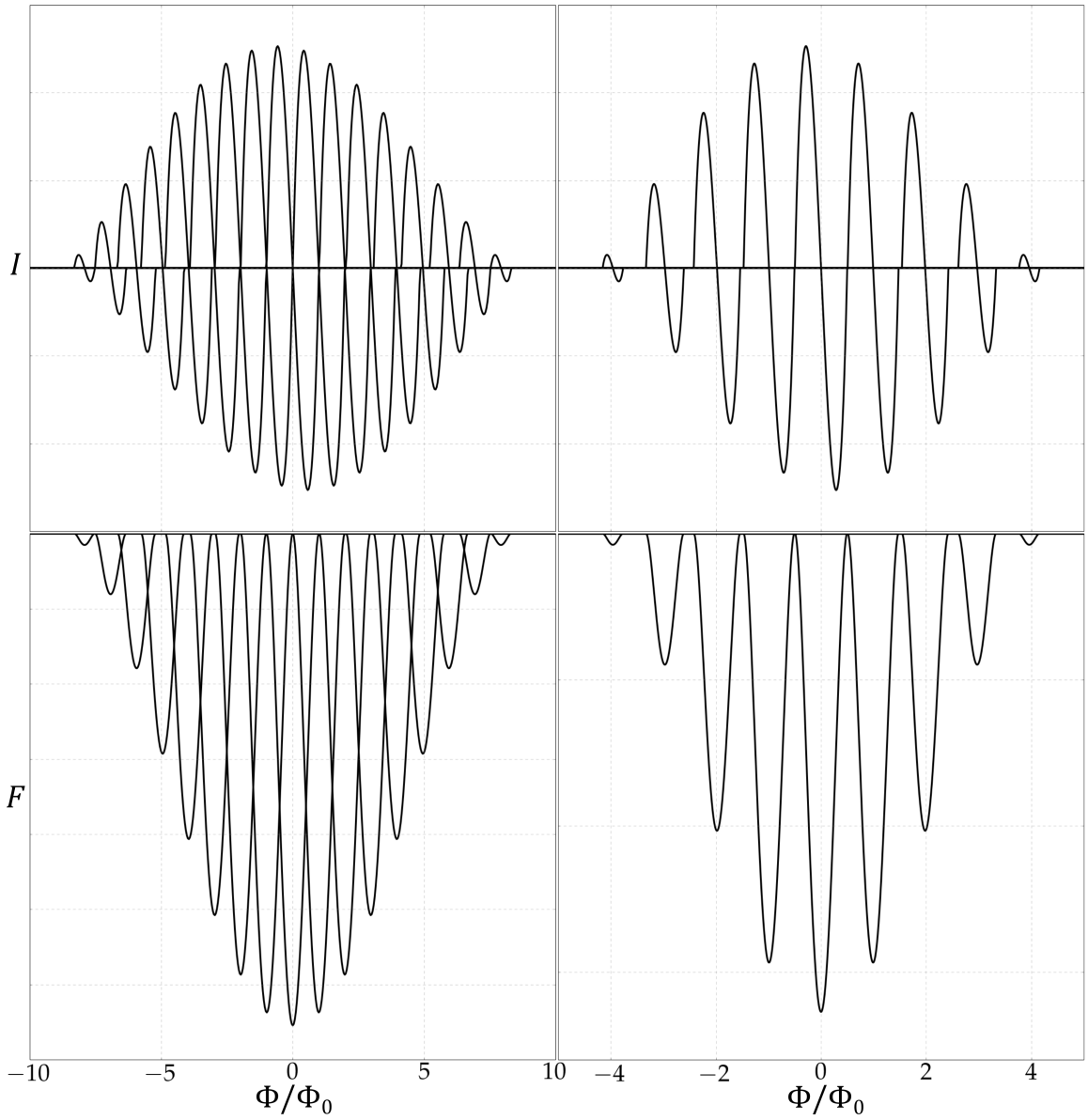

Figure 2.3: Supercurrent (top panels) and free energy (bottom panels) as a function of applied flux for a superconducting ring with $R = \xi = 5w$ (left column) and a ring of $R = \frac{1}{2}\xi = 5w$ (right column). The maximum winding number in each case is well approximated by Eq. 2.45 which predicts $n_{\max} \approx 5\sqrt{3} \approx 9.$ and $n_{\max} \approx 2.5\sqrt{3} \approx 4$ for the left column and right column respectively. For the $R = \frac{1}{2}\xi = 5w$ ring, there are intermittent fluxes below the critical flux at which there is no energetically favorable superconducting state and so the ring exists in the normal state at these fluxes.

useful as it clearly illustrates that the dependence is set by the ratio $\frac{R}{\xi}$.

2.2.5.4 Re-entrant normal state

Depending upon the ratio of R and ξ, the free energy and supercurrent can display a different qualitative behavior as a function of applied flux. From Eq. 2.50 we know that successive minima of free energy are spaced $\sim \Phi_0$ apart in flux. From Eq. 2.52 we know that each winding number will only extend $\approx \frac{R}{\xi}\Phi_0$ on either side of these minima before it is no longer energetically favorable to remain superconducting. Thus, if $\frac{R}{\xi} \lesssim \frac{1}{2}$ there will be fluxes below the superconductor's critical field at which the superconductor transitions to the normal state.[10] This is the case shown in the right column of Fig. 2.3. In cases where $\frac{R}{\xi}$ is sufficiently greater than $\frac{1}{2}$, there is always at least one energetically favorable superconducting state at every flux below the critical flux, and thus, there are no transitions to the normal state before the critical flux is reached.

2.3 The free energy barrier between fluxoid transitions

Up to this point we have only dealt with cases where the superconducting system adiabatically follows the lowest energy state as the flux is varied. With this treatment, we either assumed that there was no energy barrier between winding number transitions at the flux at which a transition would occur, or that thermal fluctuations were large enough to easily take the system over any energy barrier between transitions. While this is true of systems close to T_c, where $R < \frac{\sqrt{3}}{2}\xi(T)$, this will not be the case at lower temperatures where $R > \frac{\sqrt{3}}{2}\xi(T)$.

We will now proceed to calculate the energy barrier between fluxoid transitions. In doing so, we will find the flux at which this energy barrier vanishes, $\Phi_{c,n}$, which corresponds to the flux location at which a phase slip (a change in winding number by $\Delta n = 1$) will occur in the absence of any fluctuations. We will also discuss how this switching flux's dependence on R and $\xi(T)$ leads to hysteresis in the supercurrent when the flux is varied at lower

10. If $\frac{R}{\xi} < \frac{1}{2}$, then this re-entrant normal state will exist between every winding number. However, due to the n-dependence of Eq. 2.51 this re-entrant normal state can occur between only the highest winding numbers when $\frac{R}{\xi}$ is slightly greater than $\frac{1}{2}$.

temperatures. In the proceeding derivation, we will not consider the system's finite width as we have in section 2.2.5.1. This allows us to calculate an analytic expression for the energy barrier between fluxoid transitions, which will depend upon I_c.

2.3.1 Langer-Ambegaokar theory

Here we present the calculation from Langer and Ambegaokar of the free energy barrier between constant current carrying states in a thin wire [21]. Using Eq. 2.6 with $\mathbf{A} = 0$ we can write the GL minimization condition as

$$-\frac{\hbar^2}{2m^*}\nabla^2\psi(\mathbf{r}) - |\alpha|\psi(\mathbf{r}) + \beta|\psi(\mathbf{r})|^2\psi(\mathbf{r}) = 0 \tag{2.53}$$

where we have written $\alpha = -|\alpha|$ to remove any confusion about the sign of α. We can re-write Eq. 2.21 as

$$\mathbf{J} = \frac{e^*\hbar}{m^*}|\psi(x)|^2\nabla\varphi(\mathbf{r}) \tag{2.54}$$

We will consider constant current carrying solutions, the simplest case being those with constant amplitude and phase that increases linearly with distance. In one dimension these solutions are $\psi(\mathbf{r}) = \psi_k = f_k e^{ikx}$. In the beginning of Appendix A.3 we solve for the f_k that satisfy Eq. 2.53, which are given by Eq. A.33. It is worth noting that this set-up is the same as that of section 2.2.3, except that now we have specified the phase dependence, $\varphi(\mathbf{r}) = kx$.

As each of these ψ_k are themselves local minima of the GL free energy, a free energy barrier generally exists between states with successive winding numbers ($k \rightarrow k - \frac{2\pi}{L}$), where L is the length of the system.[11] In order to calculate this barrier, we must find the optimal path in the phase space of order parameters for which the system can transition from ψ_k to $\psi_{k-\frac{2\pi}{L}}$. That is, we must determine the saddle point order parameter $\bar{\psi}(x)$ and its associated free energy. The free energy barrier for transitions $\psi_k \rightarrow \psi_{k-\frac{2\pi}{L}}$ is then the difference in free energy between $\bar{\psi}(x)$ and ψ_k

As $\bar{\psi}(x)$ is a saddle point solution it must also extremize the GL free energy. We have

11. We consider transitions $k \rightarrow k - \frac{2\pi}{L}$ as these are transitions to a state of lower energy and occur at a substantially higher rate that transitions to a state of higher energy $k \rightarrow k + \frac{2\pi}{L}$.

already exhausted solutions with a constant amplitude and linear phase, so we must expand our possible order parameters to a more general form given by

$$\bar{\psi}(x) = f(x)e^{i\varphi(x)} \tag{2.55}$$

Using this order parameter in Eq. 2.53 we obtain (suppressing the x-depdence of f and φ)

$$\begin{aligned} -\frac{\hbar^2}{2m^*}\frac{d^2}{dx^2}\left[fe^{i\varphi}\right] - |\alpha|fe^{i\varphi} + \beta f^3 e^{i\varphi} &= 0 \\ \frac{\hbar^2}{2m^*}\left(- f\varphi'^2 e^{i\varphi} + if\varphi'' e^{i\varphi} + 2if'\varphi' e^{i\varphi} + f'' e^{i\varphi}\right) + |\alpha|fe^{i\varphi} - \beta f^3 e^{i\varphi} &= 0 \\ \frac{\hbar^2}{2m^*}\left(- f\varphi'^2 + if\varphi'' + 2if'\varphi' + f''\right) + |\alpha|f - \beta f^3 &= 0 \end{aligned} \tag{2.56}$$

The imaginary part of Eq. 2.56 leads to

$$f\varphi'' + 2f'\varphi' = 0 \tag{2.57}$$

which simply states that our saddle point order parameters carry constant current as from Eq. 2.54 we can write

$$\mathbf{J} = \frac{e^*\hbar}{m^*}f^2\varphi' \tag{2.58}$$

$$\frac{d\mathbf{J}}{dx} = \frac{e^*\hbar}{m^*}f\left(2f'\varphi' + f\varphi''\right) = 0 \tag{2.59}$$

The real part of Eq. 2.56 leads to to following differential equation

$$\frac{\hbar^2}{2m^*}f'' - \frac{\hbar^2}{2m^*}f\varphi'^2 + |\alpha|f - \beta f^3 = 0 \tag{2.60}$$

With Eq. 2.58 we can write this as

$$\begin{aligned} \frac{\hbar^2}{2m^*}f'' &= \frac{m^*}{2e^{*2}}\frac{J^2}{f^3} - |\alpha|f + \beta f^3 \\ \frac{\hbar^2}{2m^*}\frac{d^2f}{dx^2} &= -\frac{d}{df}\left(\frac{m^*}{2e^{*2}}\frac{J^2}{2f^2} + \frac{1}{2}|\alpha|f^2 - \frac{1}{4}\beta f^4\right) \end{aligned} \tag{2.61}$$

If f and ϕ are interpreted as the radial and angular coordinates of the position of a particle of mass $\frac{\hbar^2}{2m^*}$ and x is the time, then the right hand side of that equation resembles the derivative of an effective radial potential $U_{\rm eff}(f)$. As long as $J < J_{\rm c}$ this potential has two extremal points, illustrated in Fig. 2.4. With this potential, we can make an analogy to orbital motion. Circular orbits are possible at f_0 and f_0' and correspond to states $\psi_k = f_k e^{ikx}$ with constant amplitude and linearly increasing phase. The non-uniform solution with amplitude $f(x)$ that we are looking for should be very close to these solutions.[12] If we consider a solution that has an infinitesimally smaller radius than that of f_0, it will spend most of its time near f_0 but it eventually spirals as far as f_1 and then returns to the vicinity of f_0. This suggests that we should consider solutions that only deviate from the constant current carrying solutions in a small and finite region along the sample length L.

We will now require conservation of energy:

$$\frac{dE}{dx} = \frac{d}{dx}\left[\frac{1}{2}\left(\frac{\hbar}{\sqrt{2m^*}}\frac{df}{dx}\right)^2 + U_{\rm eff}(f)\right] = 0 \tag{2.62}$$

which allows us to obtain an equation for x

$$\begin{aligned}\frac{\sqrt{2m^*}}{\hbar}x &= \int_{f_1}^{f} \frac{df}{\sqrt{2\left(E - U_{\rm eff}(f)\right)}} \\ \frac{\sqrt{2m^*}}{\hbar}x &= \int_{f_1}^{f} \frac{df}{\sqrt{2\left(E - \frac{m^*}{2e^{*2}}\frac{J^2}{2f^2} - \frac{1}{2}|\alpha|f^2 + \frac{1}{4}\beta f^4\right)}}\end{aligned} \tag{2.63}$$

By introducing the dimensionless quantities

$$f^2 = \frac{|\alpha|}{\beta}u, \qquad E = \frac{\alpha^2}{2\beta}\epsilon, \qquad J^2 = J_{\rm c}^2 j^2 = \frac{8e^{*2}|\alpha|^3}{27m^*\beta^2}j^2 \tag{2.64}$$

12. By close, we mean that the non-uniform solution should only vary from the uniform solution by an amount that is independent of the sample length L. This ensures that the free energy barrier does not become too large to prohibit phase slips as the sample becomes longer. As we will see, the solutions differ over a region where the length scale is set by $\xi(T)$.

where J_c is given by Eq. 2.26, we can write the integral as

$$\frac{2\sqrt{m^*|\alpha|}}{\hbar}x = \int_{u_1}^{u} \frac{du}{\sqrt{u^3 - 2u^2 + 2\epsilon u - \frac{8}{27}j^2}} \tag{2.65}$$

The denominator in the integral must vanish quadratically at $u = u_0 = \frac{\beta f_0^2}{|\alpha|}$ as f_0 is a stationary point of the potential. The denominator vanishes linearly at $u = u_1 = \frac{\beta f_1^2}{|\alpha|}$. Equating both of these forms we can write

$$u^3 - 2u^2 + 2\epsilon u - \frac{8}{27}j^2 = (u - u_1)(u_0 - u)^2 \tag{2.66}$$

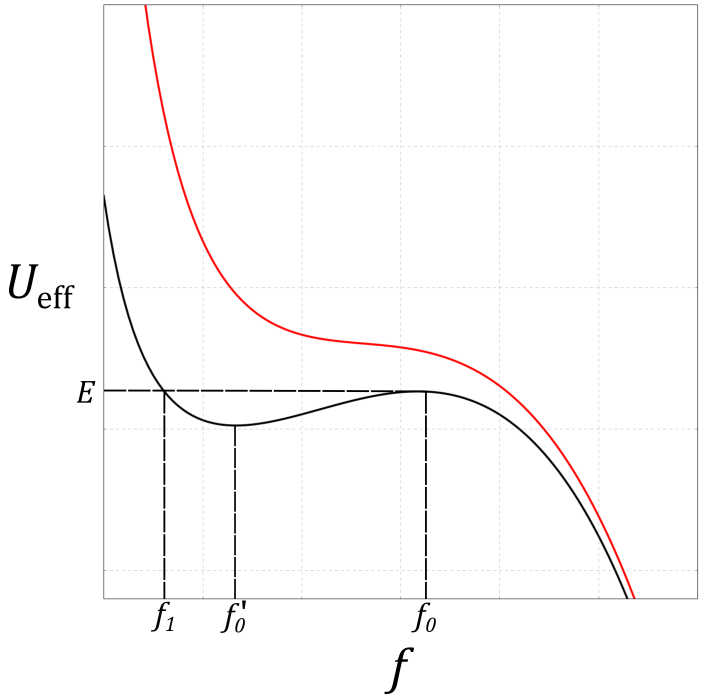

Figure 2.4: The effective radial potential as a function of order parameter amplitude f for $J < J_c$ (black) and $J = J_c$ (red). As long as the current is below the critical current, there will be two stationary points indicated by f_0 and f_0'. These points merge at the critical current and then disappear above J_c. The unstable orbit at f_0 has lower energy than the stable orbit at f_0'. E represents an energy that is infinitesimally lower than the energy at f_0, which confines the "particle" to orbits between f_1 and f_0.

which determines the relationship between u_0 and u_1 in terms of ϵ and j,

$$2u_0 + u_1 = 2 \tag{2.67}$$

$$u_0^2 + 2u_0u_1 = 2\epsilon \tag{2.68}$$

$$u_1u_0^2 = \frac{8}{27}j^2 \tag{2.69}$$

With this we can rewrite Eq. 2.65

$$\frac{2\sqrt{m^*|\alpha|}}{\hbar}x = \int_{u_1}^{u} \frac{du'}{\sqrt{(u'-u_1)\,(u_0-u')^2}} \tag{2.70}$$

$$\frac{2\sqrt{m^*|\alpha|}}{\hbar}x = \frac{2}{\sqrt{u_0-u_1}}\text{ArcTanh}\left[\sqrt{\frac{u'-u_1}{u_0-u_1}}\right]\Bigg|_{u'=u_1}^{u'=u}$$

$$u = u_1 + \Delta\text{Tanh}^2\left[x\frac{\sqrt{|\alpha|m^*\Delta}}{\hbar}\right]$$

$$u(x) = \frac{\beta}{|\alpha|}f^2(x) = u_0 - \Delta\text{Sech}^2\left[x\frac{\sqrt{|\alpha|m^*\Delta}}{\hbar}\right] \tag{2.71}$$

where $\Delta = u_0 - u_1$ and in the last line we used the identity $\text{Tanh}^2 + \text{Sech}^2 = 1$ to express $u(x)$ as a deviation from the orbit at f_0. Thus, we have found a solution for $f(x)$ which is nearly identical to the solution for a uniform current carrying state f_0, but deviates only over a small region centered around $x = 0$. The final useful identity to note is that with our definition of Δ and Eq. 2.67 and Eq. 2.69 we can write

$$(2+\Delta)^2\,(1-\Delta) = 4j^2 \tag{2.72}$$

Thus as $J \to J_c$, $\Delta \to 0$.

From Eq. 2.59 we know our saddle point order parameter must carry constant current, and given that it is identical to ψ_{k_0} over the majority of the system as illustrated in Fig. 2.5, it must carry the same constant current as ψ_{k_0}. As a consequence, in the region where $f^2(x)$ is diminished $\frac{d\varphi}{dx}$ must increase more rapidly than that of the ψ_{k_0} state to keep the current

constant. To calculate the total phase difference across the sample $\Delta\varphi$ we write

$$\Delta\varphi = \int_{-L/2}^{L/2} d\varphi = \int_{-L/2}^{L/2} dx \frac{d\varphi}{dx} = \frac{Jm^*}{\hbar e^*} \int_{-L/2}^{L/2} \frac{dx}{f^2} \tag{2.73}$$

where we have used Eq. 2.58 to replace φ'. In our notation $f^2(x)$ is symmetric about the center of the sample, so we only need to evaluate the integral from 0 to $L/2$ and double the result. Also $x = 0$, the location of the furthest departure from the constant current carrying state, corresponds to $u = u_1$. At $x = L/2$, the solution resembles the constant current carrying state so $u = u_0$. Again, this integral is far easier to calculate in our u

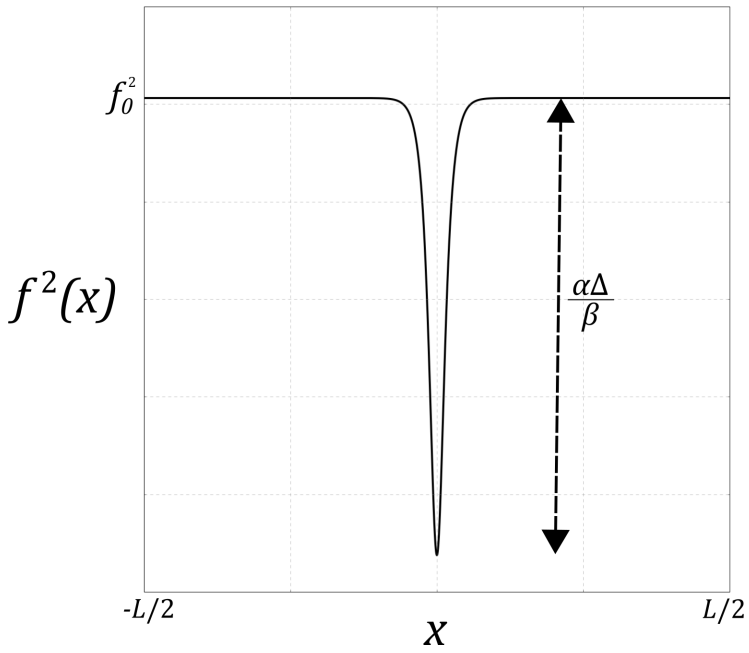

Figure 2.5: The saddle point order parameter amplitude for a 1-dimensional superconductor of length L. For the majority of the sample the order parameter is identical to that of a constant current carrying state with amplitude f_0^2. However in a finite region of the sample, the amplitude is diminished, the extent of which is set by Δ.

notation, and we can write

$$\begin{aligned}\Delta\varphi &= \frac{Jm^*}{\hbar e^*}\int_{-L/2}^{L/2}\frac{dx}{f^2} = \frac{2Jm^*}{\hbar e^*}\int_0^{L/2}\frac{dx}{f^2} \\ &= \frac{2Jm^*\beta}{\hbar e^*|\alpha|}\int_0^{L/2}\frac{dx}{u} \\ &= \frac{2Jm^*\beta}{\hbar e^*|\alpha|}\int_0^{L/2}dx\left(\frac{1}{u}+\frac{1}{u_0}-\frac{1}{u_0}\right) \\ &= \frac{Jm^*\beta L}{\hbar e^*|\alpha|u_0}+\frac{2Jm^*\beta}{\hbar e^*|\alpha|}\int_0^{L/2}dx\left(\frac{1}{u}-\frac{1}{u_0}\right)\end{aligned} \tag{2.74}$$

To relate du and dx we can use Eq. 2.70 to write $\frac{2\sqrt{m^*|\alpha|}}{\hbar}dx = \frac{du}{\sqrt{u-u_1}(u_0-u)}$. With this substitution we have

$$\begin{aligned}\Delta\varphi &= \frac{Jm^*\beta L}{\hbar e^*|\alpha|u_0}+\frac{Jm^{*1/2}\beta}{u_0e^*|\alpha|^{3/2}}\int_{u_1}^{u_0}\frac{du}{u\sqrt{u-u_1}} \\ \Delta\varphi &= \frac{Jm^*\beta L}{\hbar e^*|\alpha|u_0}+\frac{Jm^{*1/2}\beta}{u_0e^*|\alpha|^{3/2}}\left(\frac{2}{\sqrt{u_1}}\text{ArcCos}\left[\frac{u_1}{u_0}\right]^{1/2}\right) \\ \Delta\varphi &= \frac{Jm^*L}{\hbar e^*f_0^2}+2\text{ArcTan}\left[\frac{3\Delta}{2\left(1-\Delta\right)}\right]^{1/2}\end{aligned} \tag{2.75}$$

The first term of Eq. 2.75 is just the linear phase that would accumulate across the sample for a constant current carrying state.[13] The second term is the extra phase associated with the fluctuating region of $f(x)$, and this term varies from π to 0 as J is varied from 0 to J_c respectively. If we now imagine a state ψ_{k_i} with uniform current that has the same overall phase difference as $\bar{\psi}(x)$ (that is, the same winding number), as indicated by the blue curve in Fig. 2.6, then we can deduce that $\bar{\psi}(x)$ must have slightly smaller current than ψ_{k_i} to compensate for the increased phase derivative. For the uniform states of the form $\psi(x) = f_k e^{ikx}$, the overall phase difference along the circumference L of the a ring is $\Delta\varphi = kL$, and so we find

$$\delta k \equiv k_i - k_0 = \frac{2}{L}\text{ArcTan}\left[\frac{3\Delta}{2\left(1-\Delta\right)}\right]^{1/2} \tag{2.76}$$

13. Using Eq. 2.54 we can write $J = \frac{e^*\hbar}{m^*}f^2\nabla\varphi$, for a constant current carrying state with linearly increasing phase. Thus, from $\nabla\varphi = \frac{\Delta\varphi}{L}$ we can determine the total phase difference across the sample to be $\Delta\varphi = L * \frac{Jm^*}{\hbar e^* f^2}$.

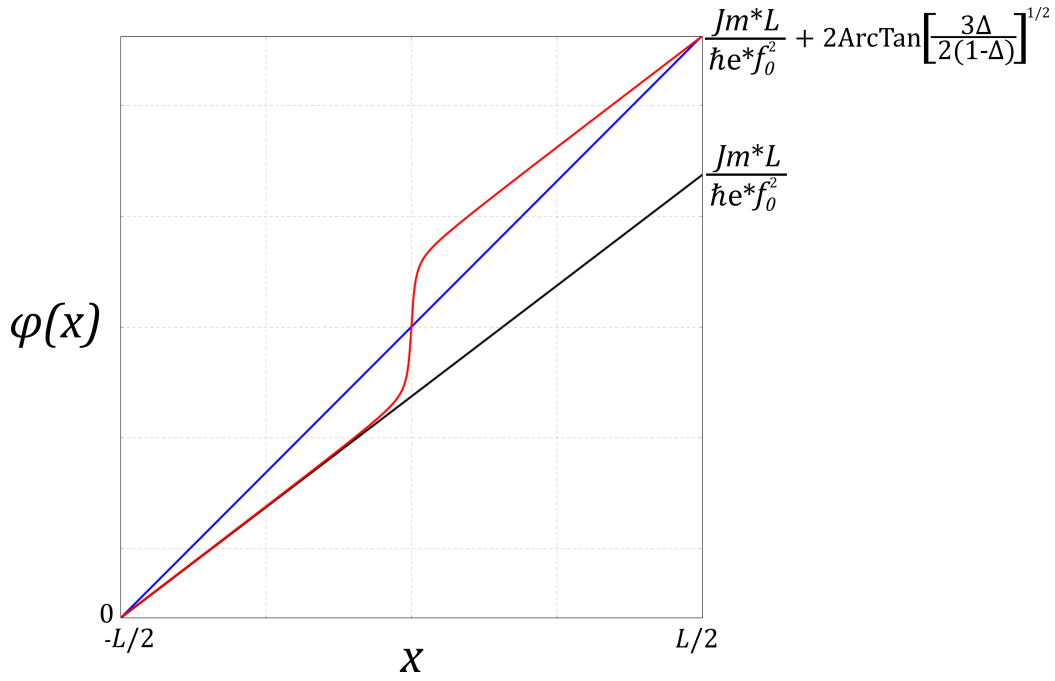

Figure 2.6: The phase $\varphi(x)$ of the order parameter for a 1-dimensional superconductor of length L. The red curve represents the phase of the saddle point solution $\bar{\psi}(x)$. The blue curve represents an order parameter that would have constant amplitude throughout the entire sample, and the same overall phase difference as $\bar{\psi}(x)$. As a result, the blue curve carries slightly higher current than the saddle point solution. The black curve represents a fictitious state assuming the uniform part of the saddle point solution extended over the entire sample.

This δk specifies a current difference δJ. From this, we conclude that the fluctuation that reduces current begins in the uniform state ψ_{k_i}, passes through $\bar{\psi}(x)$, which has a slightly reduced current, and then after $|\psi|$ has passed through zero winds up in the uniform state $\psi_{k_i - \frac{2\pi}{L}}$.[14]

Finally, we have all of the ingredients to calculate the free energy barrier between transitions. Since both our initial state ψ_{k_i} and saddle point solution $\bar{\psi}(x)$ extremize the GL free energy we can write Eq. 2.15, ignoring the field term and in the gauge $\nabla - \frac{ie^*}{\hbar c}\mathbf{A} \to \nabla$,

14. I want to emphasize that the phase slip is from the state ψ_{k_i} through $\bar{\psi}$ and not from ψ_{k_0} through $\bar{\psi}$. In our experiments, the ring geometry imposes periodic boundary conditions on the allowed wave functions and the applied magnetic field specifies the overall phase difference along the circumference of the ring. ψ_{k0}, ψ_{ki}, and $\bar{\psi}$ are all constant current carrying solutions with their respective currents satisfying $I_{\psi_{k0}} = I_{\bar{\psi}} < I_{\psi_{ki}}$. However, only ψ_{k_i} and $\bar{\psi}$ have the same overall phase difference. During a phase slip the phase at the endpoints (far away from the fluctuation region) remains fixed and so to respect the boundary conditions a phase slip must be a transition which begins in ψ_{ki}, passes through $\bar{\psi}$, which carries reduced current, and ends in $\psi_{ki-\frac{2\pi}{L}}$. As phase slips are an intrinsic property of the system, this imposed boundary condition should not have a major impact on the predictions of this theory.

as

$$F = -\frac{1}{2}\sigma\beta \int f^4(x)dx \tag{2.77}$$

where σ is the cross-sectional area of the superconductor. The free energy barrier δF is thus

$$\delta F = F_{\bar{\psi}(x)} - F_{\psi_{k_i}} = -\frac{1}{2}\sigma\beta \int \Big(f^4(x,J) - f_i^4(J_i)\Big)dx \tag{2.78}$$

where we explicitly specified that f and f_i carry different current, and that f_i has no x-dependence as it's the uniform amplitude solution. Expanding f_i^4 to first order in $\frac{1}{L}$

$$\begin{aligned}
f_i^4(J_i) &= f_0^4(J) + \frac{\partial f_0^4}{\partial k_0}\delta k \\
f_i^4(J_i) &= f_0^4(J) + \frac{\partial}{\partial k_0}\left[\frac{\left(|\alpha| - \frac{\hbar^2 k_0^2}{2m^*}\right)^2}{\beta^2}\right]\delta k \\
f_i^4(J_i) &= f_0^4(J) - \frac{4\hbar^2}{2m^*}k\frac{|\alpha| - \frac{\hbar^2 k_0^2}{2m^*}}{\beta^2}\delta k \\
f_i^4(J_i) &= f_0^4(J) - \frac{4\hbar J}{\beta e^* L}\text{ArcTan}\left[\frac{3\Delta}{2\left(1-\Delta\right)}\right]^{1/2}
\end{aligned} \tag{2.79}$$

With the above equation we can write Eq. 2.78 as

$$\begin{aligned}
\delta F &= \frac{1}{2}\sigma\beta\int_{-L/2}^{L/2}\Big(f_0^4(J) - f^4(x,J)\Big)dx - \frac{2\sigma\hbar J}{e^*}\text{ArcTan}\left[\frac{3\Delta}{2\left(1-\Delta\right)}\right]^{1/2} \\
\delta F &= \frac{\alpha^2}{2\beta}\sigma\int_{-L/2}^{L/2}\left(u_0^2 - \left(u_0 - \Delta\text{Sech}^2\left[\frac{x}{\xi}\sqrt{\frac{\Delta}{2}}\right]\right)^2\right)dx \\
&\quad - \frac{8\sqrt{2}}{3}\frac{\alpha^2}{2\beta}\sigma\xi\frac{J}{J_c}\sqrt{\frac{2}{3}}\text{ArcTan}\left[\frac{3\Delta}{2\left(1-\Delta\right)}\right]^{1/2} \\
\delta F &= \frac{8\sqrt{2}}{3}\frac{\alpha^2}{2\beta}\sigma\xi\left(\sqrt{\Delta} - \sqrt{\frac{2}{3}}\frac{J}{J_c}\text{ArcTan}\left[\frac{3\Delta}{2\left(1-\Delta\right)}\right]^{1/2}\right)
\end{aligned} \tag{2.80}$$

where we have used the $f(x)$ given by Eq. 2.71 and the definition of ξ from Eq. 2.18 and J_c from Eq. 2.64. The prefactor of the energy barrier is based on the condensation energy $\frac{\alpha^2}{2\beta}$ multiplied by a volume set by the cross-sectional area and more importantly the coherence length ξ. This indicates that during a phase slip it is only in a small region set by ξ that

the system transitions to the normal state, a conclusion consistent with a conjecture by Little [1] and one that has been experimentally verified [22].

2.3.2 δF near critical current and critical flux

In Appendix A.3 we show that the free energy barrier for a phase slip disappears at the critical current. Therefore, it is useful to expand the terms in Eq. 2.80 about the critical current so that its dependence upon J_c is more transparent.[15] In our experimental realization we bias the rings with flux instead of current, so we will finally express δF in terms of the critical flux Φ_c.

Looking at small deviations from the critical current we will write $j = \frac{J}{J_c} = 1 - \eta$ and with Eq. 2.72 we have

$$\begin{aligned} (2+\Delta)^2 (1-\Delta) &= 4(1-\eta)^2 \\ \Delta = 2\sqrt{\frac{2}{3}}\sqrt{\eta} &= 2\sqrt{\frac{2}{3}}\Big(1 - \frac{J}{J_c}\Big)^{1/2} \end{aligned} \tag{2.81}$$

where we have dropped anything higher order than Δ^2 and η, which are small sufficiently close to J_c. Δ goes to zero at the critical current so we may expand the Arctangent term to the same order in Δ to obtain

$$\mathrm{ArcTan}\left[\frac{3\Delta}{2(1-\Delta)}\right]^{1/2} = \sqrt{\frac{3}{2}}\sqrt{\Delta} + \mathcal{O}\left(\Delta^{5/2}\right) \tag{2.82}$$

Now we can rewrite Eq. 2.80 as

$$\begin{aligned} \delta F &= \frac{8\sqrt{2}}{3}\frac{\alpha^2}{2\beta}\sigma\xi\sqrt{\Delta}\left(1 - \frac{J}{J_c}\right) \\ \delta F &= 16\left(\frac{2}{27}\right)^{1/4}\frac{\alpha^2}{2\beta}\sigma\xi\left(1 - \frac{J}{J_c}\right)^{5/4} \end{aligned} \tag{2.83}$$

To match our experimental realization we will now write δF as a function of $\left(1 - \frac{\Phi}{\Phi_c}\right)$, where Φ_c is the flux at which the critical current is reached, measured from $\Phi_{\mathrm{min},n}$. Before

15. Since we are studying a uniform 1-dimensional superconductor that carries constant current, $I = \sigma J$ and $\frac{I}{I_c} = \frac{J}{J_c}$, so they can be used interchangeably.

deriving this expression, we will note that we can only obtain a simple analytic solution if we consider the free energy barrier for the first winding number $n = 0$, and in the case of $w = 0$.

With these considerations Eq. 2.49 becomes

$$\Phi_c = \frac{R}{\sqrt{3}\xi}\Phi_0 \tag{2.84}$$

and the current, given by Eq. 2.47, takes the form

$$I(n=0,w=0) = \frac{2V\alpha\xi^2|\psi_\infty|^2}{\Phi_0 R^2}\left(1 - \frac{\xi^2}{R^2}\left(\frac{\Phi}{\Phi_0}\right)^2\right)\frac{\Phi}{\Phi_0} \tag{2.85}$$

and so the critical current is

$$I(n=0,w=0,\Phi=\Phi_c) \equiv I_c = \frac{2V\alpha\xi^2|\psi_\infty|^2}{\Phi_0 R^2}\frac{2R}{3\sqrt{3}\xi} \tag{2.86}$$

Now, we will express Eq. 2.85 about the critical flux such that $\Phi = \Phi_c - \eta$, where η is again a small parameter. The current, with Eq. 2.86, is thus

$$\begin{aligned} I(\Phi_c - \eta) &= \frac{3\sqrt{3}\xi}{2R} I_c \left(1 - \frac{\xi^2}{R^2}\left(\frac{\Phi_c - \eta}{\Phi_0}\right)^2\right)\frac{\Phi_c - \eta}{\Phi_0} \\ I(\Phi_c - \eta) &= I_c\left(1 - \frac{3}{2}\left(\frac{\eta}{\Phi_c}\right)^2\right) \end{aligned} \tag{2.87}$$

where we have used Eq. 2.84 for Φ_c and Φ_0 and dropped term of order η^3. Substituting η back into this equation we arrive at

$$\begin{aligned} \frac{I}{I_c} &= -\frac{1}{2} + 3\frac{\Phi}{\Phi_c} - \frac{3}{2}\left(\frac{\Phi}{\Phi_c}\right)^2 \\ \frac{I}{I_c} &= 1 - \frac{3}{2}\left(1 - \frac{\Phi}{\Phi_c}\right)^2 \end{aligned} \tag{2.88}$$

Substituting this equation into Eq. 2.83 we obtain

$$\delta F = 8\sqrt{3}\frac{\alpha^2}{2\beta}\sigma\xi\left(1 - \frac{\Phi}{\Phi_c}\right)^{5/2} \tag{2.89}$$

One final note is that in the above equation Φ is not the absolute flux and instead represents the flux distance from $\Phi_{\min,n}$. If using the absolute total flux Φ_{Abs}, one should write $\Phi = \Phi_{\text{Abs}} - \Phi_{\min,n}$.

2.3.3 Hysteresis in $I(\Phi)$

Now that we have determined that the free energy barrier for phase slips disappears at I_c, or equivalently Φ_c, we can explain the origin of hysteresis in the measured supercurrent. This will complete the discussion started in Section 2.2.5.4.

As long as $\frac{R}{\xi} > \frac{1}{2}$ there will not be a re-entrant normal state. However if $\frac{1}{2} < \frac{R}{\xi} < \frac{\sqrt{3}}{2}$, then the free energy barrier for a phase slip (in the case of increasing flux to drive a transition from state ψ_n to state ψ_{n+1}) will always disappear before ψ_{n+1} has lower free energy than that of state ψ_n. Transitions to states of higher energy are not favorable and do not occur, so a phase slip does not occur until the flux at which the free energy of ψ_{n+1} and ψ_n are equal. If we then reverse this argument and decrease the flux to drive transitions from ψ_{n+1} to ψ_n, again we find that the barrier disappears before state ψ_n has lower energy than state ψ_{n+1}, and so the phase slip does not occur until the exact same location where ψ_n and ψ_{n+1} have the same energy. Thus, in this regime the location of a phase slip is the same regardless of the flux ramp direction and no hysteresis is observed. This is illustrated in the left column of Fig. 2.7.

In the case of $\frac{R}{\xi} > \frac{\sqrt{3}}{2}$, the energy barrier for phase slips is non-zero at the flux where two states have equal free energy. Thus, a phase slip is prohibited at this flux and the system will remain in the same state (which is now metastable). Only when the critical flux is reached can the system transition. Consequently, the system will trace a difference path along the free energy diagram depending upon the direction of the flux bias, illustrated in the right column of Fig. 2.7. This path difference can lead to a substantial hysteresis in the measured supercurrent.

2.3.4 Finite length correction

There is one final correction we need to make to $\Phi_{c,n}$ given by Eq. 2.49. In Appendix A.3, we found that the free energy barrier between constant current carrying states disappears

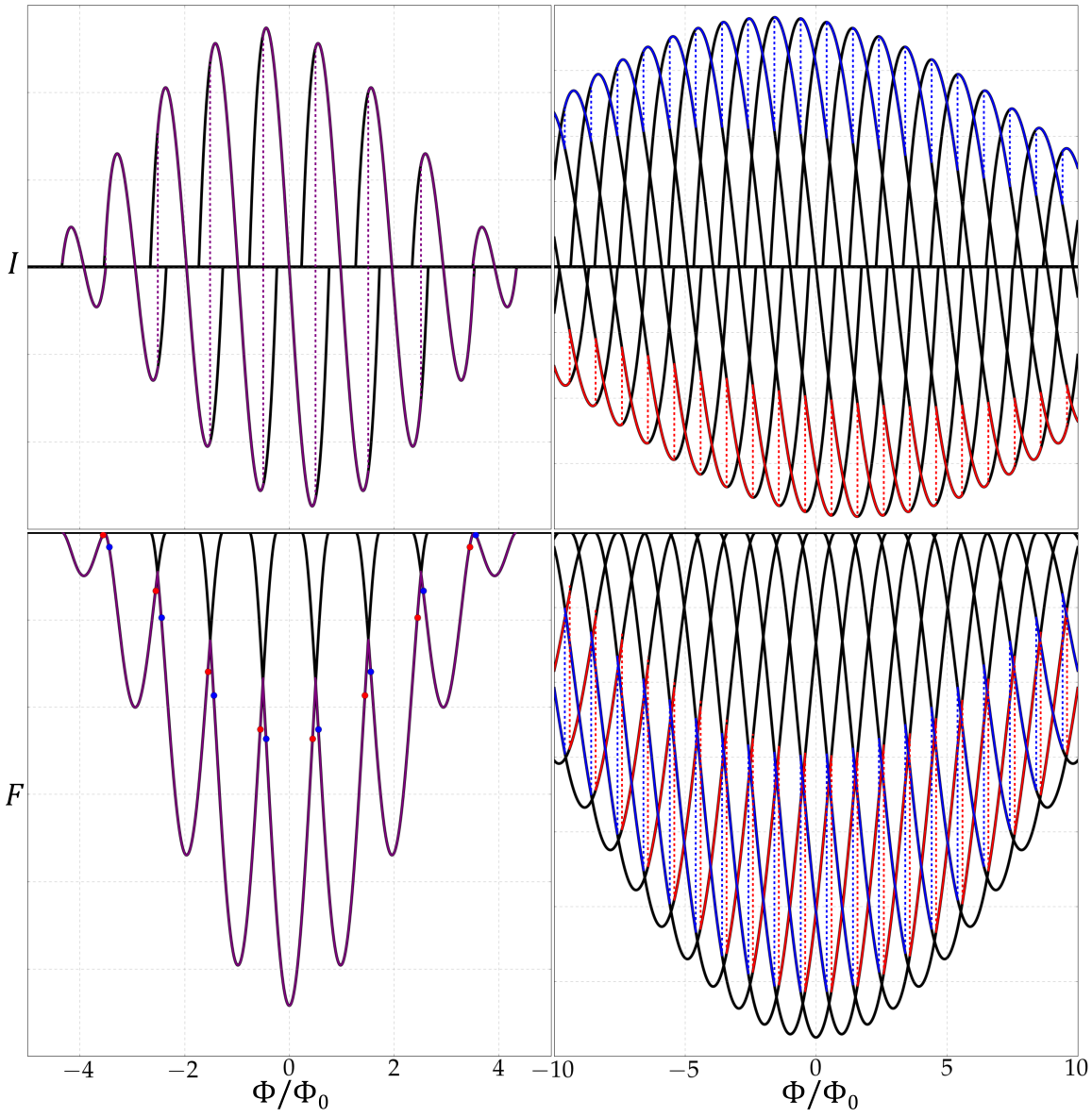

Figure 2.7: Supercurrent (top panels) and free energy (bottom panels) as a function of applied flux for a superconducting ring with $R = 0.75\xi$ (left column) and a ring of $R = 3\xi$ (right column). Black curves represent the full free energy and supercurrent landscape. Red and blue curves correspond to actual path taken when increasing or decreasing flux, respectively. Purple is used when red and blue overlap and dashed lines are used as a visual guide when a phase slip causes a discontinuous transition from one curve to another. In the left column the dots mark the location where the free energy barrier goes to zero for the given flux ramp direction. As there is no superconducting state of lower energy available at these fluxes, the system must wait until energy levels cross to undergo a phase slip. In the right column, transitions are prohibited by a finite free energy barrier when neighboring states have equal free energy. As a result, phase slips do not occur until Φ_c and the system will trace out a different path dependent upon the flux ramp direction. As a result, the corresponding supercurrent displays a noticeable hysteresis.

when $|\alpha| = 3\frac{\hbar^2 k^2}{2m^*}$, a condition that is identical to that of the critical current at $\Phi_{c,n}$. Thus, we deduced that a phase slip occurs at this critical flux. However, to obtain this result we took the limit $p \to 0$ in Eq. A.46, and in doing so we neglected the boundary condition of the ring, as p cannot take on an arbitrarily small value. Now we will revisit that problem and properly impose a boundary condition on p.

We must solve for the point at which an eigenvalue given by Eq. A.46 first becomes negative, without assuming anything about p. The general solution to this problem is given by the parabola

$$|\alpha| = \frac{\hbar^2}{2m^*}\left(3k^2 - \frac{1}{2}p^2\right) \tag{2.90}$$

and so we see that this result is consistent with our previous result if we allow $p \to 0$. However, we must recall that in this derivation (now simplifying to one dimension) we were looking at some initial state $\psi_k = f_k e^{ikx}$ and a perturbation $\nu(x) = \mathrm{Re}[Ae^{i(k+p)x}]$, where A is some amplitude. Due to the ring geometry and the fact that ψ must be single-valued there is a quantization on k and $k+p$ given by

$$\frac{Lk}{2\pi} = n_1 \qquad\qquad \frac{L(k+p)}{2\pi} = n_2 \tag{2.91}$$

where L is the circumference of the ring and n_1 and n_2 are integers. This restricts the valid forms of $\nu(x)$ that we can consider. Since $\frac{Lk}{2\pi}$ is an integer it follows that $\frac{Lp}{2\pi}$ must also be an integer, and thus the smallest non-zero value[16] of p we can consider is $p = \frac{2\pi}{L}$. With this, our stability condition given by Eq. 2.90 becomes

$$|\alpha| = \frac{\hbar^2}{2m^*}\left(k^2 - \frac{2\pi^2}{L^2}\right) \tag{2.92}$$

Now using $m^* v_s = \hbar k$ from Eq. 2.22, the definition of ξ from Eq. 2.18 and re-writing the circumference $L = 2\pi R$ we find that the velocity including the finite length, v_f, is stabilized

16. We do not consider $p = 0$ because the perturbation and the initial state would be identical up to some amplitude, so by simply renormalizing $\psi_k + \nu(\mathbf{x})$ we would arrive at the exact same initial state.

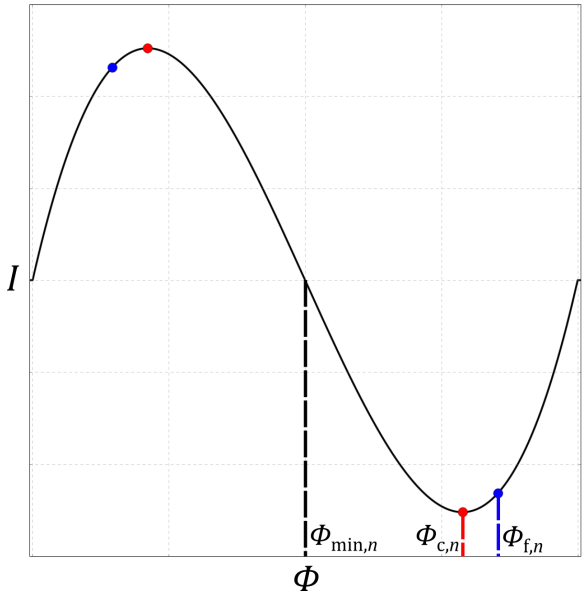

Figure 2.8: Supercurrent as a function of magnetic flux for $n = 0$ and a ring with dimensions $R = \xi(T)$. The location of the critical current and critical flux, given by Eq. 2.49, are denoted with red circles. The blue circles indicate the switching flux including the finite length correction, which allows the system to remain stable beyond the critical current.

past the normal critical velocity without this boundary condition v_c such that

$$v_f^2 = \frac{2|\alpha|}{3m^*}\left(1 + \frac{\xi^2}{2R^2}\right) = v_c^2\left(1 + \frac{\xi^2}{2R^2}\right) \tag{2.93}$$

It is important to note that critical values are always referenced from where $I = 0$, which in our notation is a distance from $\Phi_{\min,n}$. Thus, the finite length correction does not affect $\Phi_{\min,n}$ and we can write the finite length stabilized critical flux $\Phi_{f,n}$ as a correction to Eq. 2.49,

$$\frac{\Phi_{f,n}}{\Phi_0} = \frac{\Phi_{\min,n}}{\Phi_0} \pm \frac{\sqrt{\xi^2\left(1 + \left(\frac{w}{2R}\right)^2\right)\left[3R^2\left(1 + \left(\frac{w}{2R}\right)^2\right) - \xi^2 n^2\left(\frac{w}{2R}\right)^2\left(4 + \left(\frac{w}{2R}\right)^2\right)\right]}}{3\xi^2\left(1 + \left(\frac{w}{2R}\right)^2\right)}\sqrt{1 + \frac{\xi^2}{2R^2}} \tag{2.94}$$

$$\Phi_{f,n} = \Phi_{\min,n} \pm \Phi_0 \frac{R}{\sqrt{3}\xi}\sqrt{1 + \frac{\xi^2}{2R^2}} + \mathcal{O}\left(\left(\frac{w}{2R}\right)^2\right) \tag{2.95}$$

This correction will be most obvious in systems close to T_c where $\xi(T) \gg R$ or in systems

with small R. A case of $R = \xi(T)$ is illustrated in Fig. 2.8.

2.4 Thermal activation over an energy barrier

Up until this point we have only considered deterministic phase slips in the sense that we have ignored any fluctuations and have assumed that a system can only transition when $\delta F = 0$. However, superconducting systems exist at finite temperature and in the presence of external noise, both of which allow for the system to overcome a small but finite δF. In the following sections we consider thermal fluctuations and discuss how this stochastic process affects experimentally measurable quantities like $P(\Phi_{\rm sw})$, the probability distribution of the flux at which a given phase slip will occur.

2.4.1 Arrhenius escape rate

In a simplified picture, a phase slip represents an event in which a superconducting system begins in an initial metastable state and transitions over an energy barrier to a final metastable state. While the free energy barrier given by Eq. 2.89 depends upon the details of superconductivity, the process of a escaping over an energy barrier is a ubiquitous problem treated in many fields.

In chemistry, this problem was encountered in 1889 when Hecht and Conrad measured the reaction rate k of $CH_3J + C_2H_5ONa \rightarrow CH_3OC_2H_5 + NaJ$ [23]. For such a chemical reaction to occur, the chemical reactants must pass through a transition state of higher energy before the product state is reached. The activation energy $E_{\rm a}$ is defined as the energy difference between the reactants and the transition state. Svante Arrhenius then took their reaction rate data and by plotting the logarithm of the reaction rate against reaction temperature he found an empirical law [24]

$$k = A\exp\left(-\frac{E_{\rm a}}{k_{\rm B}T}\right) \tag{2.96}$$

where A was a fitting parameter. Thus, the rate of such a transition is governed completely by the ratio of the energy barrier to the thermal energy of the system $k_{\rm B}T$. Further, it

is now understood that in some simple cases the fitting parameter A is the characteristic frequency of oscillations in the potential confining the system to its initial metastable state, $A = \frac{\omega_0}{2\pi}$ [25, 26].

The applicability of Eq. 2.96 is based upon one major assumption, that the system exists in thermodynamic equilibrium. Arrhenius argued that in thermal equilibrium the fraction of molecules that have energy greater than E_a can be calculated from statistical mechanics, and as these are the only molecules with enough energy to overcome the energy barrier the rate should only depend upon this fraction of molecules. Today, we know the fraction of such molecules in thermal equilibrium would follow a Maxwell-Boltzmann distribution given by $\exp\left(-\frac{E_\mathrm{a}}{k_\mathrm{B}T}\right)$. Further in more complicated problems, the frequency $\frac{\omega_0}{2\pi}$ can also depend upon the curvature of the potential near the transition state. Damping can further modify this frequency. Also, for multidimensional problems one needs to consider the the number of states near the initial metastable state and the number of states near the saddle point region to correctly calculate this prefactor [27].

For the rings studied in this work, the assumption of thermal equilibrium is satisfied. As we will describe in Chapter 4, cantilever torque magnetometry allows us to measure the current in superconducting rings without attaching any leads to the sample. Therefore, the superconducting rings are measured in equilibrium in an electromagnetically pristine environment. As all prior measurements have indicated that the electron temperature is the same as the helium bath temperature; that is, the rings are in thermal equilibrium, we have no reason to believe otherwise [3, 28, 29]. Though many of these previous measurements relied upon the normal state electrons, the array measurements presented in this work and prior measurements made on bulk aluminum samples [30] both indicate that the superconducting electrons are also in equilibrium with the thermal bath. Further we note that the most relevant energy barrier for the escape rate is between the "reactant state" and the transition state. This is because the majority of our data is taken when $\frac{R}{\xi} > \frac{\sqrt{3}}{2}$. In this situation, at the flux where $\delta F \to 0$ for the transition $\psi_n \to \psi_{n+1}$, there is an enormous energy barrier for the transition $\psi_{n+1} \to \psi_n$, and thus the energy decreasing transitions dominate the rate. This point is illustrated in right column of Fig. 2.7 as the location of phase slips for the increasing flux ramp is not the same as that for the decreasing flux ramp.

With both of these assumptions met, and the obvious parallels between reaction rates and phase slips, we can write that the rate of thermally activated phase slips (TAPS) Γ is given by

$$\Gamma(T,\Phi) = \frac{\omega(T)}{2\pi}\exp\left(-\frac{8\sqrt{3}}{k_{\mathrm{B}}T}\frac{\alpha(T)^2}{2\beta(T)}\sigma\xi(T)\left(1-\frac{\Phi}{\Phi_{\mathrm{f}}(T)}\right)^{5/2}\right) \tag{2.97}$$

where we have specified the temperature-dependent quantities and used the energy barrier given by Eq 2.89 with the finite length corrected switching flux. Still, we need to calculate ω for a superconducting ring. In a 0-dimensional system like a Josephson junction, where a phase slip must occur at a single specific location, the superconducting system can be described by a tilted washboard potential $U(\varphi)$, where φ is the phase difference across the Josephson junction. As this potential is only one-dimensional, it is straightforward to calculate both the energy barrier for transitions between successive minima, δF, and the curvature of the potential at the local minima, ω_0 [31]. This is in stark contrast to the lengthy calculation we employed to determine the energy difference between a metastable state and the saddle point state for a uniform ring in Section 2.3.1. We should also note that while the entire potential landscape is determined in the case of a Josephson junction, our saddle point calculation only succeeds in determining the energy difference between the initial state and saddle point state. We determine almost nothing about the overall potential landscape, which reflects the fact that in a uniform ring our potential landscape is not a function of a single variable, but spans the configuration space of all functions $\psi(x)$. Fortunately, the exponential dependence of the Maxwell-Boltzmann factor tends to dominate the behavior of $\Gamma(\Phi,T)$. Thus, while the value of ω can modify the $\Gamma(\Phi,T)$ by orders of magnitude, as we will show in Section 2.4.3 the resulting probability distribution is typically insensitive to the detailed form of ω [32].

One way to estimate the prefactor of Eq. 2.97 is through the use of time-dependent Ginzburg Landau theory [33]. McCumber and Halperin calculated that in the case of $I = 0$, the prefactor is

$$\frac{\omega(T)}{2\pi} \equiv \Omega(T) = \frac{L\sqrt{3}}{2\pi^{3/2}\xi(T)}\frac{1}{\tau_{\mathrm{GL}}(T)}\sqrt{\frac{\delta F(I=0)}{k_{\mathrm{B}}T}} \tag{2.98}$$

where $\tau_{\rm GL}(T)$ is a microscopic Ginzburg Landau time given by

$$\tau_{\rm GL}(T) = \frac{\pi h}{8k_{\rm B}(T_{\rm c} - T)} \tag{2.99}$$

As we are at $I = 0$ our expansion of δF about the critical current or critical flux is not valid, so we should use Eq. 2.80 for the energy barrier. When $I = 0$, $J = 0$ and $\Delta = 1$. Thus, $\delta F(I = 0) = \frac{8\sqrt{2}}{3}\frac{\alpha^2}{2\beta}\sigma\xi$. With this, the full form of the prefactor at zero current is

$$\Omega(T) = \frac{8 * 2^{3/4} L}{\pi^{5/2} h\xi(T)} k_{\rm B}\left(T_{\rm c} - T\right)\sqrt{\frac{1}{k_{\rm B}T}\frac{\alpha(T)^2}{2\beta(T)}\sigma\xi(T)} \tag{2.100}$$

Expanding this to finite current, in the limit that $I \to I_{\rm c}$ they find that prefactor for current decreasing fluctuations (phase slips to states of lower free energy) is given by[17]

$$\Omega(I \to I_{\rm c}, T) \approx \frac{1}{8\sqrt{6}}\left(\frac{3}{e}\right)^3 \Delta^{15/4}\Omega(T) \tag{2.101}$$

$$\Omega(I \to I_{\rm c}, T) \approx \frac{4}{9}\left(\frac{2}{27}\right)^{1/8}\left(\frac{3}{e}\right)^3\left(1 - \frac{I}{I_{\rm c}}\right)^{15/8}\Omega(T) \tag{2.102}$$

$$\Omega(I \to I_{\rm c}, T) \approx \frac{2^{1/4}}{\sqrt{3}}\left(\frac{3}{e}\right)^3\left(1 - \frac{\Phi}{\Phi_{\rm c}}\right)^{15/4}\Omega(T) \tag{2.103}$$

where $e \approx 2.718$, Δ is given by Eq. 2.81 close to $I_{\rm c}$ and $\Omega(T)$ is the prefactor when $I = 0$. In the last line we related current and flux close to the critical current using Eq. 2.88. Also, over the full range of current this prefactor is approximated by

$$\Omega(I, T) \approx \left(1 - \sqrt{1 - \Delta}\right)^{15/4}\left(1 + \frac{1}{12}\left(1 - \Delta\right)\right)\Omega(T) \tag{2.104}$$

Ultimately, regardless of the precise form of Ω the overall temperature dependence is still set by $\frac{1}{\xi\tau_{\rm GL}}\sqrt{\frac{\delta F(I=0)}{k_{\rm B}T}}$.

17. Langer & Ambegaokar (LA) [21] and McCumber & Halperin (MH) [33] both calculate the free energy barrier for a phase slip (Eq. 3.22 and Eq. 2.13a in their respective reference) and arrive at the same answer, with slightly different notation. While LA use $\frac{\alpha^2}{2\beta}$ MH use $\frac{H_{\rm c}^2}{8\pi}$ and by the definition of condensation energy, Eq. 2.10, these two are exactly equal. The other difference is that LA and this text work with Δ which is defined by Eq. 2.72. MH work with κ and the two are related by $\Delta = 1 - 3\kappa^2$. As a result, in LA when $I \to I_{\rm c}, \Delta \to 0$ while for MH this implies $\kappa \to \frac{1}{\sqrt{3}}$

2.4.2 The switching distribution $P(\Phi_{\rm sw})$

In the previous section we derived the phase slip rate, Eq. 2.97. In this section, we will relate Γ to the probability distribution of observing a phase slip at a given flux $P(\Phi_{\rm sw})$, which can be directly measured by slowly varying the flux Φ and recording the value of Φ when a phase slip occurs and then repeating that same measurement many times.

To set up this derivation, we will consider ramping flux at a constant rate given by $\Phi(t) = \dot{\Phi}t$. While our experimental realization consists of ramping flux in a sawtooth pattern N times over a single ring, for the purpose of this derivation it is equivalent to consider a system of N identical rings all initialized in the same state and a single flux ramp. A phase slip would then cause a single ring to transition to a final state of lower energy (for a ramp of increasing flux we are considering $\psi_n \rightarrow \psi_{n+1}$). In this system we can define $W(t)$ as the fraction of rings that still remain in the initial state at time t, which given a phase slip rate $\Gamma[\Phi(t)]$ will evolve according to

$$\frac{dW(t)}{dt} = -\Gamma[\Phi(t)]W(t) \tag{2.105}$$

That is, the number of rings that will undergo a phase slip is proportional to the phase slip rate and the population of rings that has yet to experience a phase slip. As $\delta F_{n+1\rightarrow n} \gg \delta F_{n\rightarrow n+1}$ we only need to consider the phase slips which decrease $W(t)$. With the initial condition $W(0) = 1$ we can solve this differential equation to obtain

$$W(t) = \exp\Big(-\int_0^t \Gamma[\Phi(t')]dt' \Big) \tag{2.106}$$

$$W(\Phi_{\rm sw}) = \exp\Big(-\int_0^{\Phi} \frac{\Gamma[\Phi']}{\dot{\Phi}} d\Phi' \Big) \tag{2.107}$$

where we have imposed the condition of our linear flux ramp in Eq. 2.107. $W(\Phi_{\rm sw})$ is the normalized probability that a ring remains in its initial metastable state up to flux Φ, and thus $1 - W(\Phi_{\rm sw})$ is the cumulative distribution function for the probability of a phase slip occurring at flux Φ. The probability density function is the derivative of the cumulative

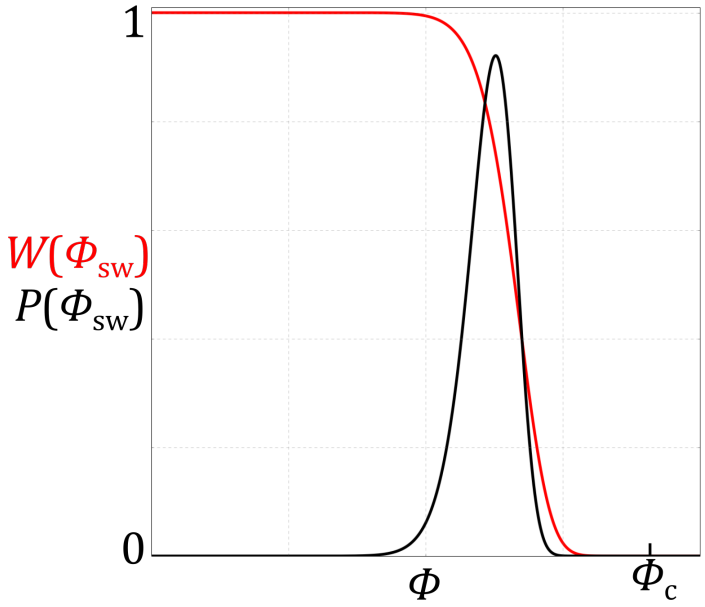

Figure 2.9: Cumulative distribution function (red) and normalized probability distribution function (black) for the flux at which a phase slip occurs in a uniform superconducting ring given an escape rate $\Gamma(\Phi) \sim \exp\left[-\frac{\delta F}{k_B T}\left(1-\frac{\Phi}{\Phi_c}\right)^{5/2}\right]$. In this figure flux is increased from 0 to Φ_c, which drives transitions from ψ_n to ψ_{n+1}. Thermal fluctuations allow phase slips to occur below Φ_c where there is still a small but finite energy barrier. The PDF is negatively skewed for the case of increasing flux, while for decreasing the flux the PDF is positively skewed.

distribution function, thus,[18]

$$P(\Phi_{sw}) = \frac{d}{d\Phi}\Big(1 - W(\Phi_{sw})\Big) = \frac{\Gamma(\Phi)}{\dot{\Phi}}\exp\Big(-\int_0^{\Phi}\frac{\Gamma[\Phi']}{\dot{\Phi}}d\Phi'\Big) \tag{2.108}$$

An example of the expected shape of $W(\Phi_{sw})$ and $P(\Phi_{sw})$ is shown in Fig. 2.9.

2.4.3 Langer-Ambegaokar temperature dependence of thermally activated phase slip cumulants

Many of the parameters in the phase slip rate equation are temperature-dependent, and as a result, $P(\Phi_{sw})$ will vary with temperature. Experimentally we can control and vary temperature, and so in this section we will derive the temperature dependence of the first two cumulants, mean and variance, for TAPS within the LAMH theory. We will

18. Here we use the fundamental theorem of calculus, $\frac{d}{dx}\int_a^x f(t)dt = f(x)$

also indicate that the higher cumulants, namely the skewness γ_1 and kurtosis γ_2, take on universal values that are to first order temperature-independent.

Garg studied the first two cumulants in a general treatment where the escape rate can be written in the form [32]

$$\Gamma = \Omega_0 \left(1 - \frac{G}{G_c}\right)^{a+b-1} \exp\left(- B \left(1 - \frac{G}{G_c}\right)^{b} \right) \tag{2.109}$$

where a, b, A, B and Ω_0 depend on the specific system being studied and G represents a bias with its corresponding critical value G_c. For a ring biased with flux, as is studied in this work, we would use $G = \Phi$, $b = 5/2$, $B = \frac{\delta F(I=0)}{k_B T} = \frac{8\sqrt{2}}{3}\frac{\alpha^2}{2\beta}\sigma\xi\frac{1}{k_B T}$, and $\Omega_0 = \Omega(T)$ of the previous section, but for now we will keep the treatment more general. With the general escape rate of Eq. 2.109, the mean $\langle G_{sw}\rangle$ and standard deviation $\sigma_{G_{sw}}$ of the switching distribution of G are approximated by[19]

$$\langle G_{sw}\rangle = G_c \left(1 - \frac{\ln\left(\Omega_0 t_\sigma\right)^{1/b}}{B^{1/b}}\right) \qquad \sigma_{G_{sw}} = \frac{\pi G_c}{\sqrt{6}b}\ln\left(\Omega_0 t_\sigma\right)^{1/b-1} B^{-1/b} \tag{2.110}$$

where t_σ corresponds to the time spent sweeping through the transition region and is typically on the order of 1 second for our experiments. Consistent with our arguments of the previous section, we find that the prefactor Ω_0 only appears logarithmically and so it will not be important in determining the leading temperature-dependence. Further, the measurements discussed in Chapter 7 are taken between $0.25 - 0.75T_c$, and as a result we do not expect to observe any temperature dependent quantities to change by many orders of magnitude as would happen very close to T_c given the $\left(1 - \frac{T}{T_c}\right)$ dependence of most GL parameters. Thus, we will assume that the logarithm term is constant as a function of temperature.[20]

19. Garg derives formulas for the mean and variance of the reduced bias field $\epsilon = 1 - \frac{G}{G_c}$, and so the variance and standard deviation of G follow from the linearity of the mean and variance, $\langle\epsilon\rangle = 1 - \frac{\langle G\rangle}{G_c}$ and $\sigma_\epsilon = \frac{1}{G_c}\sigma_G$

20. Given that t_σ is on the order of 1 second, if Ω_0 varies between 10 and 10^{40}, $\ln(\Omega_0 t_\sigma)$ only varies between 2 and 115. Therefore, without much knowledge of the actual escape rate we can still get an accurate picture of how the mean and standard deviation vary.

Returning to our experimental realization, $B = \frac{\delta F(I=0)}{k_{\rm B}T}$ varies with temperature as $\frac{\alpha(T)^2}{2\beta(T)}\xi(T)\frac{1}{T}$ and in GL theory close to $T_{\rm c}$ we expect $|\alpha|$ to vary as $1-\frac{T}{T_{\rm c}}$ with $\beta \approx$ constant. ξ is related to $|\alpha|$ through Eq. 2.18, and so the total temperature dependence is

$$B = \frac{\delta F(I=0)}{k_{\rm B}T} \approx \frac{\left(1-\frac{T}{T_{\rm c}}\right)^{3/2}}{T} \tag{2.111}$$

The critical parameter $G_{\rm c}$ is $\Phi_{\rm c}$ which varies as $\frac{1}{\xi}$ for an infinitely large ring (Eq. 2.49) or $\frac{1}{\xi}\sqrt{1+\frac{\xi^2}{2R^2}}$ for a finite length ring (Eq. 2.95). Thus, we expect the following leading temperature-dependence for the $R \gg \xi(T)$ ring

$$\langle \Phi_{\rm sw,c} \rangle \approx \sqrt{1-\frac{T}{T_{\rm c}}} \qquad\qquad \sigma_{\Phi_{\rm sw,c}} \approx \frac{T^{2/5}}{\left(1-\frac{T}{T_{\rm c}}\right)^{1/10}} \tag{2.112}$$

The inclusion of finite length corrections or the B term in the mean require some assumptions about the relative ratio of R and $\xi(T)$, and an estimate of Ω_0 and $\frac{\delta F}{k_{\rm B}T}$, but ultimately will not change the trend of the above formulas. That is, we expect the mean of the phase slip distribution to decrease with increasing temperature, and the standard deviation to increase with increasing temperature for thermally activated phase slips.

One final point is that though we used the GL temperature dependence to illustrate the general temperature trends, Eq. 2.110 can still be applied with the more complete forms of $\alpha(T)$, $\beta(T)$, and $\xi(T)$ expressed in terms of the empirical parameters $B_{\rm c}(T)$ and $\lambda(T)$. Thus, this discussion of cumulants can easily be extended over a wider range of temperatures once the form of $B_{\rm c}(T)$ and $\lambda(T)$ are known.

Murphy *et al.* [34] extended the analysis of Garg to higher cumulants. By introducing the dimensionless parameter

$$Z = \ln\left[\frac{G_{\rm c}}{\dot{G}}\frac{\Omega_0}{bB^{1+a/b}}\right] \tag{2.113}$$

they expanded the moments μ_i of the distribution in an asymptotic power series in $1/Z$ and found

$$\sigma_\epsilon^2 \equiv \mu_2 = Z^{2/b-2}B^{-2/b}\left(\frac{\pi^2}{6b^2} + \frac{1}{Zb^3}\Big(\frac{a\pi^2}{3} + (1-b)\big(\frac{\pi^2}{3}(\frac{a}{b}\ln Z + \gamma_{\mathrm{E}}\big) + \psi''(1)\big)\Big)\right) \quad (2.114)$$

$$\mu_3 = B^{-3/b}Z^{3/b-3}\Big(-\frac{\psi''(1)}{b^3} + \delta_3\Big) \quad (2.115)$$

$$\mu_4 = B^{-4/b}Z^{4/b-4}\Big(\frac{30\pi^4}{20b^4} + \delta_4\Big) \quad (2.116)$$

where $\gamma_{\mathrm{E}} \approx 0.577$ is the Euler-Masheroni constant, $\psi''(1) \approx -2.404$ is the tetragamma function, and δ_3 and δ_4 are corrections of the order Z^{-1} to their respective moments. Eq. 2.114 recovers the result from Garg. From these moments they calculated the skewness and kurtosis,

$$\gamma_1 = -\frac{\mu_3}{\mu_2^{3/2}} = \frac{6^{3/2}}{\pi^3}\psi''(1) + \mathcal{O}\left(Z^{-1}\right) \quad (2.117)$$

$$\gamma_2 = \frac{\mu_4}{\mu_2^2} = \frac{27}{5} + \mathcal{O}\left(Z^{-1}\right) \quad (2.118)$$

which take on universal values to leading order in Z^{-1}. Though these are the skewness and kurtosis of the reduced bias field ϵ, since by definition these terms are normalized by the variance, $\gamma_{1,\epsilon} = \gamma_{1,G}$. Thus, $\gamma_{1,\Phi_{\mathrm{sw}}} \approx -1.139$ and $\gamma_{2,\Phi_{\mathrm{sw}}} \approx 5.4$. This result is rather remarkable as Eq. 2.109 is a general escape rate capable of modeling both thermal and quantum phase slips with various amounts of damping through the parameters a, b, A and B. However, as γ_1 and γ_2 are insensitive to these parameters, the switching distributions will always have the same skewness and kurtosis regardless of the underlying escape mechanism, provided that $1/Z \ll 1$. Given this universality, the higher moments can be used to check for undesirable noise within the measurement, as extraneous noise can lead to significant deviations from these values [34].

Given that this expansion relies upon $1/Z \ll 1$ we must ensure this is satisfied for our experiment. The magnitude of the prefactor for escape is set by the GL time. As most measurements are taken far away from T_{c} the magnitude is predominantly set by the ratio of $\frac{\hbar}{k_{\mathrm{B}}T_{\mathrm{c}}} \approx 10^{-11}$ s. The other major factor in the attempt frequency is $\sqrt{\frac{\delta F(I=0)}{k_{\mathrm{B}}T}}$ which we will show is approximately 50-100 for the experiments in this text. As a result, from Eq. 2.100,

$\Omega_0 \approx 10^{12}$ Hz. B is set by $\frac{\delta F(I=0)}{k_B T}$, which is on the order of 5000, and $\Phi_c/\dot{\Phi} \approx 100 - 1000$ for the measurements in Chapter 7. Thus, $Z^{-1} \approx 0.04$, which satisfies the assumption of $Z^{-1} \ll 1$.[21]

21. We could have also just used $Z = \ln\left(\Omega_0 t_\sigma\right)$, where in Chapter 7 we will show the typical measurement time to sweep through a the probability distribution is 10-20 s. This result equivalently leads to $Z^{-1} \approx 0.04$.

Chapter 3

Review of previous experimental work on phase slips

Phase slips play an integral role in determining the properties of certain superconducting systems and give rise to interesting phenomena such as flux-periodic oscillations of the superconducting transition temperature T_c. As a result, phase slips have been studied experimentally in a wide variety of superconducting systems, beginning as early as 1961. This chapter begins with a review of the first experimental observations of phase slips in superconducting systems and then discusses phase slips in superconducting rings and nanowires, that former of which is directly relevant to this work.

The first experimental measurement of phase slips is credited to Deaver and Fairbanks, who measured the quantization of magnetic flux trapped in hollow superconducting tin cylinders [35]. This lead to Little and Parks' measurement of T_c oscillations in similar tin cylinders [2]. Shortly after this, Josephson junctions were created and a strong effort was put forth to fully characterize the properties of these devices. Of particular interest was the effect of noise on these junctions and how it would ultimately impact their sensitivity, which lead to the measurement of thermally excited fluxoid transitions in rings closed by a Josephson junction by Jackel *et al.*, and Fulton and Dunkleberger's measurement of the lifetime of the zero-voltage state in Josephson tunnel junctions [31, 36]. These were the first measurements to study the statistics of thermally activated phase slips. As fabrication

techniques improved and pushed devices smaller and smaller, phase slips became even more important, for instance giving rise to the finite resistance of thin superconducting nanowires and causing the decay of persistent current in superconducting nanorings [1]. This, along with the goal of observing macroscopic quantum tunneling in a homogeneous superconductor, sparked recent interest in the field and has led to numerous works on phase slips in rings [22, 37–41] and nanowires [34, 42–48].

3.1 Little-Parks oscillations

In 1961 Deaver and Fairbanks fabricated hollow tin cylinders, cooled them below their superconducting transition temperature, and biased them with flux by ramping a magnetic field normal to the cylinder's cross-section. When the magnetic field reached a certain value (corresponding to approximately $0.6\Phi_0$ of flux through the cross-section of the cylinder) they found that Φ_0 of flux became trapped within the cylinder. They further observed that the amount of trapped flux remained completely constant until the field reached nearly 3 times that of the initial trapping field, at which point the trapped flux increased to twice its original amount. When the field reached roughly five times that of the original trapping field, the trapped flux again increased by Φ_0. The triumph of this work is that it proved that the quantized unit of flux for such a superconducting system is $\Phi_0 = h/2e$ and not h/e, as originally suggested by London and Onsager in the early 1950s. As this experiment was performed after the discovery of BCS theory, Byers and Yang demonstrated that the $h/2e$ quantization was simply a result of the electrons pairing within the superconductor [49]. This work also demonstrated that for a ring geometry in thermal equilibrium where $L \gg \xi(T)$, fluxoid transitions are energetically favorable when when the free energy of states of different winding numbers cross, i.e. at flux values of $(n + \frac{1}{2})\Phi_0$, which is consistent with Eq. 2.33.

Little and Parks expanded upon this work in the following year, by noting that while the superconducting free energy of these tin cylinders is Φ_0 periodic in applied flux, the normal state free energy is virtually flux-independent. Thus T_c, the temperature at which the free energy of the normal state and superconducting state are equal, must also be periodic in

applied flux. By maintaining the tin cylinders at a constant temperature just below T_c and sweeping a magnetic field, Little and Parks observed periodic oscillations in the resistance of these tin cylinders, agreeing both with the periodicity predicted by BCS theory and the magnitude predicted by Byers and Young. Again, fluxoid transitions were observed to occur at flux values of $(n + \frac{1}{2})\Phi_0$.

3.2 Phase slips in Josephson junctions

In the late 1960s a large effort was put forth to characterize thermal fluctuations and their effect on Josephson junctions. The first measurements, by Anderson and Goldman,

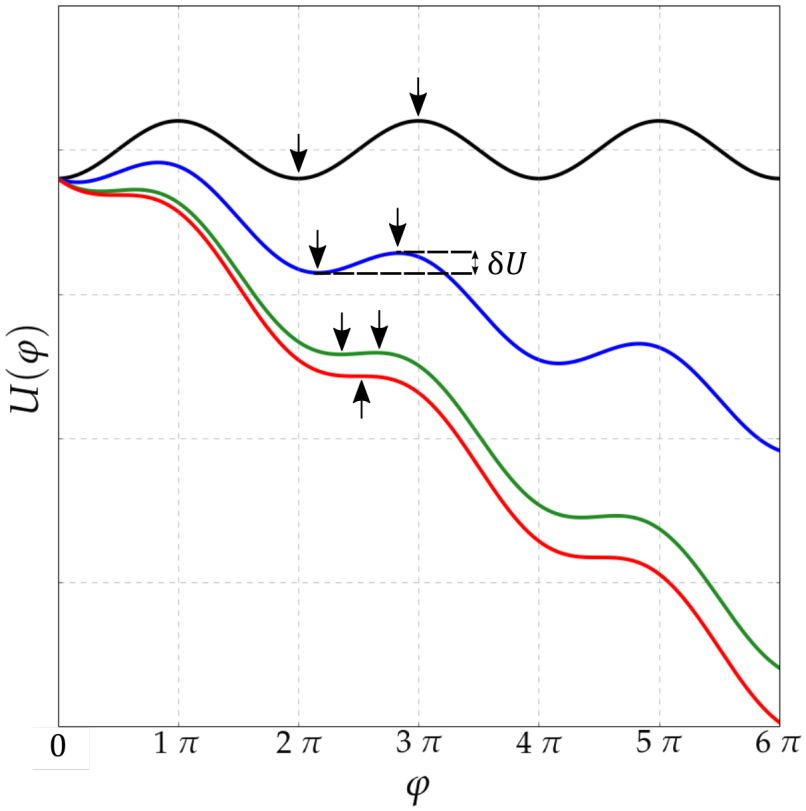

Figure 3.1: Potential energy landscape $U(\varphi)$ as a function of phase φ across a Josephson junction for $\frac{I}{I_c} = 0$ (black), $\frac{I}{I_c} = 0.5$ (blue), $\frac{I}{I_c} = 0.9$ (green), and $\frac{I}{I_c} = 1$ (red). A phase slip corresponds to an event where the system transitions between subsequent minima, in which the phase changes by 2π. For the blue curve the energy barrier δU preventing such an event is shown. The black arrows indicate the location of extremal points of the potential. As the current is increased from 0 to I_c these points merge and δU decreases. At I_c these two points merge into a single inflection point and $\delta U = 0$.

involved measuring the current-voltage characteristic of tin Josephson tunnel junctions at several temperatures just below T_c [50]. With the junction biased by current I, the phase difference φ across the Josephson junction can be described through the mechanical analogy to the motion of a particle of mass $\left(\frac{\hbar}{2e}\right)^2 C$, trapped in a potential energy landscape of the form $U(\varphi) = -\left(\frac{\hbar}{2e}\right)(I\varphi + I_c \cos\varphi)$ and subject to the viscous drag force $\left(\frac{\hbar}{2e}\right)^2 \frac{1}{R}\frac{d\varphi}{dt}$, where C, R, and I_c are the capacitance, normal-state resistance, and critical current of the Josephson junction, respectively. Ambegaokar and Halperin calculated the current-voltage characteristic for such a system including thermal fluctuations that allowed the particle to diffuse over barriers in $U(\varphi)$ leading to a phase slippage of 2π [51]. Though Ambegaokar and Halperin only performed their calculation for the case of zero capacitance, which neglects any hysteresis in the I-V characteristic, Anderson and Goldman were still able to obtain a qualitative agreement between their measured I-V curves and those predicted by Ambegaokar and Halperin. The following year, Simmonds and Parker designed an experiment that satisfied Ambegaokar and Halperin's zero capacitance calculation by measuring the I-V characteristic of Josephson junctions formed from thin films with a small constriction at one point [52]. These weak link junctions avoid the large capacitance created by the geometry of tunnel junctions and allowed Simmonds and Parker to find excellent agreement between their measurement and Ambegaokar and Halperin's prediction.

Following these works, Jackel *et al.* made the first measurement of the effect of thermal fluctuations on fluxoid transitions in a ring closed by a weak link junction. By applying a periodic flux ramp and monitoring the flux inside the ring with an rf-biased SQUID, they measured the probability distributions for the flux at which transitions from one fluxoid state to another state of lower energy occur, $P(\Phi_{sw})$. Their system was elaborately shielded to exclude external flux noise from influencing their measurement, and ultimately they found excellent agreement between their measured $P(\Phi_{sw})$ and those predicted by Kurkijärvi, finding that the width of $P(\Phi_{sw})$ scaled as[1] $T^{2/3} I_c^{-1/3}$ [53].

In the same year, Fulton and Dunkleberger performed a similar measurement where

1. This system is described by an escape rate of the form $\Gamma \sim \exp\left[-\frac{U_0}{k_B T}\left(1 - \frac{I}{I_c}\right)^{3/2}\right]$ with $U_0 \sim I_c^2$. Thus applying Eq. 2.110 with $b = 3/2$ and $B \sim \frac{I_c^2}{T}$ we arrive at $\sigma\ T^{2/3} I_c^{-1/3}$

they measured fluctuations of the critical current of tin-(tin oxide)-tin tunnel junctions. By sweeping current through these junctions at approximately 300 Hz and measuring the resulting current-voltage characteristic, they were able to collect statistics on the value of current which caused these junctions to transition to a finite-voltage state. Typically, they repeated these measurements at several temperatures, an example of which is shown in Fig. 3.2. The escape rates they measured were often in agreement with those predicted by thermal escape assuming the junction was in thermal equilibrium with the bath; however, several measurements required a higher effective temperature to obtain a good fit, indicating the presence of extrinsic noise-driven fluctuations. For their measurements that were due to thermally-limited fluctuations they were able to determine the barrier between fluxoid transitions and found that it agreed with the barrier of the tilted washboard potential, $\Delta E(I) = \frac{\hbar}{2e}\left[I\left(2\sin^{-1}(\frac{I}{I_c}) - \pi\right) + 2I_c\cos\left(\sin^{-1}(\frac{I}{I_c})\right)\right]$.

Between 1985 and 1988 a series of experiments (summarized in Fig. 3.3) were performed on Josephson junctions by Devoret, Martinis, Clarke, and Cleland in which all of the results were in good agreement with quantum predictions [55–58]. In the first experiment, Devoret, Martinis, and Clarke measured the escape rate of an underdamped current-biased Josephson

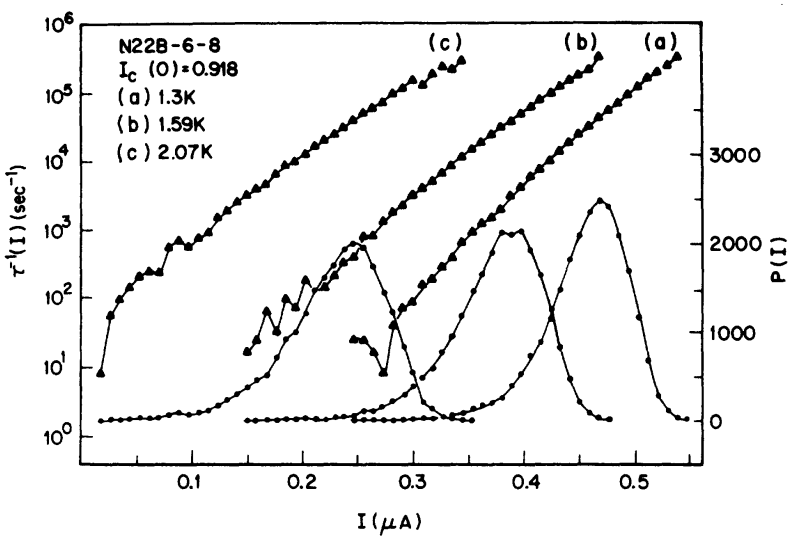

Figure 3.2: Normalized critical current distributions $P(I)$ and corresponding escape rates $\tau^{-1}(I)$ for a current-biased Sn-Sn-oxide-Sn tunnel junction measured by Fulton and Dunkleberger [31]. Typically, 2000 counts/point were achieved at the peak of each distribution. As temperature was increased the distribution of I_c broadened and the mean decreased, both of which are expected results for thermal escape from the tilted washboard potential.

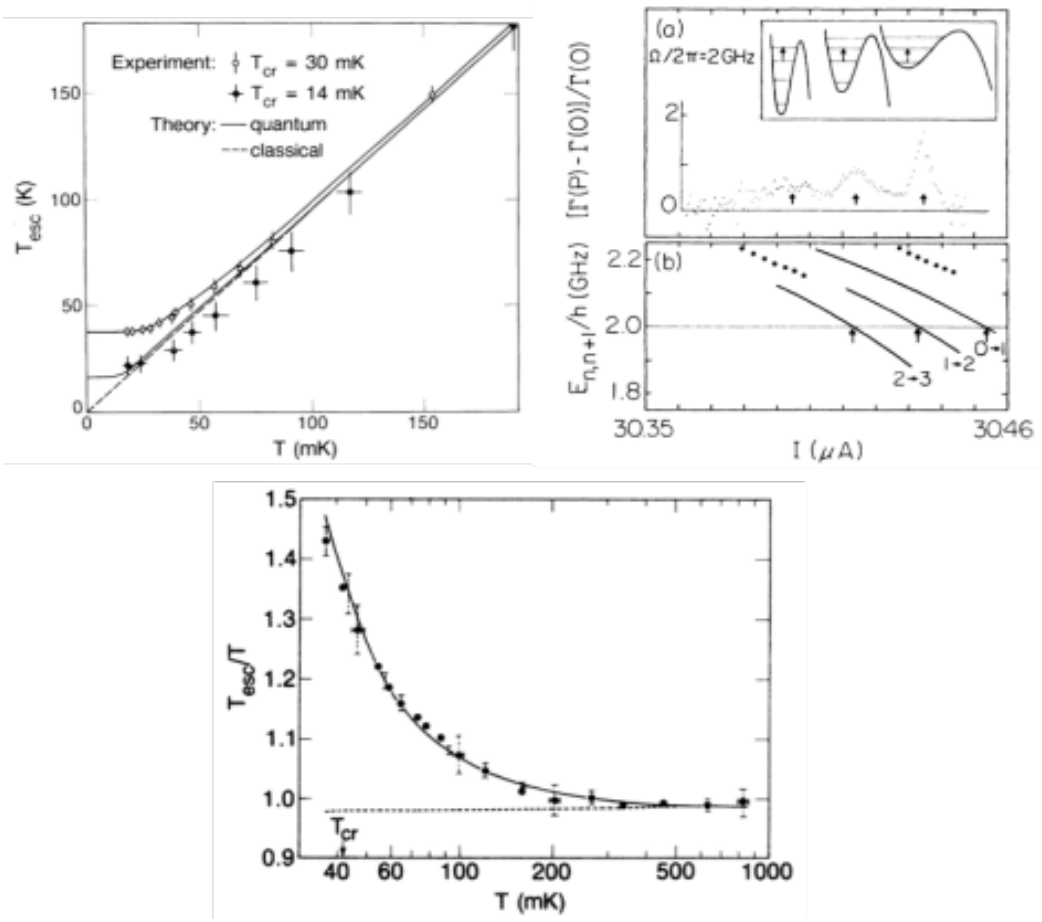

Figure 3.3: (Top left panel) $T_{\rm esc}$ as a function of device temperature T for a current-biased Josephson junction. $T_{\rm esc}$ is a way to represent the escape rate from the zero-voltage state in a way that is as independent as possible of the junction parameters. The $T_{\rm cr} = 14$ mK data were taken by applying a magnetic field to the junction to lower its critical current and rule out spurious noise as the source of their observed trend at $T_{\rm cr} = 30$ mK. The $T_{\rm cr} = 30$ mK data are consistent with the no fitted parameter quantum prediction as opposed to the no fitted parameter classical prediction. (Top right panel) The escape rate $\Gamma(P)$ of a Josephson junction measured when a microwave current of power P and frequency $\Omega/2\pi$ was injected into the current bias, normalized by the escape rate with no microwave current $\Gamma(0)$ as a function of current bias I. The escape rate shows three clearly visible resonances, which agree with the quantum-mechanical prediction for the energy levels using junction parameters independently measured in the thermal regime. (Bottom panel) Normalized escape rate $T_{\rm esc}/T$ as a function of temperature T. As T is lowered below $T_{\rm cr}$, $T_{\rm esc}/T$ becomes larger than unity which indicates that the escape temperature exceeds the classical prediction of thermal activation. The solid curve is a theory by Grabert and Weiss [54], which takes into account quantum tunneling and calculates the escape rate between the high- and low-temperature regimes. Ultimately, the authors conclue that "[t]he good agreement between the data and the theory over the entire temperature range provides the first unambiguous verification of the Grabert-Weiss theory for the enhanced escape rate," that is, the results are consistent with the prediction of macroscopic quantum tunneling. [55].

junction from the zero-voltage state. By obtaining the relevant junction parameters from other experiments in the classical regime, they showed that their measured escape rate was consistent with the quantum prediction with no fitted parameters. In a second experiment by Martinis, Devoret, and Clarke, microwave current was injected into the current bias of a junction in the quantum regime and the escape rate from the zero-voltage state was enhanced when the microwave frequency was resonant with the spacing between energy levels of the junction's potential well. Given the quantized nature of the energy levels, this result completely contradicted classical behavior. Finally Cleland, Martinis, and Clarke measured the escape rate of a Josephson junction shunted with a normal metal resistor and again found that at low temperatures, the escape rate was enhanced compared to the classically predicted escape rate. With a theory proposed by Grabert and Weiss [54] that included macroscopic quantum tunneling across the junction, they found very good agreement between their measured escape rate and theory over the entire temperature range of their data.

Recently, Krasnov *et al.* and Yu *et al.* measured the probability distribution of switching current in Josephson junctions but at $T < 100$ mK, in the hope of observing macroscopic quantum tunneling [59, 60]. In both of these experiments the authors found that the width of $P(I_{\rm sw})$ remained constant at low temperatures and then increased as temperature was increased; however, at higher temperatures the width decreased as temperature was increased. This result was strikingly different from that found by Fulton and Dunkleberger and seemed to contradict the result predicted by thermal activation. But the results are well explained in the context of phase diffusion, a process in which the particle can re-trap in a subsequent well of the titled washboard potential before ending up in the running state.

While a phase slip represents the passage from one minimum to the next of the tilted washboard potential, these experiments measured the transition from a state that is trapped in one of the potential minima to the finite voltage state where the particle cascades down the tilted washboard without stopping. In cases where a single phase slip irreversibly causes a transition to the running state, the statistics of this measured switching distribution are the same as the statistics of thermally activated phase slips (TAPS). This was the case of Fulton and Dunkleber's experiment. However, when the particle may re-trap in a subsequent well

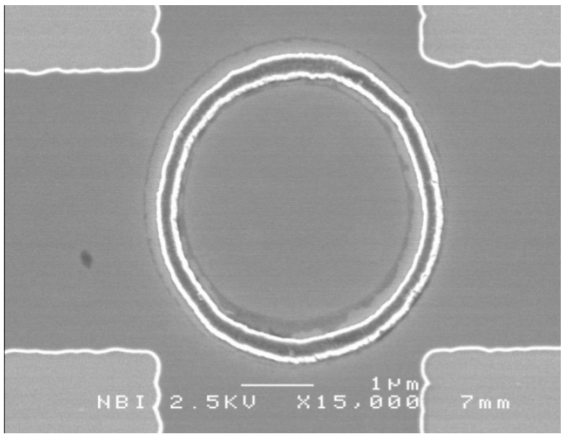

Figure 3.4: SEM image of a μ-Hall probe used by Pedersen *et al.* The cross section of the probe is 4x4 μm^2, the mean radius of the aluminum ring deposited on top of the μ-Hall magnetometer is 2.16 μm, and the ring's width is 314 nm.

of the tilted washboard potential, and multiple phase slips are required before the system reaches the finite voltage state, the statistics of $P(I_{\rm sw})$ are not the same as those of TAPS. This phase diffusion regime was present in the work of both Krasnov *et al.* and Yu *et al.*, and once it was taken into account, the expectation was that at the highest temperatures the width of $P(I_{\rm sw})$ should decrease, which was consistent with their measurements.[2]

3.3 Phase slips in superconducting rings

It is worth noting that up until this point of the text most measurements of phase slips in a superconductor have relied completely upon the normal state or the finite-voltage running state of a Josephson junction, as they were all essentially resistive measurements. In 1997 Geim *et al.* used a micro-Hall magnetometry technique, which allowed them to probe changes in the superconducting state far below $T_{\rm c}$ and over the full field range below the sample's critical field [63]. Aluminum disks were placed in the center of Hall probes where the Hall voltage is proportional to the average magnetic field in the probe's junction. By calculating the difference between the Hall voltage for probes with and without an aluminum disk, the magnetization of the aluminum disks was measured directly. These

2. This phase diffusion regime had been studied previously by Kautz and Martinis [61] and also by Vion *et al.* [62]

devices achieved a sensitivity of $\sim 10^3$ Bohr magnetons, allowing for the measurement of aluminum disks 130 nm thick with radii between 250 and 1200 nm. In the smallest devices, the magnetization evolved smoothly with applied field until the critical field was reached and the sample transitioned to the normal state. However, for the largest devices periodic discreet jumps in the magnetization were observed, and though the height of the jumps was not quantized they roughly corresponded to one extra vortex entering the sample. As $\xi(0\text{ K}) = 250$ nm, the qualitative differences were attributed to going from a regime in which $R < \xi(T)$, where superconductivity is destroyed by only a few vortices in the disk, to a regime in which $R > \xi(T)$, where the disk can support many vortices and transitions to the state that minimizes the free energy as field is ramped.[3] This is consistent with Eq. 2.45 which states that $n_{\max}$ is larger in systems with larger $\frac{R}{\xi(T)}$. The lack of magnetization quantization was attributed to the fact that though the number of vortices in the sample is quantized, vortices occurring near the edges have their flux "spill" out over the sample boundary.

Four years later, Pedersen *et al.* used micro-Hall magnetometers to measure the magnetization of a single aluminum ring ($R = 2.16$ μm and $w = 314$ nm), the results of which are shown in Fig. 3.5. At lower absolute field, successive jumps in magnetization have field separations that correspond to two flux quanta ($\Delta n = 2$), which is in contrast to the previous measurement in aluminum disks where only single quanta jumps were observed.

Given the discrepancy in the size of flux jumps between the two experiments, Vodolazov, Peeters, Dubonos, and Geim conducted another micro-Hall magnetometry experiment in 2003 on single aluminum rings of varying radius, with some rings having intentional defects in the form of narrow constrictions [64]. At low fields and for rings with a larger radius they found $\Delta n > 1$. For rings containing a defect they mostly found $\Delta n = 1$. This behavior reflects the fact that rings have multiple metastable states available at a given magnetic field; however, the ring will not transition to a state of lower energy until the applied magnetic field causes the barrier between such a transition goes to zero, or is small enough to allow for fluctuations to carry the system over or through the barrier. For smaller rings, or rings

3. Transitions would only occur if there is no energy barrier between the states, or if there are fluctuations large enough to overcome such an energy barrier.

with a constriction, there is typically only a single state of lower energy at this magnetic field, while larger rings may have multiple states of lower free energy to fall into, allowing for $\Delta n > 1$.

In 2011, Moler *et al.* measured the temperature dependence of the magnetic susceptibility of superconducting aluminum rings with a voltage biased dc SQUID [40]. The rings were 40 nm thick, 200-850 nm wide and had radii ranging from 0.5 to 1.82 μm. They were maintained just below T_c, so that the rings had sufficient thermal energy to change winding number at the flux where the free energy of its current state became greater than the free energy of a state of different winding number, even in the presence of a finite energy barrier between such transitions. This corresponds to transitions occurring at flux values of $(n + \frac{1}{2})\Phi_0$. Further, in this experiment phase slips were so frequent that an individual phase slip could not be resolved so their measurements gave the time average of phase slips, which represents a thermodynamic sampling of all metastable states energetically available

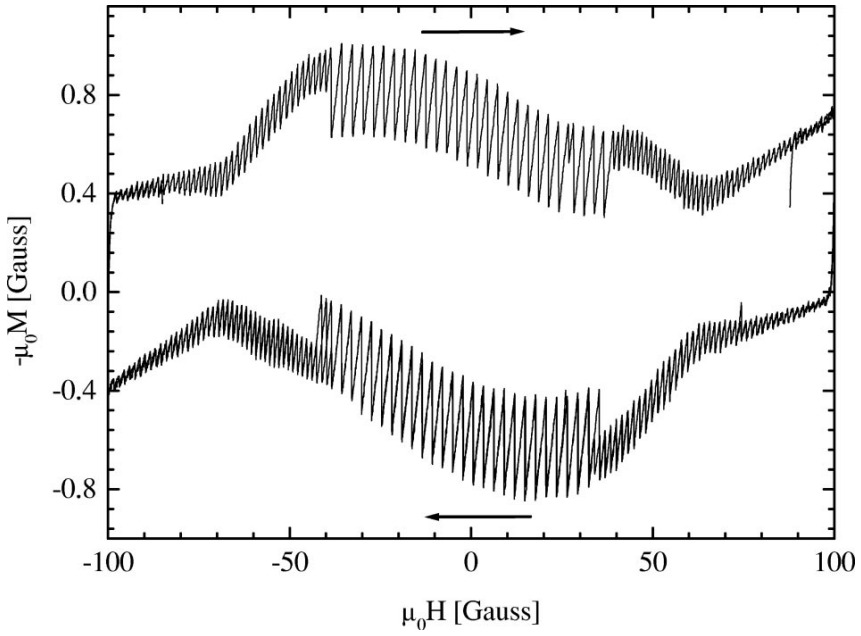

Figure 3.5: Measured magnetization $\mu_0 M$ of a single aluminum ring as a function of applied field intensity $\mu_0 H$ at 360 mK. The curves display distinct jumps each time the ring undergoes a change in winding number. The larger magnitude jumps correspond to a double flux quanta jump, while the smaller jumps correspond to a single flux quantum jump. As $R/\xi(T) \approx 11$ the large hysteresis between up and down field ramps is expected (see Section 2.3.3).

to the system. They were able to fit their data to 1-d Gizburg Landau theory and obtained excellent agreement over a small field range ($\sim$4 flux quanta through the ring) for both data taken at low temperatures with no fluxoids, and data taken in the nonhysteretic regime close to T_c where fluxoid transitions dominate. No attempt was made to fit the data in the hysteric region between these two regimes, where they found phase slips always corresponding to $\Delta n = 1$.

In these measurements, and the majority of measurements taken to date on superconducting rings, phase slips take the order parameter from one state to another, and the properties of those initial and final states were measured, but not the dynamics of the phase slip itself. However in 2017, the Budakian group pioneered a new technique (Φ_0-MFM) in which a micron-size magnetic particle is attached to the tip of an ultra-soft silicon cantilever which is placed above superconducting aluminum rings [22]. The rings are kept just below their T_c and the resonantly driven cantilever is positioned to put $(n + \frac{1}{2})\Phi_0$ of flux through the ring.[4] In this configuration, thermally activated phase slips couple to the motion of the cantilever and the rate of phase slips occurring in the superconducting ring can be seen as frequency and dissipation shifts in the silicon cantilever. For their uniform rings ($R = 1.4$ μm, $w = 212$ nm) they found excellent agreement between their measured signal and the signal predicted by LAMH theory for thermally activated phase slips in superconducting rings.

Though this substantial body of work greatly improved our understanding of phase slips and transitions between superconducting states in rings, there were still two major shortcomings. The first was the lack of quantitative comparison between experiment and theory for phase slips over a large range of temperatures and magnetic fields, especially where the measurements displayed hysteresis. Up until this point most comparisons were either qualitative, or in the case of Moler and Budakian, were confined to a small field or temperature region where the data were nonhysteretic. The second was a lack of understanding for how much Δn will change during a phase slip. From the literature the general trend is that wider rings with larger radii can undergo Δn greater than unity, while smaller and narrower rings

4. One of the aluminum rings in their paper had $T_c = 1.163$ K and all measurements were taken above $T = 1.135$ K.

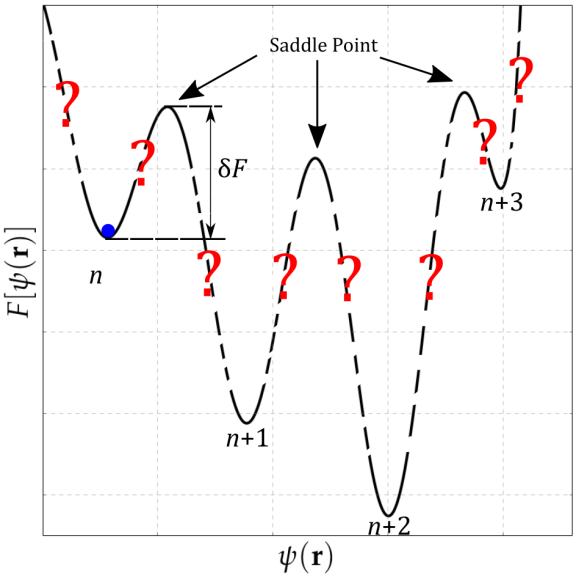

Figure 3.6: Cartoon of the free energy of a superconducting ring as a function of order parameter. In this cartoon the ring dimensions and flux are chosen such that when the system is in winding number n, there are two metastable states with lower energy available. There is also another metastable state, $n+3$, which has higher free energy at this flux (This would be the case of initializing the ring in the $n = 0$ state and then increasing the flux to $\Phi/\Phi_0 \approx 1.5$ in the bottom right panel of Fig. 2.7). The minima, labeled n, $n+1$, $n+2$, and $n+3$, correspond to equilibrium constant current carrying states that minimize the GL equations. The relative maxima between successive minima represent the saddle point solutions for transitions between neighboring states. This picture is a cartoon in the sense that while we can explicitly calculate the free energy of the equilibrium and saddle point states, $F[\psi(\mathbf{r})]$ spans the configuration space of all $\psi(\mathbf{r})$ and cannot be represented in 1 dimension.

almost always have $\Delta n = 1$. But there is no reliable way to predict into which state the system will fall when multiple metastable states are available to the system, indicating a lack of understanding about the damping in a superconducting ring.

To elaborate on damping, we refer to the cartoon in Fig. 3.6. In this picture, the relative minima are equilibrium states that carry constant current and are specified by their winding number. The saddle point solutions for a phase slip between neighboring states are the relative maxima. For a Josephson junctions this cartoon has the mechanical analogy to a ball trapped in the tilted washboard potential (Fig. 3.1), where the entire energy landscape can be calculated analytically and is only 1-dimensional. For the superconducting ring, while the free energy of these extremal solutions can be calculated explicitly, the free energy landscape between these states is more complicated as $F[\psi(\mathbf{r})]$ spans the configuration space

of all $\psi(\mathbf{r})$. Further, equilibrium states are typically separated by an energy scale of eV, while δF is on the order of meV (i.e. $\sim 100 k_{\mathrm{B}} T$) for the rings studied in this text. Still, in both cases a phase slip represents a passage from one minimum to the next. At low temperatures ($R \gg \xi(T)$), where there are multiple metastable states available to the ring, there can be a situation similar to that of the cartoon where there is more than one state of lower free energy available to the system. In the case of small damping, once δF is small enough such that thermal activation can overcome this energy barrier, the ring will transition to the $n+1$ state and it will have sufficient energy to overcome the next barrier between the $n+1$ and $n+2$ states. As the barrier between the $n+2$ and $n+3$ states has higher free energy than the initial barrier set by δF, the ring will ultimately relax to the $n+2$ state, that is $\Delta n = 2$. When the damping is large enough, the system may overcome the barrier set by δF; however, sufficient energy will be lost upon reaching the $n+1$ state and so the system will not be able to overcome the energy barrier that exists between the $n+1$ and $n+2$ states and the ring will remain in the $n+1$ state. In this case, a phase slip will only lead to $\Delta n = 1$ and the ring will not relax to the state of lowest free energy.

To compare this with a Josephson junction, the small damping case is where the particle escapes from a minimum of the tilted washboard potential (Fig. 3.1) and remains in the free-running state down the tilted washboard. In the case of large damping, the particle would escape from one potential minimum and then it would re-trap in the subsequent minimum of the tilted washboard. In this comparison we can see that a key difference between a superconducting ring and a Josephson junction is that there is no such free-running state in a superconducting ring. Despite this difference, in both cases damping plays a crucial role in determining the final state of a system after a phase slip. In Josephson tunnel junctions the form of the viscous drag force, $\left(\frac{\hbar}{2e}\right)^2 \frac{1}{R}\frac{d\varphi}{dt}$, is known and the parameters can be measured independently, which allows us to accurately predict the dynamics of such systems. As the source of damping remains an open question in isolated superconducting rings, we are unable to make such *a priori* predictions when multiple metastable states are available to the superconducting ring.

3.4 Phase slips in superconducting nanowires

Measurements of phase slips in superconducting nanowires happened concurrently with those in rings, and in 1988 Giordano investigated quantum tunneling through thin indium wires, using step-edge lithographic techniques to create wires 40-100 nm in diameter and 150 μm long [42]. If these wires are biased with a constant voltage V the Josephson relation $\frac{\partial\varphi}{\partial t} = 2eV/\hbar$ indicates that the phase difference across the wire must increase linearly in time. If left unchecked the supercurrent flowing in the wire, which is proportional to φ by Eq. 2.54, would continue to increase; however, eventually I_c is reached and superconductivity becomes unstable and the order parameter goes to zero in a localized region. This decreases φ and thus lowers the supercurrent in the wire. These phase slip events result in dissipation and can be monitored by measuring the resistance across these nanowires. Doing just that, Giordano measured the resistance of his nanowires and found it was consistent with that predicted by Ginzburg-Landau theory including Langer and Ambegaokar's theory for thermally activated phase slips, but only for temperatures within 200 mK of T_c. At lower temperatures the measured resistance was much higher than expected and to explain this Giordano proposed that quantum tunneling was important, in which the superconducting state tunnels through a free energy barrier instead of being thermally activated over a barrier. Such an explanation gave good fits to the measured resistance with reasonable fit parameters; however, they could not rule out the possibility of other unknown mechanisms being responsible for their results at low temperatures. And so while this work verified the current understanding for TAPS in nanowires, it only provided a hint of evidence for quantum tunneling.

In 2000, Bezryadin was able to create nanowires by coating carbon nanotubes with a superconducting MoGe alloy, leading to nanowires 200 nm long, 5 nm thick and only 10 nm in diameter [43]. When the resistance of different wires was measured as a function of temperature the results were strikingly different; some wires displayed an exponential decrease in resistance when they were cooled, while other wires displayed a constant resistance as temperature was decreased. The authors attributed this difference in behavior to the ratio of the wire's normal state resistance R_N to the quantum of resistance for Cooper

pairs R_q. If $R_N < R_q$, strong damping (proportional to $1/R_N$) prevents the system from tunneling through any free energy barriers, which localizes φ and leads to a superconducting state. However when $R_N > R_q$, there can be a proliferation of quantum phase slips through free energy barriers in φ-space, leading to a delocalization of the phase difference and an insulating state.

Unfortunately, this explanation broke down a year later when the same experiment was repeated on 20 similar wires that were not much longer, $L = 100-1000$ nm. For these wires, the superconducting transition seemed to be set by the the resistance per unit length, or equivalently the cross-sectional area of the wire [44]. For wires with $R_N/L < 20\,\Omega/\text{nm}$, the resistance sharply dropped when the temperature was decreased below T_c. For wires with $R_N/L > 80\,\Omega/\text{nm}$, the resistance remained roughly constant as they were cooled below T_c. Wires with intermediate resistance per unit length displayed a broad drop in resistance as temperature was decreased. Again, at temperatures close to T_c, their data was consistent with the predictions of TAPS alone, and at low temperatures the authors included the predictions of quantum phase slips.

Altomare *et al.* added to the literature in 2006 by studying the current-voltage characteristic in long aluminum wires with lateral dimensions ~ 5 nm in the presence of magnetic fields [45]. Again, LAMH theory and TAPS alone failed to fit the measured linear resistance curves at low temperatures. By adding quantum tunneling of phase slips in parallel to TAPS, they were able to obtain better fits to the resistance over the entire temperature range.

In 2009 the Bezryadin group continued to study phase slips, but this time they studied the distribution of the stochastic switching current, the current at which the resistance sharply jumps from a small value to a value close to R_N, in their MoGe nanowires [46]. The results of their first measurement are shown in the left panel of Fig. 3.7, where they found the distribution width increased as temperature was decreased. When the experiment was repeated three years later, the opposite temperature trend for the switching current was observed. While the wires in these two experiments were nearly identical there was one key difference; in the first experiment the wires were amorphous, while in the 2012 measurement the wires were annealed *in situ* to create single-crystal MoGe wires.

Despite the seemingly conflicting trends, the authors attributed both observations to quantum phase slips. In the 2009 paper TAPS are not enough to explain the data. By incorporating a runaway overheating model, in which multiple successive phase slips are required to transition to the finite voltage state at high temperatures; and quantum phase slips so that the total rate is given by $\Gamma_{\mathrm{TOTAL}} = \Gamma_{\mathrm{TAPS}} + \Gamma_{\mathrm{QPS}}$, they were able to fit the data over the full temperature range. They also found that the crossover temperature where Γ_{QPS} dominates Γ_{TAPS} decreased with the critical current of the nanowires, providing evidence that QPS were responsible for their measurement rather than a source of extraneous noise. In the 2012 paper they did not need to rely upon the overheating model and their data was well fitted with the prediction including both TAPS and QPS. They concluded that the saturation of distribution width at low temperatures, observed in every sample with high I_{c} but not the two samples with low I_{c}, illustrated that QPS were unambiguously found in single-crystal MoGe nanowires.

In 2013 the Bezryadin group expanded upon their prior measurements by measuring the higher order moments of switching distributions in both MoGe wires and weak link

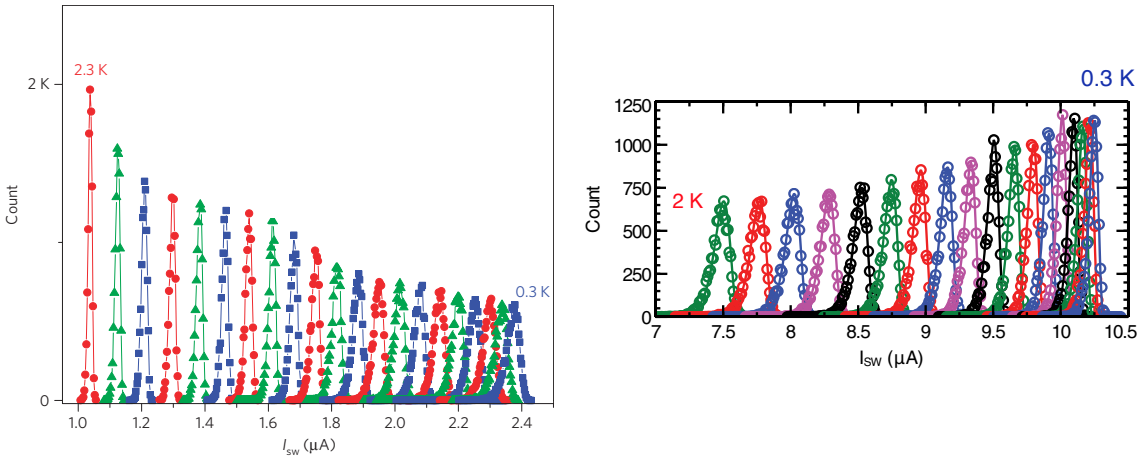

Figure 3.7: Normalized distributions of the switching current for MoGe wires at temperatures between 300 mK and 2.3 K, measured by the Bezryadin group. The left figure is from the 2009 measurement on a $Mo_{79}Ge_{21}$ wire ($L = 110$ nm, $R_N = 2662\,\Omega$, $T_{\mathrm{c}} = 4.34$ K, and $\xi_0 = 8.2$ nm) in which the measured distribution width decreased as temperature was increased. The right figure is from the 2012 measurement on a $Mo_{76}Ge_{24}$ wire ($L = 115$ nm, $R_N = 1152\,\Omega$, and $T_{\mathrm{c}} = 5.01$ K), which was crystallized by a strong voltage pulse that induced Joule heating. In this measurement the distribution width decreased as temperature was decreased and remained constant below some low temperature.

junctions formed from graphene flakes subject to the proximity effect. Regardless of the nature of the junction, they found that the skewness of the distribution was always close to -1, while the kurtosis was universally 5 for both TAPS and QPS. These results agreed with their extension of Garg's calculation for the cumulants of a general escape rate, which are summarized in Eq. 2.117 and Eq. 2.118.

From this body of literature it is clear that our understanding of TAPS close to T_c in superconducting nanowires is solid; LAMH theory is able to explain the data in these experiments without the need to invoke any other mechanism, regardless of the device. However, our knowledge of quantum phase slips is due mostly to experiments where the interpretation of results depends strongly upon less well-understood system parameters and requires other considerations like a runaway overheating model. So while quantum phase slips have been observed in these systems, there is still the need to create a fully characterized and simple system in which quantum phase slips have a straightforward interpretation.

This provided the motivation for us to study phase slips in uniform isolated superconducting aluminum rings using cantilever torque magnetometry. This technique allows us to measure the equilibrium current in the rings in an electromagnetically pristine environment [3, 28]. The interpretation of the measured data is straightforward, as our signal is directly proportional to the supercurrent in the rings and the proportionality constant only depends upon sample parameters (i.e. cantilever spring constant, cantilever resonant frequency and cantilever length) or other parameters (like applied magnetic field), which can be measured independently. Further, from transport measurements taken on aluminum wires co-deposited with our rings we can determine ξ_0, which allows us to independently verify our ability to characterize this system.

Chapter 4

Cantilever torsional magnetometry

The measurements presented in this work rely upon detecting small changes in the resonant frequency of a rectangular cantilever. In this chapter we will derive the harmonic frequencies and modes of a rectangular cantilever following Cleland [65] and we will determine how those frequencies are modified when a sample with a magnetic moment is placed on the tip of the cantilever.

4.1 Flexural oscillations of a singly clamped rectangular cantilever

We consider a beam of uniform cross-sectional area A, mass density ρ, and length L that undergoes displacement $U(z,t)$ in the x-direction as illustrated in Fig. 4.1. In this configuration a differential element of length dz will experience a force $-F_x(z)$ and torque $-M_y(z)$ on the face located at z and $F_x(z+dz)$ and $M_y(z+dz)$ on the face at $z+dz$. Applying Newton's second law and requiring that there be no net torque on the element we have

$$F_x(z+dz) - F_x(z) = \rho A dz \frac{\partial^2 U}{\partial t^2} \tag{4.1}$$

$$F_x(z+dz)dz + M_y(z+dz) - M_y(z) = 0 \tag{4.2}$$

where we have taken the torque about the face located at z. Taylor expanding the forces

and torques about the point z, such that $F_x(z+dz) \approx F_x(z) + \frac{\partial F_x}{\partial z} dz$ we obtain

$$\frac{\partial F_x}{\partial z} = \rho A \frac{\partial^2 U}{\partial t^2} \tag{4.3}$$

$$F_x(z) = -\frac{\partial M_y}{\partial z} \tag{4.4}$$

The torque can be related to displacement by $M_y = E_\mathrm{Y} I_y \frac{\partial^2 U}{\partial z^2}$ where E_Y is Young's modulus and I_y is the beam's bending moment of inertia, which is constant along the length of a beam with uniform cross-sectional area. Combining the above equations, the displacement of the cantilever obeys the following differential equation

$$E_\mathrm{Y} I_y \frac{\partial^4 U}{\partial z^4} = -\rho A \frac{\partial^2 U}{\partial t^2} \tag{4.5}$$

Cosine and sine waves of the form $\cos(\beta z - \omega t)$ will satisfy the above equation given the dispersion relationship

$$E_\mathrm{Y} I_y \beta^4 = \rho A \omega^2 \tag{4.6}$$

Assuming harmonic time dependence $U(z,t) = U(z) e^{-i\omega t}$ the displacement obeys

$$E_\mathrm{Y} I_y \frac{\partial^4 U(z)}{\partial z^4} = \rho A \omega^2 U(z) \tag{4.7}$$

and so cosine, sine, hyperbolic cosine, and hyperbolic sine waves will satisfy this equation with the most general solution given by the following linear combination

$$U(z) = a\cos\beta z + b\sin\beta z + c\cosh\beta z + d\sinh\beta z \tag{4.8}$$

Now we can apply boundary conditions that match our experimental realization of a beam clamped at one end ($z = 0$) and free on the other ($z = L$), which are

$$0 = U(0) \qquad\qquad 0 = \left.\frac{dU}{dz}\right|_{z=0} \tag{4.9}$$

$$0 = \left.\frac{d^2 U}{dz^2}\right|_{z=L} \qquad\qquad 0 = \left.\frac{d^3 U}{dz^3}\right|_{z=L} \tag{4.10}$$

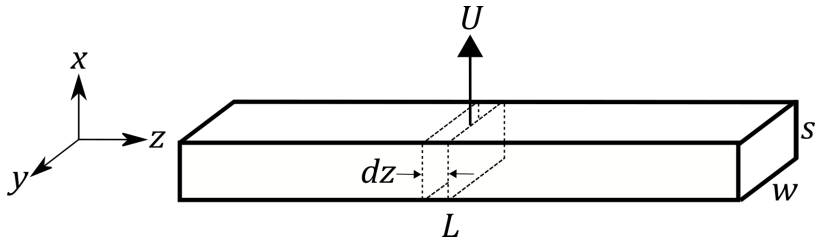

Figure 4.1: A beam of uniform cross-section undergoes transverse displacement $U(z)$, where z runs along the length of the beam. The beam has length L, thickness s and width w.

The first two conditions state that at the fixed end there can be neither displacement nor bending. This requires $a = -c$ and $b = -d$. At the free end we require zero transverse force and zero torque respectively which leads to the following equations

$$\cos(\beta_m L)\cosh(\beta_m L) + 1 = 0 \tag{4.11}$$

$$\frac{a}{b} = -\frac{\sin\beta_m L + \sinh\beta_m L}{\cos\beta_m L + \cosh\beta_m L} \tag{4.12}$$

the first of which has solutions $\beta_m L = 1.875, 4.694, 7.855, 10.996....$

To summarize these results, it is useful to define the normalized variables $\beta_n = \frac{\beta_m}{L}$ and $\eta = \frac{z}{L}$ and set $b = 1$, which allows us to express the cantilever's displacement as a function of a normalized mode shape $U_{\mathrm{N}}(\eta)$ and the displacement at the cantilever's tip x_{tip} through $x(\eta) = x_{\mathrm{tip}} U_{\mathrm{N}}(\eta)$, where

$$U_{\mathrm{N}}(\eta) = \frac{a_n\Big((\cos\beta_n\eta) - \cosh(\beta_n\eta)\Big) + \sin(\beta_n\eta) - \sinh(\beta_n\eta)}{a_n\Big(\cos\beta_n - \cosh\beta_n\Big) + \sin\beta_n - \sinh\beta_n} \tag{4.13}$$

$$a_n = -\frac{\sin\beta_n + \sinh\beta_n}{\cos\beta_n + \cosh\beta_n} \tag{4.14}$$

$$-1 = \cos(\beta_n)\cosh(\beta_n) \tag{4.15}$$

An example of the first three flexural modes of a cantilever are plotted in Fig. 4.2. Using $I_y = \frac{ws^3}{12}$ for a rectangular cantilever, the fundamental frequencies from Eq. 4.6 are

$$\omega_n = \sqrt{\frac{E_{\mathrm{Y}} s^2}{12\rho L^4}}\beta_n^2 \tag{4.16}$$

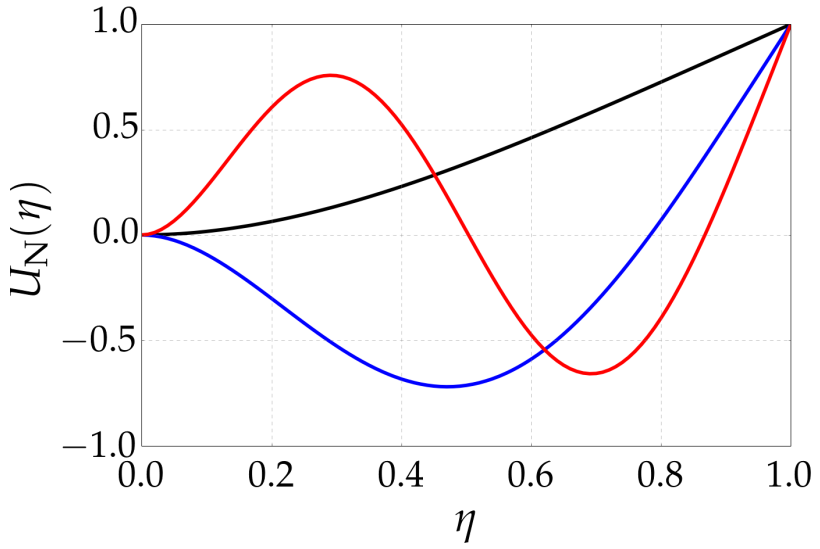

Figure 4.2: Normalized displacement for the first (black), second (blue), and third (red) flexural modes of a rectangular cantilever as a function of normalized position along the length of cantilever, $\eta = \frac{z}{L}$.

Thus, the flexural mode resonant frequencies are independent of width and shorter and thicker cantilevers will have higher resonant frequencies. The spring constant k is related to these frequencies by $k = m_{\text{eff}}\omega^2$ where $m_{\text{eff}} = \frac{1}{4}\rho wsL$ for a cantilever. Therefore,

$$k_n = \frac{E_Y w s^3}{48 L^3}\beta_n^4 \tag{4.17}$$

4.2 Cantilever frequency shift due to superconducting persistent current

To derive an expression for the cantilever's frequency shift due to a sample placed on its tip, we will examine the cantilever's spring constant. When a magnetic object is placed at the end of a cantilever it will interact with the external magnetic field, which exerts a torque on the cantilever. This torque acts to stiffen or soften the cantilever, which modifies the cantilever's spring constant, and thus, resonant frequency. The k of Eq. 4.17 represents the curvature of the cantilever's potential energy, $k = \frac{\partial^2 E}{dx^2}$, at equilibrium, so adding a sample with its own energy E_{sample} will modify the total spring constant as

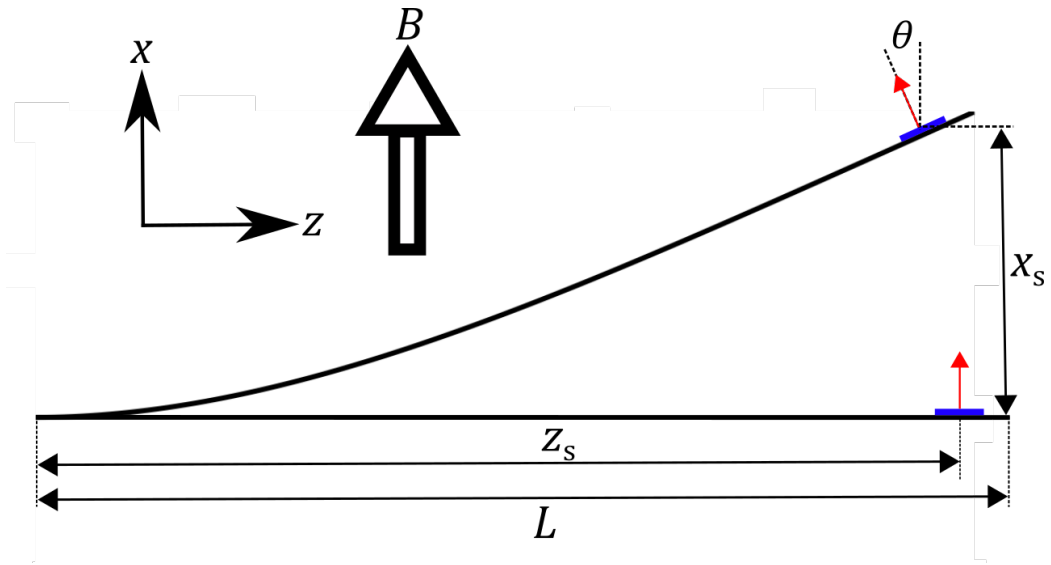

Figure 4.3: Cantilever beam profiles for the equilibrium cantilever (straight line) and the maximal deflection of the first flexural mode. A ring (blue) is placed a distance z_s from the base of the cantilever and as the cantilever flexes it undergoes both a linear displacement x_s and an angular deflection θ. As the ring is rigidly attached to the cantilever, its magnetic moment (red arrow) is titled by the same angle θ with respect to a uniform magnetic field B in the x-direction.

$$k_{\text{tot}} = k + \frac{\partial^2 E_{\text{sample}}}{\partial x^2} \tag{4.18}$$

When $\frac{\partial^2 E}{dx^2} \ll k$, this new spring constant will modify the cantilever's bare resonant frequency ω_0 by a small amount as

$$\begin{aligned} \omega &= \sqrt{\frac{1}{m_{\text{eff}}}\left(k + \frac{\partial^2 E_{\text{sample}}}{\partial x^2}\right)} \\ \omega &\approx \omega_0 \left(1 + \frac{1}{2k}\frac{\partial^2 E_{\text{sample}}}{\partial x^2}\right) \end{aligned} \tag{4.19}$$

Thus, the resonant frequency shift Δf (in Hz) due to a sample placed on its tip is

$$\Delta f = \frac{f_0}{2k}\frac{\partial^2 E_{\text{sample}}}{\partial x^2} \tag{4.20}$$

To relate E_{sample} to the motion of the cantilever it is useful to introduce θ, the angular

deflection of the ring.[1] We will consider placing a sample a distance $\eta_s = \frac{z_s}{L}$ from the base of the cantilever, such that its linear displacement is given by $x_s = x_{tip} U_N(\eta_s)$ as illustrated in Fig. 4.3. The angular displacement is related to this linear displacement through the normalized, dimensionless derivative of the cantilever mode shape $\alpha(\eta) = \partial_\eta U_N(\eta)$ such that

$$\theta = \alpha(\eta_s)\frac{x_{tip}}{L} \tag{4.21}$$

Thus, we can rewrite Eq. 4.20 as

$$\Delta f = \frac{f_0}{2k}\left(\frac{\alpha(\eta_s)}{L}\right)^2 \frac{\partial^2 E_{sample}}{\partial\theta^2} \tag{4.22}$$

For a measurement that consists of arrays of rings, each ring will have its own $\alpha(\eta)$ as each ring will be at a slightly different position along the length of the cantilever. As a result, we

1. When the cantilever oscillates the ring experiences both a linear displacement x and an angular displacement θ from its equilibrium position. The linear displacement couples to gradients of the applied magnetic field, while the angular displacement couples to the magnitude of the magnetic field (Shanks Eq. 4.19 [3]). Our experiment uses a uniform magnetic field, so θ is more useful.

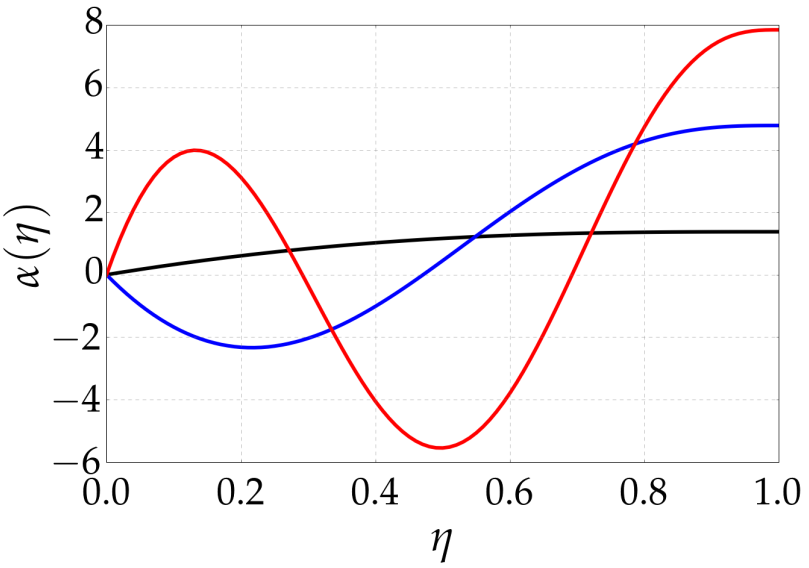

Figure 4.4: Normalized mode shape derivative for the first (black), second (blue), and third (red) flexural modes of a rectangular cantilever as a function of position along the cantilever $\eta = \frac{z}{L}$. Due to the boundary condition of zero transverse force at the free end of the cantilever, α is roughly constant near the end of the cantilever. For the first flexural mode, alpha changes by only $\sim 1\%$ from $\eta = 0.8$ to $\eta = 1$.

should use an effective α that reflects this, but in practice all measurements are taken on the first flexural mode where $\alpha(\eta) \approx 1.375$ over the last 20% of the cantilever, as illustrated in Fig. 4.4.

In Chapter 2 we calculated that the free energy of a ring depends on flux (Eq. 2.41), and the flux depends on the angular deflection, $E_{\text{sample}} = F(\Phi(\theta))$. Therefore,

$$\frac{\partial^2 E_{\text{sample}}}{\partial \theta^2} = \frac{\partial F}{\partial \Phi}\frac{\partial^2 \Phi}{\partial \theta^2} + \frac{\partial^2 F}{\partial^2 \Phi}\left(\frac{\partial \Phi}{\partial \theta}\right)^2 \tag{4.23}$$

Using Eq. 2.46 we can express this in terms of the supercurrent,

$$\frac{\partial^2 E_{\text{sample}}}{\partial \theta^2} = -I\frac{\partial^2 \Phi}{\partial \theta^2} - \frac{\partial I}{\partial \Phi}\left(\frac{\partial \Phi}{\partial \theta}\right)^2 \tag{4.24}$$

and in our experimental realization all measurements are taken in a constant magnetic field B, so the angular dependence of the flux is simply $\Phi = AB\cos\theta$, which leads to

$$\frac{\partial^2 E_{\text{sample}}}{\partial \theta^2} = IAB\cos\theta - \frac{\partial I}{\partial \Phi}\left(AB\sin\theta\right)^2 \tag{4.25}$$

In our experimental realization $\theta = 0$ and so the total frequency shift due to a single ring is

$$\Delta f = \frac{f_0}{2k}\left(\frac{\alpha(\eta_s)}{L}\right)^2 IAB \tag{4.26}$$

For arrays of N superconducting rings, $\Delta f = N\Delta f_{\text{single ring}}$. The nice feature of this experimental orientation is that the frequency shift is directly proportional to the supercurrent of the rings. All of the other parameters are characteristics of the cantilever or ring and can be measured independently, which makes the data analysis straightforward. Fortunately, the supercurrent is large ($\sim \mu$A) which leads to $\Delta f/f_0 \sim 10^{-9}$ for a single ring in this orientation, which, as we will show in Chapter 7, is possible to measure with enough averaging, so long as the noise floor is set by the thermal Brownian motion of the cantilever.

Chapter 5

Experimental set-up

The set-up used in this experiment to measure the supercurrent of aluminum rings was nearly identical to that used by William Shanks and Ania Bleszynski-Jayich to measure the normal state persistent current of aluminum rings [3, 28]. For the superconducting array measurements, the key difference was that we upgraded our lock-in amplifier to a more advanced model which allowed for improved precision in monitoring the cantilever resonant frequency. I also re-designed the sample stage to allow for measurements at $\theta = 0$ and the possible inclusion of a small magnetic coil. In this chapter, I will describe all equipment and measurement procedures common to the array and single ring measurements. Chapter 7 details the additional equipment and procedures specific to the single ring measurements.

5.1 Sample

The sample measured in this text was fabricated by William Shanks and Ania Bleszynski-Jayich as part of a set of samples used to measure the normal state persistent current in aluminum rings. The process began with a silicon-on-insulator wafer. Cantilevers were patterned out of the top silicon layer with optical lithography followed by a reactive ion etch. Rings were then fabricated on top of the patterned cantilevers using standard electron-beam lithography with a polymethyl methacrylate (PMMA) mask. Aluminum was then evaporated in a high-vacuum thermal evaporator. After lift-off in N-Methyl-2-pyrrolidone, the top of the wafer was protected and the backing silicon layer was etched with a deep

reactive ion etch. This was followed by a BOE etch of the SiO_2 layer. The sample was then dried in a critical point dryer, which resulted in suspended cantilevers. Images of the cantilevers and rings measured in this dissertation are shown in Appendix B. For a more detailed step-by-step fabrication recipe see Shanks [3].

5.2 Cryostat and insert

We performed the experiments in a helium-3 refrigerator (Janis Research Company, He-3 SSV), which was inserted into a 70 liter helium Dewar (Precision Cryogenic Systems). The helium dewar sat on top of a felt-covered aluminum frame, which was supported by ultra-soft polyurethane and elastomer pads. No other vibrational isolation was used for these experiments.

The He-3 refrigerator consists of an internal vacuum chamber (IVC), which was immersed in liquid helium-4. Inside the IVC there were three cryogenic stages: a charcoal sorption pump (sorb), a 1 K pot, and a He-3 pot as shown in Fig. 5.1. The He-3 pot was connected in a closed system to a room temperature reservoir of He-3, which was liquefied to obtain temperatures down to 300 mK. Capillary tubes from the He-4 bath cooled the sorb and the 1 K pot to 4 K, at which point all of the He-3 was adsorbed onto the charcoal in the sorb. The flow of liquid helium into the 1 K pot was controlled using a needle valve. By reducing the flow of He-4 into the 1 K pot and pumping on the helium, temperatures down to 1.7 K were achieved. To cool the system further, the sorb was heated to 45 K while the 1 K pot was maintained below 1.8 K. In this configuration, He-3 was desorbed from the charcoal and then liquefied on the walls of the closed He-3 system near the 1 K pot and dripped into the He-3 pot. Once the He-3 pot was sufficiently filled,[1] the sorb and the 1 K pot were brought back to 4 K and the He-3 pot reached a base temperature of 300 mK. For our system, base temperature lasted 10 full days.[2] Afterwards, all of the liquid He-3 in the He-3 pot will have evaporated and adsorbed back onto the charcoal sorb

1. We maintained the sorb at 45 K and the 1 K pot below 1.8 K for 1 hour.

2. Any operations which would heat the He-3 pot or sample stage, either through direct heating or eddy currents from ramping the magnet, shortened the hold time. For normal fridge operation we expected ~ 9 days below 4 K.

and the He-3 pot temperature returned to 4 K. By simply repeating the above procedure, the fridge could be cooled back down to 300 mK within 3 hours. The key benefit of this system is that low temperatures were maintained for extended periods of time without any mechanical pumping, which greatly reduces vibrational noise.

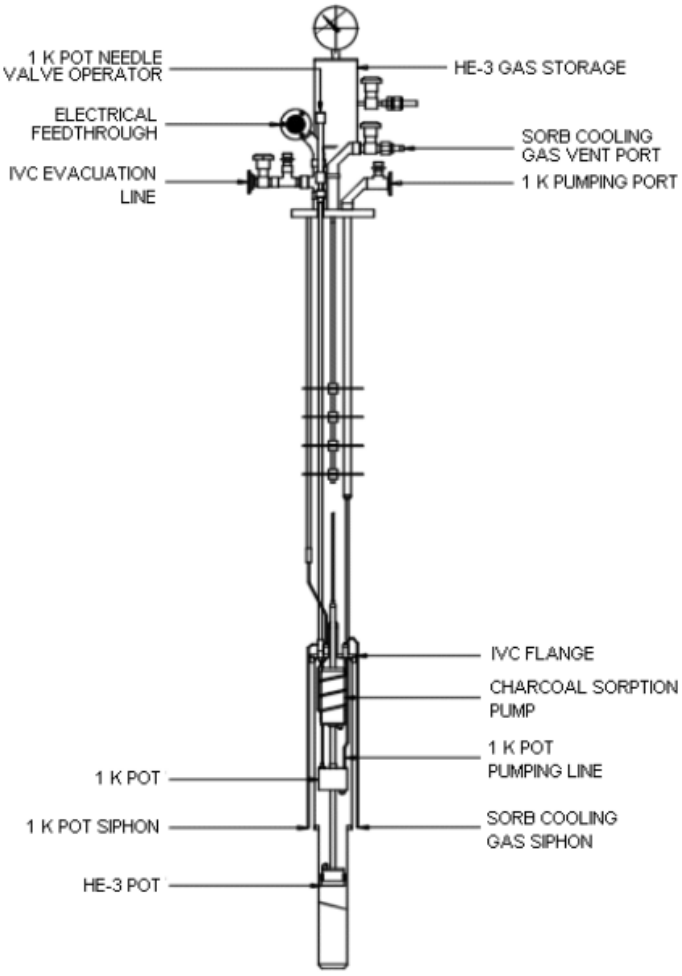

Figure 5.1: Mechanical drawing of the HE-3 SSV insert provided by Janis [66]. The bottom of the insert consists of three cryogenic stages housed within an IVC, which was immersed in a liquid helium filled Dewar. The top of the insert (which exists above the helium Dewar and at room temperature) consists of various helium venting ports and pumping lines, which allowed us to pump on He-4 and liquefy He-3 to attain temperatures as low as 300 mK as described in the text. An electrical feedthrough allowed us to make electrical connections from our sample stage to equipment in the lab.

5.3 Thermometers and temperature control

To measure the temperature at each stage we used four thermometers. A silicon diode thermometer was placed on the sorb and the 1 K pot. We placed a ruthenium oxide thermometer (Lake Shore Cryotronics, RX102-A) on the He-3 Pot and we epoxied another ruthenium oxide thermometer (Lake Shore Cryotronics, RX202-A) onto the sample stage. As these last two thermometers were close to the sample and the middle of the magnetic field, the ruthenium oxide thermometers provided low magnetic field errors for temperature measurements below 1 K. The RX202-A model provided the least magnetic field-induced errors, and so that model was used on the sample stage, where a reliable measurement of the sample's temperature was most important. These thermometers were measured by a temperature controller (Lake Shore Cryotronics, Model 340 Temperature Controller) which also allowed us to control resistive heaters on the sorb and the He-3 pot.

To obtain temperatures between 300 mK and 4 K we used the resistive heaters. For temperatures between 300 mK and 500 mK we applied a small amount of power directly to the He-3 pot, while the sorb and 1K pot were maintained at 4 K. For temperatures above 500 mK, heating the He-3 pot directly required too much power and would boil off all of the liquid He-3 within an hour, which made it impossible to take a meaningful measurement. Thus, for measurements between 500 mK and 4 K we heated the sorb, while we kept the 1 K pot open and maintained at 4 K. The amount of power required to heat the He-3 pot and sample to a given temperature this way would vary depending upon how far into the condensation we were (immediately after condensing He-3 we needed to apply more power to raise the stage to 1 K than we would 6 days after condensing), which was expected due to the natural evaporation of He-3 from the He-3 pot.

To maintain a stable temperature we had to deal with two competing issues. The first is that for large field sweeps, the magnetoresistance of the thermometers slightly modified the He-3 and sample thermometer readings as they were in the middle of the solenoid. Therefore, using a thermometer's temperature as the control set-point could introduce problems during large field sweeps or when the manetoresistance errors were large. On the other hand, we could just apply a constant power to the heaters. This configuration is insensitive

to magnetoresistance; however, as the liquid He-3 continuously boiled off, this configuration would lead to a gradual linear increase in the stage temperature and could become problematic for lengthy measurements.

For low temperatures (< 500 mK), where the magnetoresistance should only lead to temperature errors of $\sim 0.3\%$ below 1.5 T for the RX-102A thermometer, we used the He-3 pot temperature as our feedback parameter for the temperature stability PID loop. For higher temperatures, where we needed to heat the sorb, the time delay between applying heat to the sorb and raising the temperature of the stage made such a control loop more difficult. As a result, for $T > 500$ mK we applied a constant power to the sorb. Though the stage temperature would gradually rise, by implementing feedback where we linearly decreased the power applied to the sorb, we were able to achieve temperature stability of $\sim$1 mK over several days.[3]

5.4 Sample stage

The sample stage was attached with 12 brass screws to the bottom of the He-3 pot. An image of the sample holder is shown in Fig. 5.2 and the fully assembled stage is shown in Fig. 5.3. All pieces were made of free machining brass as it has a higher resistivity than OFHC copper and leads to a smaller amount of eddy current heating on the stage, while still maintaining sufficient thermal conductivity. For the same reason, the amount of metal used in the sample holder was also kept to a minimum.

The sample was clamped at the top of the sample holder with a brass bar using two brass screws with spring washers. The spring washers ensured that the sample could be sufficiently clamped without accidentally applying too much force and cracking the silicon. Below the sample, we placed a ruthenium oxide thermometer in a cylindrical hole and secured it in place with epoxy (Stycast 2850 FT black epoxy with catalyst 24LV). This top half of the stage sat atop a piezo stack, which consisted of a 10 mm square and 2 mm

3. Unfortunately, because the cooling power of the He-3 pot changes throughout a given condensation, this power decreased needed to be calibrated for every measurement. Typically we would measure how the temperature on the sample increased over one hour with a constant applied power to the heater, and how the sample temperature changed when the constant applied power was varied. These two measurements allowed us to calibrate the power decrease rate fairly well.

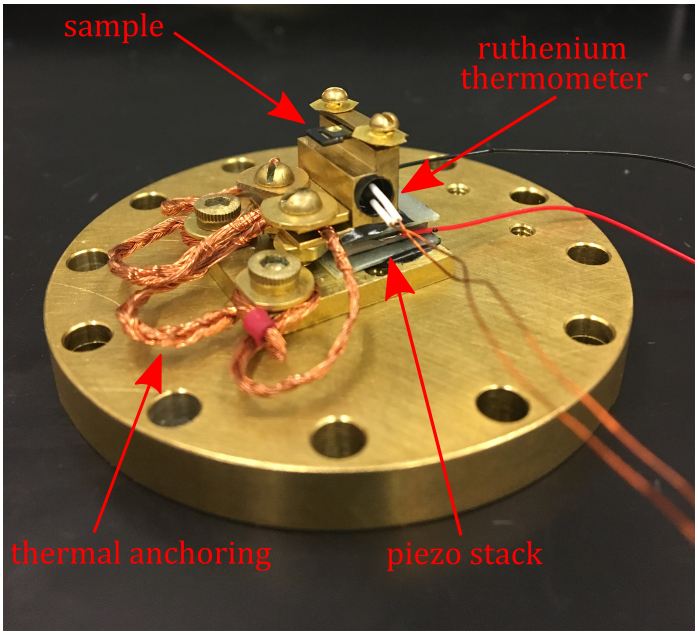

Figure 5.2: The sample holder used for all measurements in this experiment. The circular base is 2.25 inches in diameter. All pieces were made out of free machining brass, with the exception of the thermal anchoring which is OFHC fine copper wire. The silicon sample was clamped in place under a small brass bar. A ruthenium oxide thermometer was epoxied into a hole in the stage which provided good thermal contact and a reliable measurement of the sample's temperature. A piezoelectric actuator was epoxied between two thin sheets of G10 which allowed us to drive the cantilevers on resonance. As the G10 is insulating, thermal anchoring between the top and bottom halves of the stage ensured the sample reached base temperature.

thick piezoelectric actuator (PI Ceramic, PL088.31 PICMA Chip Miniature Piezo Actuator) sandwiched between two pieces of 0.30 mm thick G10. Each piece was epoxied together and then the stack was epoxied to the top and bottom halves of the brass sample holder. The piezo stack thermally isolated the top half of the sample holder, so 4 braids of OFHC fine copper wire were used to provide thermal contact between the two halves.

Once assembled, the sample holder was flipped upside down to form the top part of the sample stage as shown in Fig. 5.3. Three 3-inch long brass rods were used to attach the bottom half of the sample stage, which held the brass fiber holder. The gold coated fiber (not shown in the figure) was placed into a 14 mm long, 129 μm inner diameter, 1 mm outer diameter tapered borosilicate ferrule (Vitrocom) until the edge of the fiber was flush with one end of the ferrule. The fiber was then secured in the ferrule with Stycast 2850 black

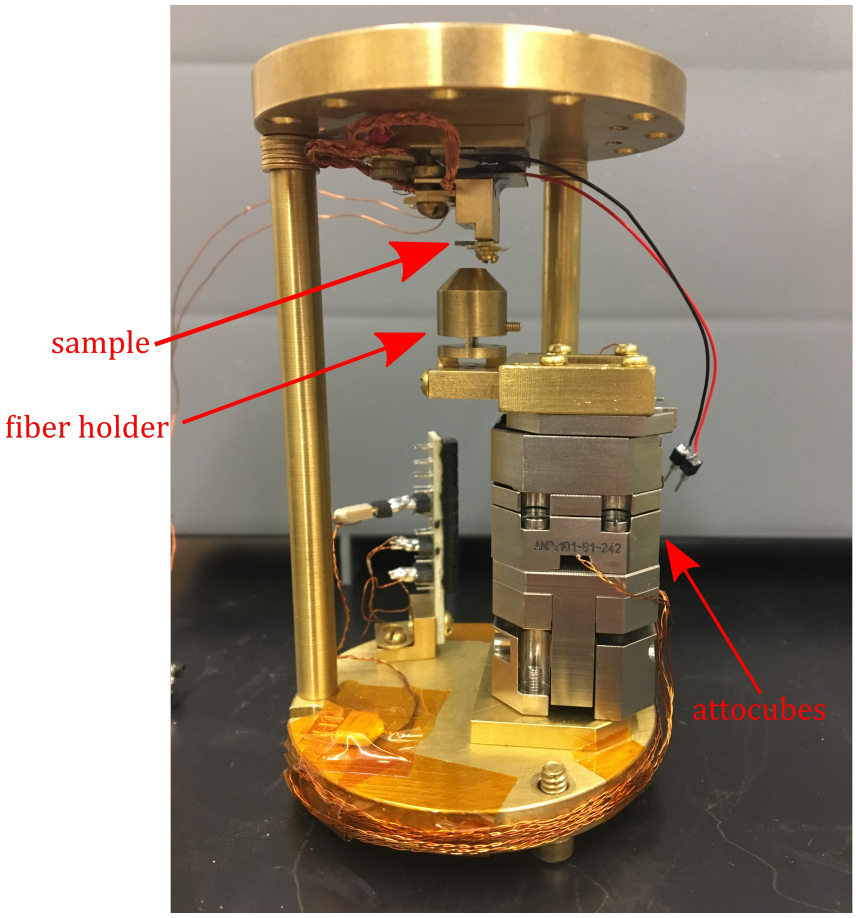

Figure 5.3: The fully assembled sample stage. In this image, the top of the stage was attached to the bottom of the He-3 pot so that the sample holder hung upside down (as shown). The fiber holder mounted atop three attocubes allowed us to move the laser and measure multiple cantilevers in a single cool down. Three 3-inch posts were used to support the bottom of the stage, but one was removed for the sake of this image.

epoxy. The glass ferrule was placed inside of the fiber holder as far as it could go[4] and it was secured with a set screw.[5] At the end of the fiber holder there was an anti-reflection coated aspheric lens (Thorlabs, Unmounted Geltech Aspheric Lens, 352140-C f=1.45 mm, NA=0.55). Using a lens, we were able to keep any objects at least ∼1.5 mm away from the silicon cantilevers, which was useful as electrostatic interactions between the cantilevers and nearby surfaces can significantly bend the cantilevers or can lead to a reduction in their mechanical quality factor.

4. A constriction was placed inside of the fiber holder so that the ferrule bumped into a lip, while the fiber remained undamaged and was positioned 1 focal length away from an aspheric lens.

5. For a detailed schematic of the fiber holder see Shanks [3].

The fiber holder was mounted on a stack of three attocubes (attocube systems, two ANPx101 and one ANPz101), which were used to position the fiber holder with respect to the cantilevers. One of the top two attocubes moved the fiber along the length of a cantilever, while the other moved in an orthogonal direction and allowed us to position the fiber over different cantilevers in a single cool down. At 4 K, each of these attocubes had ∼5 mm of total travel range, which was more than enough to traverse the entire sample. The bottom attocube moved the fiber toward and away from the sample. With this, we adjusted the distance until the laser was focused on the surface of the cantilevers, which maximized our interferometry signal.

5.5 Phase-locked loop circuit for monitoring the cantilever resonant frequency

A schematic circuit of the phase-locked loop (PLL) circuit is shown in Fig. 5.4. The cantilever motion was detected optically using a fiber-interferometer and converted to a voltage signal with a photodiode. This voltage signal was sent to a lock-in amplifier where it was mixed with a reference signal (from the lock-in's internal oscillator). As we will explain, this allowed us to determine and track the cantilever's resonant frequency. Feedback loops were employed to ensure that the PLL remained stable for extended periods of time. We will now provide a detailed description of Fig. 5.4.

5.5.1 Laser and fiber optics

We used a 1550 nm fiber-coupled diode laser from JDS Uniphase (JDS Uniphase, CQF935/66 26 50 mW 1550 nm CW DFB Laser with PM fiber for WDM applications), which was powered by a low noise current source (ILX Lightwave, LDX-3620 Ultra low noise current source) using a driving current current of ∼100 mA. We operated the current source in constant power mode, in which a photodiode (reference photodiode) measured the laser's power and provided feedback to stabilize the laser's output power. The voltage output of this reference photodiode was sent through a 1 kΩ resistor to the LDX-3620 photodiode reference port. We were able to tune the laser wavelength through temperature

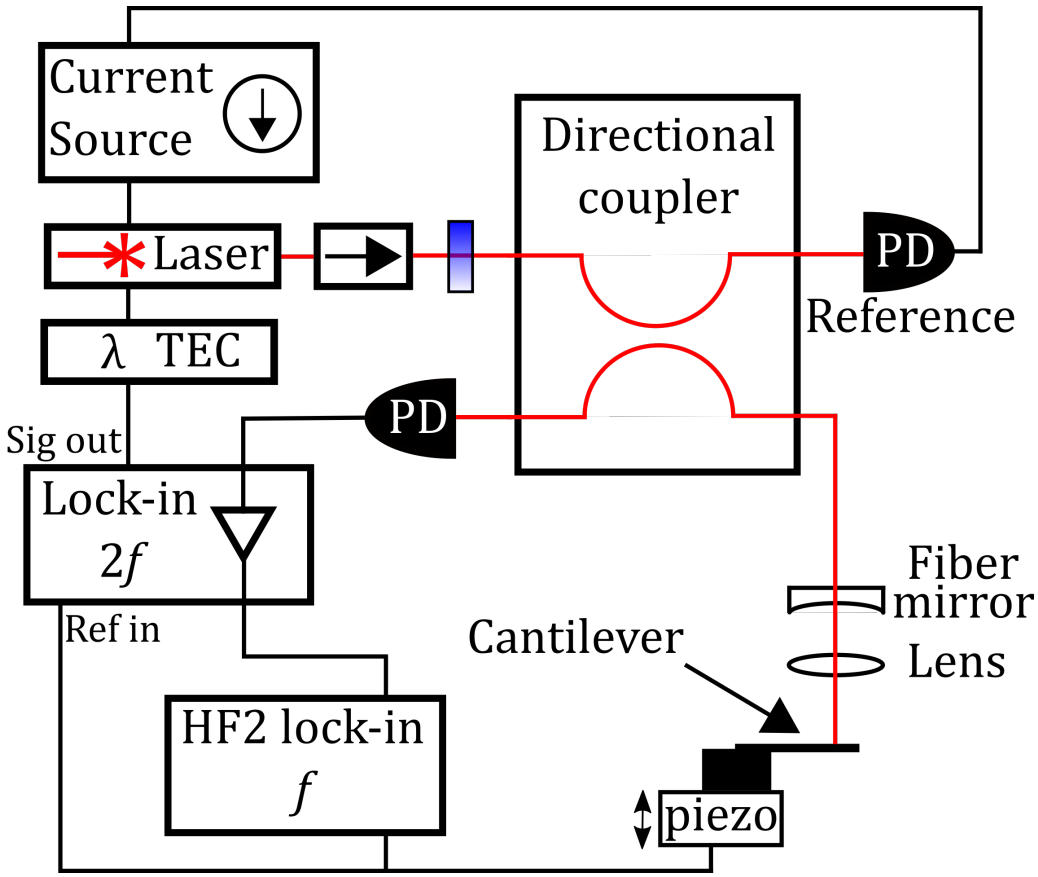

Figure 5.4: A schematic of the PLL measurement circuit. The 1550 nm laser passed through an optical isolator and variable attenuator before passing through a 99:1 directional coupler. The 99% port went to a reference photodiode (PD) which was used to stabilize the power output of the laser. The 1% port passed through a feedthrough into the fridge and created an interferometer with the gold coated fiber and silicon cantilever. This signal then passed back through the 99% coupler into a signal PD, where it was filtered and amplified. The signal was sent into a lock-in which again amplified the signal before it reached the HF2 lock-in amplifier. The HF2 drove the piezo actuator in a PLL with the cantilever signal as its reference. The piezo drive signal was also sent to the first lock-in amplifier as its reference signal. With this, the first lock-in was used to monitor the second harmonic ($2f$) of the interferometry signal. The output of this measurement was sent to a thermoelectric temperature controller (TEC), which was used to adjust the wavelength of the laser and keep the PLL stable.

using a thermoelectric cooler mount (Thorlabs, LM14S2 Universal 14-Pin Butterfly Laser Diode Mount) and temperature controller (Thorlabs, TED200C Thermoelectric Temperature Controller). The thermoelectric cooler mount also allowed for RF modulation of the laser source.

The RF modulation allowed us to reduce optical feedback noise and optical interference

noise [67]. We used a 1 MHz RF modulation signal that was generated by a voltage-controlled oscillator (Mini-Circuits, ZX95-850W+) which passed through a voltage-variable attenuator (Mini-Circuits, ZX73-2500+) and an amplifier (Mini-Circuits, ZFL-1000VH2). Effectively, this reduced the laser's coherence length to 1 cm. This distance was much shorter than the distance between any connector ports, but still larger than the length of our fiber-interferometer (∼mm), thereby removing unwanted interference.

The laser's path is illustrated in red in Fig. 5.5. The laser power was attenuated with a fixed fiber optic attenuator (Thorlabs, FA15T) before it was connected to an optical isolator (Thorlabs, 4015SAFC) and a variable attenuator (Thorlabs, VOA50-FC). As the driving current of the laser was maintained at 100 mA for all measurements, the laser's power was adjusted by either tuning the variable attenuator, or placing or removing fixed fiber optic attenuators in front of the laser. The variable attenuator's output was connected to a 99:1 directional coupler (Thorlabs, 10202A-99-FC). The through port went to a photodiode (New Focus, 2011-FC 200-kHz Front-End Photoreceiver), which served as a reference for the laser's power. The coupled port was connected to a long fiber which passed through a vacuum feedthrough at the top of the insert and was ultimately attached to the brass fiber holder in Fig. 5.3. The optical signal returning from the cantilever then passed back through the directional coupler into a second photodiode (signal photodiode) of the same model as the reference photodiode.

5.5.2 Electronics

The signal photoreceiver consists of a photodiode followed by a low-noise transimpedance amplifier which provided an adjustable gain of 10,000 for the measurements in this text. This is followed by 6-dB/octave high- and low-pass filters which were typically set to DC and 10 kHz respectively.[6] From the output of the photoreceiver, the signal was sent into the input port of a lock-in amplifier (AMETEK Advanced Measurement Technology, 7265 DSP Lock-in Amplifier) that amplified the signal. This amplified signal was then sent to a

6. Our cantilevers had resonant frequencies around 2 kHz. In practice there was no noticeable difference in measurements whether we set the top cutoff frequency to 10 kHz or kept it fully open. For measurements of higher order flexural modes the high frequency cutoff was left fully open.

second lock-in amplifier (Zurich Instruments, HF2LI Lock-in Amplifier) that controlled the PLL.

The basic idea behind the HF2's PLL is that a reference signal $V_{\mathrm{r}}(t) = \sqrt{2}e^{-i\omega_{\mathrm{r}}t}$ is sent to a device that can have amplification, phase-shifting, non-linearities, and distortions, which leads to a response signal $V_{\mathrm{s}}(t) = A_{\mathrm{s}} \cos\left(\omega_{\mathrm{s}}t + \Theta_{\mathrm{s}}\right)$ and higher harmonics. The PLL then mixes these two signals to obtain

$$V_{\mathrm{r}}(t) \cdot V_{\mathrm{s}}(t) = \frac{A_{\mathrm{s}}}{\sqrt{2}}\left(e^{i[(\omega_{\mathrm{s}}-\omega_{\mathrm{r}})t+\Theta_{\mathrm{s}}]} + e^{-i[(\omega_{\mathrm{s}}+\omega_{\mathrm{r}})t+\Theta_{\mathrm{s}}]}\right) \tag{5.1}$$

The resulting signal has a low frequency component, $\omega_{\mathrm{s}} - \omega_{\mathrm{r}}$, and a high frequency component, $\omega_{\mathrm{s}} + \omega_{\mathrm{r}}$. This signal is low-pass filtered with an infinite impulse response RC filter, with frequency response $F(\omega)$, which annihilates the high frequency component. The resulting signal is given by

$$F(\omega_{\mathrm{s}} - \omega_{\mathrm{r}})\frac{A_{\mathrm{s}}}{\sqrt{2}}e^{i[(\omega_{\mathrm{s}}-\omega_{\mathrm{r}})t+\Theta_{\mathrm{s}}]} \tag{5.2}$$

which can be expressed as an amplitude R and phase Θ_{PLL} in the complex plane. For driven cantilevers, the response frequency will equal the drive frequency and on resonance the phase difference between the reference signal and the response signal is $\pi/2$. Thus, a single value ($\Theta_{\mathrm{PLL,res}}$) specifies the resonant condition for a driven cantilever. Without modifying the reference signal, as properties of the cantilever change (which may lead to changes in the cantilever resonant frequency) Θ_{PLL} may change from $\Theta_{\mathrm{PLL,res}}$, which indicates that the cantilever is no longer resonantly excited. However, by using $|\Theta_{\mathrm{PLL}} - \Theta_{\mathrm{PLL,res}}|$ as the error signal for PID (proportional-integral-derivative) feedback on the reference signal frequency, the lock-in amplifier can modify the drive to ensure that $\Theta_{\mathrm{PLL}} = \Theta_{\mathrm{PLL,res}}$. This allows us to always drive the cantilevers on resonance and track changes in their resonant frequency.

For measurements that did not involve the small magnetic coil, the HF2 used its own internal 10 MHz clock to generate a voltage signal that drove the piezo stack on the sample stage. The piezo drive signal was also sent to the reference port of the first lock-in that was used to amplify the signal. This allowed us to use this same lock-in to monitor the $2f$ component of our signal coming from the cantilever. As our cantilever-fiber system is a

low finesse Fabry-Perot cavity with a large distance (much larger than the λ of the laser) between the reflecting surfaces, when the wavelength of laser is varied (via the TEC) the incident power on the signal photodiode from the cantilever will trace out a sinusoidal curve, the "interferometry fringe" (see Fig. 5.6). As the cantilever oscillates its motion will trace out part of that fringe. If the laser λ is chosen such that the cantilever's equilibrium position is at the middle of the fringe, then the interferometry signal at the cantilever's resonant frequency will have its maximum amplitude, while the $2f$ component of the interferometry signal will be minimized.[7] Thus, by monitoring the magnitude of the $2f$ component and minimizing its value using the TEC to control the laser λ with a PID feedback loop, we maintained the optimal fringe position throughout our measurements of the cantilever's resonant frequency.

5.6 Magnet

The large magnet used in the field sweep measurements is a 9 T actively shielded solenoid magnet (American Magnetics Inc.) with a 3" bore. This magnetic has a field to current ratio of 1021.8 Gauss/Amp and a homogeneity over 1 cm DSV of $\pm 0.1\%$. This magnet was controlled by a power supply programmer (American Magnetics Inc., Model 430), which gave us current resolution down to 15.6 μA. The magnet is equipped with a persistent switch, but for all of the large field measurements the magnet was not persisted. Instead, the magnet was ramped to the maximum field of the measurement and then ramped with a continuous linear ramp (typically $\sim$ 50 Gauss/s) down to to the minimum field of the measurement. At the minimum field the ramp direction was switched and the magnet returned to the maximum field. Data was collected continuously during these ramps so that the magnet was never paused during a ramp.

7. As the cantilever oscillates it bends slightly, which leads to an optical lever effect. As a consequence, the signal's first harmonic magnitude is not truly maximized when the second harmonic magnitude is minimized. However, in this experiment, the optical lever effect is minimal, so when the $2f$ component is minimized, the first harmonic is still within $\sim 5\%$ of its true maximum.

5.7 Cantilever detection and calibration

Accurately determining which cantilever the laser was addressing and where that laser was positioned over the cantilever was essential for us to interpret our data. In this section we will detail all of the steps required to locate the cantilevers as well as the preliminary measurements we took to determine the basic cantilever properties.

5.7.1 Locating the cantilevers and fiber placement

Locating the cantilevers began at room temperature before the IVC was sealed. After the stage was assembled and attached to the He-3 pot we positioned the fiber over the silicon chip and moved the z attocube (toward and away from the chip) to maximize the magnitude of the interferometry signal.[8] Next, we moved the x and y attocubes to scan over the window that contained the cantilevers. We did this to ensure that we had enough travel range to measure all cantilevers. To determine the location of the window we looked for extinctions of the interferometry signal. After the z optimization, when the fiber was located over the silicon the interferometry signal was around 2 volts for typical gain settings.[9] When the fiber was positioned over the window, the laser hit a machined brass surface 2 cm below the sample. As a result, none of this light returned through the fiber and the interferometry signal suddenly dropped to 0 for all practical purposes.[10] To locate the cantilevers, we then moved across the window and observed the interferometry signal appear and disappear. We counted the number of appearances, which matched the number of cantilevers we had, and then positioned the fiber over one of the cantilevers. At this point we only roughly positioned the fiber along the length of the cantilever.

Once the insert was sealed and cooled to 4 K we positioned the fiber more precisely. We again scanned the fiber across the window. We measured appearances and disappearances

8. This should be done fairly carefully as we have found that this alignment optimization typically remained after the insert was cooled down.

9. Typically we used 10,000 gain on the signal photodiode and the first lock-in amplified the signal by another factor of 5.

10. The fibers core is 9 μm in diameter, so we expected a laser spot size of the same diameter when everything was focused properly. As this spot size was much smaller than the cantilever length and width, the extinctions of the signal were still very abrupt changes.

of the interferometry signal when scanning across cantilevers, but this time we used a much slower constant travel speed and timed the extinctions and appearances with a stop watch. This allowed us to convert our measurements of time into measurements of distance, which we checked against our lithographic dimensions. This ensured that we knew which cantilever we were on. We then placed the fiber laterally in the middle of a cantilever. To determine the position along the length of the cantilever, we moved the fiber to the base of the cantilever. At 4 K, the cantilevers had quality factors $\sim$ 50,000 and thus, when the fiber went from being positioned over the cantilever to being positioned over the silicon chip near the base of the cantilever the interferometry signal changed abruptly.[11] We determined the top edge of the cantilever by finding the point where the signal dropped to zero as the fiber moved off of the cantilever. By timing the travel time between these two points we were able to reliably place the fiber at $\eta = 0.66$, two-thirds of its full length from the base of the cantilever. Finally, we repositioned the z attocube to ensure that the magnitude of our interferometry signal was still optimized. If sufficient care was taken to mount the sample so that it was not tilted with respect to the x and y attocubes, then to move to another cantilever we only needed to move 1 attocube.

5.7.2 Determination of cantilever resonant frequency and phase

To determine the resonant frequency f_0 of the cantilever we drove the piezo at a fixed voltage and stepped the frequency of this drive while we measured the resulting amplitude and phase of the cantilever's motion. For a preliminary measurement, we typically used 1 Hz frequency steps and waited 0.5 second between points. From the cantilever's dimensions, we expected resonant frequencies around 2 kHz, so we began these scans at 500 Hz and ended around 4 kHz. An example of this preliminary scan is shown in the left column of Fig. 5.5. For the majority of the frequency range, the cantilever response was minimal; however, at the resonant frequency the amplitude of motion was enhanced and the phase changed by π through the resonance. Once a high-Q mechanical mode was located we took

11. The signal suddenly changed in magnitude. Qualitatively, it also went from a signal that traveled through many interferometry fringes over the cantilevers (the attocube motion provided a white noise drive to the cantilevers, which excited their resonant motion) to one that barely traveled through a fringe over the silicon chip, which has a very low Q.

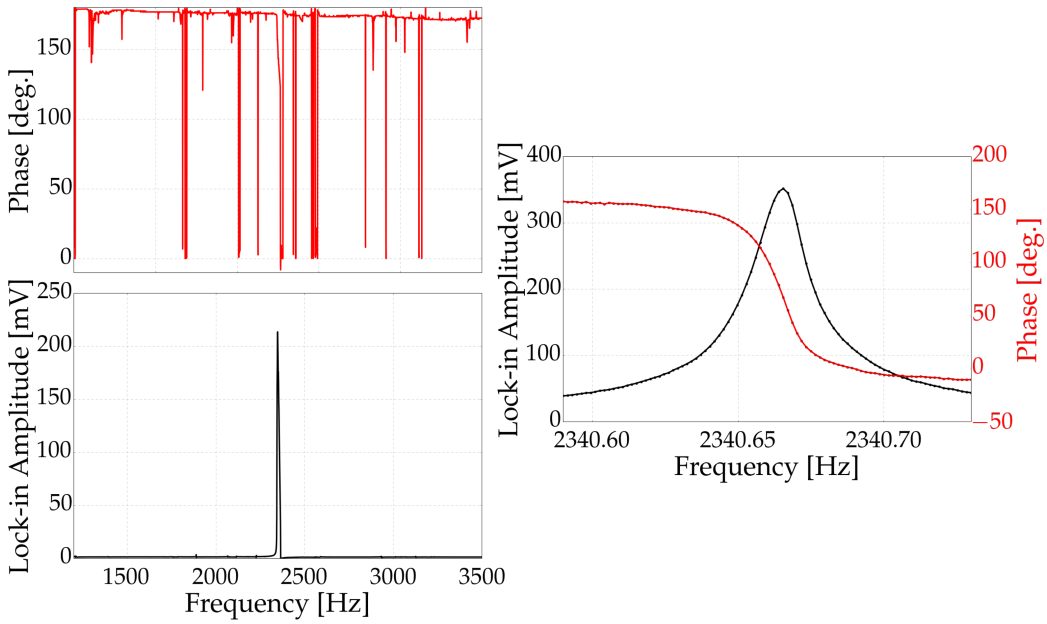

Figure 5.5: Cantilever amplitude and phase as a function of piezo drive frequency. The left column shows a preliminary scan used to locate the resonance in which the piezo frequency is varied quickly over a large range of frequencies. The right column illustrates a scan used to determine the Q and resonant phase of the cantilever. For this, we scanned a very small range of frequencies immediately around the resonance. Between each point, we waited 5 times longer than the characteristic time of the oscillator $\tau = \frac{Q}{\pi f_0}$.

a much slower and finely spaced scan around the peak, which is illustrated in the right column of Fig. 5.5.

To verify that this was the fundamental cantilever resonance, we looked for higher flexural modes. For a rectangular cantilever, the modes are not evenly spaced and their spacing from the fundamental mode is set by Eq. 4.16, which gives $f_n = f_0 \frac{\beta_n^2}{\beta_0^2}$. The second flexural mode will be at $6.26 f_0$ and the third flexural mode will be around $17.55 f_0$. We verified these higher order mechanical resonances existed and they were typically within 10% of their predicted frequency for these 340 nm thick silicon cantilevers.

5.7.3 Determination of optimal cantilever tip displacement

The signal photodiode converted the cantilever motion into a voltage signal. For most of the measurements working in terms of voltage was sufficient; however, it was still useful to determine how that voltage related to the cantilever tip displacement. We will now discuss how this calibration was performed.

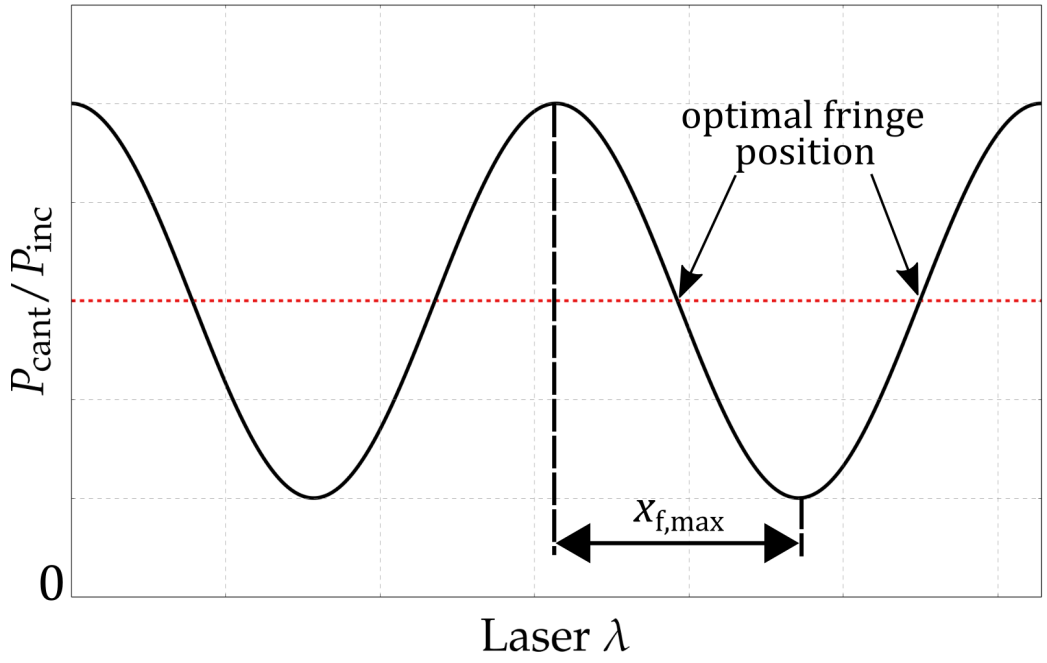

Figure 5.6: Ratio of power reflected from the cantilever that lands on the signal photodiode, P_{cant}, to the power incident on the cantilever, P_{inc}, as a function of laser wavelength. The optimal fringe position corresponds to the laser wavelength that will maximize the magnitude of the first harmonic of this ratio for a given cantilever displacement. At that optimal position, $x_{\text{f,max}} = \frac{1.841\lambda}{4\pi}$ indicates the peak-to-peak amplitude of the cantilever motion beneath the fiber that maximizes the first harmonic interferometry signal.

We sent laser light of wavelength λ through a fiber with power reflection coefficient R_{f} and power transmission coefficient T_{f} at its end and then placed that fiber a distance x_0 from a driven cantilever with a power reflection coefficient R_{c}. In this configuration, the ratio of the first harmonic of reflected power that traveled back up the fiber, P_{cant}, to that of the incoming power incident on the cantilever, P_{inc}, in the absence of an optical lever effect is given by [3]

$$\left(\frac{P_{\text{cant}}}{P_{\text{inc}}}\right)_1 = 4T_{\text{f}}\sqrt{R_{\text{f}}R_{\text{c}}}\sin\left(\frac{4\pi}{\lambda}x_0\right)J_1\left(\frac{4\pi}{\lambda}x_{\text{f,max}}\right) \tag{5.3}$$

where J_1 is a Bessel function of the first kind and $x_{\text{f,max}}$ is the cantilever's amplitude of motion below the fiber. We optimized this power by choosing the optimal fringe position (indicated in Fig. 5.6), which satisfies the relationship $x_0 = \frac{4n+1}{8}\lambda$ as this maximizes the sine term. The function $J_1(x)$ has its first maximum located at $x = 1.841$, and thus when

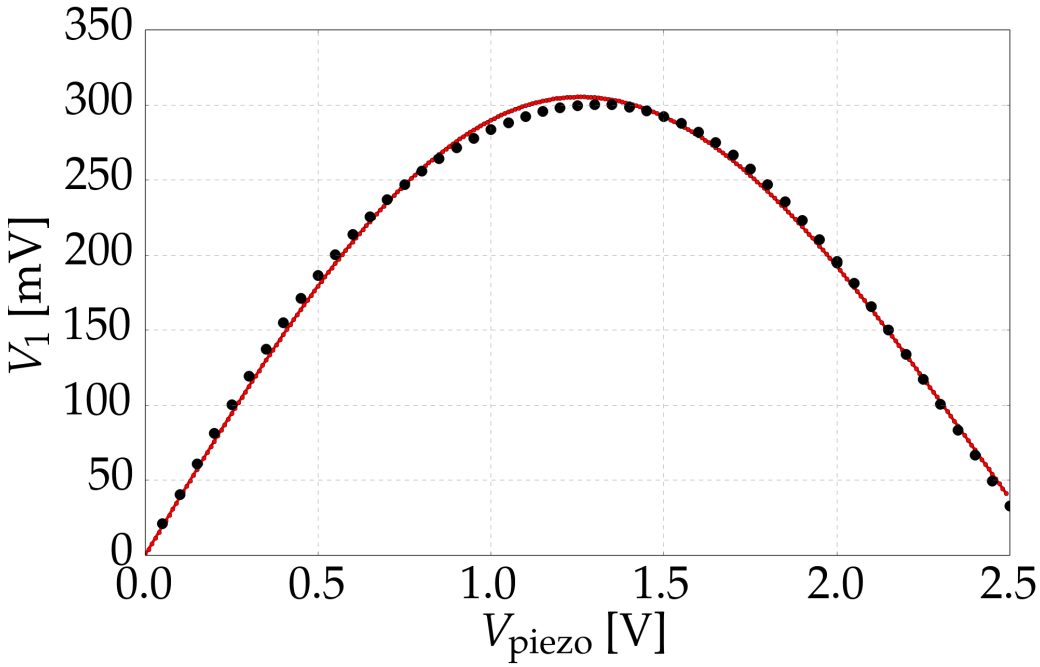

Figure 5.7: Cantilever first harmonic signal V_1 measured by the lock-in as a function of piezo drive voltage. The black points are measured data and the red curve is a fit to Eq. 5.4. The fitting coefficients are $V_{1,\text{max}} = 305$ mV, $V_{\text{peak}} = 1.26$ V and $\epsilon = 1.3 \times 10^{-6}$ V^{-1}. As ϵ is small, the optical lever effect in our system can be neglected.

$x_{\text{f,max}} = \frac{1.841\lambda}{4\pi} = 227$ nm the first harmonic signal will be maximized. If we assume that the piezo motion and cantilever motion are proportional to the piezo drive, then the lock-in first harmonic magnitude V_1 can be fit to a function of the form

$$V_1 = \frac{V_{1,\text{max}}}{0.582}\left|J_1\left(1.841\frac{V_{\text{piezo}}}{V_{\text{peak}}}\right) + \epsilon V_{\text{piezo}}\right| \tag{5.4}$$

where we have now included an optical lever effect with the optical lever coefficient ϵ. The number 0.582 approximates the magnitude of the first maximum of the Bessel function, $J_1(1.841)$. $V_{1,\text{max}}$ and V_{peak} are fitting parameters which represent the maximum first harmonic voltage measured on the lock-in and the piezo drive voltage that leads to $V_{1,\text{max}}$, respectively.

Comparing Eq. 5.3 and Eq. 5.4 we arrive at a calibration between piezo drive and

cantilever displacement beneath the fiber, given by[12]

$$x_{\mathrm{f,max}} = \frac{1.841\lambda}{4\pi}\frac{V_{\mathrm{piezo}}}{V_{\mathrm{peak}}} \tag{5.5}$$

More importantly, we can relate the motion of the cantilever under the fiber to the motion of the cantilever's tip using the normalized mode shape. Thus, our ultimate calibration of cantilever tip displacement is given by

$$x_{\mathrm{tip}} = \frac{1.841\lambda}{4\pi}\frac{V_{\mathrm{piezo}}}{V_{\mathrm{peak}}}\frac{1}{U_{\mathrm{N}}(\eta)} \tag{5.6}$$

where η is determined from timing as explained in Section 5.7.1.

With this calibration of tip displacement, the final step was to determine the optimal tip displacement (piezo drive) for our measurements, with the main goal of minimizing the frequency noise of our PLL. One restriction was set by the cantilever's Brownian motion. As the cantilever oscillated it experienced a small amount of damping, which converted some of its kinetic energy into heat. Conversely, through the fluctuation-dissipation theorem, the cantilever's finite temperature converted its thermal energy into a white noise force that drove the cantilever. This random drive competed with the coherent piezo drive and set a limit to the frequency resolution of the PLL δf, which is given by [68]

$$(\delta f)^2 = \frac{1}{2\tau_{\mathrm{M}}}\frac{f_0 k_{\mathrm{B}} T}{\pi Q k x_{\mathrm{tip}}^2} \tag{5.7}$$

where τ_{M} is the measurement time. Therefore, at low tip displacement the Brownian motion became problematic if the desired frequency shift was small. Another concern was that due to the $J_1(x_{\mathrm{f,max}})$ term the magnitude of the first harmonic signal does not monotonically increase with tip displacement. When the magnitude became too small the HF2 could not maintain a stable PLL. Finally, though our cantilevers displayed nearly perfect Lorentzian resonances at low drives (Fig. 5.5), at higher drives they typically displayed a small amount

12. As shown by the fit in Fig. 5.7, the optical lever term leads to corrections on the order of 1 μV, while the interferometry signal is $\sim$ 100 mV over the range of relevant piezo drives. Therefore, it is safe to ignore this effect completely.

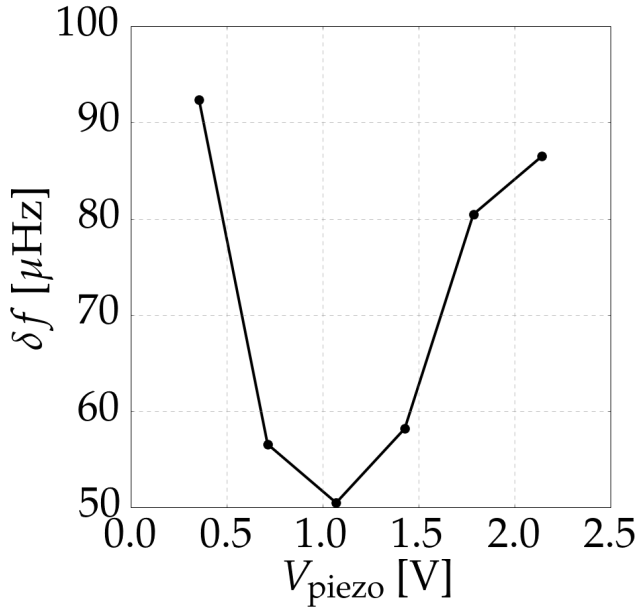

Figure 5.8: Cantilever frequency stability δf as a function of piezo driving voltage. At low drives, the frequency stability was reduced due to Brownian motion and at higher drives, the Duffing non-linearity of our cantilevers led to greater frequency noise. The set-up of this experiment was the same as that used for Fig. 5.7, and so we can see that the frequency stability was best near the piezo drive that maximized the first harmonic signal.

of Duffing non-linearity. In this regime, the cantilever's amplitude and frequency became dependent upon each other, and thus any noise that affected the cantilever's amplitude led to a frequency error. As a result, the optimal piezo drive was somewhere between these two regimes.

To determine this optimal drive, we took 60 1-second measurements of the cantilever's resonant frequency with the HF2. We determined the standard deviation of those frequency measurements and repeated this for multiple drives. By finding the drive which minimized this standard deviation we knew the drive (and thus tip displacement through Eq. 5.6) that would lead to the best sensitivity for our PLL. An example of such a measurement is shown in Fig. 5.8. As we found for all cantilevers, the best frequency stability was achieved at a piezo drive near V_{peak}. Since we always placed the fiber at $\eta \approx 0.66$, the typical x_{tip} used in all measurements was ~ 500 nm.

Chapter 6

Analysis of superconducting persistent current array data

In this chapter, we will describe the procedure to convert measured traces of the cantilever resonant frequency versus magnetic field into supercurrent versus magnetic field. We will then present the results of measurements of supercurrent in 4 array samples with different lithographic dimensions.

6.1 Conversion from cantilever resonant frequency to supercurrent

As described in Chapter 5, we drove the cantilevers in a PLL and monitored their resonant frequency. As we did this we also applied a linear magnetic field at $\theta = 0$ with respect to the sample, which allowed us to measure the cantilever's resonant frequency as a function of magnetic field, or equivalently flux $\Phi = BA$, where $A = \pi R^2$ is the area of the aluminum rings. An example of one measurement at $T = 471$ mK with a field ramp rate of $\dot{B} = 30\,\mu$T/s for cantilever 13 (CL13) is shown in Fig. 6.1

From this raw data we need to determine the frequency shift Δf which is only due to the supercurrent in the aluminum rings. We see that as a function of field, there is both a periodic sawtooth oscillations and a smoothly varying background. The former is due to

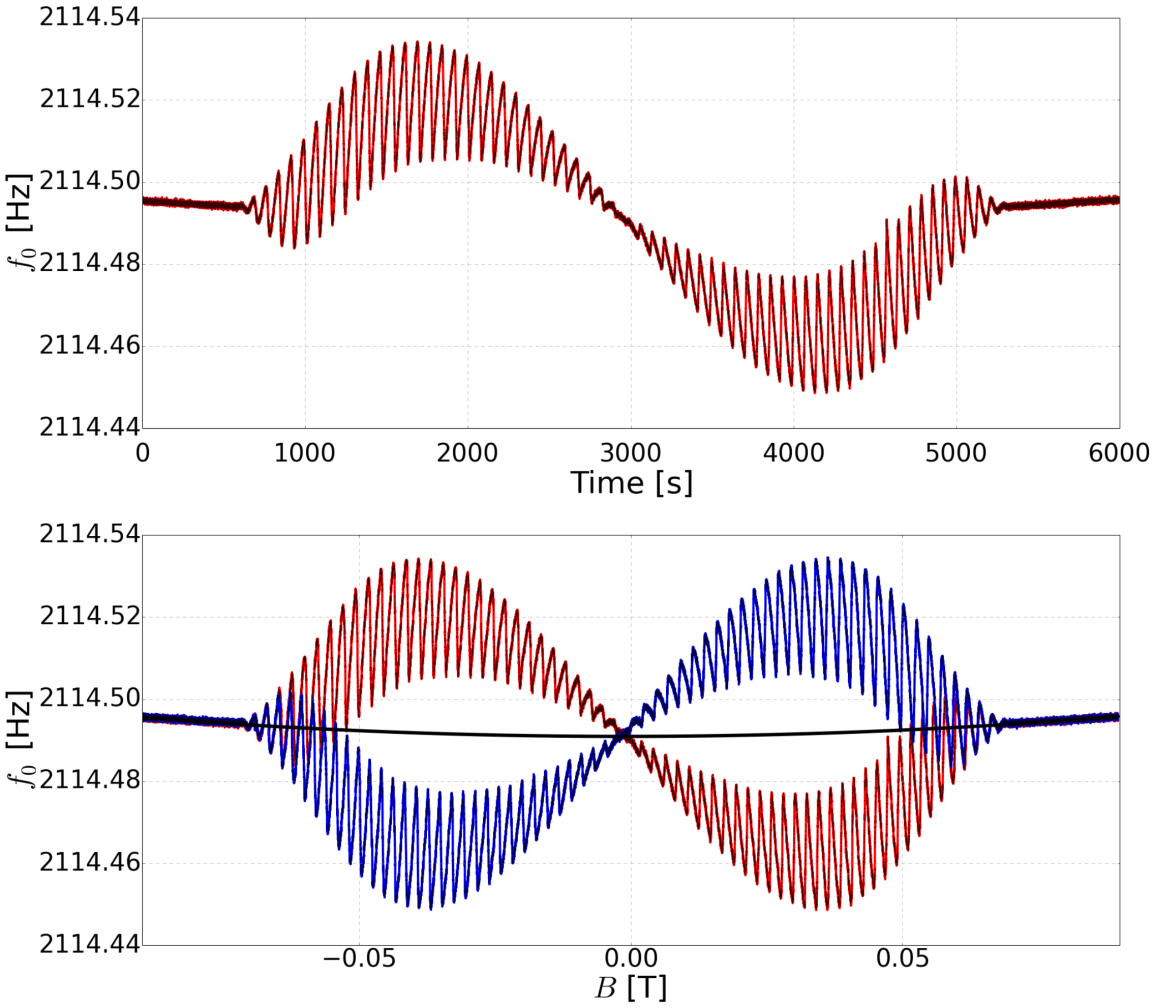

Figure 6.1: Measured cantilever resonant frequency as a function of time (top panel) and magnetic field (bottom panel) for CL13 at $T = 471$ mK. Red curves correspond to increasing B while blue curves are for decreasing B. As a function of field, the cantilever's resonant frequency displays periodic oscillations as well as a smooth field-dependent background. The black curve is a third-order polynomial fit to this smooth background. The overall envelop is set by hysteresis in the supercurrent (see Fig. 2.7 right column) and should not be removed by this background subtraction.

the rings' superconductivity, while the latter is likely due to impurities within the silicon cantilevers.[1] The first step in signal processing is to remove this background. For each ramp we fit the data above the rings' critical field (fields at which there were no longer any periodic oscillations) to a third-order polynomial and subtract that curve from the raw data. The next step is to correct for hysteresis in our magnet. From Fig. 6.1 we can see that the

1. Field sweeps taken on empty cantilevers display a smoothly varying resonant frequency without sawtooth oscillations as a function of field.

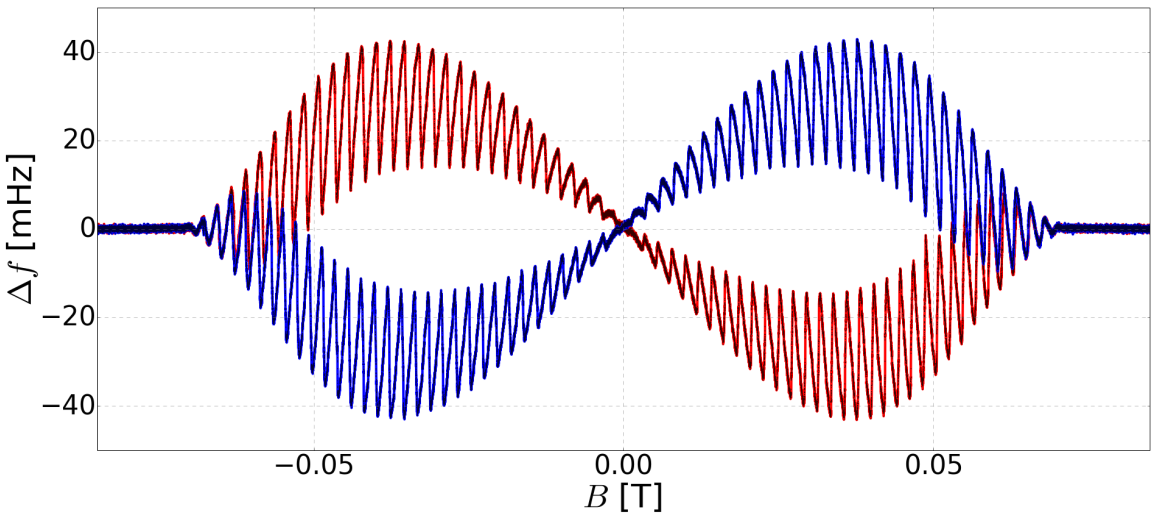

Figure 6.2: Frequency shift due to superconducting rings as a function of field obtained by removing a smooth background from the curves in Fig. 6.1. The measured fields have been shifted by 14 G to correct for hysteresis in the large magnet.

field traces are not symmetric about $B = 0$ and have a very small offset to negative fields. To correct for this, we add the same constant field offset ($\sim$15 G) to the measured fields for all field traces within a given measurement.[2] Within a given experimental cooldown (several months), across all measurements we found that this offset was constant to within $\sim 10\%$.

The result of these two processing steps is shown in Fig. 6.2. Above the rings' critical field, the frequency shift is 0 as the rings are no longer superconducting.[3] This condition is basically imposed by our polynomial background subtraction. However, we impose nothing about the frequency shift at $B = 0$ and after shifting the fields we can see that $\Delta f(B{=}0) = 0$, which is expected. Once both ramp directions have their fields corrected by the same shift, we see that there is an obvious symmetry, $\Delta f_{\dot{B}>0}(B) = \Delta f_{\dot{B}<0}(-B)$.

2. To determine this offset we recall that $F(B)$ is symmetric about B. Thus, the critical field should have the same magnitude whether we are at negative or positive applied magnetic fields. Further, both $I(B)$ and B are odd functions of applied magnetic field, so the resulting frequency shift will be an even function. However, due to hysteresis in the supercurrent, the true symmetry is $\Delta f_{\dot{B}>0}(B) = \Delta f_{\dot{B}<0}(-B)$. As the critical field represents only a single point, we determine the shift by finding the field offset which best enforces the symmetry $\Delta f_{\dot{B}>0}(B) = \Delta f_{\dot{B}<0}(-B)$

3. Technically, there should be a small contribution due to the rings' normal state persistent current above the critical field. However, given that the normal state persistent current is orders of magnitude smaller and only scales with the square-root of the number of rings, it is immeasurably small ($\Delta f \approx 0.5$ nHz) at these low magnetic fields with a $\theta = 0$ field orientation

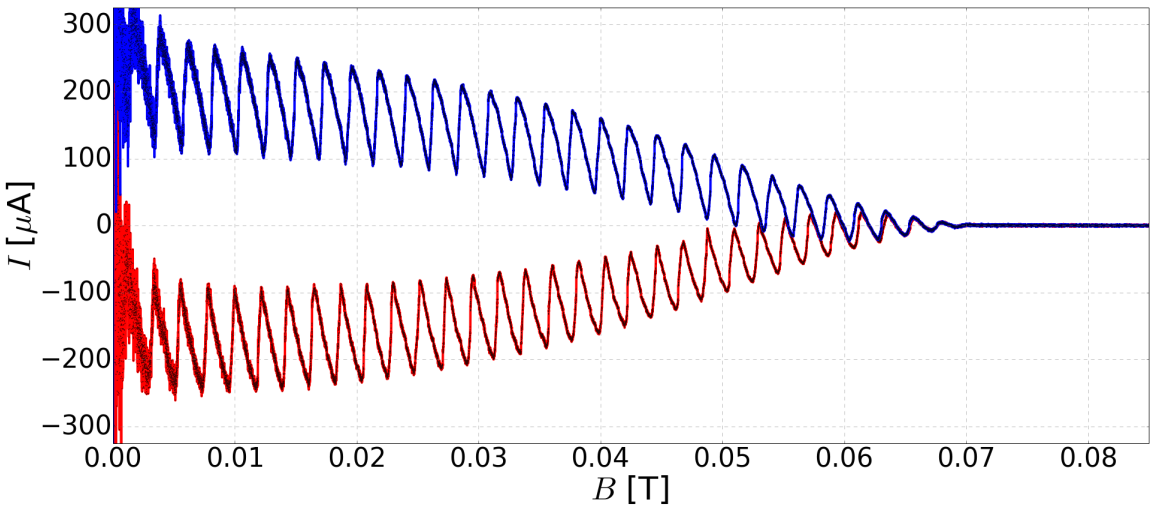

Figure 6.3: Supercurrent per ring as a function of field obtained using Eq. 6.1 with the traces of Fig. 6.2. CL13 has 450 rings with $R = 538$ nm.

Finally, using this Δf we determine the supercurrent using Eq. 4.26, which can be rewritten as

$$I = \frac{1}{N}\frac{2k\Delta f}{f_0}\left(\frac{l}{\alpha}\right)^2 \frac{1}{\pi R^2 B} \tag{6.1}$$

As will be explained in Section 6.2.2.1, the spring constant and ring radius are ultimately determined through fits to the Ginzburg-Landau supercurrent. The best-fit value for the spring constant is within 20% of the expected value computed by $k = (2\pi f_0)^2 m_{\text{eff}}$. The ring radius is highly constrained by the periodicity of oscillations and also agrees with the SEM measurements of the rings' diameter described in Appendix B. The cantilever length and number of rings are determined from imaging and $\alpha = 1.375$ given the placement of the ring arrays on the cantilever. An example of this conversion is shown in Fig. 6.3. Close to zero applied magnetic field we expect no frequency shift as $\Delta f \propto B$. However, we expect the noise on the cantilever to remain constant with magnetic field, and thus close to zero field any small fluctuation is amplified by dividing by a very small B, which leads to unreliable results. For all future plots we will not display I for B very close to 0. Also, as $I(B) = -I(-B)$ negative fields are redundant so we will only display the positive half of the field traces where necessary.

Sample	$R_{\mathrm{ring,SEM}}$ [nm]	$w_{\mathrm{ring,SEM}}$ [nm]	$l_{\mathrm{cant,opt}}$ [μm]	$w_{\mathrm{cant,opt}}$ [μm]	N
CL11	785	85	470	40	242
CL13	550	110	470	40	450
CL15	415	85	465	60	990
CL17	297	110	465	80	1680

Table 6.1: Cantilever parameters for the array measurements. The ring dimensions (mean radius and width) were determined from SEM images like those shown in Appendix B and the cantilever dimensions (length and width) were measured from optical images. All cantilevers are 340 nm thick. The number of rings per cantilever was counted from SEM images.

6.2 Supercurrent as a function of field and temperature

A measurement of the full supercurrent below the rings' critical field took ∼3 hours given our ramp rates. Thus, within a few days this measurement could be repeated at several temperatures for a single cantilever (see Section 5.3 for how the temperature was stabilized). Once this set was complete we moved to a different cantilever, repeated all of the calibrations of Section 5.7, and measured $I(B)$ at different temperatures for that cantilever. Ultimately, we measured 4 cantilevers with rings of varying lithographic dimensions, which are summarized in Table 6.1. The result of these measurements are summarized in Fig. 6.4 and Fig. 6.5. In the subsequent sections, we will describe the qualitative and quantitative aspects of this comprehensive dataset within the context of the theory developed in Chapter 2.

6.2.1 Qualitative analysis of measured $I(B)$

The most obvious qualitative feature of our $I(B)$ temperature series is a distinct periodic sawtooth oscillation. The smooth parts of the sawtooth represent current in equilibrium states characterized by the order parameter winding number n, and the jumps correspond to phase slips between these states. For a given array of rings, these oscillations have a periodicity that is independent of temperature and only depends upon the ring size, with smaller rings having a larger field-periodicity. Using the ring dimensions estimated from

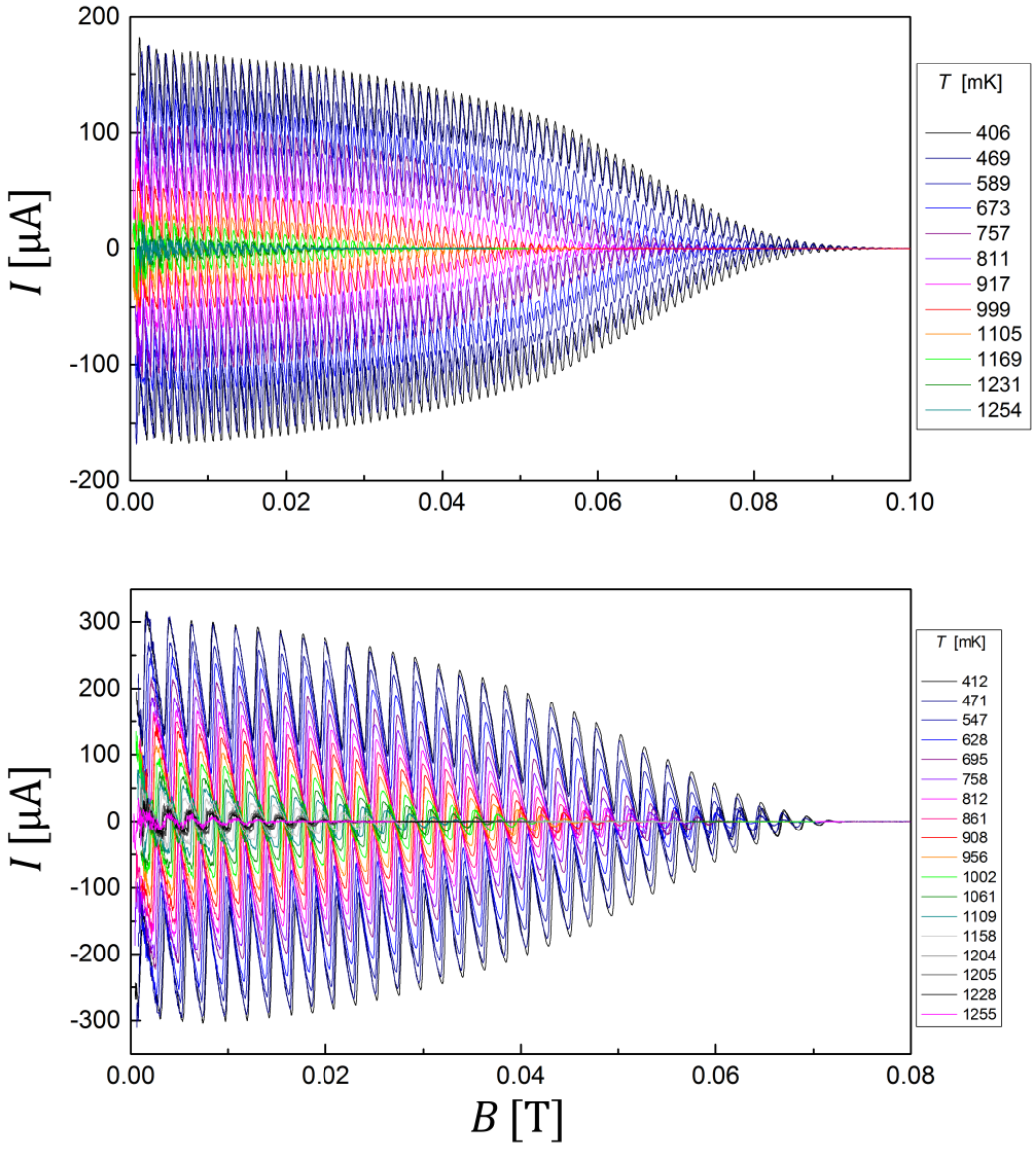

Figure 6.4: Supercurrent per ring as a function of field for CL11 (top panel) and CL13 (bottom panel) at various temperatures below the rings' T_c. The current was calculated from frequency shift following the treatment of Section 6.1. For each temperature there are two curves; the lower curves correspond to increasing B and the upper curves correspond to decreasing B.

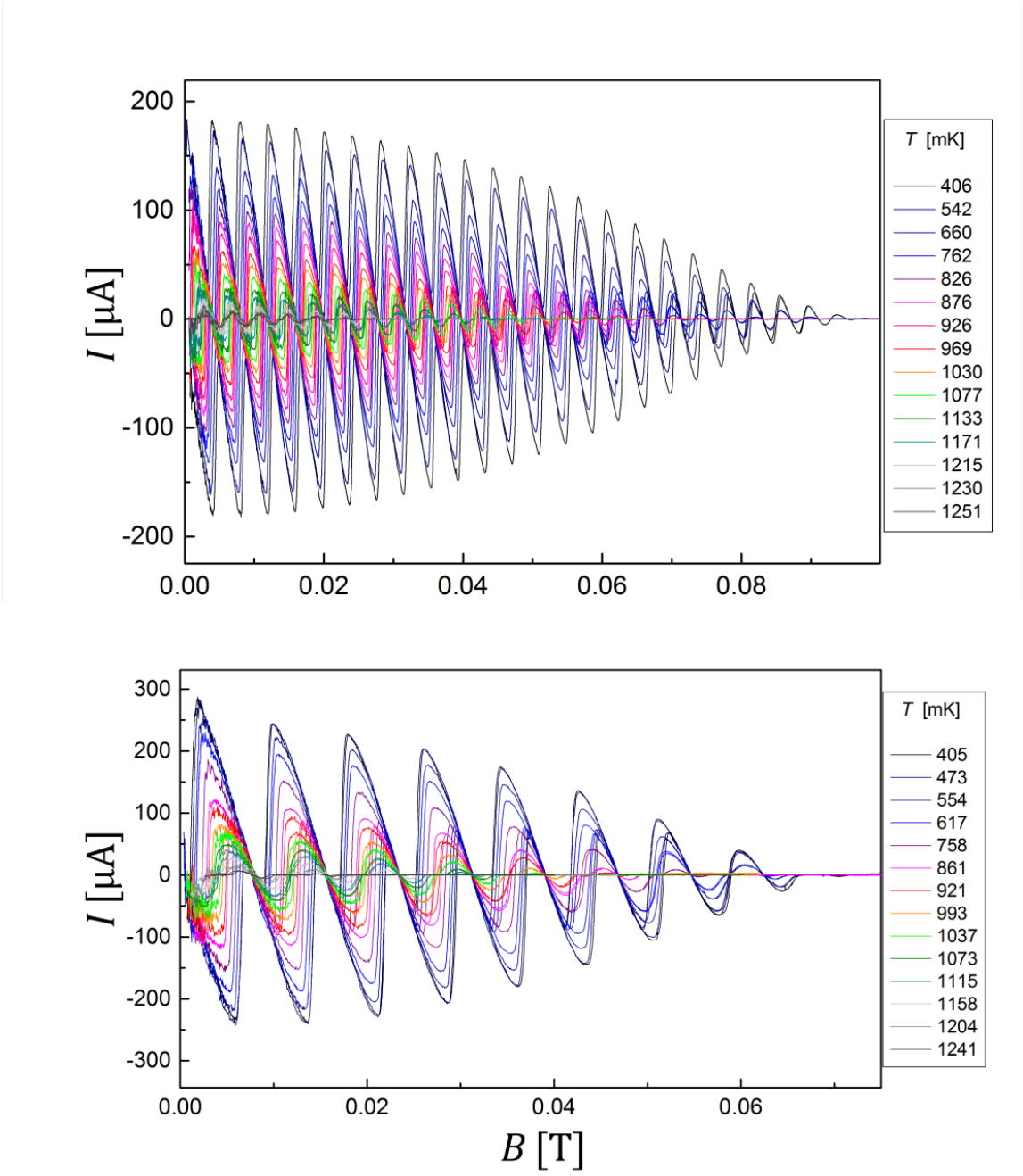

Figure 6.5: Supercurrent per ring as a function of field for CL15 (top panel) and CL17 (bottom panel) at various temperatures below the rings' T_c. The current was calculated from frequency shift following the treatment of Section 6.1. For each temperature there are two curves; the lower curves correspond to increasing B and the upper curves correspond to decreasing B.

SEM images and the expected periodicity from Eq. 2.50 of

$$B = \frac{1}{\pi R^2}\frac{1}{1+\left(\frac{w}{2R}\right)^2}\Phi_0 \tag{6.2}$$

we expect field periodicities of $B \sim 1$ mT, 2.1 mT, 3.8 mT and 7.2 mT for CL11, CL13, CL15 and CL17 respectively.[4] We can see that these expected periodicities match our measured periodicities and thus these represent the Aharonov-Bohm oscillations of the Cooper pair enclosing a flux set by the mean radius of our rings.

Another obvious qualitative feature is that above some absolute field value these oscillations die out completely, and that this field value decreases with increased temperature. This field represents the critical field of our rings B_{c3}, at which it is no longer energetically favorable to expel flux from the rings compared with the normal state. The simplest way to interpret the temperature dependence is to recall that for a ring of finite width, the $|\psi|^2$ coefficient in the free energy expansion (Eq. 2.40) is flux dependent. Above some critical flux value Φ_{c3} this coefficient will be positive regardless of winding number and thus there is no energetically favorable superconducting state. If we proceed similarly to how we estimated the maximum allowed winding number, but this time find the maximum allowed flux of Eq. 2.42 as a function of winding number, and then determine the winding number n_* that maximizes this function we arrive at the overall critical flux given by

$$\Phi_{\max}(n_*) \equiv \Phi_{c3} = \frac{\sqrt{3}R^2\Phi_0}{\xi w}\left(1+\frac{1}{24}\left(\frac{w}{2R}\right)^2\right)+\mathcal{O}\left(\left(\frac{w}{2R}\right)^3\right) \tag{6.3}$$

Noting that for our rings, $\Phi = \pi R^2 B$ we have

$$B_{c3} \approx \frac{2\sqrt{3}\Phi_0}{2\pi\xi w}\left(1+\frac{1}{24}\left(\frac{w}{2R}\right)^2\right) \tag{6.4}$$

The first coefficient, $2\sqrt{3} \approx 3.46$, is the exact coefficient for the critical field of a thin

4. This is the expected field-periodicity between zeroes of the supercurrent, or equivalently the minimum value of the free energy, for successive winding numbers. It is important to make this distinction as the periodicity of where the current abruptly decays (phase slips) has a winding number dependence, which can be seen from Eq. 2.94. In this case, to see the periodicity we would plot $\Phi_{f,n}$ versus n for both field-sweep directions, and the linear slope will be given by $\frac{\Phi_0}{1+\left(\frac{w}{2R}\right)^2}$.

plate [69]. The other corrections depend upon the exact ratio of w and R; however, Geim [38] found that a simplified analytic approximation of the form

$$B_{c3} = 3.67\frac{\Phi_0}{2\pi\xi w} \tag{6.5}$$

fit their numerically calculated critical fields for rings of $w < 2\xi$ and $R/w \sim 1-2$ within a few percent, and so we will adopt this equation. Regardless of the exact coefficient, the temperature dependence of B_{c3} is set by $\xi(T)^{-1}$. As $\xi(T)$ increases with increased temperature, the critical field must decrease with increased temperature, which is exactly what is observed. Further, CL11 and CL15 have a larger B_{c3} at a given temperature than CL13 and CL17, which indicates the $\frac{1}{w}$ scaling of B_{c3}.

There is also a clear hysteresis in the measured supercurrent, which decreases with increased temperature and increased applied magnetic field magnitude. Since $\xi(T)$ increases with temperature, the decrease in hysteresis is expected as $\frac{R}{\xi(T)}$ becomes smaller, which is explained in detail in Section 2.3.3. For large $\frac{R}{\xi(T)}$, there are multiple metastable states available to the system at each value of flux. In a free energy diagram, these metastable states cross at fluxes below the rings' critical flux and thus an increasing applied magnetic field ramp traces out a different path in the free energy diagram than a decreasing applied magnetic field trace does. However once $\frac{R}{\xi(T)} < \frac{\sqrt{3}}{2}$, neighboring metastable states cross in free energy at a flux above the rings' critical flux and so as flux is varied the system adiabatically follows the lowest energy state and there is no hysteresis. Increasing the magnetic field has the same effect as increasing temperature as they both act to diminish the condensation energy. At low fields where the condensation energy is large, there can be multiple metastable states available to the system. But close to B_{c3} the condensation energy is smaller and the rings can only support a single metastable state. Thus, at low fields there will be hysteresis while at large fields the system can only take one path and will display no hysteresis.

Finally, though it is difficult to see in the comprehensive data plots, we do observe the Little-Parks regime at T close to T_c and B near B_{c3} as shown in Fig. 6.6. In this regime, the persistent current goes through zero when the flux bias equals an integer number of flux

quanta, while the winding number changes at half-integer values. Below the critical field of the rings, there are extended field regions where $I = 0$, which indicates that the ring is no longer superconducting at those fields. As explained in Section 2.2.5.4, this reentrant normal state will occur between all winding numbers when $\frac{R}{\xi(T)} < 0.5$. As CL17 has the smallest rings with $R \sim 290$ nm we should observe this regime when $\xi(T) \sim 600$ nm. However, we should still observe the Little Parks regime only between the highest winding numbers when $\xi(T)$ is slightly smaller than 600 nm. As we will show in Section 6.2.2.2, this

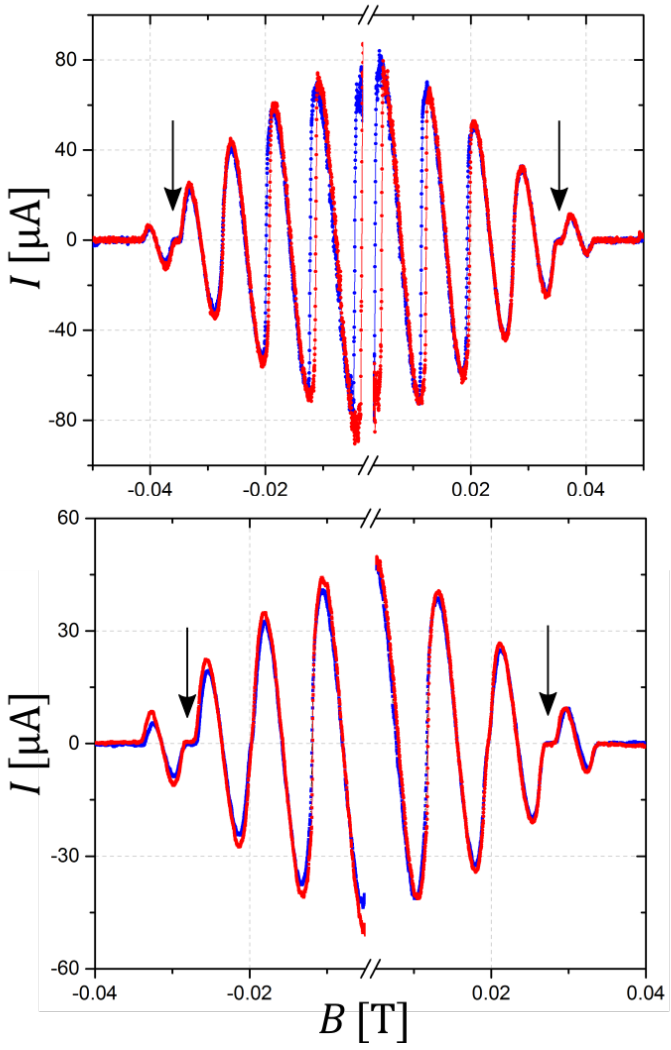

Figure 6.6: $I(B)$ traces from measured $\Delta f(B)$ for CL17 at $T = 993$ mK (top panel) and $T = 1073$ mK (bottom pannel). Red (blue) curves are for increasing (decreasing) field. Normal regions where $I = 0$, denoted by the black arrows, correspond to regions below B_{c3} where there is no energetically favorable superconducting state available to the rings.

occurs around 1 K, which is consistent with our observations in Fig. 6.6.

6.2.2 Fit to 1-dimensional Ginzburg-Landau theory

We will now proceed with a quantitative analysis of our frequency shift data. We fit our frequency shift data to Eq. 4.26, mutlipled by the number of rings N with $A = \pi R^2$ and the the current given by the equilibrium GL current for a ring of finite width, that is Eq. 2.47. Through Eq. 2.12 and Eq. 2.13 and expressing the bulk critical field through Eq. 2.20 we can ultimately express the supercurrent with 4 fitting parameters; the coherence length $\xi(T)$, the Pearl penetration depth $\lambda_{\mathrm{P}}(T)$, the ring radius R, and the ring width w. We use the Pearl penetration depth, $\lambda_{\mathrm{P}} = \lambda^2/d$ as the bulk penetration depth is larger than the sample thickness s [4, 70]. The frequency shift requires a fifth fitting parameter, which is the spring constant k.[5] While Eq. 2.47 specifies the dependence of $I(B)$ on $\xi(T)$ and $\lambda_{\mathrm{P}}(T)$ it does not specify any particular temperature dependence for $\xi(T)$ and $\lambda_{\mathrm{P}}(T)$. Thus, at each temperature we allow $\xi(T)$ and $\lambda(T)$ to remain unconstrained and the temperature-dependence is found from the fits to frequency shift data taken over a broad range of temperatures.

6.2.2.1 Step-by-step walkthrough of signal fitting for array measurements

The first step of this fitting procedure is to determine the winding number for each segment of $\Delta f(B)$. For measurements taken with increasing B, we count the number of segments (the regions of smoothly varying Δf between jumps) between B_{c3} and $-B_{\mathrm{c3}}$. This number is $2n_{\mathrm{max}}+1$, which allows us to determine n_{max}. Starting from B_{c3} and counting down from n_{max} to $-n_{\mathrm{max}}$ we then number the segments. We apply the equivalent process to measurements taken with decreasing B. An example of this numbering process is illustrated in Fig. 6.7.

The next step is to remove all of the jump regions from our data. Our GL current formula

5. The cumbersome frequency shift formula depends on many other variables, but those were all measured independently. N was measured from counting rings in the SEM images. The ring thickness s was measured with a crystal monitor during thermal evaporation and was 90 nm. l and α were determined from optical images of the cantilevers. f_0 was measured directly by the HF2 and B was measured by the magnet power supply controller.

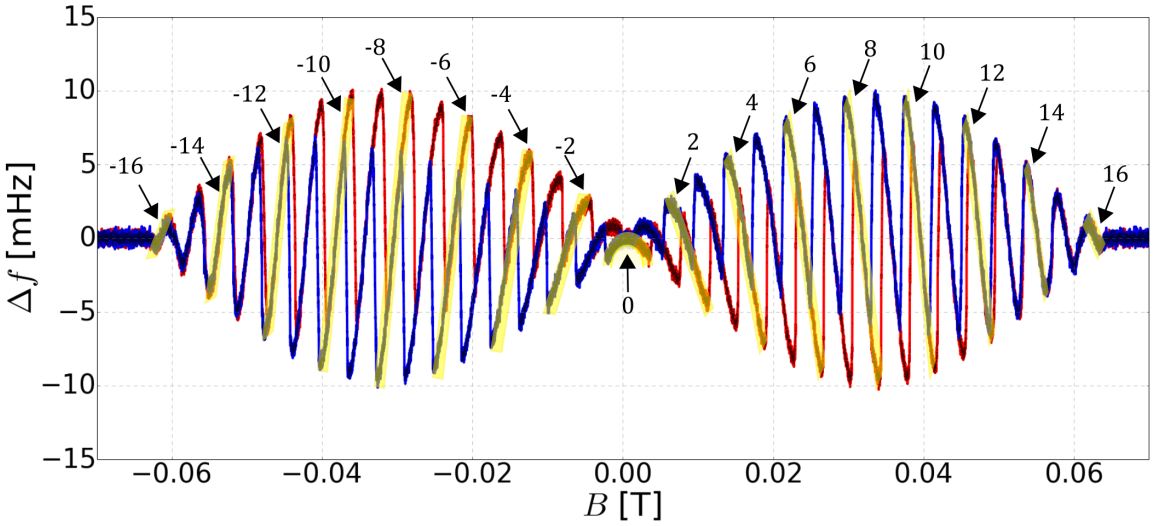

Figure 6.7: Measured $\Delta f(B)$ curves for CL15 at $T = 920$ mK. Red (blue) curves are for increasing (decreasing) field. Between $-B_{c3}$ and B_{c3} there are 33 smoothly varying segments, indicating that $n_{max} = 16$ for this measurement. Hilighted in yellow are the regions of Δf that belong to that specific winding number. We have only labeled even winding numbers for clarity. It is important to begin labeling from $\pm n_{max}$ at $\pm B_{c3}$ as the $n = 0$ branch occurs on different sides of zero depending upon the ramp direction, which can lead to accidental mislabeling.

only applies to equilibrium states, so we cannot use it to fit the regions that correspond to phase slips. Ideally, a phase slip would be seen as an instantaneous jump in our frequency shift data so this would amount to removing 1-2 points at each jump. However as we will show in Section 6.2.4.4, small lithographic imperfections from ring to ring ($\sim$0.5%R) broaden the phase slip regions in our arrays and thus we remove these entire regions. This removal step is illustrated in Fig. 6.8.

At this point, the frequency shift data are fully processed and we can begin the GL fit. For each sample we have several $\Delta f(B)$ traces taken at different temperatures. Three of our fitting parameters (R, w, and k) are physical parameters of the sample and do not vary with temperature. We first undertake a preliminary fit of all $\Delta f(B)$ for a given sample where we allow all 5 parameters to vary. At the end of this preliminary fit, we determine R, w and k as the mean value returned by these fits across all temperatures. Further, in these preliminary fits there is a degeneracy between λ_P and k as they both set the overall amplitude of the signal. λ_P affects the condensation energy and therefore the amplitude of the current, while k determines the proportionality between current and frequency shift.

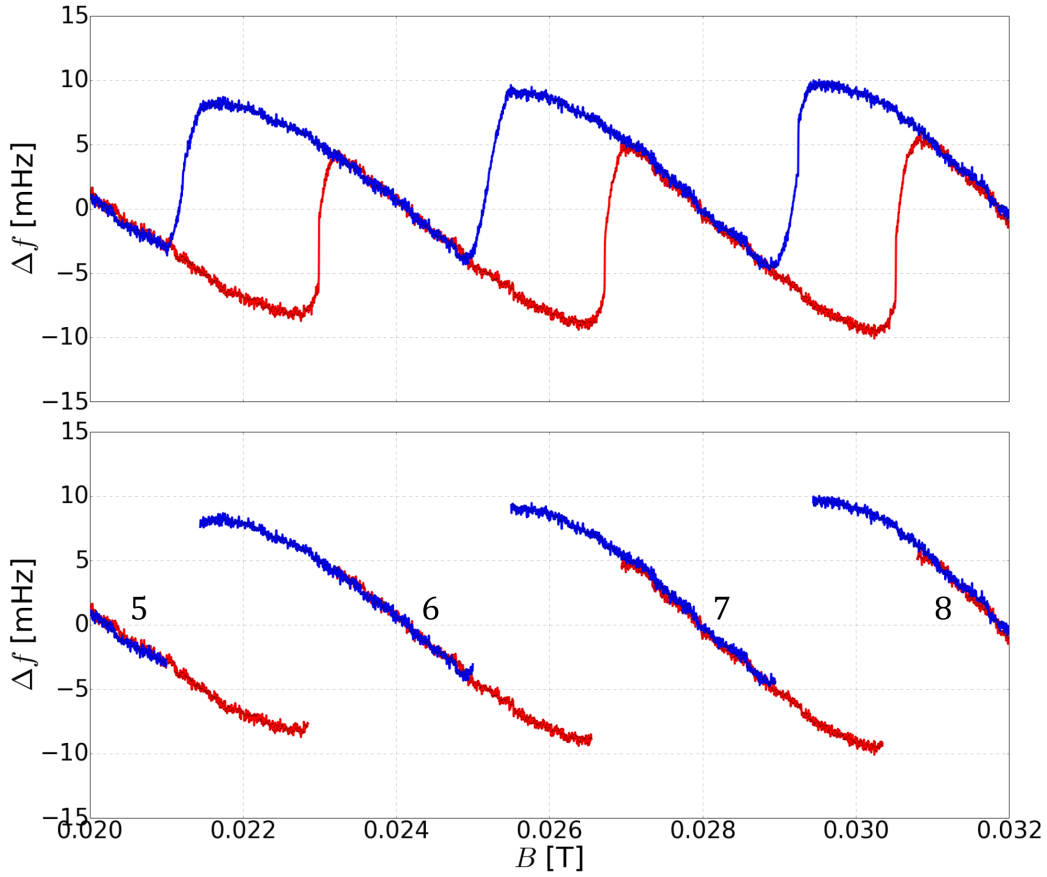

Figure 6.8: Subsection of the measured $\Delta f(B)$ curves for CL15 at $T = 920$ mK. Red (blue) curves are for increasing (decreasing) field. The top panel indicates the full dataset including the phase slip regions. The bottom panel contains only parts of Δf that correspond to equilibrium states that carry constant current, and are the only data used in the GL fit. The winding number of each branch is labeled in the bottom panel.

As a result, we initialize the spring constant to its expected value $k_{\text{in}} = (2\pi f_0)^2 m_{\text{eff}}$ and λ_{in} is initialized such that the zero temperature bulk critical field B_{c0} of aluminum is 0.01 T [4]. The scatter between the obtained values for k, R, and w at different temperatures is rather small (k and w vary by a few percent and R varies by less than 1 nm).

After this preliminary fit, we go back and fit the $\Delta f(B)$ traces for a given sample at all temperatures with only two fitting parameters at each temperature, $\xi(T)$ and $\lambda_{\text{P}}(T)$ as R, w, and k are now fixed. Both ξ and λ_{P} affect the condensation energy and thus the overall signal amplitude, however they are not degenerate as from Eq. 6.5 we can see that B_{c3} is set only by ξ and not λ_{P}. An example of this second round of fitting is illustrated in Fig. 6.9. With the fit parameters, we can convert our measured $\Delta f(B)$ into $I(B)$ traces and display

the corresponding GL $I(B)$ fits, which are illustrated in Figs. 6.10, 6.11, 6.12, and 6.13.[6] Though we took data for $T > 400$ mK we only display results for $T > 750$ mK. Below 750 mK we found that the values of w, ξ_0, and λ_0 returned by the fits do not converge to a fixed value as we will show they do for $T > 750$ mK. This likely reflects the decreasing applicability of GL theory at lower temperatures, given that 750 mK is already $\sim T_c/2$.

For each sample, we display data and fits for the lowest temperature near 750 mK, the highest temperature below T_c for which we have a decent signal, and one temperature in between. The most pronounced discrepancy between the data and the fit is found for the largest rings (CL11) at the lowest temperature. For these rings, the self-inductance L may play a role as we estimate $LI \sim 0.13\Phi_0$ at 750 mK using

$$L \approx \mu_0 \mu_r R\Big(\ln\Big[\frac{8R}{w}\Big] - \frac{7}{8}\Big) \tag{6.6}$$

where the relative permeability of aluminum is $\mu_r \approx 1$. This approximation assumes the current is uniformly distributed over the cross-sectional area of the ring and ignores terms of order $\left(\frac{w}{R}\right)^2$ and higher. This self-inductance may lead to a non-negligible skewing of the rings' current-phase relationship [71]. For the largest rings, the mutual inductance is only

6. As $I(B)$ is the physically interesting quantity we opt to display data as $I(B)$ instead of $\Delta f(B)$.

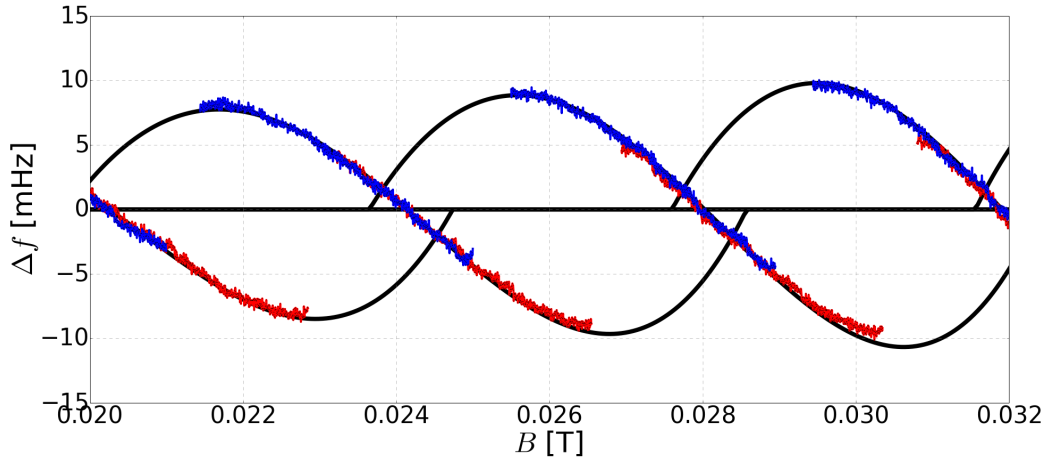

Figure 6.9: Subsection of the measured $\Delta f(B)$ curves for CL15 at $T = 920$ mK. Red (blue) curves are for increasing (decreasing) field. The GL fit is illustrated in black, with each separate curve corresponding to a different winding number.

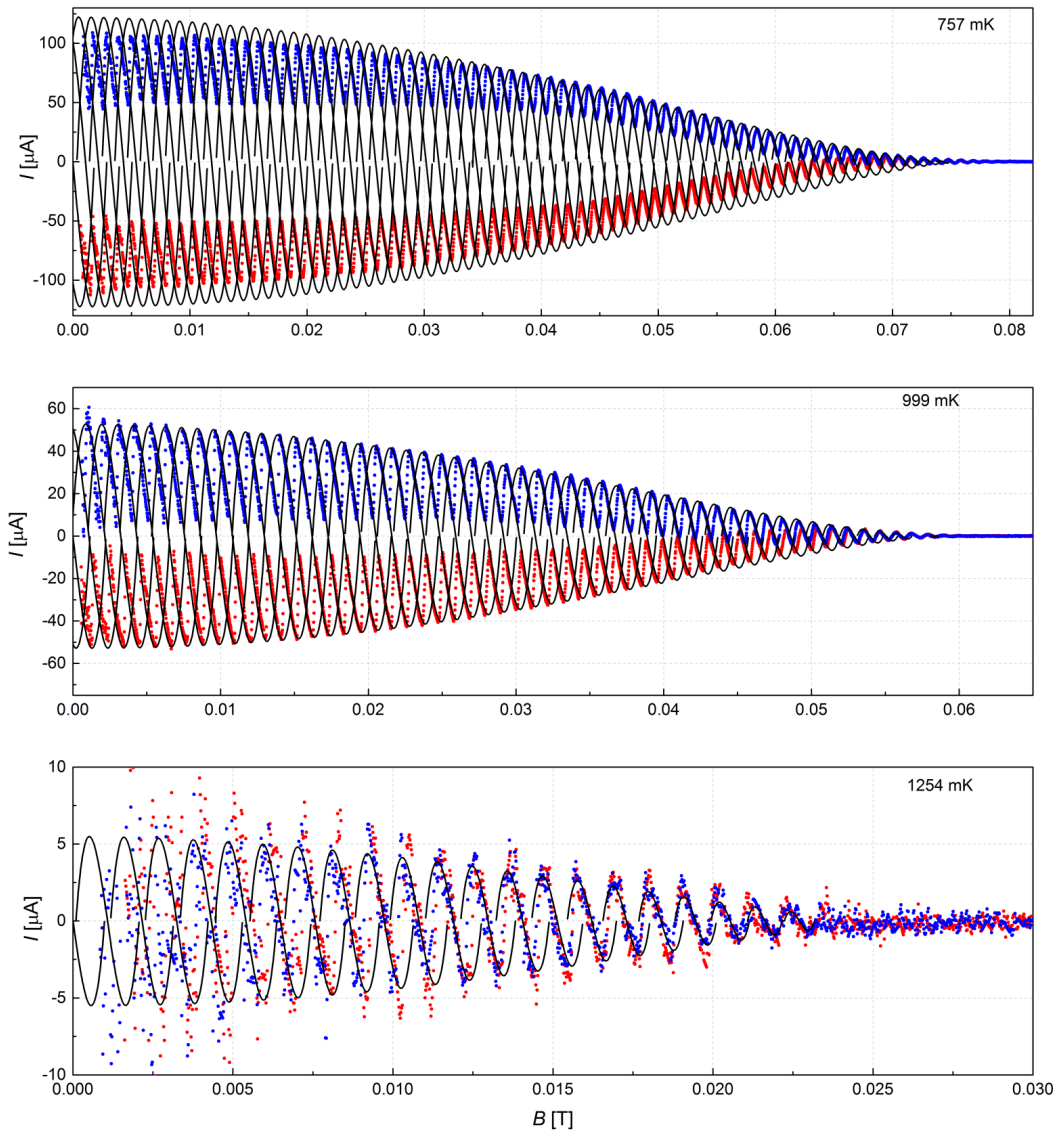

Figure 6.10: $I(B)$ for CL11 at three different temperatures. Red (blue) points are data for increasing (decreasing) field. Black curves are the GL fits.

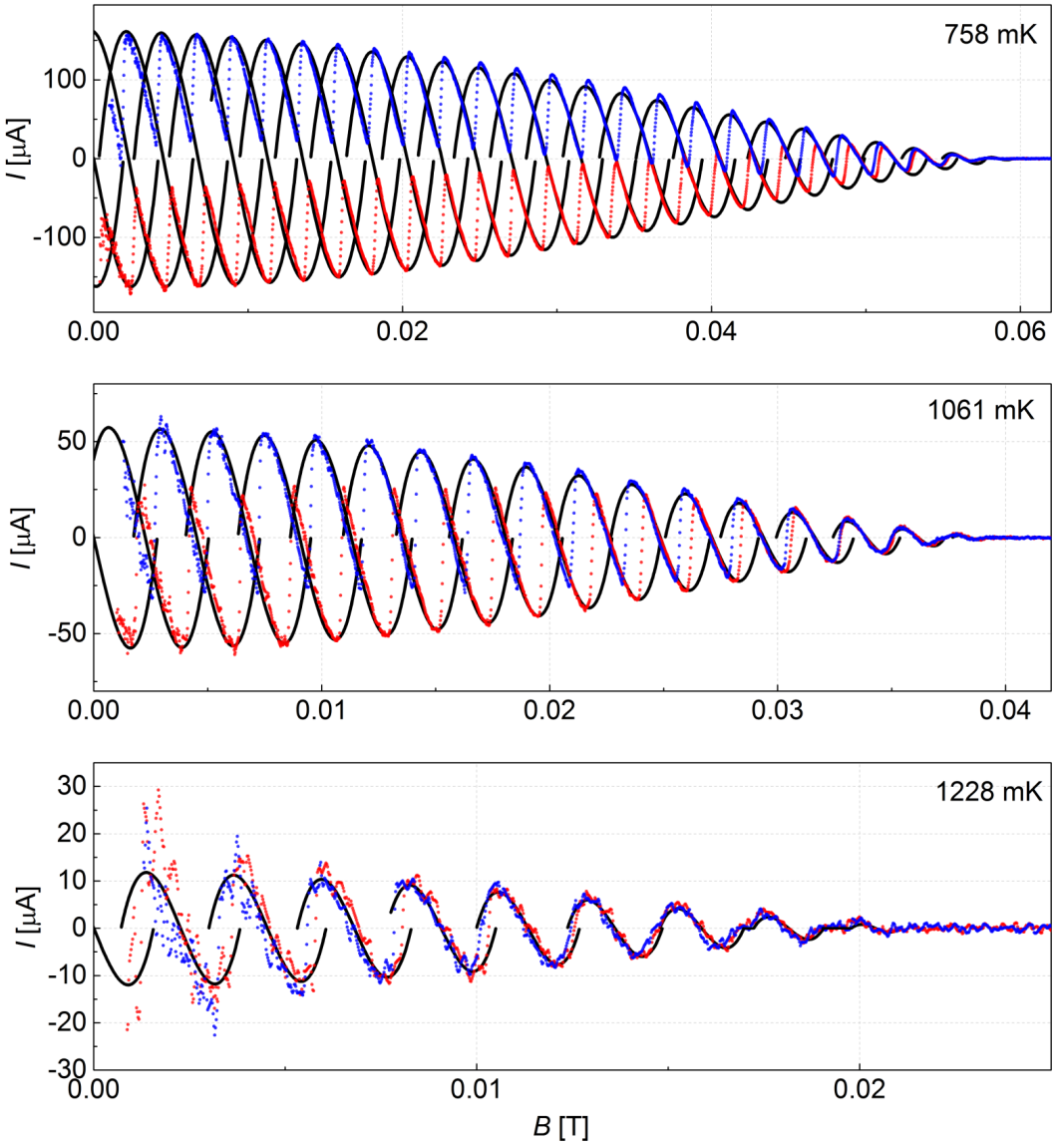

Figure 6.11: $I(B)$ for CL13 at three different temperatures. Red (blue) points are data for increasing (decreasing) field. Black curves are the GL fits. Between superconducting states states the extended regions over which $I = 0$ (horizontal black lines) are regions where there is no energetically favorable superconducting state, and thus the rings exist in the normal state (see Section 2.2.5.4).

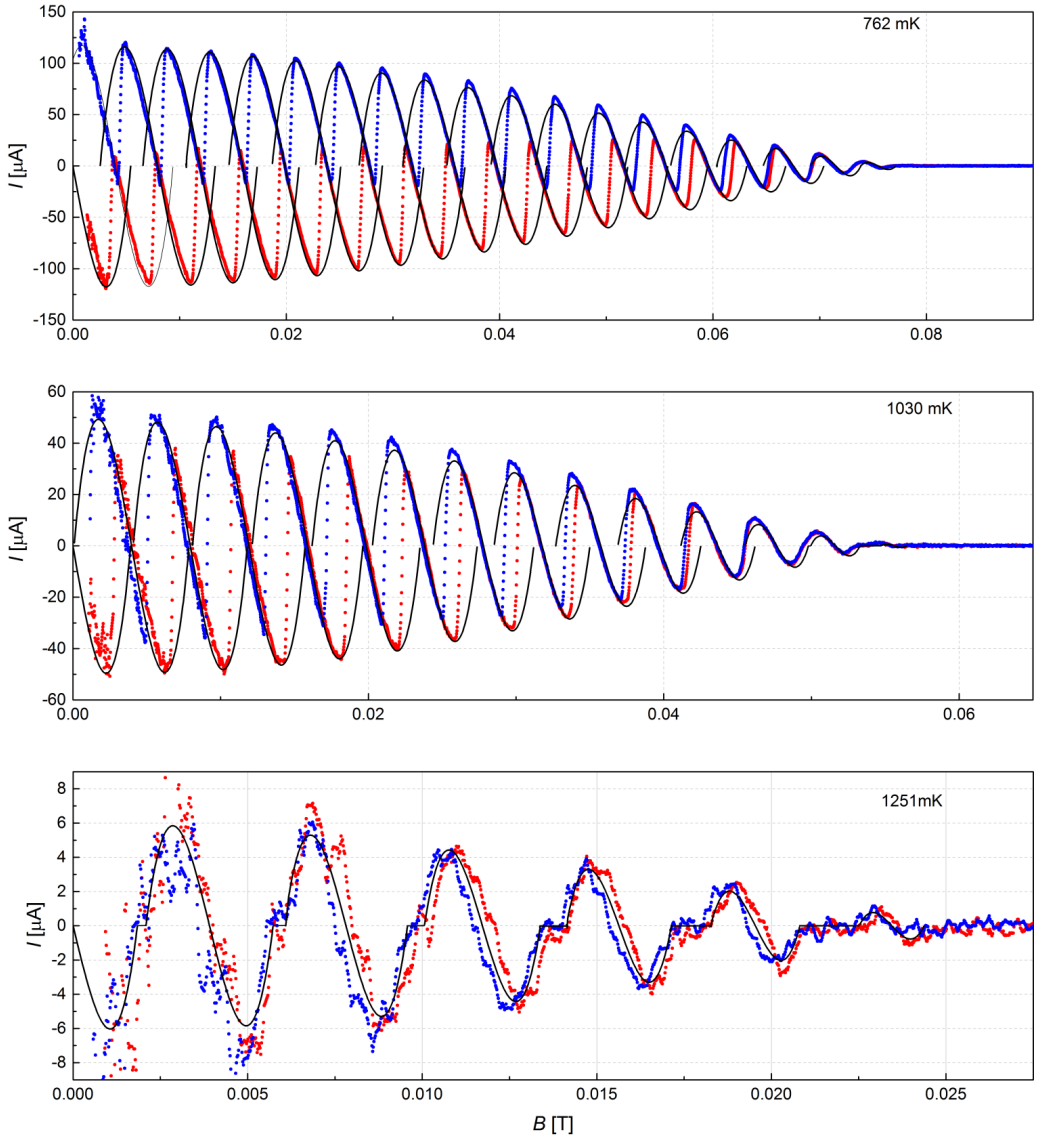

Figure 6.12: $I(B)$ for CL15 at three different temperatures. Red (blue) points are data for increasing (decreasing) field. Black curves are the GL fits. Between superconducting states states the extended regions over which $I = 0$ (horizontal black lines) are regions where there is no energetically favorable superconducting state, and thus the rings exist in the normal state (see Section 2.2.5.4).

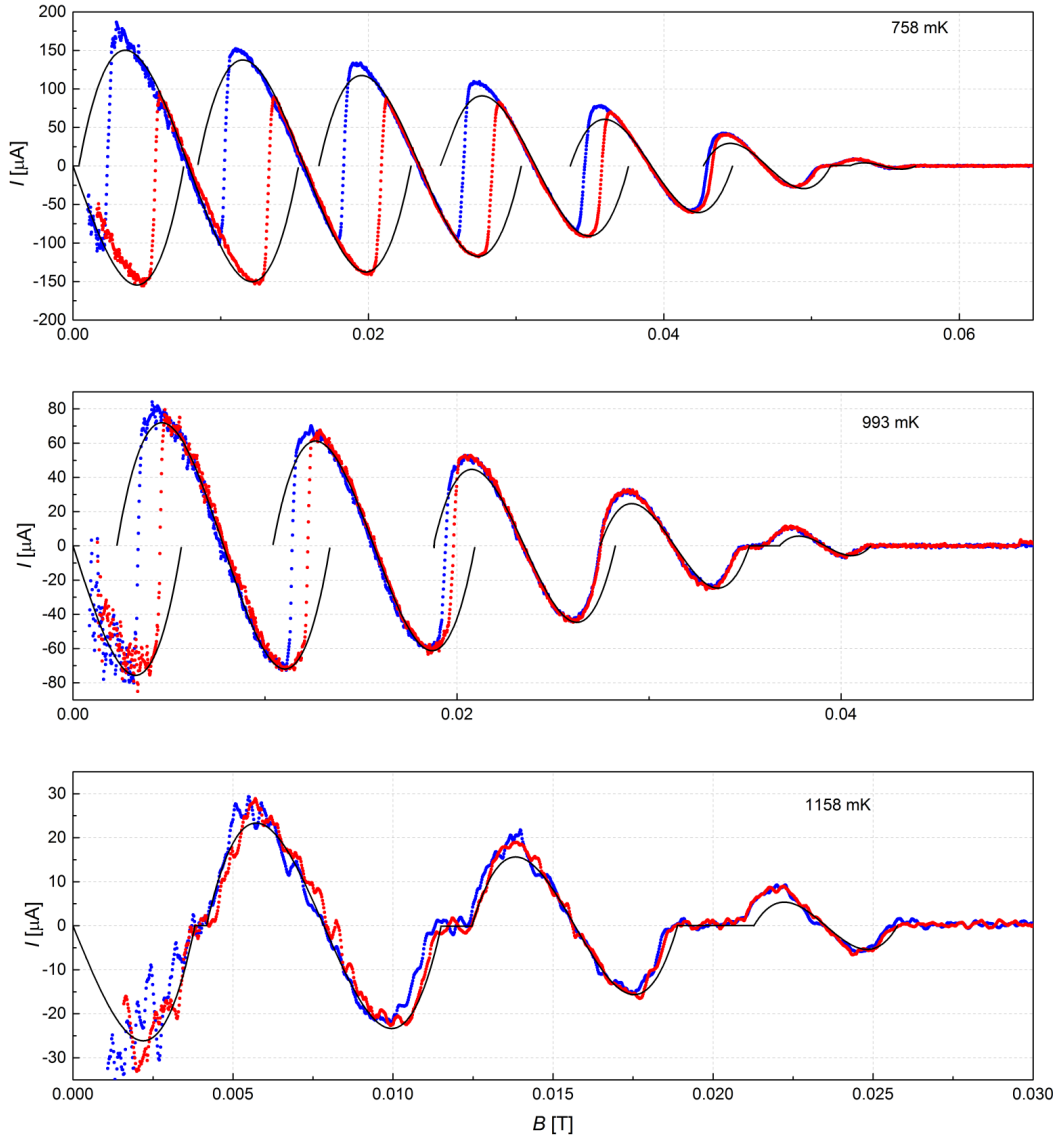

Figure 6.13: $I(B)$ for CL17 at three different temperatures. Red (blue) points are data are for increasing (decreasing) field. Black curves are the GL fits. Between superconducting states states the extended regions over which $I = 0$ (horizontal black lines) are regions where there is no energetically favorable superconducting state, and thus the rings exist in the normal state (see Section 2.2.5.4).

Sample	R_{GL} [nm]	w_{GL} [nm]	ξ_0 [nm]	λ_{P0} [nm]	λ_0 [nm]	$B_{\mathrm{c3,0}}$ [T]	$B^{GL}_{\mathrm{c3,0}}$ [T]
CL11	780	51	190(3)	107(2)	98(1)	0.1131(7)	0.125(2)
CL13	538	65	208(2)	101(2)	95(1)	0.0830(6)	0.089(1)
CL15	406	48	202(2)	100(2)	95(1)	0.1107(7)	0.125(1)
CL17	288	65	214(2)	104(2)	97(1)	0.0796(6)	0.087(1)

Table 6.2: Sample parameters determined by the GL fit to data for 750 mK $< T < T_{\mathrm{c}}$. R_{GL} and w_{GL} are determined as the mean values returned by preliminary fits of $\Delta f(B)$ across all temperatures for a given sample. ξ_0, λ_{P0}, and $B_{\mathrm{c3,0}}$ represent the zero temperature coherence length, Pearl penetration depth and sample critical field respectively and are determined from the temperature fits described in Section 6.2.2.2. For completeness we also calculate the bulk penetration depth, $\lambda_0 = \sqrt{\lambda_{\mathrm{P0}} s}$ where $s = 90$ nm. $B^{GL}_{\mathrm{c3,0}}$ calculates the critical field from Eq. 6.5 using w_{GL} and ξ_0. The quoted error in the final digit of each fit value corresponds to the statistical uncertainty of the fit (one standard deviation).

$\sim 0.02\Phi_0$. Given the dimensions of our rings, we estimate $L \sim 0.9 - 3.8$ pH, which leads to $LI \sim 0.13, 0.07, 0.05, 0.03\Phi_0$ at 750 mK for CL11, CL13, CL15, and CL17 respectively. At higher temperatures LI is diminished as I decreases with temperature. Thus, the inductance is only important for the largest rings at the lowest temperatures as in all other measurements $LI \ll \Phi_0$.

The resulting fit parameters for each sample are summarized in Table 6.2. Though we have two fitting parameters at each temperature, $\xi(T)$ and $\lambda_{\mathrm{P}}(T)$, we can ultimately express these in terms of a single coherence length and penetration depth at zero temperature, ξ_0 and λ_{P0}. This temperature-dependence will be discussed in Section 6.2.2.2.

6.2.2.2 $\xi(T)$, $\lambda(T)$ and $B_{c3}(T)$, fit results

Empirically, it has been found that the temperature-dependence of the bulk critical field and bulk penetration depth follow [4]

$$B_{\mathrm{c}}(T) = B_{\mathrm{c0}}\Big(1 - t^2\Big) \tag{6.7}$$

$$\lambda(T) = \frac{\lambda_0}{\sqrt{1 - t^4}} \tag{6.8}$$

where $t = \frac{T}{T_{\mathrm{c}}}$. The two-fluid theory of superconductivity predicts that B_{c3} should follow

$$B_{\mathrm{c3}}(T) \sim B_{\mathrm{c}}(T)\lambda(T) = B_{\mathrm{c3,0}}\Big(\frac{1 - t^2}{1 + t^2}\Big)^{1/2} \tag{6.9}$$

and to be consistent with Eq. 6.5 this leads to a coherence length temperature-dependence of

$$\xi(T) \sim \frac{1}{B_{c3}(T)} = \xi_0 \left(\frac{1+t^2}{1-t^2}\right)^{1/2} \tag{6.10}$$

As GL theory is only valid in the limit of $T \to T_c$ its temperature-dependence will clearly break down at our lowest temperatures as $t = 0.5$. Augmenting the GL theory with the two-fluid temperature-dependencies described above allows us to accurately represent our results within the macropscopic GL theory down to $\approx T_c/2$. In the past, such a treatment was used to successfully explain the parallel critical field of thin aluminum films (5-20 nm) [72] and thin aluminum films and foils (140-1100 nm) in both parallel and perpendicular field orientations down to $T = T_c/2$ [73]. Given that our rings are made of aluminum and have a thickness of 90 nm we expect this treatment to be equally successful in explaining our measurements. Also, sufficiently close to T_c we can write $1 + t^2 = 2$ and $1 - t^2 = 2(1 - t)$ so the two-fluid model coherence length reproduces the GL result, $\xi(t) \sim \frac{1}{\sqrt{1-t}}$.

The obtained GL fit parameters are plotted in Fig. 6.14. The solid curves represent fits to Eq. 6.10 and Eq. 6.8 where we have two free fitting parameters, ξ_0 or λ_0 and T_c. In each case, the zero temperature length is allowed to vary from sample to sample; however, we fix T_c to

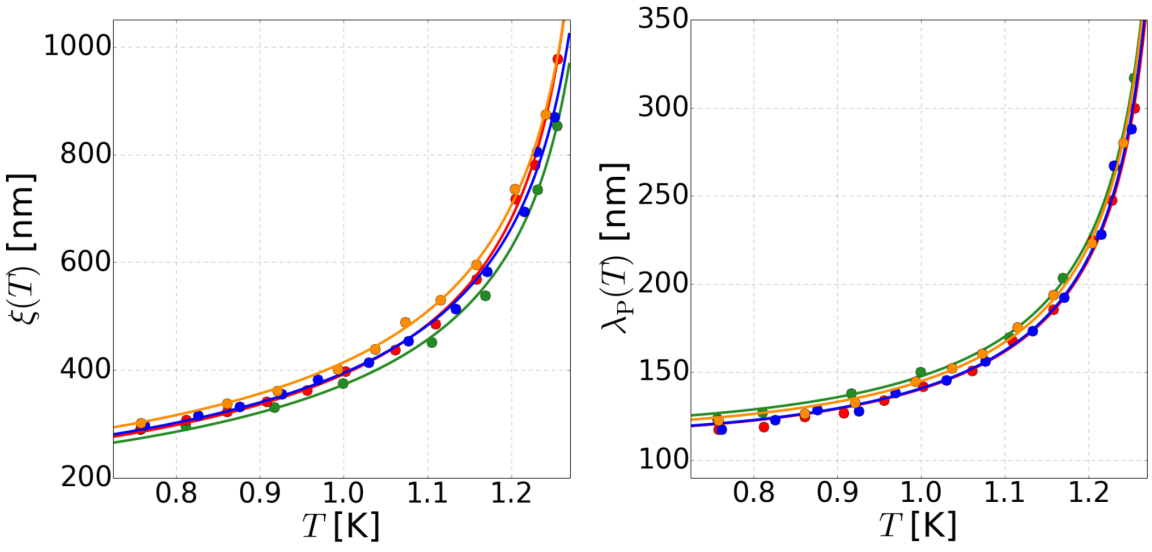

Figure 6.14: $\xi(T)$ and $\lambda_P(T)$ obtained from fits of $\Delta f(B)$ at each temperature for CL11, CL13, CL15, and CL17 in green, red, blue, and orange respectively. The points are values returned from the GL fits, while the solid lines represent a fit of these points to Eq. 6.10 and Eq. 6.8.

be the same across all samples. We allow T_c to be different for the measurements of ξ and λ, and we find that $T_c = 1.316 \pm 0.001$ and 1.391 ± 0.004 K, respectively. The corresponding zero length parameters are summarized in Table 6.2 for each sample. Physically, T_c must be the same for each of these measurements. We will show that a third measurement of $B_{c3}(T)$ gives us another measurement of $T_c = 1.318 \pm 0.002$ K and thus the T_c determined from measurements of $\lambda_P(T)$ is approximately 5% too large. We attribute this discrepancy to the fact that at the lowest temperatures $\lambda_P(T)$ is not much larger than the thickness of our aluminum rings and so the system is only marginally in the regime where the Pearl penetration depth applies.

The value of ξ_0 obtained from this fit can be compared against a completely independent transport measurement. During the evaporation of the rings, aluminum wires were also evaporated on the silicon chip and transport measurements found the electron mean free path to be $l_e = 35 \pm 5$ nm [28]. For a dirty superconductor, this mean free path is related to the coherence length through $\xi_0 = 0.855\sqrt{\xi_0^b l_e}$, where $\xi_0^b = 1.6\ \mu$m is the bulk zero temperature coherence length of aluminum [4]. From this measurement we expect $\xi_0 = 205 \pm 15$ nm, which is consistent with measurements of ξ_0 inferred from $\Delta f(B)$.

We can also measure B_{c3} directly from $I(B)$ by locating the field after which I remains zero. An example of this is indicated in Fig. 6.15. As the $I(B)$ curves are symmetric about the origin, we can also look at $-B_{c3}$ to verify that we are properly locating the critical field. For low temperatures we can can locate B_{c3} to within 200 μT, though this becomes more difficult at higher temperatures where the current is small and distinguishing the last oscillation from the noise becomes difficult (see for example the lower panel of Fig. 6.12). Even in the worst conditions we are able to locate B_{c3} within $\sim$500 μT.[7]

From the measured B_{c3} we can perform a fit to Eq. 6.9 where we allow $B_{c3,0}$ to vary across the samples but only have a single T_c. These fits are shown as solid curves in Fig. 6.16 and we find $T_c = 1.318 \pm 0.002$ K. The critical fields for each sample are displayed in Table 6.2. We have also used w_{GL} and ξ_0 from the GL fits of $\Delta f(B)$ in Eq. 6.5 to calculate the

7. We always have 4 measurements of B_{c3} within a single measurement ($\pm B_{c3}$ for both the up and down ramp), and so though the error on locating a single traces B_{c3} is around 1 mT at the highest temperatures, the error on the average value of B_{c3} is approximately half as large ($1/\sqrt{4}$).

expected critical field, $B_{c3,0}^{GL}$. For each sample we find that $B_{c3,0}$ and $B_{c3,0}^{GL}$ agree to within 10%. The grouping of curves in Fig. 6.16 is expected as $w_{\mathrm{CL11}} \approx w_{\mathrm{CL15}} < w_{\mathrm{CL13}} \approx w_{\mathrm{CL17}}$.

6.2.3 Reconstructing LAMH $F(B)$

With the fit parameters R, w, $\xi(T)$, and $\lambda_{\mathrm{P}}(T)$ we can calculate the free energy diagram $F(B)$ from Eq. 2.41. From our determination of winding number we are able to fully specify which part of the diagram each ramp occupies, which is shown in Fig. 6.17. We can see that phase slips occur nearly symmetrically around the minima of $F_n(B)$ and are roughly located near the inflection points of $F_n(B)$, that is, where the current is maximized. At lower temperatures there is a noticeable hysteresis at low applied magnetic field magnitude while for higher B and higher temperatures the increasing and decreasing applied magnetic field ramps occupy the same parts of $F_n(B)$ for the majority of the measurement. Finally, we can see that at higher temperatures we directly measure the minima of $F_n(B)$ and as temperature is decreased we measure smaller and smaller regions around these minima. In fact, for the lowest temperatures in the smallest rings we do not directly measure the

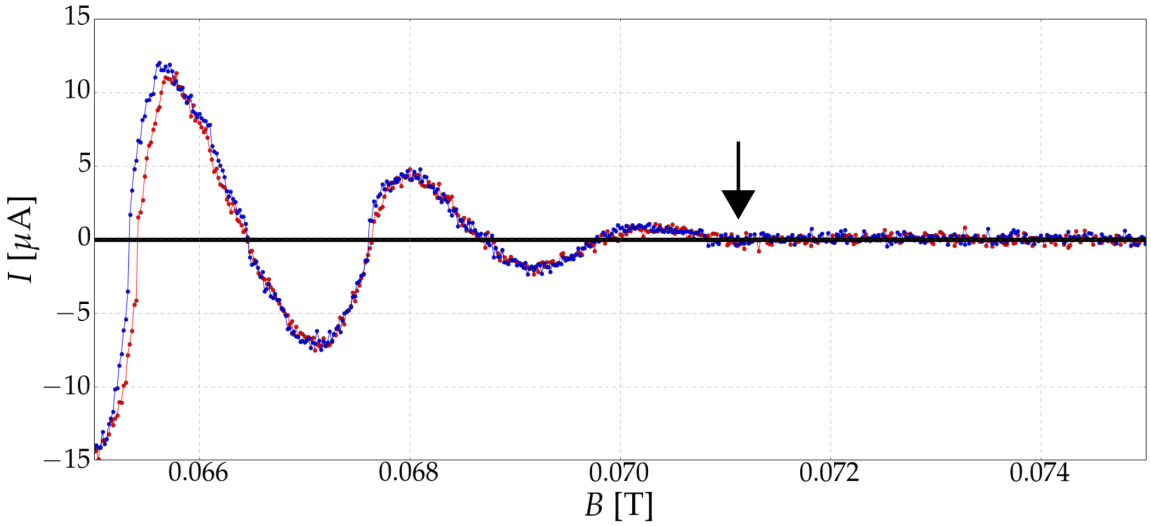

Figure 6.15: Zoomed in view of $I(B)$ for CL13 at $T = 471$ mK from Fig. 6.3. Red (blue) curves are for increasing (decreasing) field. On this scale we can clearly see the last hysteretic oscillation of $I(B)$, which is typically followed by $\sim 1-2$ non-hysteric, smooth oscillations. This indicates that there is only a single metastable state available to the system, which is expected just below B_{c3}. The black arrow at $B = 0.0710 \pm 0.0002$ T marks the ultimate extinction of the current after which $I = 0$ for all fields.

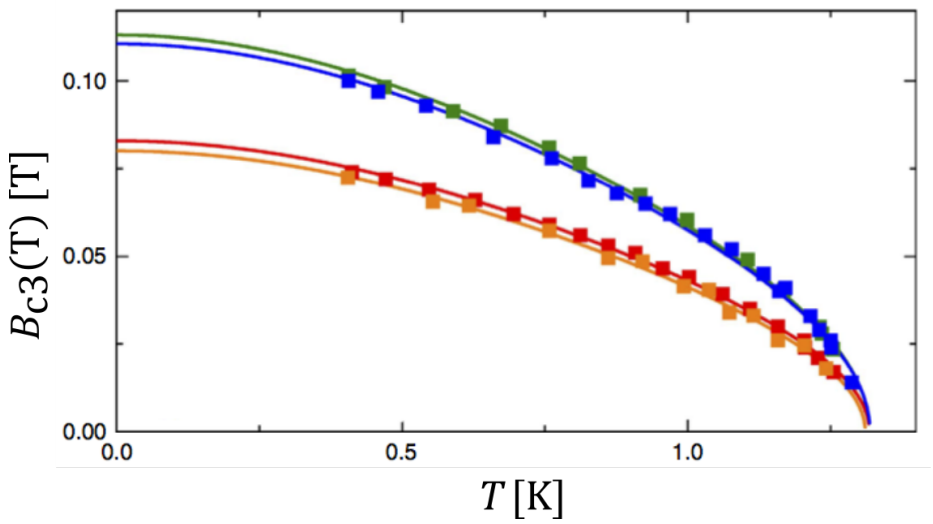

Figure 6.16: $B_{c3}(T)$ for CL11, CL13, CL15 and CL17 in green, red, blue, and orange respectively. Points represent direct measurements from $I(B)$ traces while curves correspond to fits of Eq. 6.9 with two fitting parameters, $B_{c3,0}$ and T_c.

minima of $F_n(B)$.[8] Thus, where possible we will use our measurement to determine $\Phi_{\min,n}$, and in all other cases we can determine the flux which minimizes the free energy by a linear extrapolation between smoothly varying parts of the up and down ramps of $I(B)$ (for example, see the middle panel of Fig. 6.10).

6.2.4 Phase slip flux

Given our success in using GL theory to explain the equilibrium parts of $I(B)$, we can now analyze the parts of $I(B)$ that correspond to phase slips. Phase slips occur on a timescale that is much shorter than our measurement time, thus, we will focus on a quantitative analysis of the field, or equivalently flux, at which these phase slips occur. In our measurements we directly observe the flux at which a phase slip occurs for each winding number, $\phi_n^{\pm}$, where the $\pm$ indicates the ramp direction and we have defined a normalized flux $\phi = \Phi/\Phi_0$. It is useful to determine this flux with respect to the flux that minimizes $F_n(\Phi)$ and so we define

$$\Delta\phi_n^{\pm} = \phi_n^{\pm} - \phi_{\min,n} \tag{6.11}$$

8. Minima of $F_n(B)$ correspond to $I = 0$. In Fig. 6.10, many of the curves never cross $I = 0$ for the lowest temperatures and lowest applied magnetic field magnitudes.

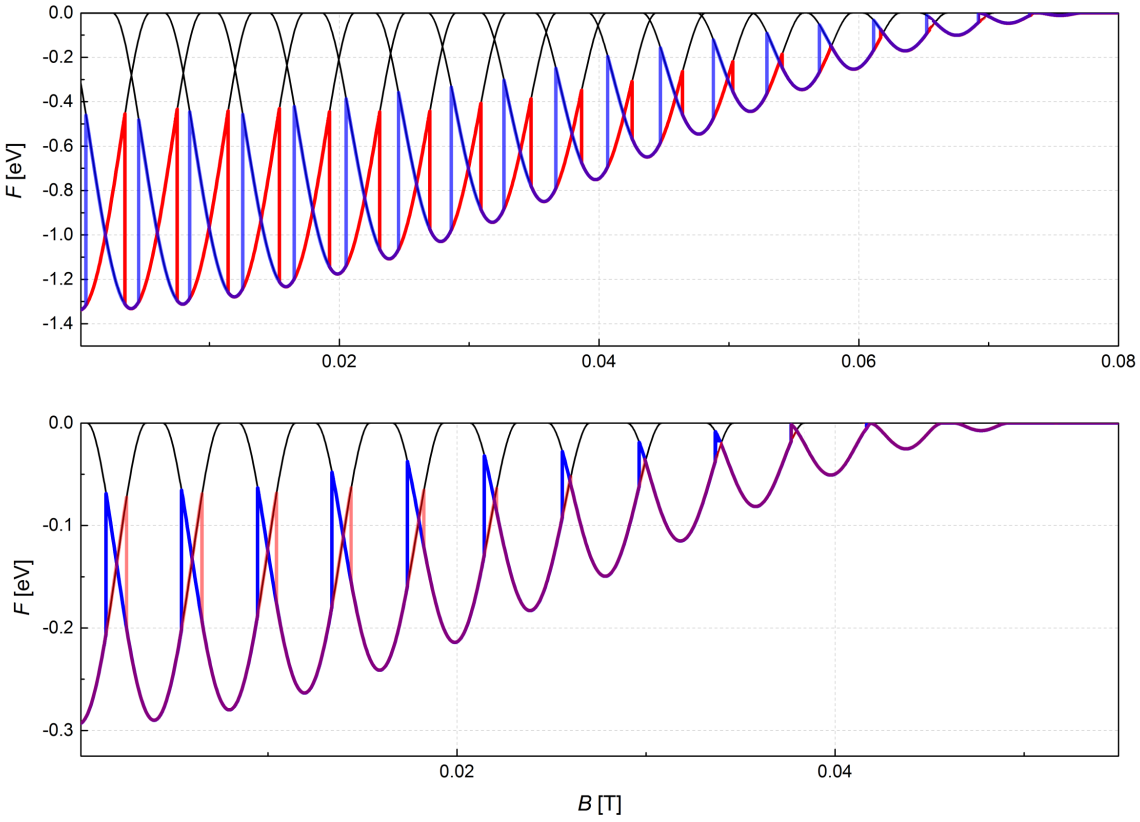

Figure 6.17: Free energy as a function of magnetic field for CL15 at $T = 762$ mK (top panel) and $T = 1077$ mK (bottom panel). Black curves correspond to the full free energy landscape and red (blue) curves are the actual paths taken during the measurement for increasing (decreasing) field. Purple corresponds to parts of $F(B)$ that are occupied by both ramps.

With this definition $\Delta\phi_n^+$ is positive ($\dot{B} > 0$, for which $n \to n+1$) and $\Delta\phi_n^-$ is netagive ($\dot{B} < 0$, for which $n \to n-1$). As we derived in Chapter 2 in the absence of boundary conditions for a finite width ring this critical flux $\Phi_{\mathrm{c},n}$ occurs where I is maximized and is given by Eq. 2.48. Thus,

$$\Delta\phi_{\mathrm{c},n}^{\pm} = \pm\frac{R}{\sqrt{3}\xi} + \mathcal{O}\Big(\Big(\frac{w}{2R}\Big)^2\Big) \tag{6.12}$$

However, with the inclusion of the rings' periodic boundary condition the critical flux $\Phi_{\mathrm{f},n}$ is given by Eq. 2.94 which leads to

$$\Delta\phi_{\mathrm{f},n}^{\pm} = \pm\frac{R}{\sqrt{3}\xi}\sqrt{1+\frac{\xi^2}{2R^2}} + \mathcal{O}\Big(\Big(\frac{w}{2R}\Big)^2\Big) \tag{6.13}$$

The $\mathcal{O}\left(\left(\frac{w}{2R}\right)^2\right)$ terms contain the n-dependence of the critical fluxes and are not necessarily negligible for $n/n_{\max} > 0.5$. We will ultimately use the full expressions given by Eq. 2.48 and Eq. 2.94 in our analysis; however, given that they are opaque and cumbersome to write we will adopt the short-hand notation above, which makes it obvious that the finite length correction is set by the ratio of $\frac{\xi}{R}$.

6.2.4.1 Experimental determination of switching flux

From our measured $I(B)$ traces we can determine $\phi_n^{\pm}$ by locating the field at which a phase slip occurs and multiplying that field by the area of the ring, given our GL fit result for R. To determine the switching field we look at the numerical derivative $\frac{dI(B)}{dB}$ of our measured data. For example, assuming that B is always increasing, the equilibrium parts of $I(B)$ will have a negative slope and the phase slip regions have a positive slope. By setting a lower threshold on this slope to rule out false detections due to point-to-point fluctuations and stabilization past the critical current, we can systematically locate these phase slip regions. An example of the result of this procedure is shown in Fig. 6.18. Lithographic inhomogeneities in the array of rings broaden the transition region, and thus we define the

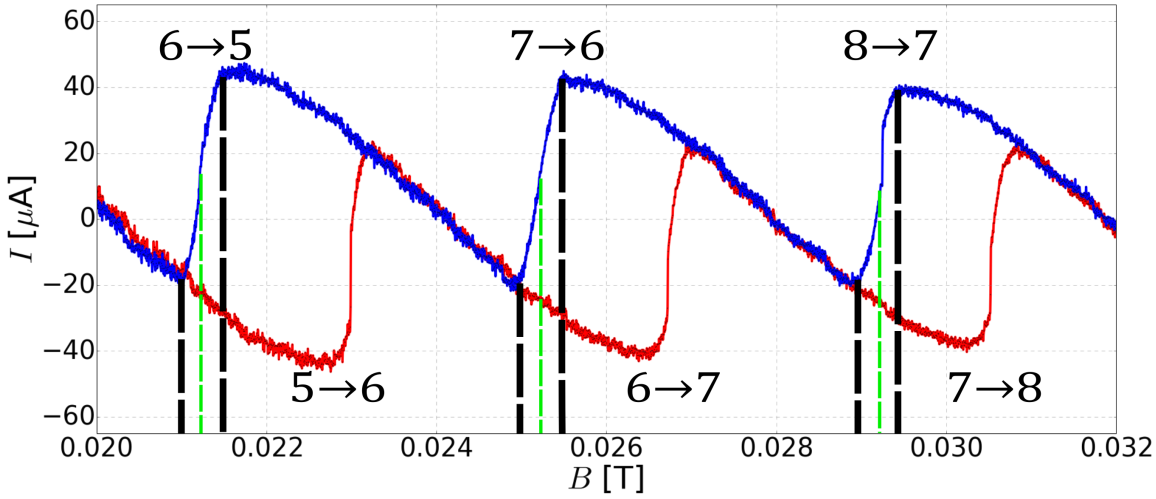

Figure 6.18: Measured $I(B)$ for CL15 at $T = 920$ mK. Red (blue) curves are for increasing (decreasing) field. For each transition we define the critical flux as the middle of the transition region which is indicated by the green dashed line. The black dashed lines represent the width of the transition region and are what we use as the error bar on our experimentally determined value of $\phi_n^{\pm}$. The numbers above each transition correspond to the change in n for each phase slip.

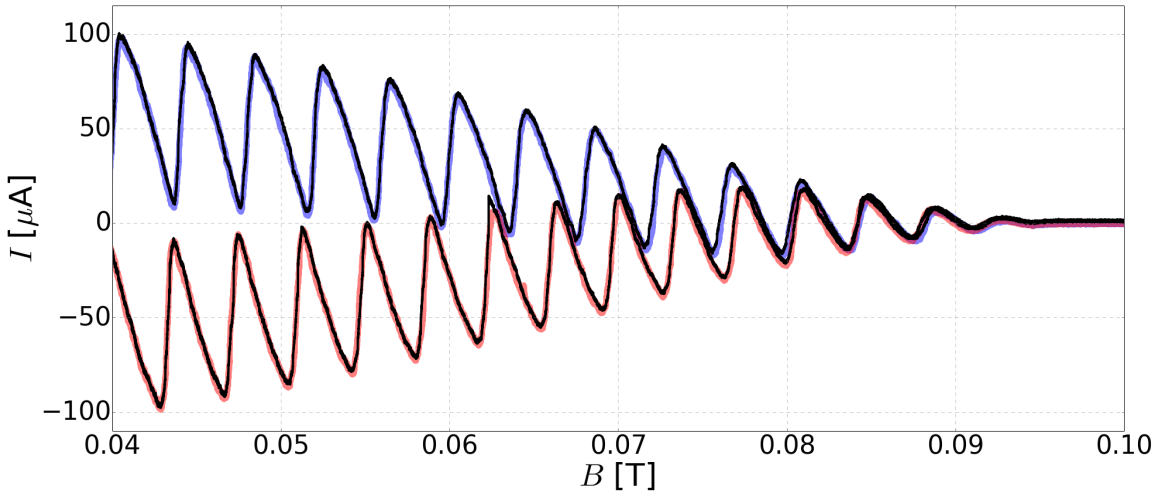

Figure 6.19: Measured $I(B)$ for CL15 at $T = 660$ mK. Red (blue) curves are for increasing (decreasing) field. The black curves, which lie almost exactly on top of the red and blue curves, correspond to an additional ramp taken in each sweep direction. The reproducibility of these $I(B)$ traces indicates that our background subtraction is accurate and that the transition width is not set by a stochastic process.

critical flux as the middle of this transition region, with the error given by the full width of this region. This transition width is not due to an underlying stochastic process. As we will show in Chapter 7, stochastic thermal fluctuations should broaden this transition, but the expected scale is ∼100 mG. Here we observe transition regions that extend over several Gauss. Further, if we take multiple ramps for a given measurement we find that these transition regions are perfectly reproducible, as shown in Fig. 6.19.

6.2.4.2 Phase slip flux as a function of winding number, temperature, and ring size

We will now display the results of our measured phase slip flux for all 4 array samples across all measured temperatures. As each sample has a different ring radius and width, the maximum winding number and absolute value of switching flux from $\Phi_{\min,n}$ will vary from sample to sample. To effectively collapse all data onto a single curve, we will always normalize $\Delta\phi_n^{\pm}$ by $\Delta\phi_{\mathrm{f},0}^{+}$ and we will normalize n by $n_{\max}$.[9] The data are displayed in Fig. 6.20,

9. As each sample has a slightly different ratio of R/w and each temperature has a slightly different ratio of ξ/R, the predictions do not exactly collapse to a single curve, and are instead given by a family of closely spaced curves.

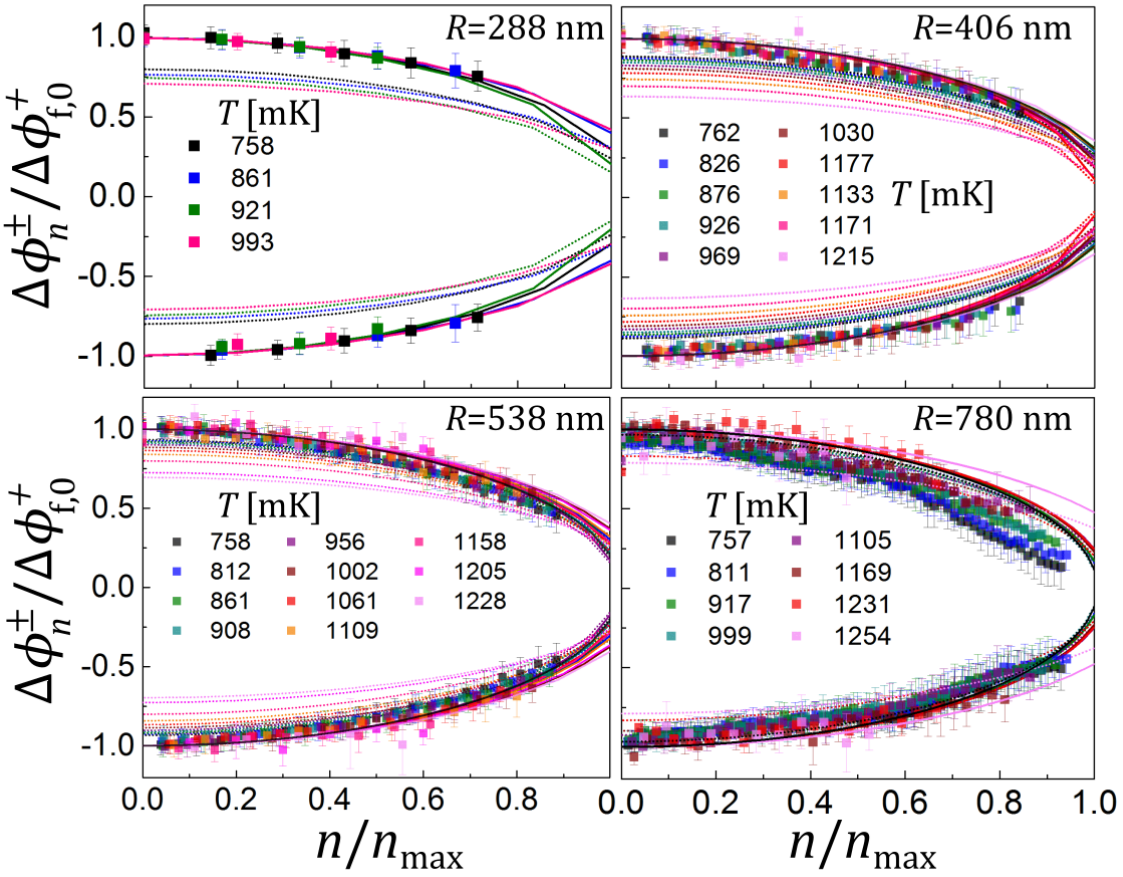

Figure 6.20: Measured phase slip flux $\Delta\phi_n^{\pm}$ as a function of winding number. The normalization is explained in the text. Data are shown as points with the error given by the transition region width. Solid lines correspond to the finite length corrected switching flux $\Delta\phi_{f,n}^{\pm}$, while dashed lines correspond to the critical flux $\Delta\phi_{c,n}^{\pm}$.

where the dashed lines are given by Eq. 6.12, and the solid lines are from Eq. 6.13.[10] The difference between these two curves, which is set by the ratio $\xi(T)/R$, is most pronounced for small rings or at high temperatures. For CL11 ($R = 780$ nm), we can see that there is a noticeable discrepancy between the data and predictions for $n/n_{max} > 0.6$. Again, we attribute this to the increased importance of the rings' self-inductance, which skews the current-phase relation and as a consequence the GL fit does not work as well. For CL11

10. Our predictions for $\Phi_{c,n}$ and $\Phi_{f,n}$ require there to be a metastable state of lower F available to the system at these fluxes. If there is no metastable state of lower F, then a phase slip will not occur until a flux beyond flux $\Phi_{c,n}$ or $\Phi_{f,n}$ where two metastable states cross in free energy. This situation typically occurs close to B_{c3}, or equivalently n_{max}. As a consequence, we can only plot data up to $n/n_{max} \approx 0.8$.

the transition width makes our measurement consistent with either prediction at the lowest temperatures. However, at higher temperatures (red and pink squares) the measured switching flux is consistent with switching at $\Phi_{\mathrm{f},n}$. This conclusion is solidified as we look at samples with smaller radii. For CL17 ($R = 288$ nm) the two predictions are distinct enough that even with the transition width it is clear that the rings switch at $\Phi_{\mathrm{f},n}$ and not $\Phi_{\mathrm{c},n}$, even at the lowest temperatures.

6.2.4.3 Direct observation of finite-length correction to phase slip flux in supercurrent signal

The finite-length effect on the switching flux can be seen directly in our measurements of $I(B)$. Without this effect, a phase slip occurs should occur at $\Phi_{\mathrm{c},n}$, the flux where the current magnitude is maximized. The periodic boundary condition allows the system to remain stable beyond this critical flux and thus the system will switch at a current that has a smaller magnitude than the critical current, as shown in Fig. 2.8. In Fig. 6.21 we

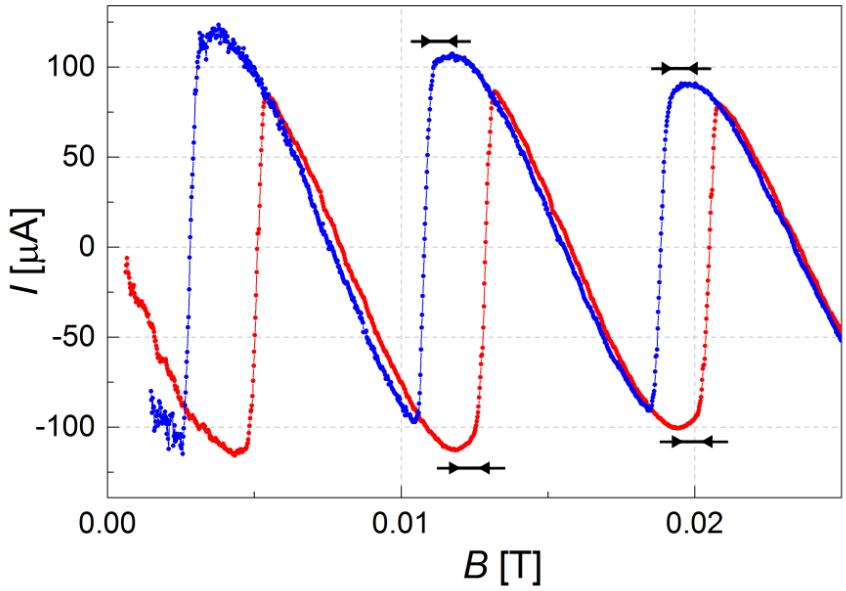

Figure 6.21: $I(B)$ traces for CL17 ($R = 288$ nm) at $T = 861$ mK. Red (blue) curves are for increasing (decreasing) field. The regions over which $I(B)$ is diminished from its maximal amplitude are indicated by black arrows.

plot the supercurrent per ring for our smallest rings at $T = 861$ mK. For this measurement, the finite-length switching flux should be ~25% further from $\Phi_{\min,n}$ than the critical flux is from $\Phi_{\min,n}$, making it easy to directly observe despite the large transition region due to lithographic variations. For both the up and down field ramps, we observe the sawtooth oscillation reach a maximum current and then diminish before the switching region begins.

6.2.4.4 Phase slip flux transition width

The measured transition widths $\delta\Phi$ as a function of winding number are shown in Fig. 6.22. As n is linear with B, we see that the transition widths increase roughly linearly with B. The slope of the B-dependence is independent of T and decreases with R. This slope is consistent with lithographic ring-to-ring imprecision $\Delta R = 1.9$, 1.5, 2.1, and 2.0

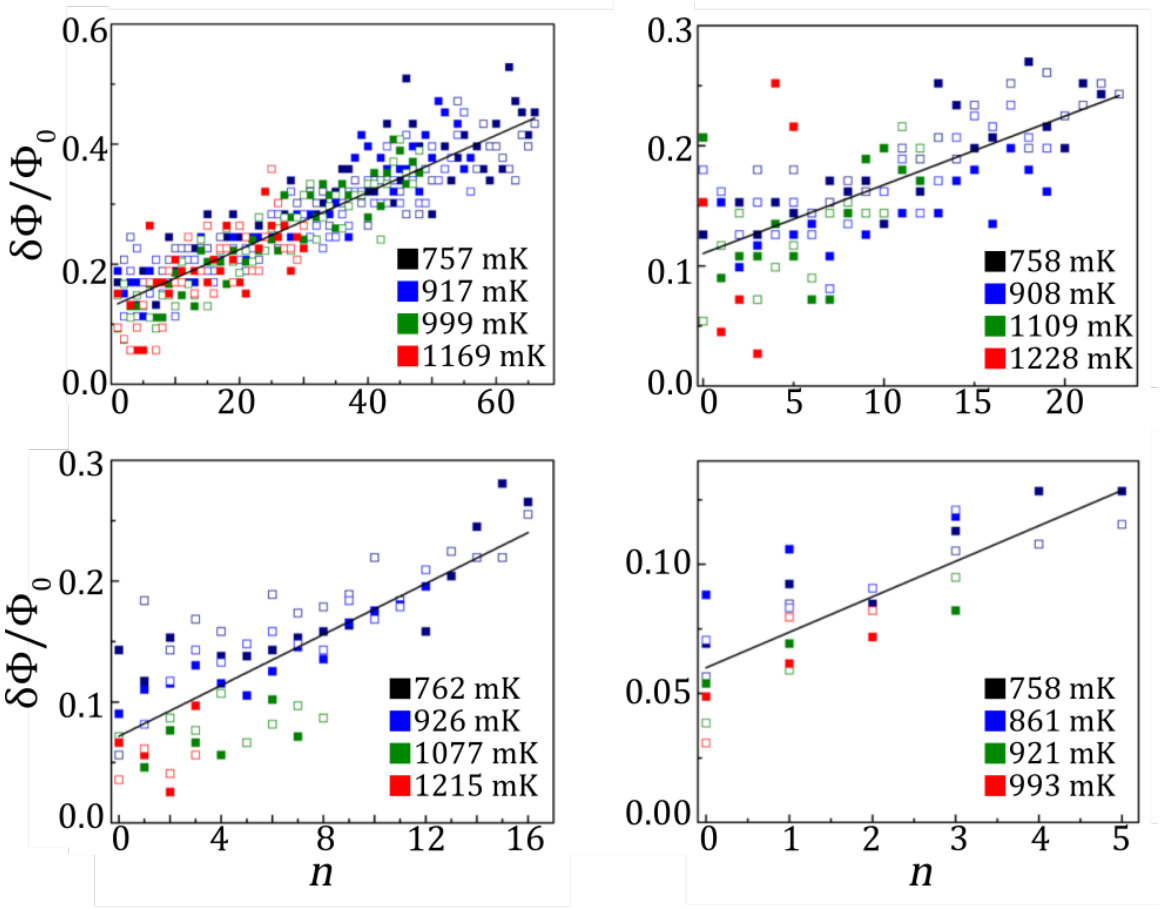

Figure 6.22: Measured transition width $\delta\Phi$ as a function of winding number for CL11, CL13, Cl15 and CL17 (top left, top right, bottom left, and bottom right respectively). Solid lines indicate a linear fit to the entire data set for each ring size.

nm for rings with R = 780, 538, 406, and 288 nm respectively. We also notice a sizable transition width at $n = 0$, which shows no discernible temperature dependence. We do expect some transition with for the $n = 0$ transition as it occurs at $\Phi \approx \Phi_0 \frac{R}{\sqrt{3}\xi}\sqrt{1+\frac{\xi^2}{2R^2}}$ and not $\Phi = 0$. Taking this into account, the expected transition width should be $\sim 0.005\Phi_0$ for all rings for the $n = 0$ transition, which is a factor of 5-10 smaller than observed. We also considered the rings' mutual inductance, as rings at the corner of the array have 2 nearest neighbors, while rings in the middle have 4 nearest neighbors. Thus, rings at the corner experience a slightly different field than those at the center of the array. Taking this into account, we find the mutual inductance difference between the center and the corner, $(M_{\text{center}} - M_{\text{corner}})I$, to be $0.01 - 0.03\Phi_0$, which is again too small to explain our observed transition width. If we extrapolate the linear behavior of the transition width to zero field, we see that $\delta\Phi$ increases with ring radius.

We conclude from these observations that the rings' temperature does not influence the transition widths of the arrays. This is consistent with the fact that the expected transition width for thermally activated phase slips is roughly an order of magnitude smaller than our observed widths.

Chapter 7

Analysis of superconducting persistent current single ring data

In this chapter, we will describe our measurements of the current of individual isolated superconducting aluminum rings. The first set of measurements are of the cantilevers' frequency shift as a function of applied magnetic field, similar to the measurements presented in Chapter 6, from which we extract the relevant sample parameters, R, ξ_0 and λ_{P0}. The data analysis here is very similar to that of the array measurements; however, we will point out the key differences in this analysis due to the fact that for a single ring measurement our signal is ∼500x smaller than our array signal. We will then describe our measurements of the distribution of applied magnetic fields at which a given phase slip occurs. We will present the mean, standard deviation, and skewness of these distributions as a function of temperature for 2 rings, each of different radius.

7.1 Cantilever resonant frequency as a function of field for individual rings

We performed the same calibrations as described in section 5.7 and again found that the PLL frequency stability was optimized at $x_{\rm tip} \sim 500$ nm. After this calibration, we monitored the cantilever's resonant frequency as we applied a linear magnetic field ramp

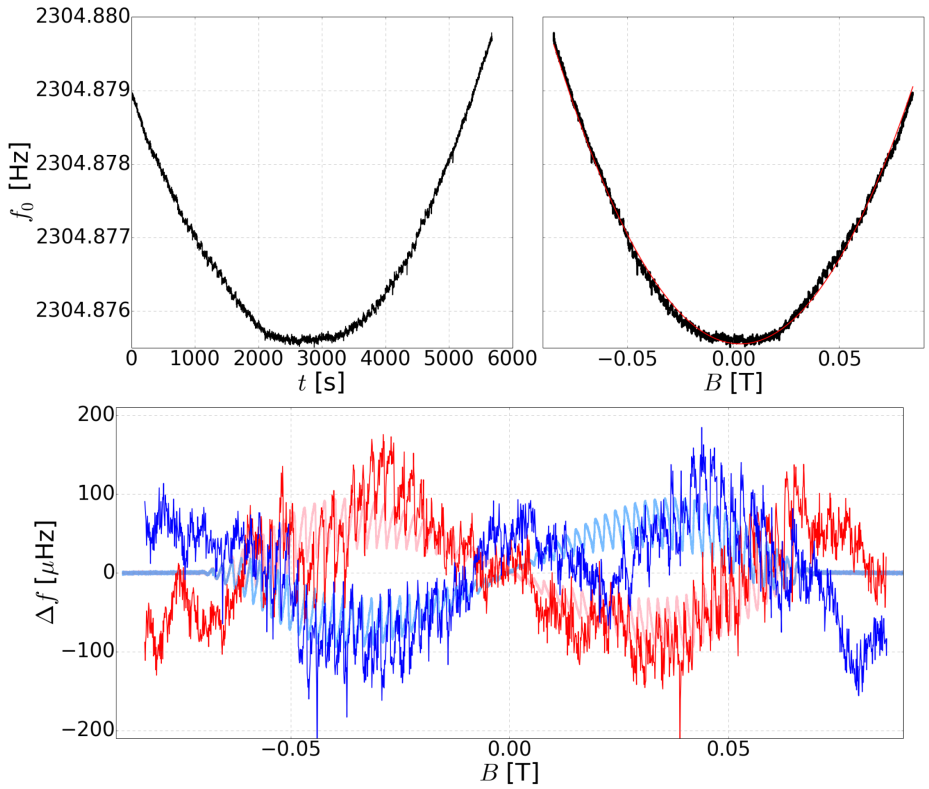

Figure 7.1: (Top panels) Measured cantilever resonant frequency f_0 as a function of time (left panel) and applied magnetic field B (right panel) for CL12 at $T = 462$ mK (similar to the ring parameters and temperature of Fig. 6.1, except this is now only a single ring). The parabolic field-dependent background due to the cantilever is similar to the background for the array measurement ($\sim$4 mHz between $-0.09 < B < 0.09$ T). However, given that the signal is 450x smaller, the background now dominates the raw data. The red curve in the upper right panel illustrates a second order polynomial fit to the field-dependent background. (Bottom panel) Resonant frequency shift as a function of magnetic field for increasing (decreasing) applied field in red (blue). As the frequency shift due to the superconducting ring is only $\sim$100 μHz, slow drifts in the cantilever resonant frequency are now clearly visible in the data. The thicker red and blue curves are the array data of Fig. 6.1, divided by the number of rings ($N = 450$).

at $\theta = 0$ with respect to the sample. An example of one of these measurements on a cantilever with a single ring is shown in Fig. 7.1. In the bottom panel we display the resonant frequency shift due to the aluminum ring, which is obtained by subtracting a second order polynomial from the $f_0(B)$ data. For comparison, this individual ring has the same lithographic dimensions as the rings of CL13, and the temperature (462 mK) is close to that of Fig. 6.1 (471 mK). Due to the N scaling of Δf, we expect the single ring signal to be a factor of 450 smaller.

7.1.1 Single ring frequency shift GL fit

Though the $\Delta f(B)$ signal for the single aluminum ring is qualitatively similar in magnitude, applied magnetic field extent, and periodicity to the scaled array $\Delta f(B)$ signal, small drifts in the cantilever's resonant frequency obscure the hysteretic background. The size of the hysteresis is set by the ratio of $\frac{R}{\xi(T)}$ and so applying the same GL fitting procedure of section 6.2.2 results in large errors for the fit value for $\xi(t)$. As a result, we modified our fitting procedure so that this hysteretic background was not important.

7.1.1.1 Determination of ring radius from switching field

The first step in the single ring fitting procedure was to precisely determine R, and we did this by looking at the field locations of phase slips in the $\Delta f(B)$ data. Drifts in $\Delta f(B)$ do not affect the determination of the applied magnetic field at which a phase slip occurs, and so this determination is insensitive to cantilever frequency drifts. The expected phase slip fields from Eq. 2.95 are given by

$$B_{\rm sw}(n) \approx \frac{n}{1+\left(\frac{w}{2R}\right)^2}\frac{\Phi_0}{\pi R^2} \pm \frac{\Phi_0}{\pi R^2}\frac{R}{\sqrt{3}\xi}\sqrt{1+\frac{\xi^2}{2R^2}} \tag{7.1}$$

With this equation we can see that if we plot $B_{\rm sw}(n)$ for both ramp directions, the linear slope will be given by $\frac{1}{1+\left(\frac{w}{2R}\right)^2}\frac{\Phi_0}{\pi R^2}$, which allows us to determine R. From the lithography and SEM images, we have a good estimate for the ring's R, which allows us to unambiguously specify n for each observed jump in Δf.[1] The location of these jumps are shown in Fig. 7.2 for all measured temperatures of CL12.[2] We fit a line to this entire dataset and find $R = 546 \pm 1$ nm.

The slope of $B_{\rm sw}(n)$ has a very small dependence upon w due to the ring's finite width, and thus the best fit value of R will vary slightly depending upon our choice of w. From the previous GL fits to the array we expect $w \sim 50$ nm. Fortunately, the spread in R is less

1. For the single ring measurements, we cannot distinguish the signal from the noise near $B = 0$, so we cannot simply count the number of jumps and set that equal to $2n_{\rm max} + 1$ as we did for the array measurements. Typically, the first jump in $\Delta f(B)$ we can distinguish from the noise is for $n = 3$.

2. This figure also serves as a check that we have specified n correctly for each phase slip. If we mislabeled n, then $B_{\rm sw}(n)$ would not be symmetric about a line that goes through the origin.

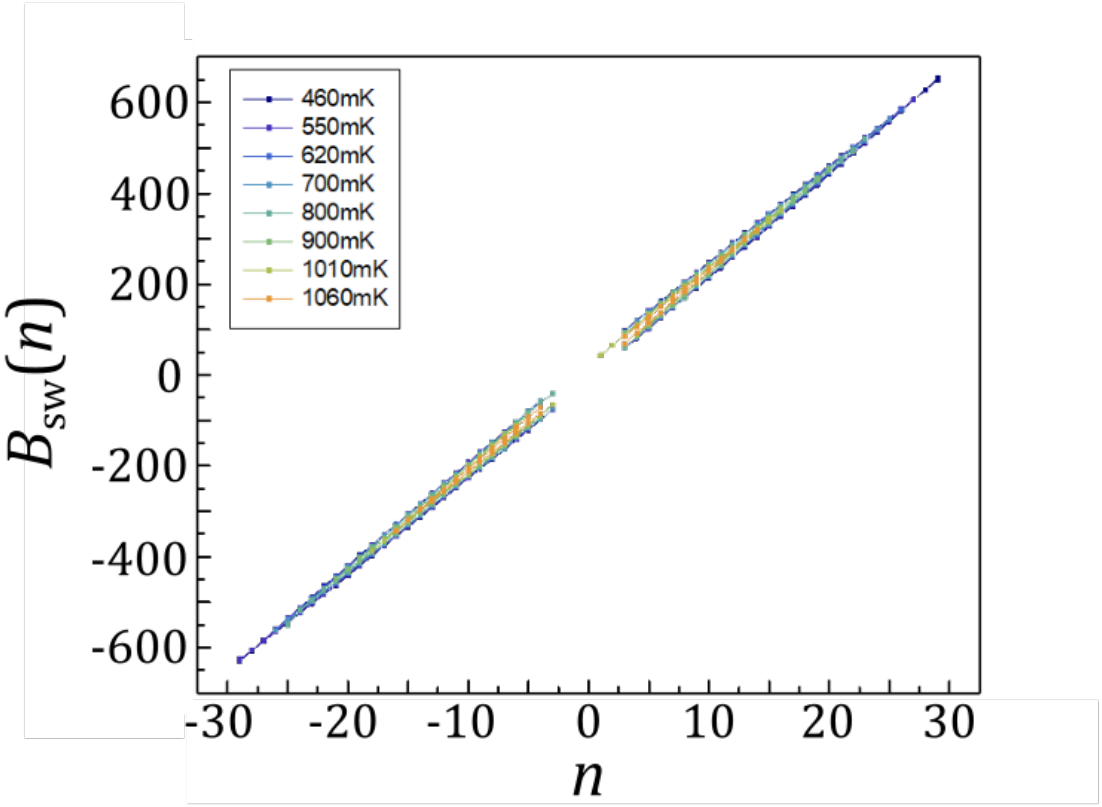

Figure 7.2: Measured applied magnetic field at which a phase slip (i.e. observed jump in $\Delta f(B)$) occurs as a function of winding number at multiple temperatures for CL12. The linear slope of this entire dataset allows us to determine R to within 1 nm.

than 1 nm for reasonable estimates of w. For $w = 0$, 50, 65 nm we find $R = 546.8$, 546.1, 545.9 nm respectively.

7.1.1.2 Step-by-step walk-through of signal fitting to determine k, ξ, w, and λ

With R determined, we can now proceed with the modified GL fit. To do this, we first remove drift and hysteric backgrounds from the measured $\Delta f(B)$ traces with a low order polynomial, so that we obtain a trace with oscillations centered around $\Delta f = 0$ as illustrated in Fig. 7.3. We have also excluded all data for $B \approx 0$ G as there were no clearly visible oscillations, and so that data was not useful for the fit.[3] Unlike the array data, for

3. Anticipating that we would not have a visible signal around $B = 0$, we varied the magnetic field more quickly between $-0.2 < B < 0.2$ T and thus the data was not useful for the fit, given the decreased measurement time, which lead to increased frequency noise. This allowed us to spend more time on the measurement in the region in which we expected the largest signal.

the single ring data there is an ambiguity about $n_{\max}$. Since the $\Delta f(B)$ signal is comparable to the noise near B_{c3} it is unclear whether the last oscillation we observe is the actual last oscillation, or if there several more oscillations buried in the noise. This uncertainty in $n_{\max}$ leads to an uncertainty in B_{c3} as the two are related through $B_{c3} \approx n_{\max}\frac{\Phi_0}{\pi R^2}$.[4]

Because of this uncertainty in $n_{\max}$ and our low signal to noise ratio, we found that we could not have 5 fitting parameters for the GL fits as we did for the array measurements. With R determined from phase slip locations, we were left with 4 more parameters to determine: w, k, λ_{P0} and ξ_0. Of these, ξ_0 is the most important as it (along with R) determines the flux at which δF goes to zero ($\Phi_{f,n}$ in Eq. 2.94 depends upon R and $\xi(T)$). An error on ξ leads to an error on $\Phi_{f,n}$, and given that the escape rate depends exponentially on $\Phi_{f,n}$, a small error on ξ can lead to an enormous error on Γ.[5] To make any meaningful comparison between our measured phase slip distributions and those predicted by theory, which are derived from Γ, we choose to use ξ and k as the only fitting parameters. The other parameters, λ_{P0}, and w, are derived from Eqs. 2.20 and 6.5 respectively, with $B_{c0} = 0.01$ T for bulk aluminum [4], B_{c3} calculated from $n_{\max}$, and our fit result for R and ξ_0.

For the actual fitting procedure we begin by assuming an integer for $n_{\max}(T = 0)$, which is estimated from the $\Delta f(B)$ data. We then set k to its value expected from the cantilever's dimensions. Next, we perform the GL fit to all $\Delta f(B)$ traces for a given cantilever for 750 mK $< T < T_c$ (i.e., all data in Fig. 7.3 including the $B < 0$ data not shown), where we vary ξ_0 (to get $\xi(T)$ at each temperature we assume the temperature dependence given by Eq. 6.10,

4. Here we use approximate as this field would correspond to the minimum of the free energy for the maximum winding number, while the superconducting state defined by $n_{\max}$ can still extend to larger applied magnetic fields. However, close to B_{c3}, where the condensation energy is extremely small, these states do not extend much beyond this field (see, for instance, the $n = 4$ state in the bottom right panel of Fig. 2.3).

5. For an escape rate of the form $\Gamma = \Omega_0 \exp\left[-\frac{\delta F(\Phi=0)}{k_B T}\left(1 - \frac{\Phi}{\Phi_{f,n}}\right)^{5/2}\right]$, the fractional error on the escape rate is $\delta\Gamma/\Gamma = \frac{5}{2}\frac{\delta F}{k_B T}\frac{\delta\Phi_{f,n}}{\Phi_{f,n}}\frac{1}{1-\frac{\Phi}{\Phi_{f,n}}}$, where $\delta F = \delta F(\Phi = 0)\left(1 - \frac{\Phi}{\Phi_{f,n}}\right)^{5/2}$ and assuming only an error on ξ, $\frac{\delta\Phi_{f,n}}{\Phi_{f,n}} \approx \frac{\delta\xi}{\xi}$. We know that phase slips occurs close to the critical flux, so assuming a 2.5% error on ξ, and that phase slips occur at 90% of the critical flux where the barrier is 40 times larger than the thermal energy, we estimate $\delta\Gamma/\Gamma = 25$. This reflects that the magnitude of $\left(1 - \frac{\Phi}{\Phi_{f,n}}\right)^{5/2}$ is extremely sensitive to small changes in $\Phi_{f,n}$ for $\Phi \to \Phi_{f,n}$. (An error on ξ will also cause an error on $\delta F(\Phi = 0)$, but the point here was just to illustrate that a relatively small error on ξ can lead to an order of magnitude error on Γ for switching near the critical flux)

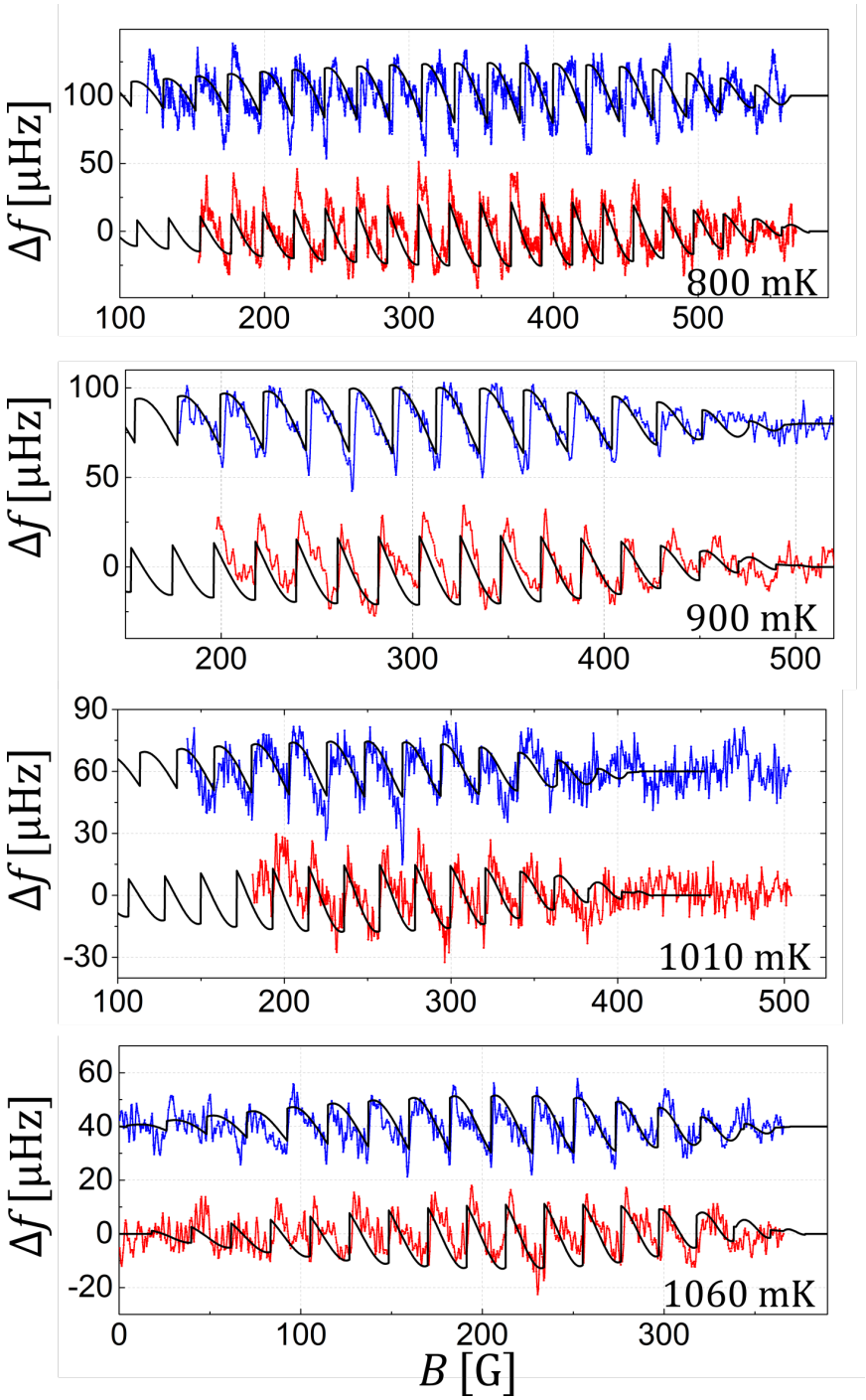

Figure 7.3: Frequency shift as a function of magnetic field for CL12. For each trace, we have subtracted a low order polynomial background from $f_0(B)$ to ensure that the oscillations in $\Delta f(B)$ are centered around zero so that all of the background due to hysteresis or cantilever drift has been removed. Red (blue) curves correspond to increasing (decreasing) the applied magnetic field. The blue curves are vertically offset for clarity. The black curves are the GL fits without the hysteretic background for a single set of parameters k, $n_{\max}$ and ξ_0 that minimize the residual variance between the fit and all displayed data (including $B < 0$ not shown).

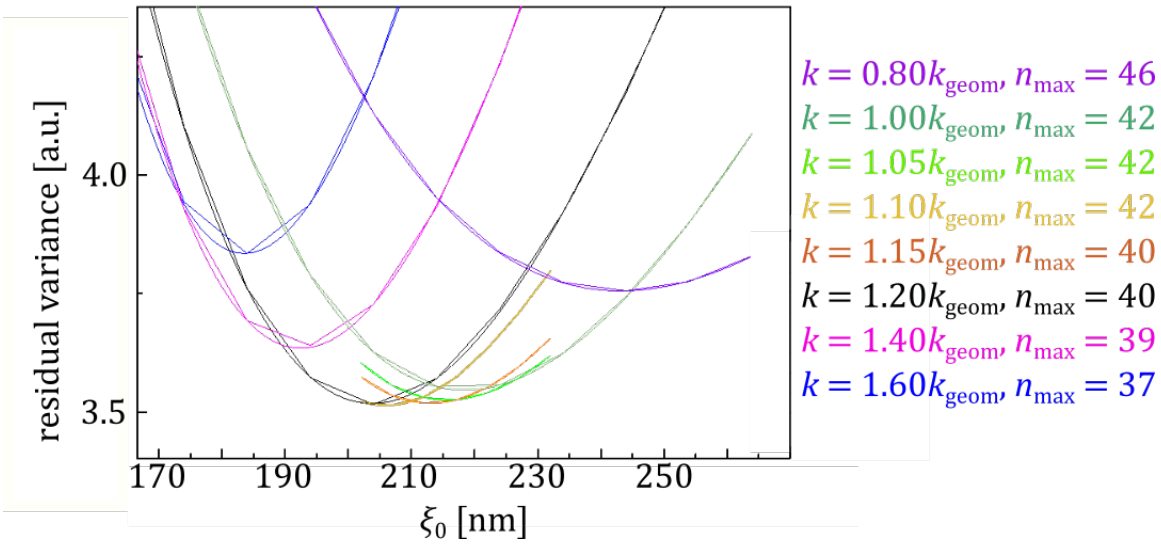

Figure 7.4: Total residual variance across all data for CL 12 as a function of fitting parameter ξ_0. Different curves correspond to fits with different values for k and $n_{\max}$. After this large exploration of parameter space, we perform a finer search in this vicinity of values that minimize the overall residual variance ($n_{\max} \approx 41$, $k \approx 1.15k_{\text{geom}}$, and $\xi_0 \sim 210$ nm) and find the overall residual variance is minimized for $k = 1.14 \pm 0.01 k_{\text{geom}}$, $\xi_0 \approx 208.7 \pm 1.5$ nm, $n_{\max}(T = 0) = 41 \pm 1$, $\lambda_{P0} = 111.5 \pm 0.8$ nm, and $w = 64.4 \pm 1.3$ nm. (For each choice of k and $n_{\max}$ we display two curves. One corresponds to an initial cursory exploration in which we vary ξ_0 in 10 nm increments. The other varies ξ_0 by 1 nm and was used to determine the value of ξ_0 that minimizes the overall residual variance)

which we demonstrated for the array measurements). Given our choices of $n_{\max}$, k and ξ_0 we calculate the sum of the residual variance for the fit across all temperatures. We then vary k in 5% increments and repeat the fitting procedure. Once we have exhausted the parameter space of k and ξ_0, we change $n_{\max}(T = 0)$ by 1 and repeat the procedure for varying k and ξ_0. The result of this systematic exploration of parameter space is that we guarantee that we locate the set of physically reasonable parameters which absolutely minimizes the residual variance. The results of this fitting procedure for CL12 are summarized in Fig. 7.4. Though we initially vary k by 5% to explore parameters space, we ultimately use a much finer resolution $\sim 1\%$ in the vicinity of k, ξ_0, and $n_{\max}$ that minimize the total residual variance.

The result of the GL fit for the parameters that minimize the overall variance for CL12 are shown in Fig. 7.3. Here, we have removed the hysteretic background in the GL $\Delta f(B)$

Sample	R [nm]	$n_{\max}(T{=}0)$	k [mN/m]	ξ_0 [nm]	$B_{c3,0}$ [mT]	w [nm]	λ_{P0} [nm]
CL12	546 ± 1	41 ± 1	0.79 ± 0.01	208.7 ± 1.5	91 ± 4	64.4 ± 1.3	102 ± 1

Table 7.1: Sample parameters for the single ring. The ring radius R was first determined from the slope of $B_{sw}(n)$. $n_{\max}(T{=}0)$, k, and ξ_0 are then found by minimizing the residual variance between measured $\Delta f(B)$ traces and GL fits with all backgrounds removed. Using these fit parameters we then calculate $B_{c3,0}$ using $B_{c3,0} = n_{\max}(T{=}0)\frac{\Phi_0}{\pi R^2}$. With Eq. 6.5 we then determine w. Using our fit result for ξ_0 and that $B_{c0} = 0.01$ T for aluminum together with Eq. 2.20 we calculate λ_{P0}.

traces so it coincides with the treatment we performed on our data to remove all backgrounds. With this background removed, the important fitting features are the field at which the phase slips occur (which is mostly set by ξ_0), and the magnitude of the frequency jump for each phase slip (which is mostly set by k). The fitting parameters and all calculated parameters from this procedure are summarized in Table 7.1 for CL12. Comparing these parameters to those of Table 6.2, we see that our determination of ξ_0, λ_{P0} and $B_{c3,0}$ is consistent with our array measurements. Further, the R and w determined from the single ring measurements agree with those determined from the array measurements, which is expected as the arrays and single ring cantilevers were defined with identical lithographic dimensions.

7.1.1.3 Fitting $f_0(B)$ for CL16

At the time of this dissertation for CL16 we could not reliably perform GL fits to $f_0(B)$ to obtain material parameters. This limitation was due to the small ring radius ($R \approx 290$ nm). For this sample we expect $n_{\max} \approx 7$ at $T = 750$ mK, and given that our frequency shift signal is small at low fields as $\Delta f \propto B$ and near B_{c3} where $I \to 0$, we are only left with 3-4 oscillations in $f_0(B)$ that we can hope to observe. This severely limits the quality of the fits.[6] Though the change in current during a phase slip should be largest for CL16 (see Fig. 6.10 versus Fig. 6.13), which would help to make these oscillations visible, the frequency shift signal scales as flux. So though the jump in current is nearly 4 times as large for CL16 when compared to the ΔI for CL12, the Δf jump will be of the same

6. For CL16 we can only observe 4-5 oscillations at $T = 700$ mK, while for CL12 we have at least 10 visible oscillations at $T = 1060$ mK.

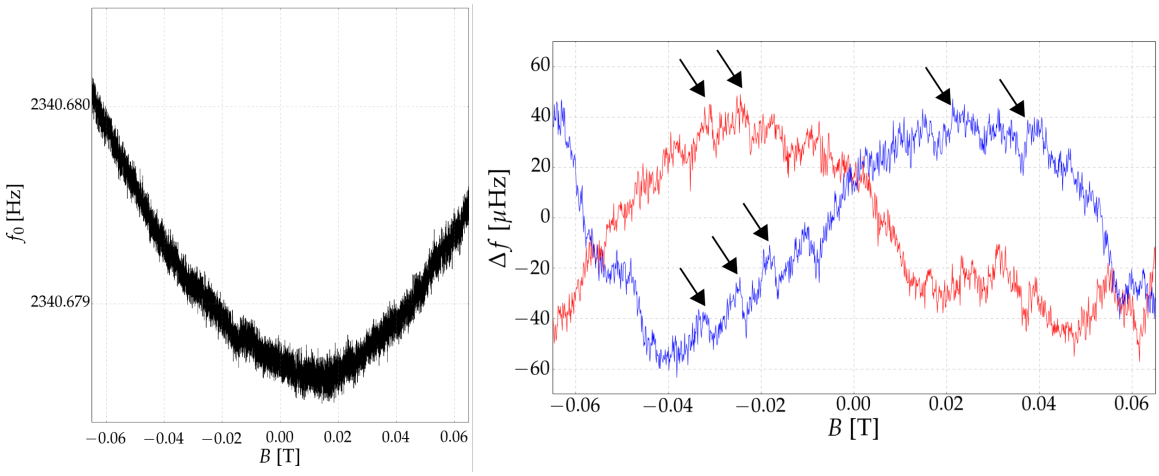

Figure 7.5: (Left panel) A single measurement of cantilever resonant frequency as a function of magnetic field for CL16 at $T = 800$ mK with $\dot{B} < 0$. (Right panel) Cantilever resonant frequency shift after the subtraction of a second order polynomial. Red (blue) are for increasing (decrasing) B. Here each curve represents the average of 60 individual $f_0(B)$ traces in each direction, which corresponds to a total measurement time of 48 hours. The black arrows indicate the location of clearly visible phase slips. The curves have been shifted by 14 G to correct for the large solenoid hysteresis, as found in all other measurements.

magnitude as $R_{16} \approx \frac{1}{2} R_{12}$.

The small ring radius also limits the highest temperature at which we can observe a phase slip as a sharp jump in $f_0(B)$. As explained in Section 2.3.3, when $\frac{R}{\xi(T)} < \frac{\sqrt{3}}{2}$ the ring will adiabatically remain in the lowest energy state as the applied field is varied. For rings with smaller R, this condition is met at lower temperatures as $\xi(T)$ does not need to be as large. Though the winding number will still change, there will be no sharp features in the measured $f_0(B)$ traces. Given the low signal to noise, this makes detecting phase slips for the GL fits difficult. This limits our ability to determine the winding number for data near the phase slip regions, which is important for the GL fits. From the array measurements we can see that at $T = 1$ K, the phase slip near $B = 300$ G is already non-hysteretic for the smallest rings (Fig. 6.13), while the largest rings still display a clear hysteresis and sharp jump in the measured $f_0(B)$ traces (Fig. 6.10). Given that we can only apply the GL fits above 750 mK, we have a much smaller temperature range over which we can fit data for CL16. For CL16 we only only have 3 full field measurements at $T = 460$ mK, $T = 700$ mK, and $T = 800$ mK, and only the last measurement falls within the temperature range where we expect the GL fits to be valid.

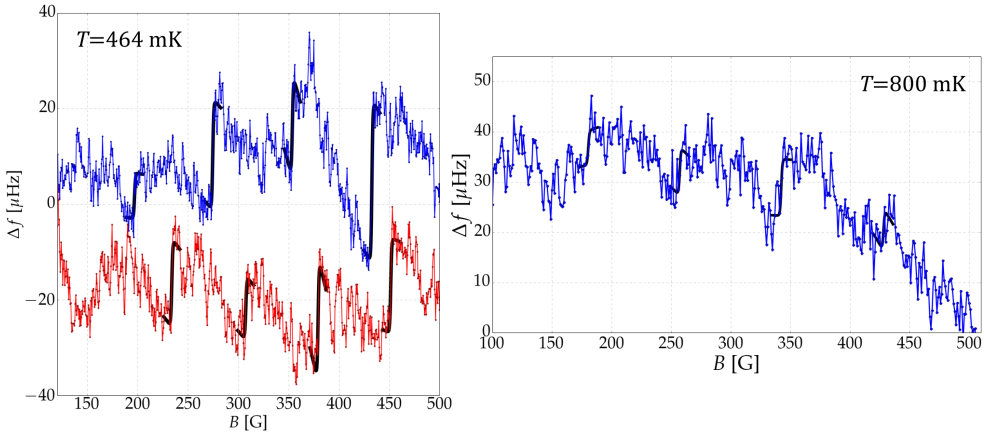

Figure 7.6: Measured cantilever frequency shift as a function of applied magnetic field for CL16 at $T = 464$ mK and $T = 800$ mK. Red (blue) is for increasing (decreasing) B. Steps (phase slips) are detected by the fits illustrated in black.

The measurement at $T = 800$ mK is shown in Fig. 7.5. In the individual $f_0(B)$ trace we are not able to observe oscillations. And after averaging 48 hours of continuous data we are still barely able to distinguish the location of phase slips. However, we are able to obtain a measurement of R, given that it almost completely determines the periodicity of oscillations. From the SEM images (Fig. B.2) we have an idea of what periodicity to expect and thus where the phase slips should occur. We perform a fit, looking in 40 G regions around the expected phase slip location, and find the jump location which gives the best R^2 when fit to a step of the form

$$f_0(B) = \delta f \mathrm{Tanh}\Big(B - B_{\mathrm{sw}}\Big) + c + d\,(B - B_{\mathrm{sw}}) \tag{7.2}$$

with 4 fitting parameters: the frequency shift magnitude of the phase slip δf, the applied magnetic field location of the phase slip B_{sw}, and c and d which allow for a linear background and offset. This is illustrated in Fig. 7.6. From these three temperatures, we are able to plot $B_{\mathrm{sw}}(n)$ as we did for CL12 and determine the linear slope, $\frac{1}{1+\left(\frac{w}{2R}\right)^2}\frac{\Phi_0}{\pi R^2}$ which gives the best fit. We find $R = 295 \pm 3$ nm, as indicated by the fit in Fig. 7.7. This measurement is consistent with the dimensions found in the SEM images.

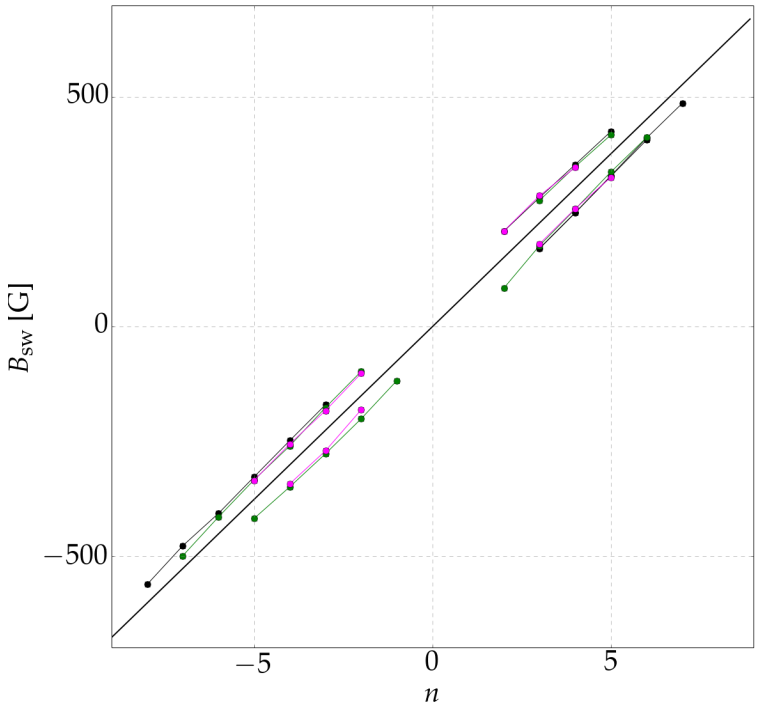

Figure 7.7: Measured applied magnetic field at which a phase slip (i.e. observed jump in $\Delta f(B)$) occurs as a function of winding number at multiple temperatures for CL16 (black, green and magenta are for T =460 mK, T = 700 mK, and T = 800 mK respectively). The linear slope of this entire dataset allows us to determine R to within 3 nm.

7.2 Measurement of persistent current with the small coil

The switching field distribution $P(B_{\mathrm{sw}})$ is expected to have a width on the order of 100 mG for our experimental configuration. As the large solenoid in our setup has a field to current ratio of 1021.8 G/A and is connected to a 100 A power supply, even at the slowest programmable ramp rate we would sweep through this switching region in less than 1 second, which is not ideal for our measurement where we require several seconds of averaging at every field point to obtain a signal to noise ratio greater than unity. Thus, we decided to use a smaller magnetic coil capable of producing a constant 100 G field at its center, which we powered with an ultra-low noise voltage controlled current source. In this section, we will describe the smaller magnetic coil and how it was integrated into the experimental setup used in Chapter 6.

7.2.1 Small coil and sample stage

An image of the small coil used in this experiment is shown in Fig. 7.8. The spool of the coil is made of free machining brass and the amount of metal was minimized to reduce eddy current heating. For the same reason, the spool was cut in half and then epoxied (Stycast 2850 FT black epoxy) back together with 0.3 mm thick G10 spacers between each half. We used mono-filament NbTi superconducting wire (T48B-M Supercon Inc.) with 0.008" bare diameter and 0.009" insulating diameter. The wires are insulated with Formvar. At room temperature, the total length of superconducting wire has a resistance of 280 Ω, and at 4.2 K the resistance is 5.95 Ω, which is measured through the fridge wiring. The inductance of the coil is 42 mH at 4.2 K, and as we will show in section 7.2.3, the coil has a field to current ratio of 550 G/A.

The coil was attached to the sample stage as shown in Fig. 7.9. A 0.23" tall free machining brass spacer elevated the coil from the base of the stage so that the sample was in the middle of the field created by the coil. Between the spool and the spacer, we placed a piece of cryogenic-compatible Kapton tape, and we also covered the washers in Kapton tape. This ensured that the spool was electrically isolated from the rest of the sample stage

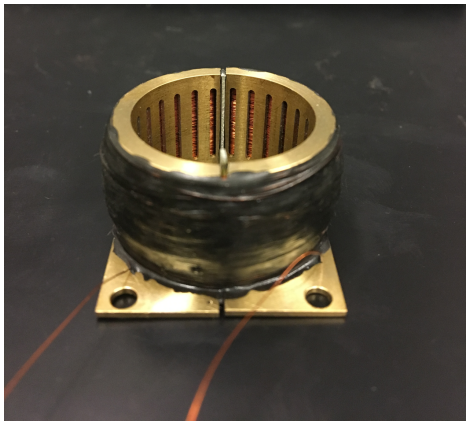

Figure 7.8: Image of the small coil used in this experiment. The coil has a diameter of 1 inch and is wound around a free machining brass spool. Small ovular holes were placed around the spool to decrease the amount of metal to reduce eddy current heating. Two 0.3 mm thick G10 spacers were placed in the middle of the spool to further prevent eddy currents. The superconducting wire is a single filament NbTi wire, which was epoxied in place to prevent any movement during the year of measurements in which the coil was used.

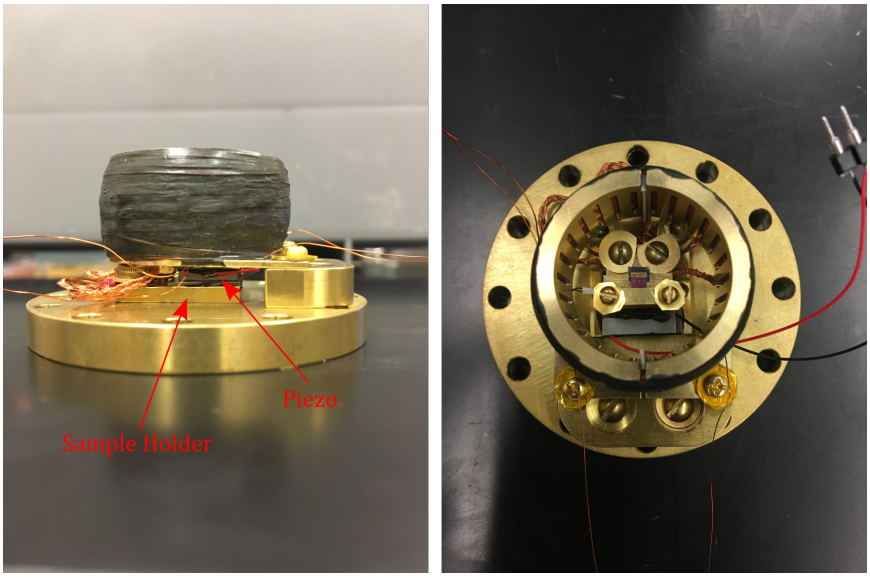

Figure 7.9: Image of the assembled sample stage with the small coil. The coil is elevated by a free machining brass spacer which ensures that the sample is vertically located in the middle of the small coil. This elevation also ensures that no wires or thermal anchoring contact the small coil brass spool. In the top-down view we can see that the sample sits directly in the middle of the coil.

and helped to minimize eddy current heating on our sample stage.

7.2.2 Small coil measurement circuit

The small coil circuit was almost entirely independent of the PLL measurement circuit of Section 5.5, except that we used the auxiliary inputs of the HF2 to measure the current through the small coil. We used a 50 MHz function/arbitrary waveform generator (Berkeley Nucleonics Model 645) to supply an ultra-low noise voltage controlled current source (Stanford Research Systems Model CS580). From the current source, the current passed through two low pass filters (Thorlabs EF504 and Mini-Circuits 15542) which have pass bands between DC-240 kHz and DC-1.9 MHz respectively. The current then passed through an ultra-high precision LED (light-emitting-diode) bulk metal foil resistor (Vishay LED221T) ($R = 10.066 \pm 0.001\Omega$) at room temperature, and with a four-point measurement we measured the voltage across the resistor. The resistor was attached to a 400 g block of brass to provide thermal anchoring and mitigate any temperature fluctuations. The LED resistors are ideal for precise and stable current measurements as they have low temperature

coefficients of resistance (0.05 ppm/°C at room temperature), a low power coefficient (i.e. ΔR due to self-heating of 5 ppm for powers up to 8 W) and Johnson noise $< 0.01\mu V_{RMS}/V$ of applied voltage. After this resistor, the current passed through the small coil in the fridge and returned to the current supply. Finally, for measurements with the small coil we used a universal frequency counter (Agilent Model 53132A) with the ultra high stability oven timebase option to provide a 10 MHz clock signal to both the HF2 and the arbitrary function generator. This circuit is illustrated in blue in Fig. 7.10.

7.2.3 Small coil field to current ratio calibration

The most important calibration of the small coil was the precise determination of its field to current ratio. At room temperature, we used a digital Gaussmeter to ensure that the coil was producing a magnetic field (that is, to ensure there were no breaks in the wire after it was epoxied) and obtained a rough calibration of 500 G/A at its center. To obtain a more precise calibration, we cooled the sample and small coil down to 400 mK and took $f_0(B)$ data with both the large solenoid and the small coil, as illustrated in Fig. 7.11. The red and blue traces correspond to raw resonant frequency data for array sample CL15 at T= 464 mK taken by linearly increasing or decreasing the applied field of only the large solenoid. We have not subtracted any field-dependent backgrounds; however, we have corrected for the 14 G offset of the large magnet (the same offset we found in Fig. 6.2). We then repeated this measurement on CL15 by applying a linear current ramp to the small coil while the large solenoid was kept off. From this, we obtained $f_0(V)$, where V is the voltage across the 10.066 Ω resistor. We used Ohm's law to convert this into $f_0(I)$. We then determined the field to current ratio which gave the best agreement between the measured $f_0(B)$ for both magnets. The result with 550 G/A for the small coil is plotted in black.[7]

7. These two measurements were taken over a month apart. In addition to field dependent backgrounds, the cantilever resonant frequency also drifts in time. To get the absolute frequencies to match we added 10 mHz to the small coil f_0 measurement, which corresponds to a 5 ppm drift in f_0.

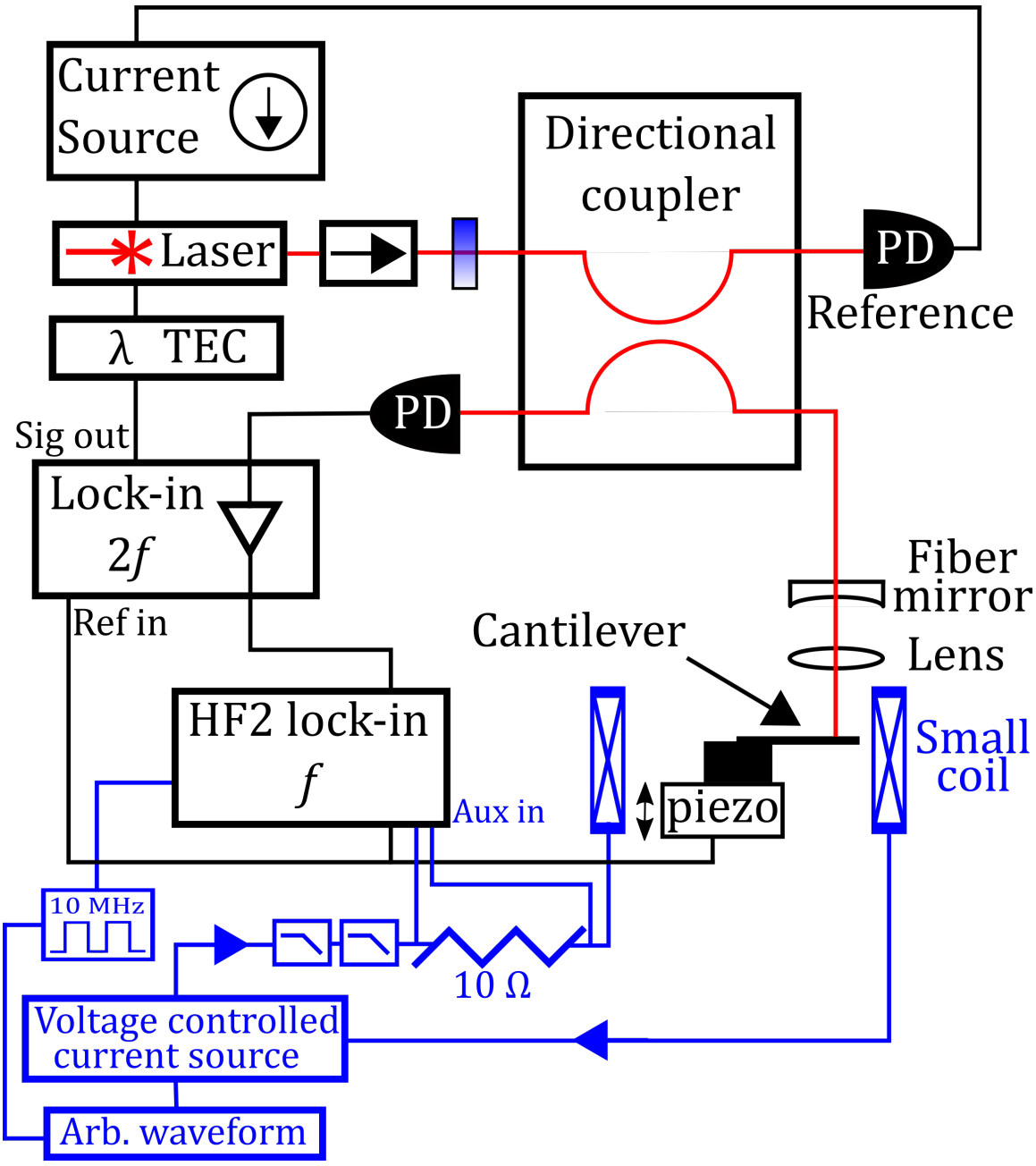

Figure 7.10: Complete measurement circuit including the small coil. The PLL circuit, indicated in black, is identical to that of Fig. 5.4. The small coil circuit, indicated in blue, consists of an arbitrary waveform generator, which controls a voltage controlled current source. The current source provides a drive to the small coil in the fridge. The current first passes through two low pass filters and a 10 Ω resistor at room temperature, which allows us to measure the current in the coil with a four-point measurement. An ultra high stability 10 MHz clock is provided to both the HF2 and the waveform generator.

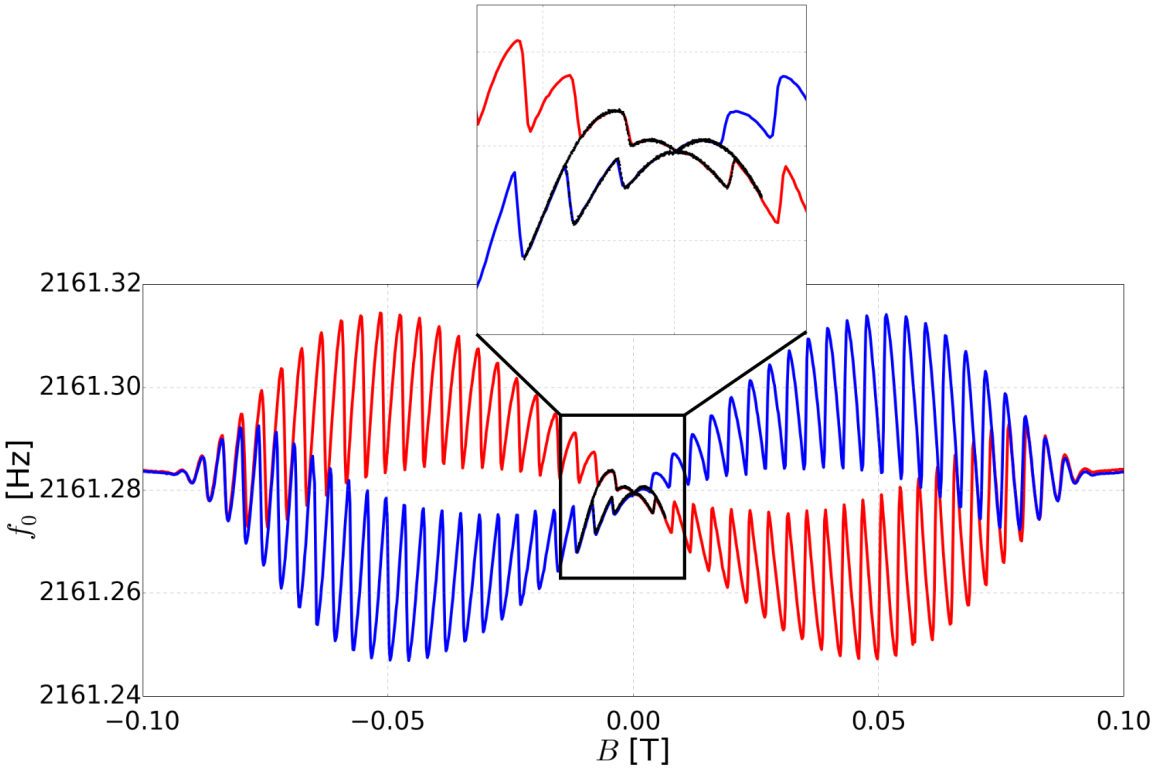

Figure 7.11: Cantilever resonant frequency as a function of applied magnetic field for CL15 at $T = 464$ mK. Red (blue) curves are for increasing (decreasing field) with the large solenoid only. The black curve corresponds to resonant frequency data for CL15 taken by applying a linear current ramp to the small coil at $T = 464$ mK while the large solenoid was turned off. We used a four-point measurement across a 10 Ω resistor as described in the text to determine the current in the coil, and using a field to current ratio of 550 G/A, we find the excellent level agreement shown in the inset.

7.2.4 Set-up of the magnetic field ramp

The frequency shift signal is proportional to B and I (Eq. 4.26), but the supercurrent is diminished at fields close to B_{c3}. Thus, the largest frequency shift jump due to a phase slip occurs around 300 G (see, for instance, Fig. 6.2). Unfortunately, our small coil could only produce 100 G of field before transitioning to the normal state.[8] To get around this problem, we used the large solenoid to provide a field offset of ∼290 G and then used the small magnetic coil to vary the applied magnetic field.

To bring the large solenoid to field we applied a linear ramp (∼1 G/s), but would

8. Though the T48B-M wire is specified to support several amps of current at 4.2 K, we were limited to 100-200 mA of current. We suspect this limitation was set by the solder joint between the superconducting coil wire and the fridge wiring.

overshoot the desired field by 10 G. We would then ramp the field 9 G below the desired field. Then we ramped the field to 8 G above the desired field. We continued this process until the large solenoid was at the desired field, and then we persisted the magnet and ramped the leads back down to zero current. At this point, the magnet power supply and controller were completely unplugged from the wall.

For the small coil, we needed to create a magnetic field ramp that would allow us to study the same phase slip (i.e. the transition $\psi_{n=12} \rightarrow \psi_{n=13}$) many times. For a measurement of the transition $\psi_n \rightarrow \psi_{n+1}$, we also obtained a measurement of the transition $\psi_{n+1} \rightarrow \psi_n$ as we needed to reinitialize the system in ψ_n at some point. The transition $\psi_n \rightarrow \psi_{n+1}$ occurs at approximately[9] $\Phi_{\min,n} + \frac{R}{\sqrt{3}\xi}\sqrt{1+\frac{\xi^2}{2R^2}}\Phi_0$, while the transition $\psi_{n+1} \rightarrow \psi_n$ occurs at approximately $\Phi_{\min,n+1} - \frac{R}{\sqrt{3}\xi}\sqrt{1+\frac{\xi^2}{2R^2}}\Phi_0$. Thus, the flux separation between neighboring transitions, $\Delta\Phi_{n\rightarrow n+1\rightarrow n}$, is given by

$$\Delta\Phi_{n\rightarrow n+1\rightarrow n} \approx \Big(\frac{2R}{\sqrt{3}\xi}\sqrt{1+\frac{\xi^2}{2R^2}} - \frac{1}{1+\left(\frac{w}{2R}\right)^2}\Big)\Phi_0 \tag{7.3}$$

At low temperatures, where $R \gg \xi(T)$, this separation is larger than Φ_0; however, the expected width of $P(\Phi_{\rm sw})$ is only fraction of Φ_0. Because of this, the majority of the applied flux ramp does not contain any interesting information about phase slip statistics. Thus, we decided to use an applied field ramp where we varied the applied field slowly ($\sim$13 mG/s) over a small field region centered around the expected phase slip field, and varied the field more rapidly ($\sim$1 G/s) in all other regions. This allowed us to maintain a decent level of signal to noise in the region of interest, while minimizing the time of a single measurement. An example of this field ramp is displayed in Fig. 7.12.

One major difference between this switching measurement and the previous switching measurements performed on Josephson junctions or wires is the rate at which we can collect statistics. Fulton and Dunkleberger were able to apply current ramps at 300 Hz to their junctions [31], and the Bezryadin group typically collects 10^4 events for each of their measured switching distributions [46, 47]. In contrast, even under optimal conditions, our

9. Approximate as we have suppressed the winding number dependence in Eq. 2.94 to make the equations manageable.

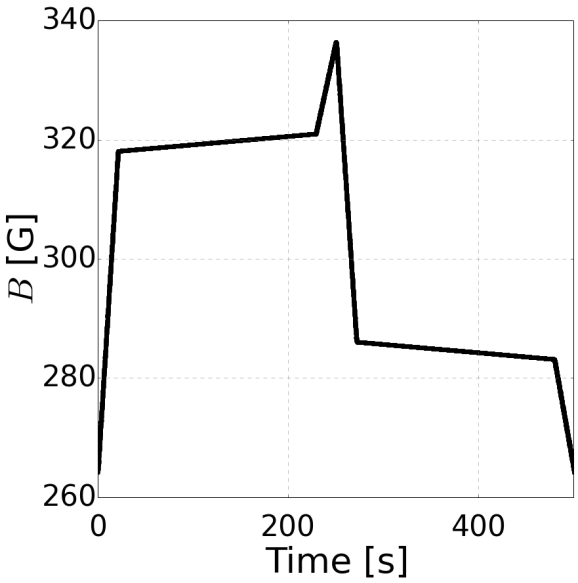

Figure 7.12: Applied magnetic field ramp created by the small coil as a function of time. The 290 G offset is created by persisting the large solenoid as explained in the text. The slow ramp regions are chosen so that a phase slip is expected to occur near the middle of these regions. To ensure that a phase slip always occurs in this region, we extend these regions an extra $\sim 1-2$ G on either side. Here, the overall ramp frequency is 2 mHz.

ramp frequencies were limited to $\sim$10 mHz so in a 24 hour measurement we were able to collect 800 events for a given winding number transition.[10]

7.3 Phase slip switching field measurements

We will now present our measurements of $f_0(B)$ with the small coil for CL12 and CL16. We will go through a step-by-step analysis of a measurement for CL12 at $T = 471$ mK to illustrate the process of detecting individual phase slips in the $f_0(B)$ data. We will discuss two methods for converting this measurement into a measurement of $P(B_{\rm sw})$, the distribution of applied magnetic field at which a given phase slip occurs. The first method is

10. This limitation was set by two main factors. First, at fast ramp rates eddy current heating would raise the stage temperature. For all measurements, we ensured that the field ramp did not change the stage temperature as measured by the sample thermometer. Second, if we wanted to maintain the same magnetic field resolution (field bin size), but increased the overall ramp speed, we would have less measurement time within each field bin. Given that our signal to noise was already small in this single ring experiment, fast ramp rates made it impossible to distinguish a $\sim$20 μHz jump from the noise. In practice, we found a ramp rate of 13 mG/s near the expected switching field gave us the field resolution and sufficient signal to noise ratio to measure a single switching distribution with sufficient statistics in a 24 hour period for CL12. Depending upon the total extent of this slow ramp region, which was determined independently for each measurement, this corresponded to overall ramp speeds of 2-15 mHz.

based on direct phase slip detection (and is useful for $T \leq 800$ mK).[11] The second method is insensitive to our ability to directly detect individual phase slips, and is applicable at much higher temperatures ($T < 1100$ mK); this latter method will ultimately be used to determine the mean and standard deviation of $P(B_{\rm sw})$.

7.3.1 Direct detection of individual phase slips

Using the small coil to continuously vary the applied magnetic field in a manner illustrated by Fig. 7.12 we can vary the applied magnetic field slowly enough so that it only changes by ∼10-20 mG over 1 second. This is necessary as this amount of measurement time allows us to keep the frequency noise small (σ_f∼30 μHz) compared to the expected phase slip signal (∼100 μHz). Given that the characteristic width of $P(B_{\rm sw})$ for CL12 is on the order of 30-60 mG, this also ensures we have sufficient resolution to measure the distribution. An example of two ramps are shown in Fig. 7.13. We can clearly distinguish a sharp jump in f_0 with a magnitude ∼100 μHz, which is a phase slip. To determine the location of the phase slip, we fit each curve to a function of the form

$$f_0(B) = \delta f \ \mathrm{Tanh}\Big(a\,(B - B_{\rm sw})\Big) + c \tag{7.4}$$

where δf is the frequency shift magnitude of the phase slip, a sets width of the phase slip region, $B_{\rm sw}$ is the applied magnetic field location of the phase slip, and c is the resonant frequency offset. For each fit, we calculate the R^2 value of the fit over a 0.7 G region centered around the jump. For the upper and lower curves in Fig. 7.13 we find $\mathrm{R}^2 = 0.81$ and 0.73 respectively.

For this particular measurement, we collected 470 measurements of the transition $\psi_{n=12} \rightarrow \psi_{n=13}$ and $\psi_{n=13} \rightarrow \psi_{n=12}$, which corresponds to a continuous measurement for 58 hours.[12]

11. At lower temperatures the frequency noise on our cantilever is smaller (Eq. 5.7) and the condensation energy of the ring is larger which leads to a larger change in current (equivalently resonant frequency) during a phase slip. At higher temperatures, the combination of increased frequency noise and a smaller signal makes it difficult to distinguish an individual phase slip directly.

12. At low temperatures, the applied field loop needs to span a larger field to capture both phase slips (Eq. 7.3). And to ensure that the sample does not heat, we can only ramp ∼1 G/s over the fast regions. Further we found that at lower temperatures the switching distributions were broader, which required us to ramp the applied field slowly over a larger region. Together, this leads to very slow overall ramp rates for the lowest temperatures (< 2 mHz).

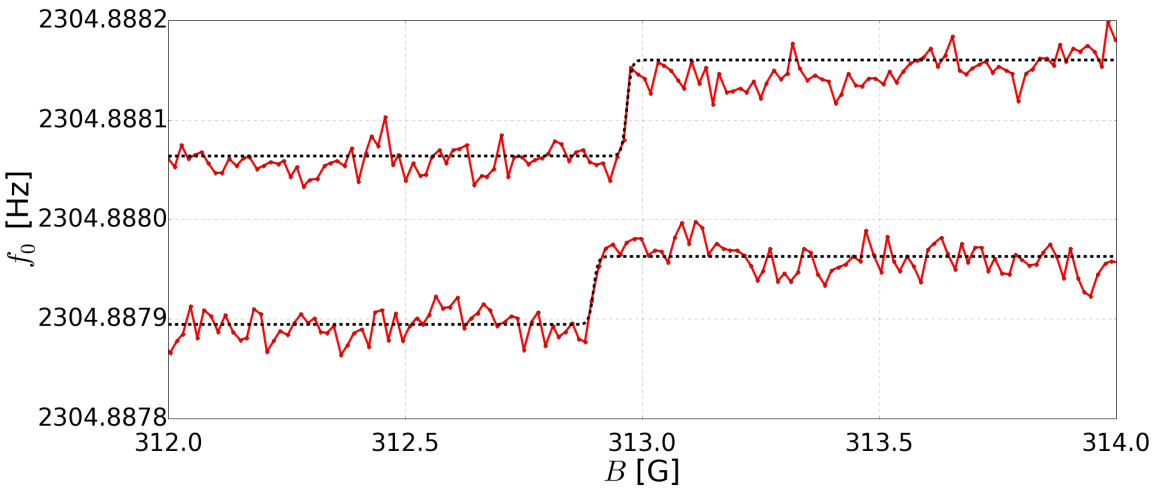

Figure 7.13: Resonant frequency for CL12 at $T = 471$ mK as a function of applied magnetic field from the small coil for two separate ramps with $\dot{B} > 0$ (red curves). Here, we only display a small region centered around the expected phase slip field where the ramp rate is 13.6 mG/s. The upper curve is offset by 150 μHz for clarity. In black we illustrate a Tanh fit to the data from which can extract the phase slip field and the height of the jump.

With this number of measurements, we can plot $B_{\rm sw}$ as a function of ramp number (equivalently time), which is illustrated in Fig. 7.14. Ideally, we would expect to find the phase slip fields distributed around a value that is constant in time. Instead, we find that $B_{\rm sw}$ is distributed around a value that tends to increase with time. To explain this, we recall that our field ramps are taken with the large solenoid persistent. A perfect superconducting magnet should maintain this field indefinitely; however, small solder connections between the length of multi-filament wire used in the 9 T magnet can lead to a small, but finite, resistance, which leads to a slow decrease of the current over time.[13] As a result, the "true" field that the ring sees will be smaller than the field we calculate ignoring decay in the large magnet, and thus, the observed switching field should slowly increase with time. We also find that the applied field drift is different for the $\psi_{n=12} \rightarrow \psi_{n=13}$ and $\psi_{n=13} \rightarrow \psi_{n=12}$ transitions. As the applied field separation of these transitions is 35 G ($\sim$11% of the overall applied magnetic field) they exist in slightly different magnetic environments. It is possible that pinned flux in the large solenoid could be different in each of these environments, so there is no a priori guarantee that the field drifts should be identical.

13. Drifts may also be due to the movement of trapped flux within the magnet

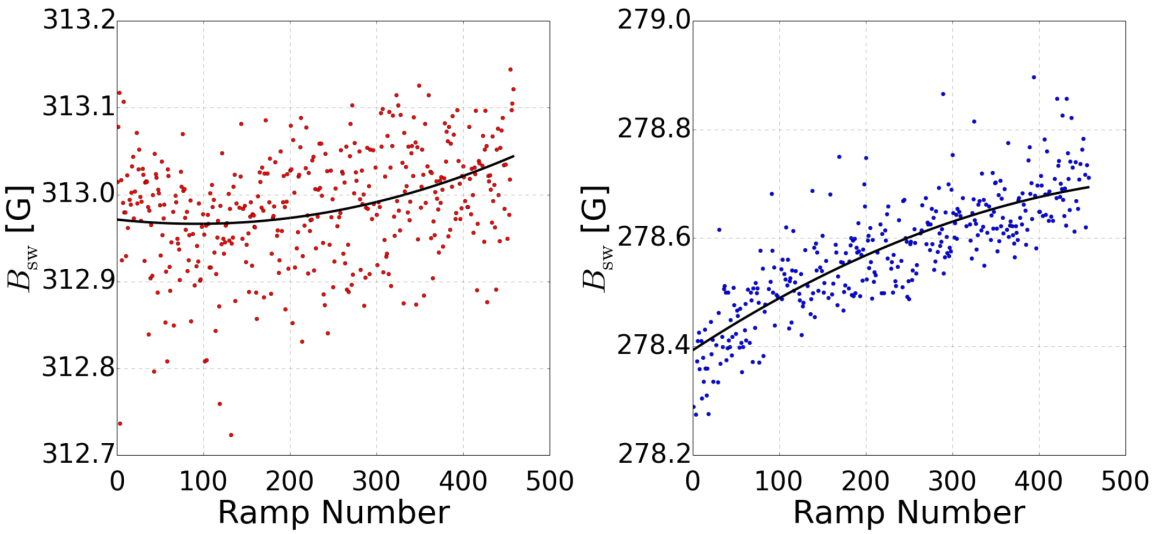

Figure 7.14: Determined phase slip location B_{sw} as a function of ramp number (i.e. time) for CL12 at $T = 471$ mK. Red (blue) are for increasing (decreasing) B. Black curves correspond to a second order polynomial fit to the drift. This measurement spans 58 hours and the total field drift is approximately 100 mG for the $\psi_{n=12} \rightarrow \psi_{n=13}$ transition and 300 mG for the $\psi_{n=12} \rightarrow \psi_{n=13}$ transition.

To check for systematic errors in our determination of B_{sw} we look at correlations between B_{sw}, R^2, and δf. There should be no correlation between B_{sw} and R^2, as we should fit a phase slip in $f_0(B)$ equally well regardless of the field at which the jump is located. B_{sw} and δf should also be uncorrelated, as over the width of $P(B_{\mathrm{sw}})$ we expect a phase slip to result in the same magnitude of frequency shift. Finally, there should be a positive correlation between δf and R^2, as a larger frequency shift will result in an improved fit. We expect a phase slip to result in a frequency shift of approximately 100 μHz for CL12 at $T = 471$ mK. Fits that return $\delta f \ll 100$ μHz are likely the result of an unfortunate noise spike or cantilever drift that obscured the phase slip. An example of one of these ramps is shown in Fig. 7.15. To quantify the correlation we use the Pearson correlation coefficient defined as

$$r_{x,y} = \frac{\mathrm{cov}(x,y)}{\sigma_x \sigma_y} = \frac{\sum_{i=1}^{N} \Big(x_i - \bar{x}\Big)\Big(y_i - \bar{y}\Big)}{\sqrt{\sum_{i=1}^{N} \Big(x_i - \bar{x}\Big)^2} \sqrt{\sum_{i=1}^{N} \Big(y_i - \bar{y}\Big)^2}} \tag{7.5}$$

where N is the total number of measurements and $\bar{x}$ and $\bar{y}$ are the arithmetic average of the quantities x and y. The correlations between fitting parameters are illustrated in

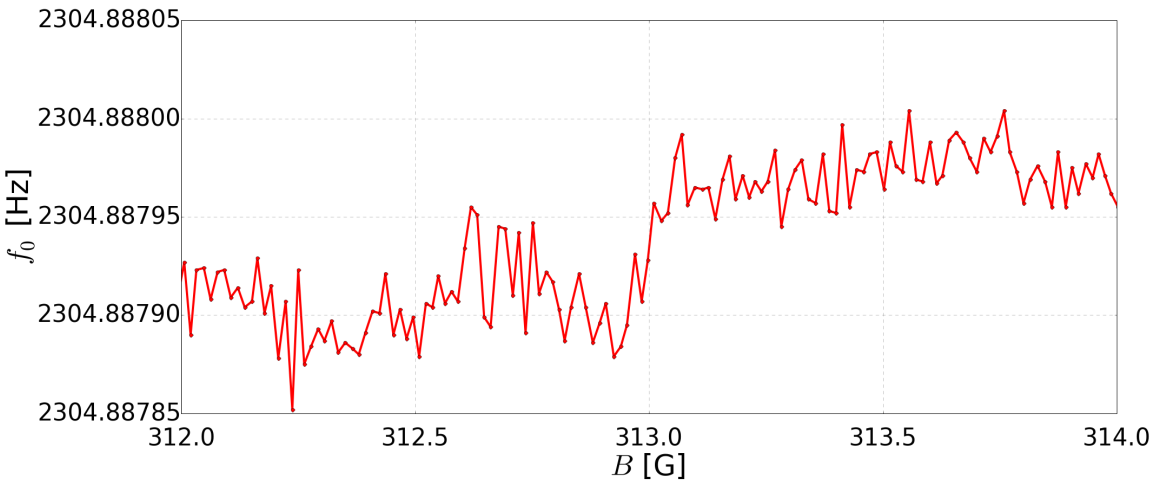

Figure 7.15: Resonant frequency for CL12 at $T = 471$ mK as a function of applied magnetic field from the small coil with $\dot{B} > 0$. For this ramp, the noise added to f_0 in a way that obscured the phase slip and leads to a small value for δf (32 μHz) and a low overall R^2 (0.48) for the Tanh fit.

Correlation	$\psi_{n=12} \rightarrow \psi_{n=13}$	$\psi_{n=13} \rightarrow \psi_{n=12}$
$r_{\delta f, B_{\rm sw}}$	-0.011	0.041
$r_{B_{\rm sw}, R^2}$	-0.005	0.032
$r_{\delta f, R^2}$	0.841	0.827

Table 7.2: Correlation coefficients of phase slip fitting parameters calculated from Eq. 7.5 for CL12 at $T = 471$ mK. The data are plotted in Fig. 7.16.

Fig. 7.16, and the correlation coefficients are summarized in Table 7.2. As expected, there is essentially no correlation between the location of phase slips and the magnitude of frequency shift and the location of the phase slip and the goodness of fit. Further, fits with small δf are typically the fits with the worst R^2.

After these diagnostics, we need to subtract the applied field drift from the measured $B_{\rm sw}$ versus ramp number N as this field drift is due to the decaying current in the large solenoid and not the underlying physics of phase slips. Given the correlation between δf and R^2, we only consider points with $R^2 > 0.55$ when we determine the fit to $B_{\rm sw}(N)$, which results in the black lines in Fig. 7.14. The result of this field subtraction is illustrated in Fig. 7.17. Again, we check for correlations between $B_{\rm sw}$ and R^2 and $B_{\rm sw}$ and δf after this field removal and find $|r| < 0.05$, which indicates that this background removal does not introduce any unnecessary correlations.

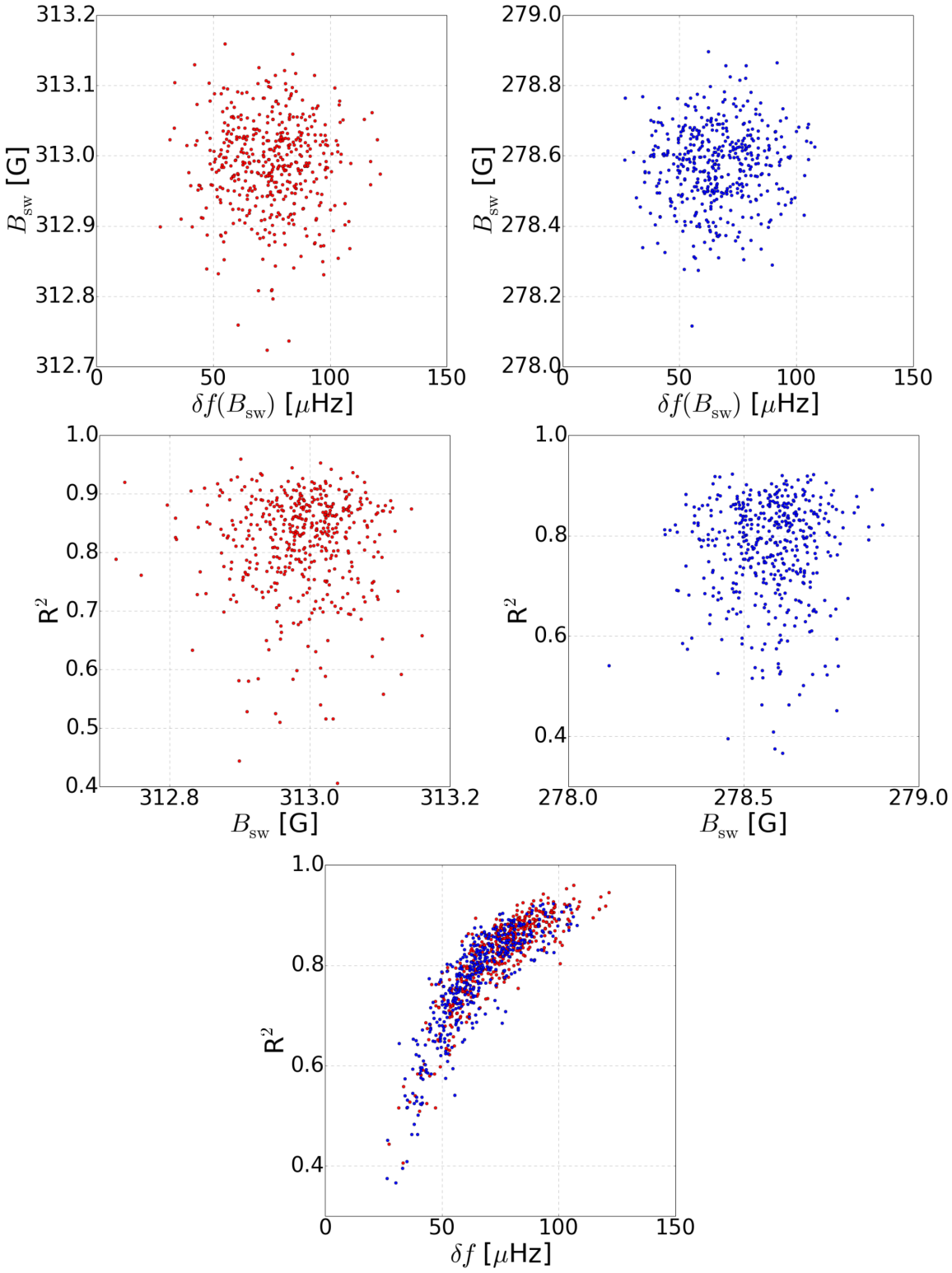

Figure 7.16: Correlations between the phase slip location B_{sw}, the magnitude of frequency shift due to a phase slip δf, and the coefficient of determination R^2 for the Tanh fit to $f_0(B)$ over a 0.7 G window centered around B_{sw}. Red (blue) are for increasing (decreasing) applied magnetic field.

To visualize the phase slip field distribution $P(B_{\rm sw})$, we bin the data of Fig. 7.17, which is shown in Fig. 7.18. These data are a *sample* of measurements representative of the underlying distribution of $P(B_{\rm sw})$ (the *population* in statistics literature). To describe the sample, we can define the n-th central moments μ_n for measurements of $B_{\rm sw}$

$$\mu_n = \frac{1}{N}\sum_{i=1}^{N}\Big((B_{{\rm sw},i} - \langle B_{\rm sw}\rangle\Big)^n \tag{7.6}$$

where $\langle B_{\rm sw}\rangle = \frac{1}{N}\sum_{i=1}^{N} B_{{\rm sw},i}$ is first raw moment (the mean). The second central moment is the sample variance $\sigma^2_{{\rm sample},B_{\rm sw}}$, and the third and fourth normalized moments, given by $\frac{\mu_n}{\sigma^n_{{\rm sample},B_{\rm sw}}}$, are the sample skewness and kurtosis respectively.[14] While these terms describe the sample distribution, they are biased estimators of the underlying $P(B_{\rm sw})$ distribution (for instance, the sample variance assumes we have N independent measurements, while we need to estimate both the mean and σ^2 from our data). Formally, to estimate the *population* moments from a sample of N elements, the unbiased estimators are the k-statistics [74].

14. This definition of kurtosis is not the excess kurtosis, so a normal distribution has a kurtosis of 3 under this definition.

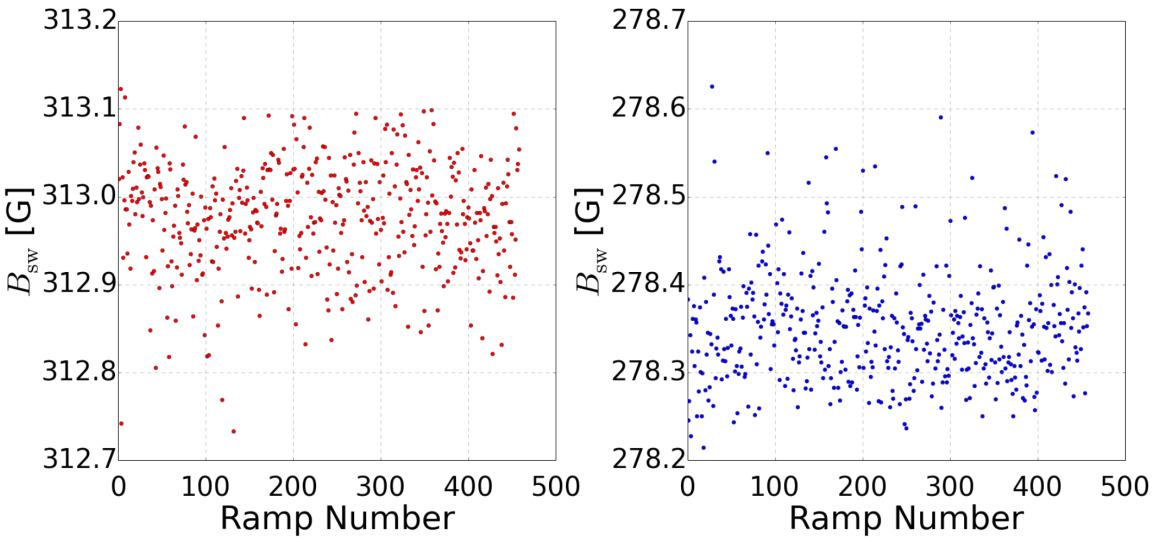

Figure 7.17: Phase slip field location as a function of ramp number for CL12 at $T = 471$ mK after the applied field drift removal. Red (blue) are for increasing (decreasing) B. This data is the same data of Fig. 7.14, with the black curves subtracted as a background. As a result, the phase slip locations are now distributed around a value that remains constant with time.

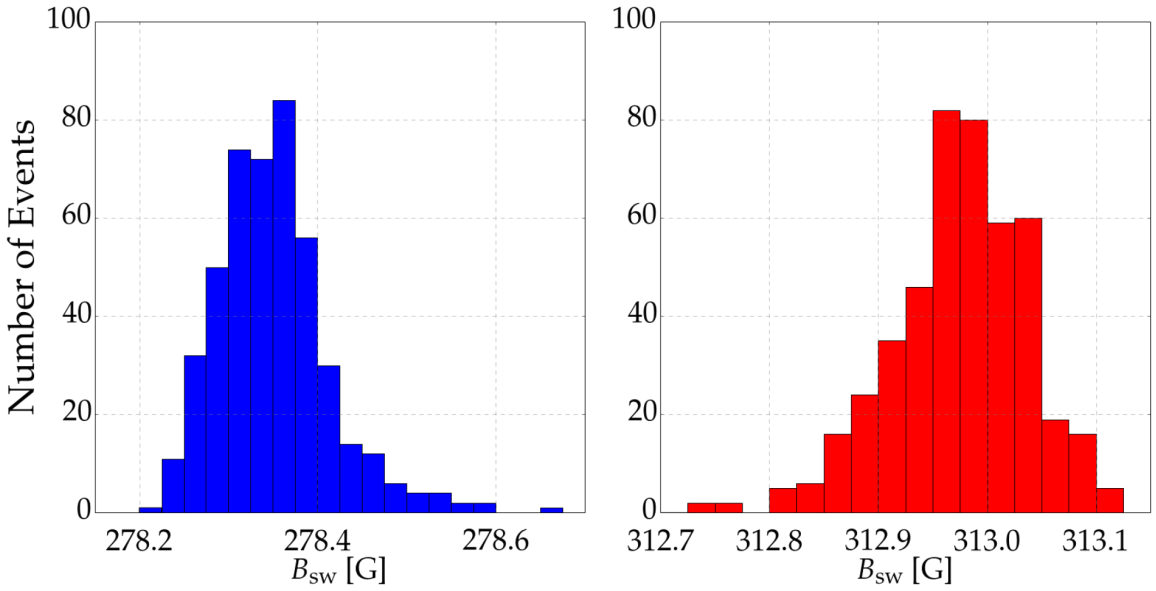

Figure 7.18: Distribution of applied magnetic fields at which a phase slip occurs, unnormalized $P(B_{\rm sw})$, for CL12 at $T = 471$ mK. Red (blue) is used for the transition $\psi_{n=12} \rightarrow \psi_{n=13}$ ($\psi_{n=13} \rightarrow \psi_{n=12}$). These histograms are created from the measured phase slip locations after background subtraction (i.e., the data from Fig. 7.17 using 25 mG bins).

The first three are given by

$$k_1 = \frac{1}{N}\sum_{i=1}^{N} B_{{\rm sw},i} \tag{7.7}$$

$$k_2 = \frac{N}{N-1}\mu_2 = \frac{1}{N-1}\sum_{i=1}^{N}\Big((B_{{\rm sw},i} - \langle B_{\rm sw}\rangle\Big)^2 \tag{7.8}$$

$$k_3 = \frac{N^2}{(N-1)(N-2)}\mu_3 = \frac{1}{(N-1)(N-2)}\sum_{i=1}^{N}\Big((B_{{\rm sw},i} - \langle B_{\rm sw}\rangle\Big)^3 \tag{7.9}$$

We can also calculate the variances of the k-statistics, which gives us the square of the statistical error associated with each each k-statistic, δk_i. These are

$$(\delta k_1)^2 = \frac{\kappa_2}{N} = \frac{\sigma^2_{{\rm sample},B_{\rm sw}}}{N} \tag{7.10}$$

$$(\delta k_2)^2 = \frac{\kappa_4}{N} + \frac{2\kappa_2^2}{N-1} \tag{7.11}$$

$$(\delta k_3)^2 = \frac{\kappa_6}{N} + \frac{9\kappa_2\kappa_4}{N-1} + \frac{9\kappa_3\kappa_2}{N-1} + + \frac{6N\kappa_2^3}{(N-1)(N-2)} \tag{7.12}$$

where κ_n is the n-th cumulant, and we used the fact that $\kappa_2 = \mu_2$.[15] To summarize, the mean switching field $\langle B_{\rm sw}\rangle$ is given by Eq. 7.7, the variance of the switching field $\sigma^2_{B_{\rm sw}}$ is given by Eq. 7.8. The skewness γ_1 and kurtosis γ_2 are given by

$$\gamma_1 = \frac{k_3}{k_2^{3/2}}, \qquad \gamma_2 = \frac{k_4}{k_2^2} \tag{7.13}$$

These summary statistics are illustrated in Fig. 7.19 for measurements taken on CL12 for $T \leq 800$ mK. For these plots, only fits with $\mathrm{R}^2 > 0.55$ are considered in the statistics. For $T > 800$ mK we cannot detect individual phase slips with enough confidence to perform such an analysis. In Section 7.3.2, we will analyze the data by averaging together all of the $f_0(B)$ traces, which is insensitive to our ability to distinguish an individual phase slip. This will allow us to extend our analysis to $T \approx 1100$ mK. We notice that $\langle B_{\rm sw}\rangle$ does not monotonically decrease (increase) as a function of temperature for the increasing (decreasing) applied magnetic field ramps as expected in Fig. 7.19a. However, both traces move together. This reflects the fact that though we took care to bring the large solenoid to 290 G each time a new temperature is set, when the magnet is persisted and the heater switch is disconnected, the field jumps very slightly. This leads to a $\sim$2 G offset error every time the magnet is persisted. However, by studying the *difference* between the means for the increasing and decreasing winding number transitions we can remove this systematic offset. This is illustrated in black in Fig. 7.20. In light blue, we illustrate the theoretical prediction for this distance in the absence of fluctuations given the fit parameters of Table 7.1, with Eq. 2.94 for the $n = 12 \rightarrow n = 13$ and $n = 13 \rightarrow n = 12$ transitions. This prediction overestimates the observed distance between the means, but this is expected as the prediction is for deterministic phase slips and thermal fluctuations will cause phase slips to occur when there is still a finite δF.

The standard deviation of the switching distributions displays a clear decrease as temperature is increased, and within the measurements' error bars the $\Delta n = 1$ and $\Delta n = -1$ tran-

15. I emphasized the formal distinction between the *sample* and *population* in the hope of removing confusion about N versus $N-1$ factors. Though the k-statistics are a formal definition, k_1 and δk_1 represent the typical sample mean and sample standard error on the mean, and k_2 is just the variance with division by $N-1$ instead of N.

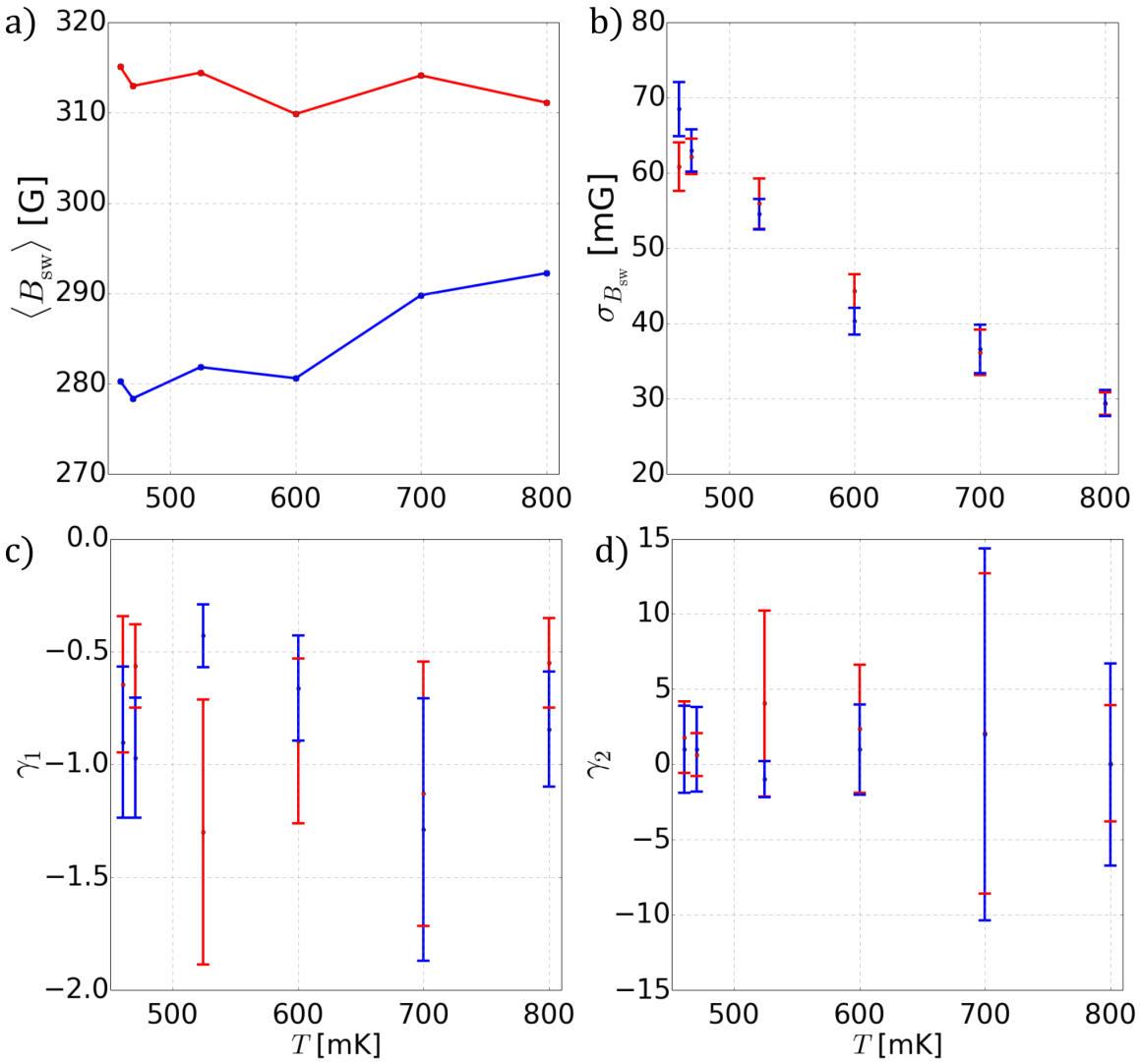

Figure 7.19: Mean (top left), standard deviation (top right), skewness (bottom left) and kurtosis (bottom right) as a function of temperature for the measured phase slip switching distributions for CL12. Red (blue) corresponds to the transition $\psi_{n=12} \rightarrow \psi_{n=13}$ ($\psi_{n=13} \rightarrow \psi_{n=12}$). For the skewness plot we have multiplied the blue points ($\dot{B} < 0$) by -1, this way we area always comparing the skewness with respect to the ramp direction that decreases the free energy barrier for phase slips.

sitions have identical widths (Fig. 7.19b). We find that the normalized skewness (Fig. 7.19c) is consistent with -1, as found by the Bezryadin group [34]. Averaging our measurements across all temperatures we find $\gamma_1 = -0.85 \pm 0.17$, and $\gamma_1 = +0.85 \pm 0.14$ for the increasing and decreasing winding number transition respectively.[16] The kurtosis (Fig. 7.19d) illus-

16. $\gamma_1 = +0.85 \pm 0.14$ for the $\dot{B} < 0$ ramp is still consistent with the Bezryadin group's result of -1 for the skewness. Their finding of -1 was with respect to a ramp direction that decreases the free energy barrier. For the $\psi_{n=13} \rightarrow \psi_{n=12}$ transition this corresponds to decreasing the applied magnetic field, so the distribution should be skewed toward larger absolute field magnitudes and we should find $\gamma_1 = 1$

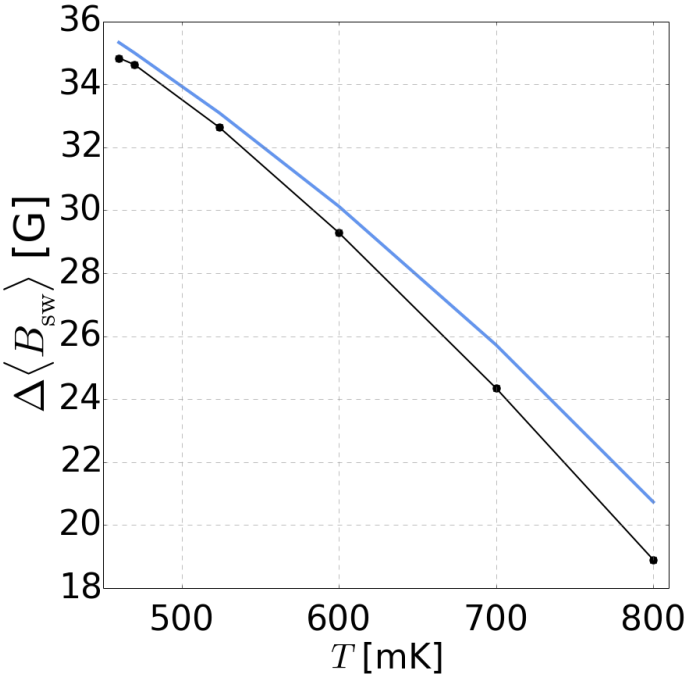

Figure 7.20: Applied magnetic field distance between the transition $\psi_{n=12} \rightarrow \psi_{n=13}$ and $\psi_{n=13} \rightarrow \psi_{n=12}$ for CL12 as a function of temperature (black). By subtracting the blue curve from the red curve in the top left panel of Fig.7.19 we obtain a monotonically decreasing curve. The light blue curve is our theoretical prediction for this distance given our fit parameters for CL12 (from Eq. 2.94) in the absence of fluctuations.

trates the limit of our measurement. By definition, the kurtosis can only take on a value between +1 and $+\infty$. For all of the measurements an unobtainable value for the kurtosis falls within error bars, so we cannot make any meaningful conclusions for the fourth or higher moments of these distributions. In particular, the large error bars for the $T = 700$ mk and $T = 800$ mK kurtosis measurements indicate that we are approaching the temperature limit of this analysis. This reflects our inability to fit phase slips with an $R^2 > 0.55$ when the signal to noise ratio becomes close to 1. Taking an average across all temperatures, we find $\gamma_2 = 1.8 \pm 2.3$ and $\gamma_2 = 1.2 \pm 2.5$ for the increasing and deceasing winding number transition respectively. For completeness, in Appendix C we display the unnormalized $P(B_{\rm sw})$ distributions for all measurements of CL12 for $T \leq 800$ mK. In Appendix D, we repeat this individual detection analysis over a region that does not include a phase slip as a null test of this analysis.

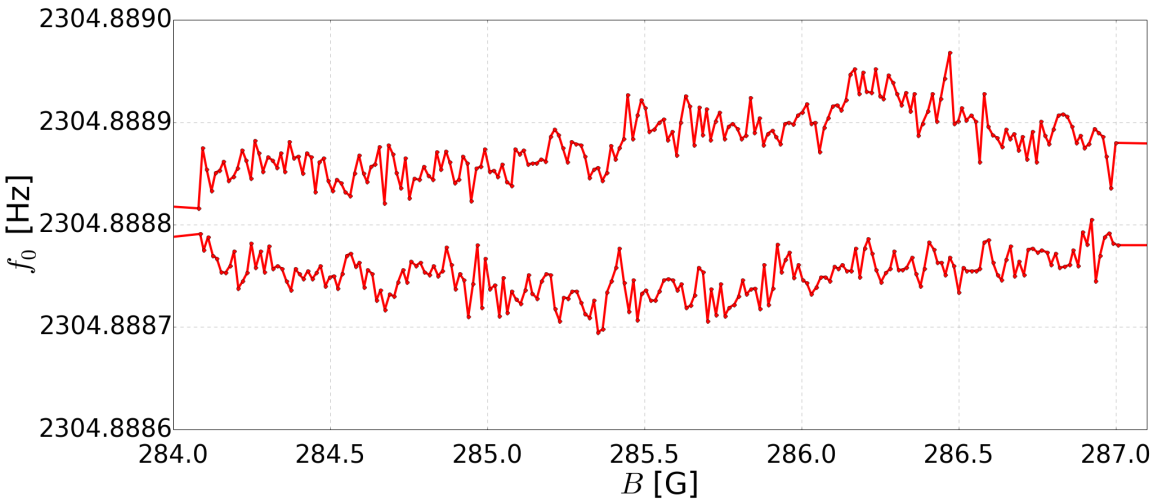

Figure 7.21: Cantilever resonant frequency as a function of applied magnetic field for CL12 at $T = 1052$ mK with $\dot{B} > 0$. The upper curve is offset for clarity. Given our fit parameters for CL12, we know that the deterministic phase slip location (where $\delta F = 0$) falls within this field span, so a phase slip must occur. However, given the noise on our measurement of $f_0(B)$ it is difficult to pinpoint the location of the phase slip.

7.3.2 Switching field distributions calculated from averaged frequency shift traces

The $f_0(B)$ traces of Fig. 7.13 and Appendix C represent typical frequency shift traces, that is, they are not simply best case scenarios where the jumps are clearly visible. However, as T approaches T_c the signal to noise ratio becomes smaller than one and it is no longer possible to distinguish an individual phase slip from the noise. An example of two typical $f_0(B)$ traces taken at $T = 1052$ mK for CL12 are shown in Fig. 7.21. At this temperature, noise spikes are of comparable frequency shift to (if not greater than) the expected phase slip frequency shift, and thus an attempt to detect individual phase slips will be ruined by numerous false detections.

From the previous section, we know that a real phase slip event is well-fitted by a Tanh function whose width is approximately one or two data points. Further, over the extent of $P(B_{sw})$ (~ 500 mG) the expected resonant frequency shift due to a phase slip is virtually constant. Under these conditions, if multiple phase slips are averaged together the resulting curve represents $\int P(B_{sw})$, the cumulative distribution function for a phase slip to occur at B_{sw}. Following Eq. 2.108 we can convert this into a measurement of $P(B_{sw})$. This form

of averaging is particularly useful because while our signal is always a consistent step that occurs at a different field position, the thermal noise which leads to frequency fluctuations is a white force noise. Thus, upon averaging multiple $f_0(B)$ traces the signal will remain while the thermal noise will average to zero.

This effect is simulated in Fig. 7.22. In Fig. 7.22a we model a phase slip in the absence of noise as a jump between two data points (red), similar to what we find in our $\Delta f(B)$ data, and we determine the probability distribution (black) through numerical differentiation. In Fig. 7.22b we illustrate the same phase slip of Fig. 7.22a, but with the addition of gaussian distributed white noise with a standard deviation equal to that of the phase slip signal (that is, a signal to noise ratio of 1). In this situation, direct phase slip detection will rarely find the true phase slip which is located in the middle of the panel. In Fig. 7.22c we average together 3000 phase slips in the absence of noise (red curves of Fig. 7.22a) where the phase slip location is gaussian distributed as illustrated by the blue histogram. As expected, the probability distribution from numerical differentiation agrees with the distribution of phase slip locations. In Fig. 7.22d we average the same 3000 gaussian distributed phase slips with the addition of gaussian distributed noise on each individual trace. Though each individual trace is noisy, the average trace has a 50 times greater signal to noise ratio, and as a result, the probability distribution determined through numerical differentiation (black) agrees very well with the true underlying distribution (blue).

Before we can average all $f_0(B)$ traces for a single measurement, we must correct for the applied magnetic field drift due to the large solenoid. Initially, we used individual phase slips to determine this drift, but at higher temperatures this is no longer an option. As we stated in the previous section, the field drift represents a variation in the mean of $P(B_{\rm sw})$ over time and thus it is only necessary that we determine how this mean varies. To do that, we average together several ($\sim 2-20$) consecutive $f_0(B)$ traces.[17] This diminishes the thermal noise to a level where the cumulative probability distribution is clearly visible from the noise as shown in Fig. 7.23. We then fit this average curve to Eq. 7.4 and extract the phase slip location. Though this curve represents an average of several phase slips that

17. Near 850 mK we only need to average 2 traces to get a signal to noise ratio > 1. Close to $T_{\rm c}$ we need to average more traces as both the frequency shift signal decreases and the thermal noise increases.

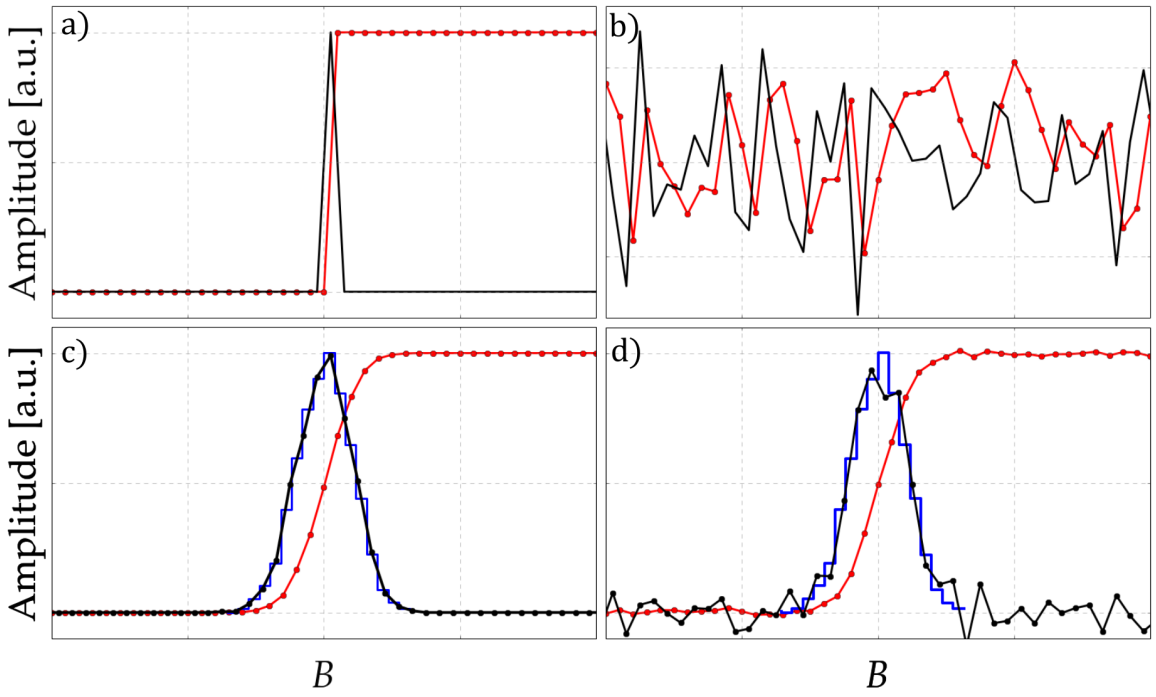

Figure 7.22: Red curves represent $\Delta f(B)$ traces where a phase slip is a jump between two data points. Black curves are the probability distribution determined through numerical differentiation of the red curve. a) Phase slip and probability distribution in the absence of noise. b) Phase slip with gaussian distributed white noise whose standard deviation is equal to the phase slip height and the corresponding probability distribution. c) Average of 3000 phase slips without noise with gaussian distributed phase slip locations given by the blue histogram. d) Average of 3000 phase slips with white noise given the same phase slip location distribution of panel c).

occur at different applied field locations, the location of $B_{\rm sw}$ extracted from the fit is a good estimate of the average phase slip location. Therefore, we can apply the same analysis and fit $B_{\rm sw}(N)$ from the average curves to a second order polynomial to determine the applied field drift. After correcting each ramp for this applied magnetic field drift we obtain the corrected field B' and then average together all $f_0(B')$ traces to obtain $\int P(B_{\rm sw})$. These traces are shown in Fig. 7.24 for CL12 at $T = 471$ mK.[18]

We calculate $P(B_{\rm sw})$ by taking a numerical derivative of the average $f_0(B)$ trace, $\frac{f_{0,i+1}-f_{0,i}}{B_{i+1}-B_i}$. The result is illustrated by the solid lines in Fig. 7.25 for CL12 at $T = 471$

18. For $\dot{B} > 0$, the average $f_0(B)$ trace is proportional to $1 - W(B_{\rm sw})$, and so its numerical derivative is $P(B_{\rm sw})$. For $\dot{B} < 0$, the average curve shown is not $1 - W(B_{\rm sw})$. However, given that the the applied field magnitude is decreasing and that phase slips lead to $\Delta f < 0$ for this ramp, calculating a numerical derivative from left to right still yields $P(B_{\rm sw})$.

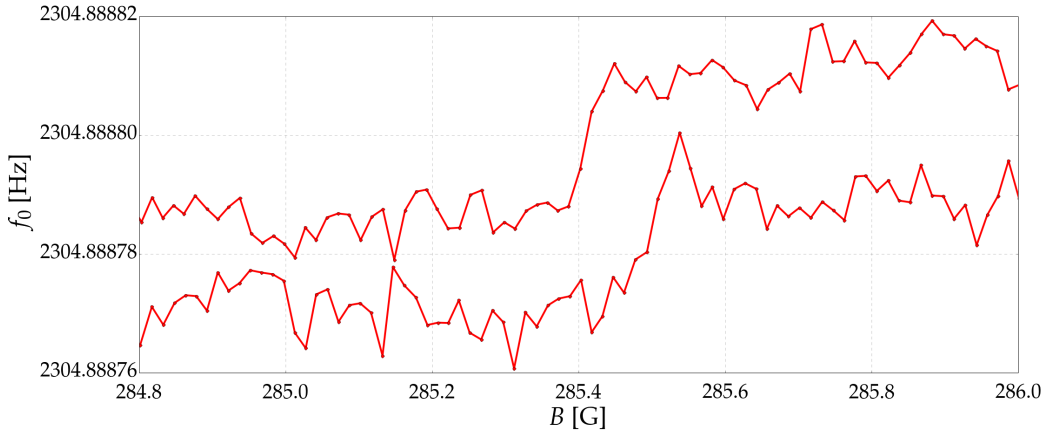

Figure 7.23: Average of 14 consecutive $f_0(B)$ traces for CL12 at $T = 1050$ mK for $\dot{B} > 0$. Two examples traces are shown with the top curve offset for clarity. Though it is difficult to distinguish a phase slips in the individual $f_0(B)$ traces (Fig. 7.21), the average curves shown here have an easily detectable step.

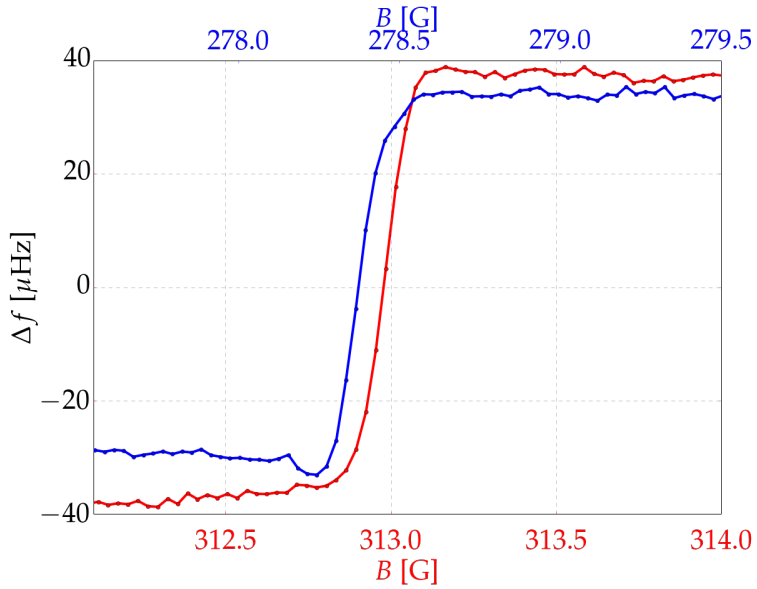

Figure 7.24: Average of all $f_0(B)$ traces for CL12 at $T = 471$ mK after field drift removal. We have removed the resonant frequency from the vertical scale. Red (blue) is for increasing (decreasing) B. As the frequency shift signal is proportional to B, Δf for the blue curve is expected to be $\sim 11\%$ smaller in magnitude with respect to the red curve, which agrees with this measurement. The numerical derivative (from left to right) of these curves is the unnormalized $P(B_{\mathrm{sw}})$.

mK. We have also included the histograms from the individual jump detection analysis of Section 7.3.1 for comparison. Within the $\sqrt{N}$ error bars, these two methods agree. Further, in the average $f_0(B)$ analysis we include every ramp. In the direct phase slip detection

method we only included data where the Tanh fit returned $R^2 > 0.55$.

We can use the two-sample Kolmogorov-Smirnov (KS) test to verify that these two methods are equivalent. For two empirically measured continuous cumulative distribution functions, $C_{1,N}(x)$ and $C_{2,M}(x)$ with N and M corresponding to the number of measurements in each distribution respectively, the KS statistic is defined as

$$D_{N,M} = \sup\left|C_{1,N}(x) - C_{2,M}(x)\right| \tag{7.14}$$

where sup( ) is the supremum function. That is, the statistic is only concerned about the largest vertical distance between $C_{1,N}(x)$ and $C_{2,M}(x)$. Under the KS test, the null hypothesis is that both samples are drawn from the same underlying distribution. This hypothesis is rejected if

$$D_{N,M} > \sqrt{0.5 \ln\left(\frac{\alpha}{2}\right)}\sqrt{\frac{N+M}{NM}} \tag{7.15}$$

where α is the significance level. We have illustrated this test for all measurements of CL12 with $\dot{B} > 0$ in Fig. 7.26. In every case, $D_{N,M}$ is smaller than the $\alpha = 0.05$ significance level, so there is no statistical significance between these analysis methods. Still, we should

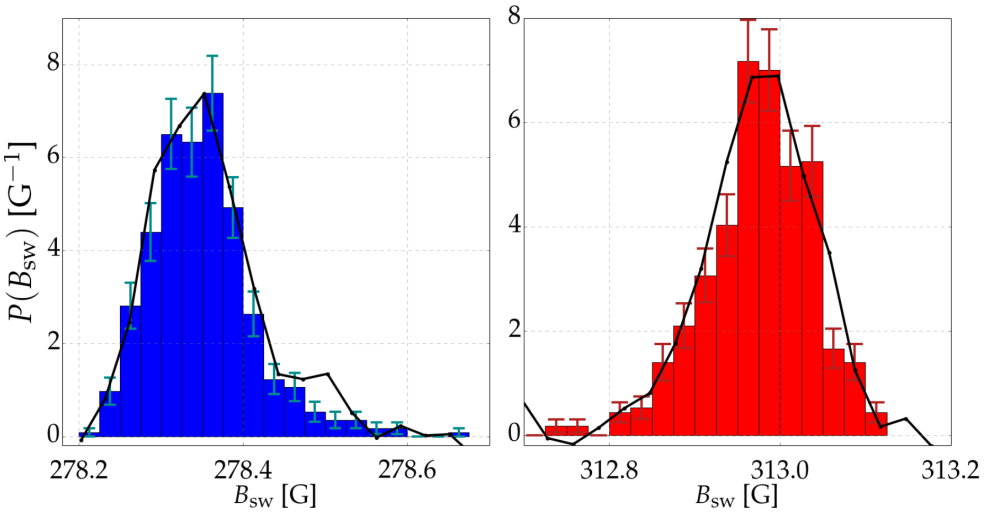

Figure 7.25: Normalized probability distribution for a phase slip to occur at $B = B_{sw}$ for CL12 at $T = 471$ mK. Red (blue) is for the transition $\psi_{n=12} \rightarrow \psi_{n=13}$ ($\psi_{n=13} \rightarrow \psi_{n=12}$). This histograms are determined by directly detecting phase slips with a Tanh fit, while the solid line is found by averaging together all $f_0(B)$ traces and taking a numerical derivative. The error bars on the histogram are $\sqrt{N}$ in magnitude.

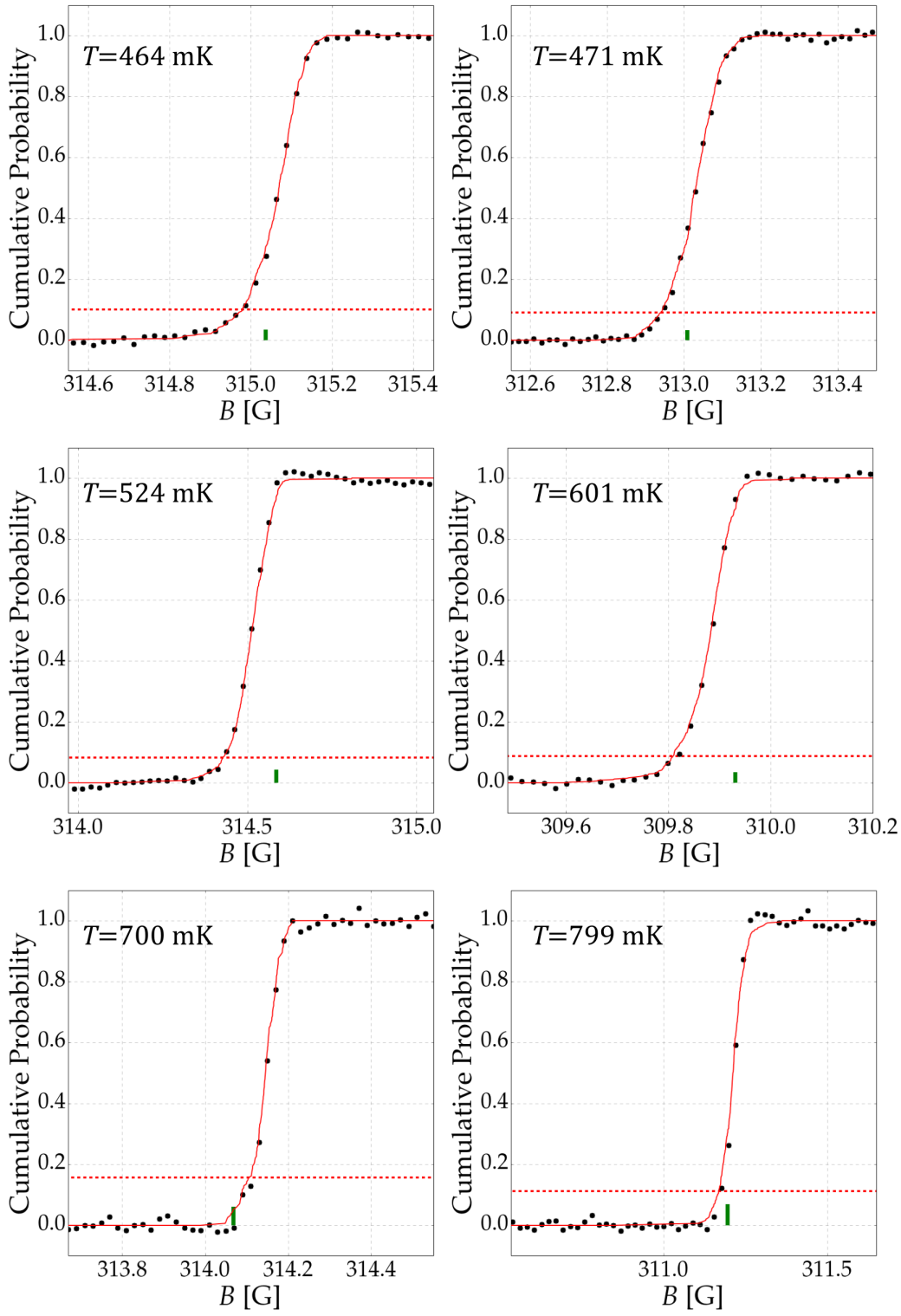

Figure 7.26: Cumulative distribution function for measurements made on CL12 with $\dot{B} > 0$. Red curves are determined by direct jump detection of individual jumps, while black curves are the averaged $f_0(B)$ traces. In each case a red dashed line corresponds to the level at which we reject the null hypothesis for $\alpha = 0.05$ and the green bar indicates the location and magnitude of $D_{N,M}$.

be cautious when interpreting this result. For the direct detection, to determine the cumulative distribution function we simply normalize the number of measurements by the total number of observations, which is unambiguous. However, for the average $f_0(B)$ curve we must normalize an averaged trace in the presence of noise. In this sense, we modify the vertical scale of the distribution function, and any error on this normalization leads to an error in $D_{N,M}$. Fortunately, with the large number of points we have before and after the jump and the relatively low frequency noise after averaging, we are able to determine this normalization within 3%. In all cases, this error would not change our conclusion.

7.3.2.1 Determination of $\langle B_{sw} \rangle$ and $\sigma_{B_{sw}}$ through fitting

When calculating $P(B_{\rm sw})$ through numerical differentiation, fluctuations in f_0 can lead to both negative values of $P(B_{\rm sw})$ and/or $P(B_{\rm sw}) > 0$ arbitrarily far from the mean of the distribution. Thus, calculating the moments directly from this distribution becomes problematic. A more appropriate method to determine $\langle B_{sw} \rangle$ and $\sigma_{B_{sw}}$ is to fit the $P(B_{\rm sw})$ curves and calculate the moments from this fit. Within the theory developed in Chapter 2, we expect an escape rate of the form[19]

$$\Gamma(B) = a \exp\left[- b \left(1 - \frac{B}{c} \right)^{5/2} \right] \tag{7.16}$$

For this escape rate, the probability distribution has an expression of the form

$$P(B) = a_1 \exp\left[- b \left(1 - \frac{B}{c} \right)^{5/2} + \frac{2}{5} a \left(c E_{\frac{3}{5}}(b) + (B - c) E_{\frac{3}{5}}\left(b \left(1 - \frac{B}{c} \right)^{5/2} \right) \right) \right] \tag{7.17}$$

where a, a_1, b, and c are fit parameters and $E_n(z) = \int_1^\infty e^{-zt}/t^n \ dt$ is the exponential integral function. These fits are shown for all measured temperatures of CL12 in Figs. 7.27, 7.28, 7.29, and 7.30, and for CL16 in Figs. 7.31, 7.32, and 7.33. After performing the fit to the numerical differentiation of $f_0(B)$, the data and fit curves are normalized by the same overall scale factor so that $\int P(B) = 1$, and thus, they are true probability densities.

19. This is from Eq. 2.109. We have ignored the B-dependence of the prefactor as we are only using these fits to capture the shape of the distributions, instead of extracting physical parameters. As we will show, there is a clear disagreement between our measured trend in $\sigma_{B_{SW}}$ and that predicted by Eq. 2.109 for a ring biased with flux.

For comparison we have also illustrated the integrated probability density for CL12 in Fig. 7.34 and for CL16 in Fig. 7.35. For measurements with $\dot{B} > 0$, $1 - W(B)$ is directly proportional to the average $f_0(B)$ trace; however for measurements with $\dot{B} < 0$, $W(B)$ is directly proportional to $f_0(B)$. We have also subtracted $\langle B_{\rm sw}(T)\rangle$ from each trace which makes it easy to observe a narrowing of the distribution width as temperature is increased. Though the critical temperature of these samples is ≈ 1200 mK at $B = 290$ G (Fig. 6.16), we were only able to take measurements up to $T = 1071$ and $T = 910$ mK for CL12 and CL16 respectively. This limitation was set by the low signal to noise ratio given the increased thermal noise and decreased frequency shift signal from a phase slip as the condensation energy is decreased. In particular the $T = 1073$ mK measurement with $\dot{B} > 0$ and $T = 910$ mK measurement with $\dot{B} < 0$ show deviations from $1 - W(B) = 1$ by more than 20%. Despite the difficulty of fitting full $f_0(B)$ traces for CL16, we were still able to obtain reliable measurements of $P(B_{\rm sw})$. This is because while the full field traces require us to measure over a 1800 G region, the phase slip statistics measurement is only concerned with a region that extends $\sim$2 G around the phase slip location. As a result, we gain nearly a factor of 1000 in averaging time when compared to a full field scan of the same duration, which should decrease the thermal noise by a factor of 30.

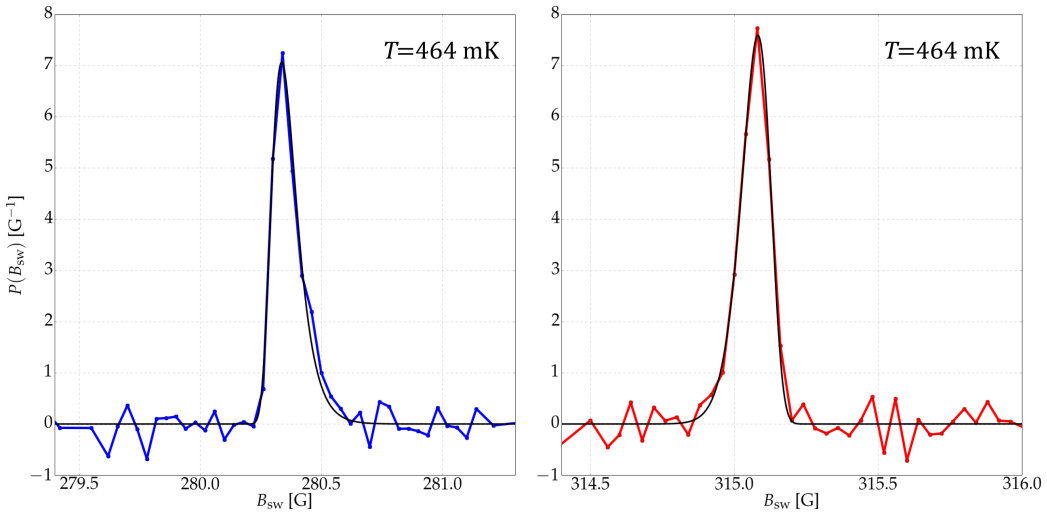

Figure 7.27: Normalized probability distribution for a phase slip to occur at $B = B_{\rm sw}$ for CL12 at $T = 464$ mK. Red (blue) is for the transition $\psi_{n=12} \rightarrow \psi_{n=13}$ ($\psi_{n=13} \rightarrow \psi_{n=12}$). Fits to Eq. 7.17 are shown in black with 4 fitting parameters: a_1, a, b, and c.

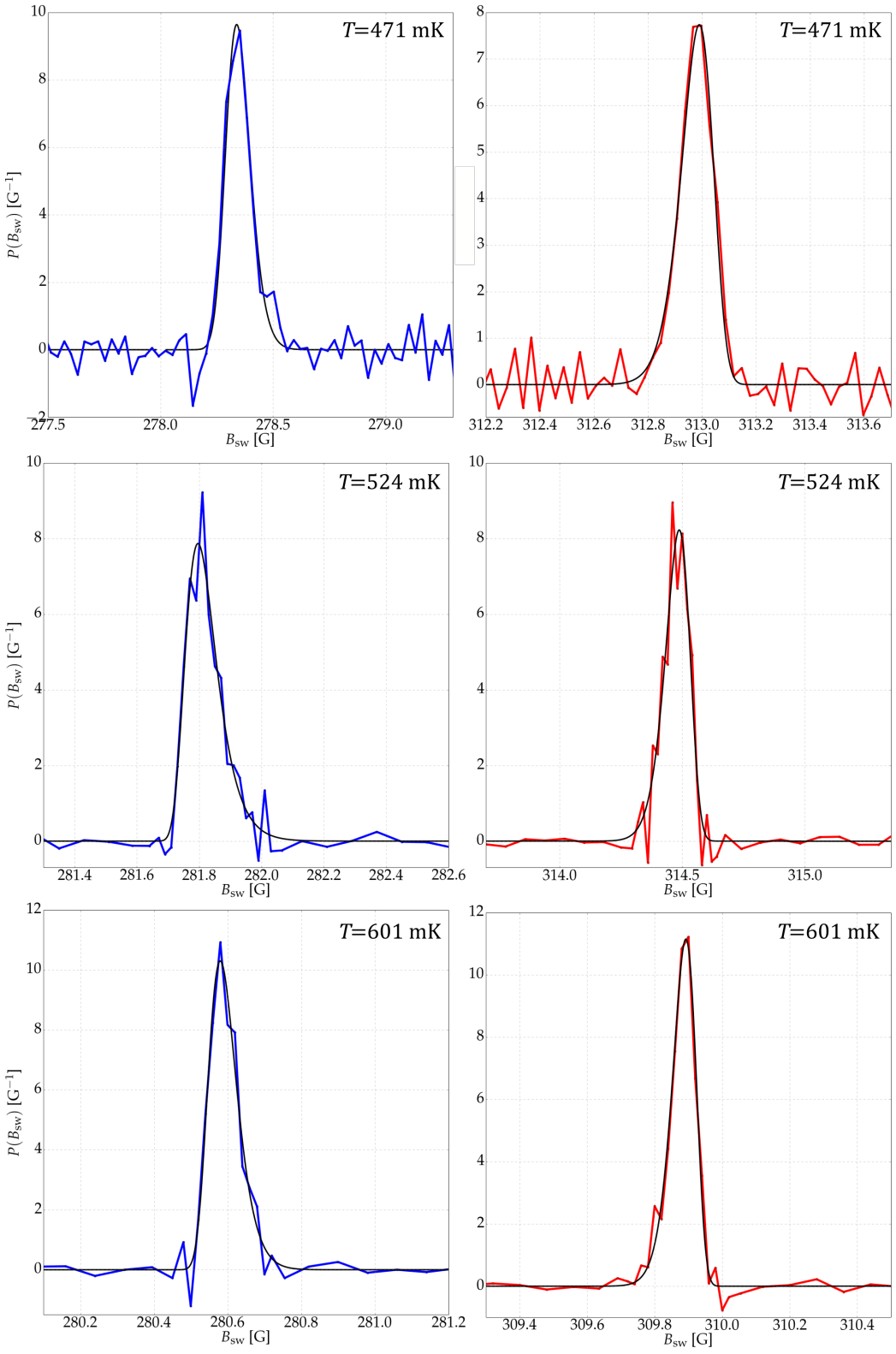

Figure 7.28: Normalized probability distribution for a phase slip to occur at $B = B_{\rm sw}$ for CL12 at various T. Red (blue) is for the transition $\psi_{n=12} \rightarrow \psi_{n=13}$ ($\psi_{n=13} \rightarrow \psi_{n=12}$). Fits to Eq. 7.17 are shown in black with 4 fitting parameters: a_1, a, b, and c.

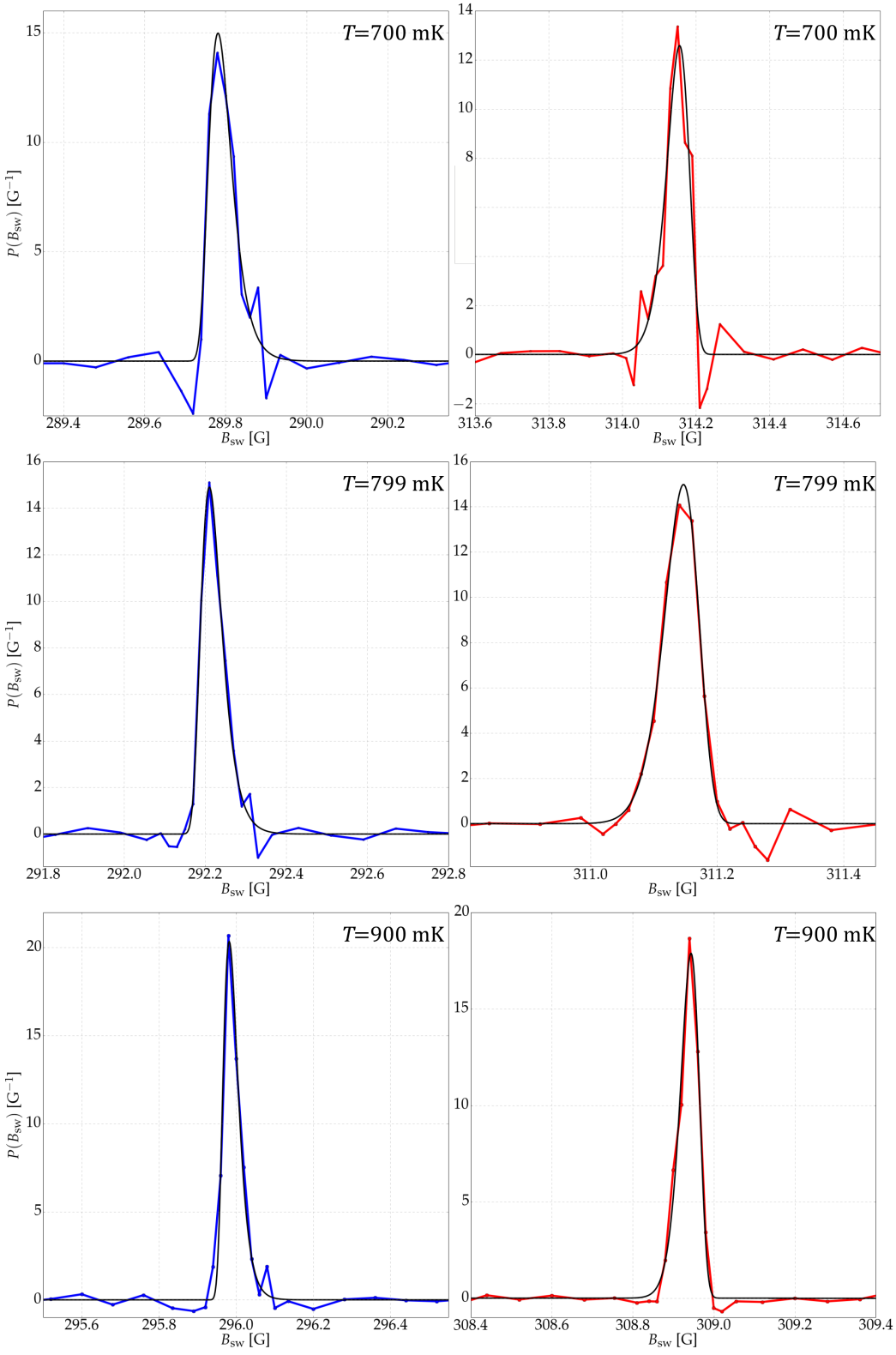

Figure 7.29: Normalized probability distribution for a phase slip to occur at $B = B_{\rm sw}$ for CL12 at various T. Red (blue) is for the transition $\psi_{n=12} \rightarrow \psi_{n=13}$ ($\psi_{n=13} \rightarrow \psi_{n=12}$). Fits to Eq. 7.17 are shown in black with 4 fitting parameters: a_1, a, b, and c.

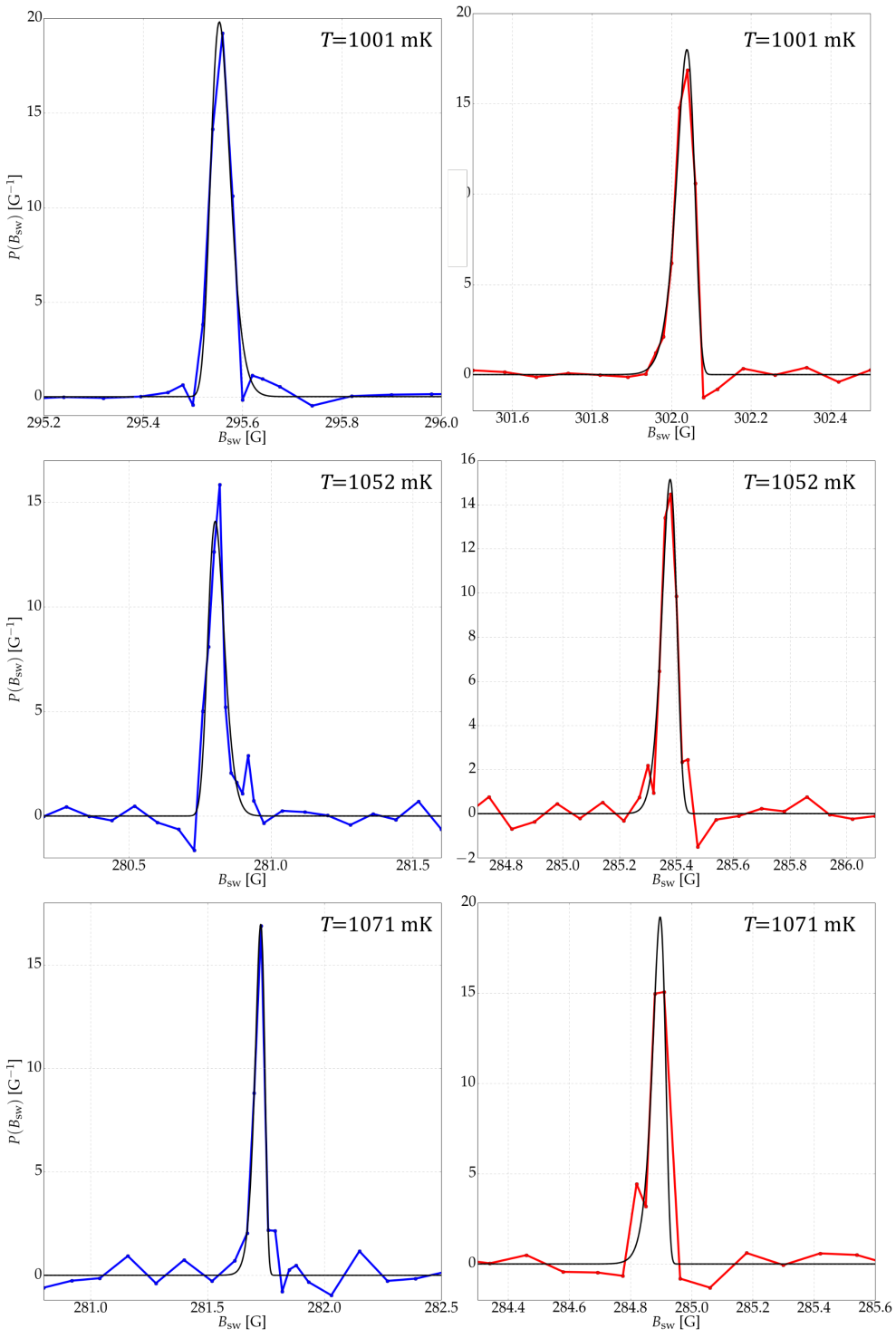

Figure 7.30: Normalized probability distribution for a phase slip to occur at $B = B_{\rm sw}$ for CL12 at various T. For $T = 1001$ mK red (blue) is for the transition $\psi_{n=12} \rightarrow \psi_{n=13}$ ($\psi_{n=13} \rightarrow \psi_{n=12}$). For $T = 1052$ and 1071 mK red (blue) is for the transition $\psi_{n=11} \rightarrow \psi_{n=12}$ ($\psi_{n=12} \rightarrow \psi_{n=11}$). Fits to Eq. 7.17 are shown in black with 4 fitting parameters: a_1, a, b, and c.

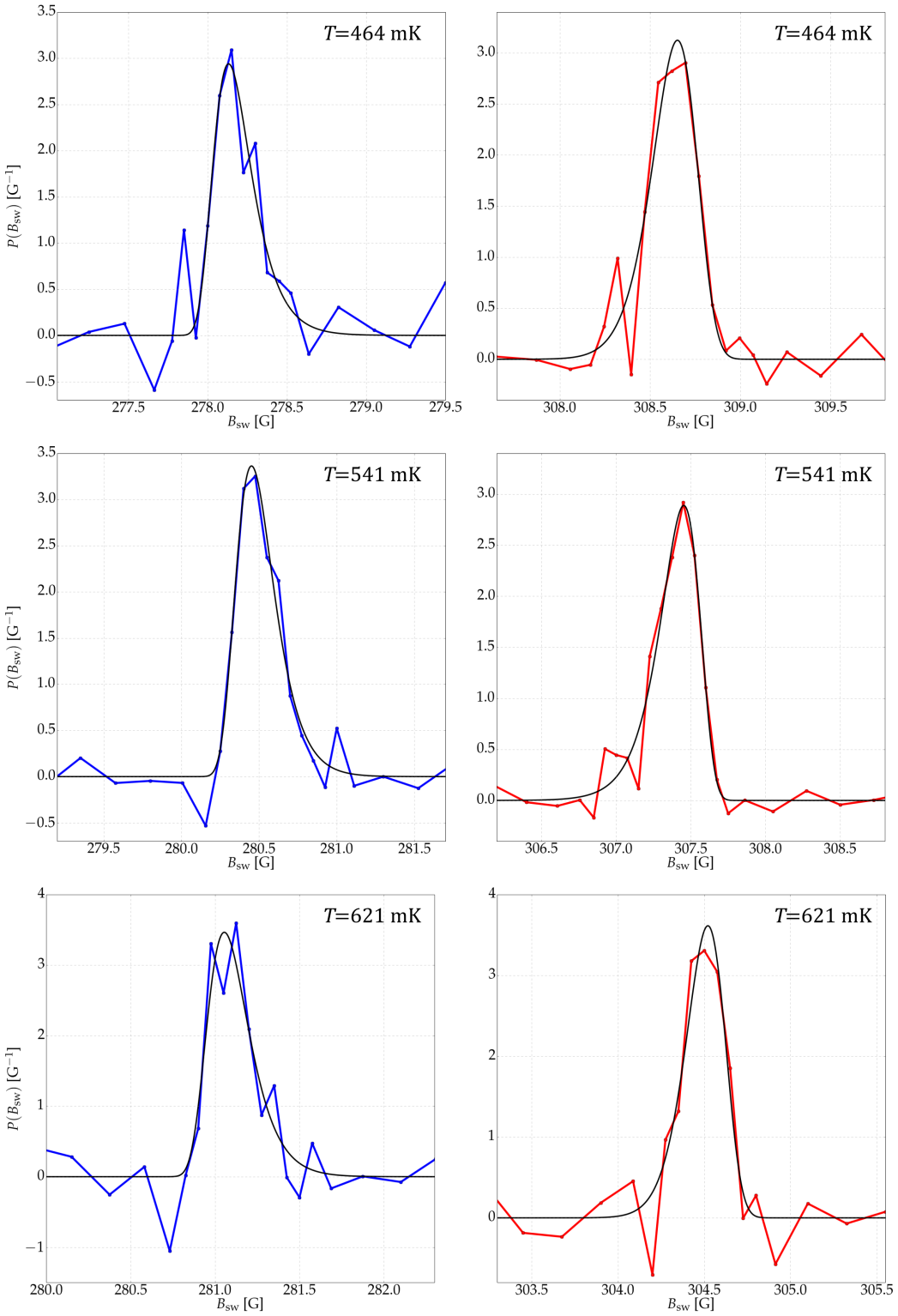

Figure 7.31: Normalized probability distribution for a phase slip to occur at $B = B_{\rm sw}$ for CL16 at various T. Red (blue) is for the transition $\psi_{n=3} \to \psi_{n=4}$ ($\psi_{n=4} \to \psi_{n=3}$). Fits to Eq. 7.17 are shown in black with 4 fitting parameters: a_1, a, b, and c.

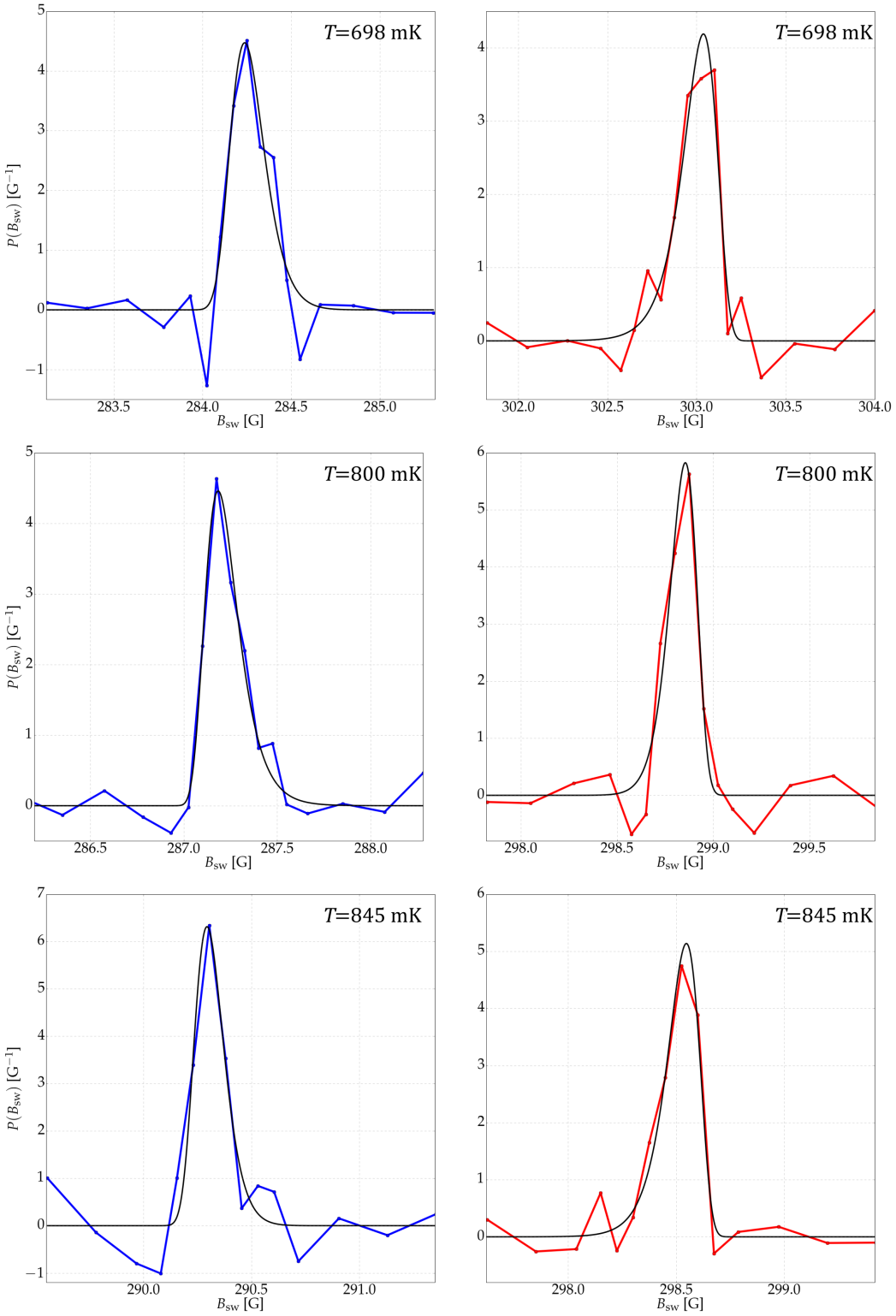

Figure 7.32: Normalized probability distribution for a phase slip to occur at $B = B_{\rm sw}$ for CL16 at various T. Red (blue) is for the transition $\psi_{n=3} \to \psi_{n=4}$ ($\psi_{n=4} \to \psi_{n=3}$). Fits to Eq. 7.17 are shown in black with 4 fitting parameters: a_1, a, b, and c.

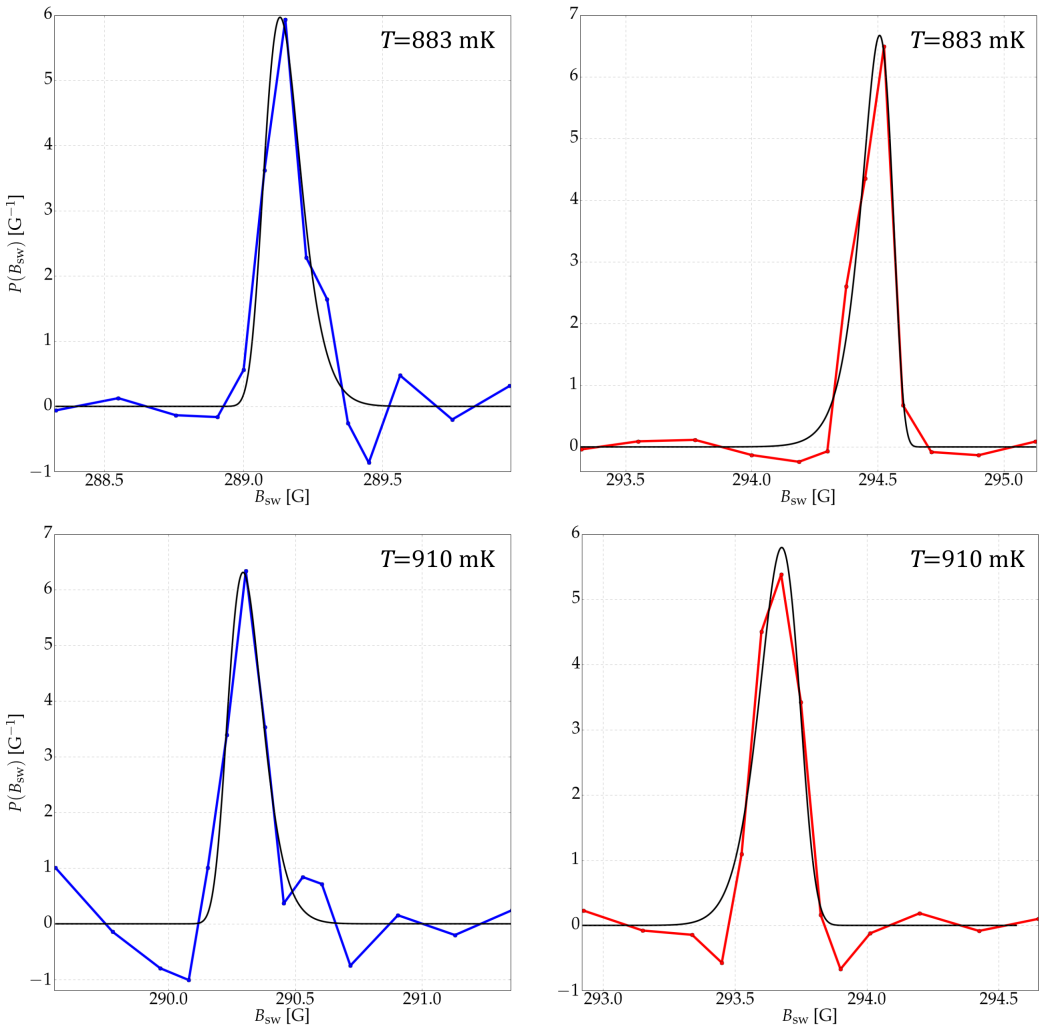

Figure 7.33: Normalized probability distribution for a phase slip to occur at $B = B_{sw}$ for CL16 at various T. Red (blue) is for the transition $\psi_{n=3} \rightarrow \psi_{n=4}$ ($\psi_{n=4} \rightarrow \psi_{n=3}$). Fits to Eq. 7.17 are shown in black with 4 fitting parameters: a_1, a, b, and c.

The mean and standard deviations calculated from the fits to measured $P(B_{sw})$ are illustrated in Fig. 7.36. As the mean of each distribution is susceptible to the systematic offset of the large solenoid, we have plotted the difference of the mean applied field between the increasing and decreasing winding number transition. The difference is expected to follow Eq. 7.3. For both samples, we observe that both the difference of the means and the standard deviation of $P(B_{sw})$ decreases with temperature. The fit extracted parameters for CL12 match that of the individual phase slip detection, which was expected given the level of agreement between the cumulative distribution functions for each method (Fig. 7.26). As we were able to perform the GL fits to the single ring data for CL12, we have shown

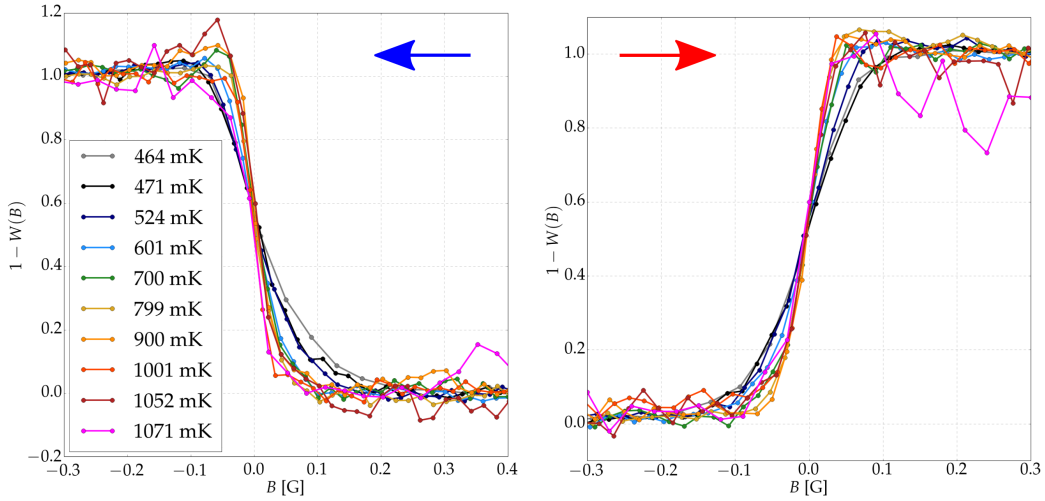

Figure 7.34: Integrated probability density $1 - W(B)$ for a phase slip to occur at applied magnetic field B for CL12. The mean phase slip field has been subtracted from each curve. The arrows indicate the direction of the applied field variation.

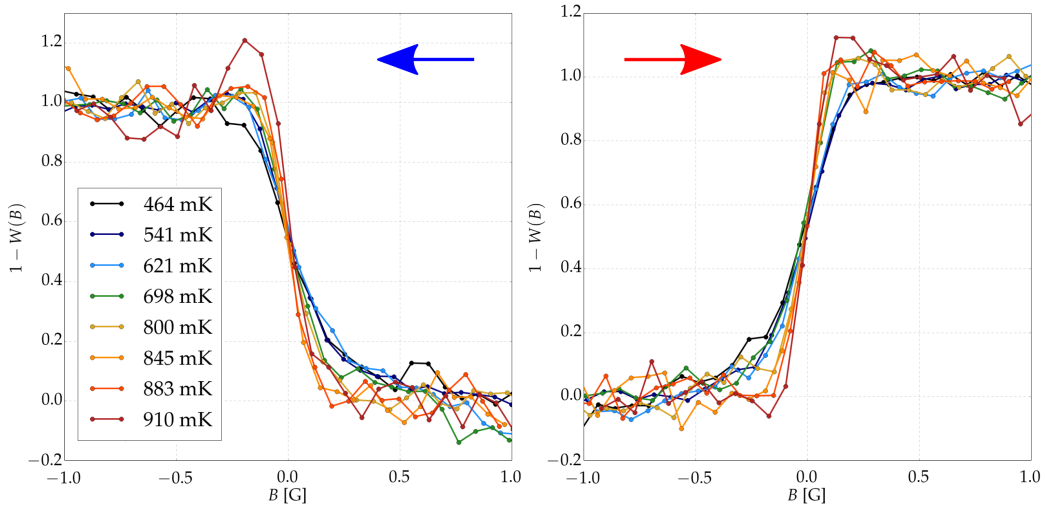

Figure 7.35: Integrated probability density $1 - W(B)$ for a phase slip to occur at applied magnetic field B for CL16. The mean phase slip field has been subtracted from each curve. The arrows indicate the direction of the applied field variation.

the theoretical expectation in green. For this, we used the escape rate given by Eq. 2.97, with the frequency $\frac{\omega}{2\pi}$ given by Eq. 2.103 as we know the switching occurs near the critical current, or equivalently the critical flux. In order to express the critical current in terms of the critical flux through Eq. 2.88 we needed to limit our argument to $n = 0$ and without considering the finite length correction so that Φ_c is given by Eq. 2.84. These theoretical distributions are shown in Fig. 7.37.

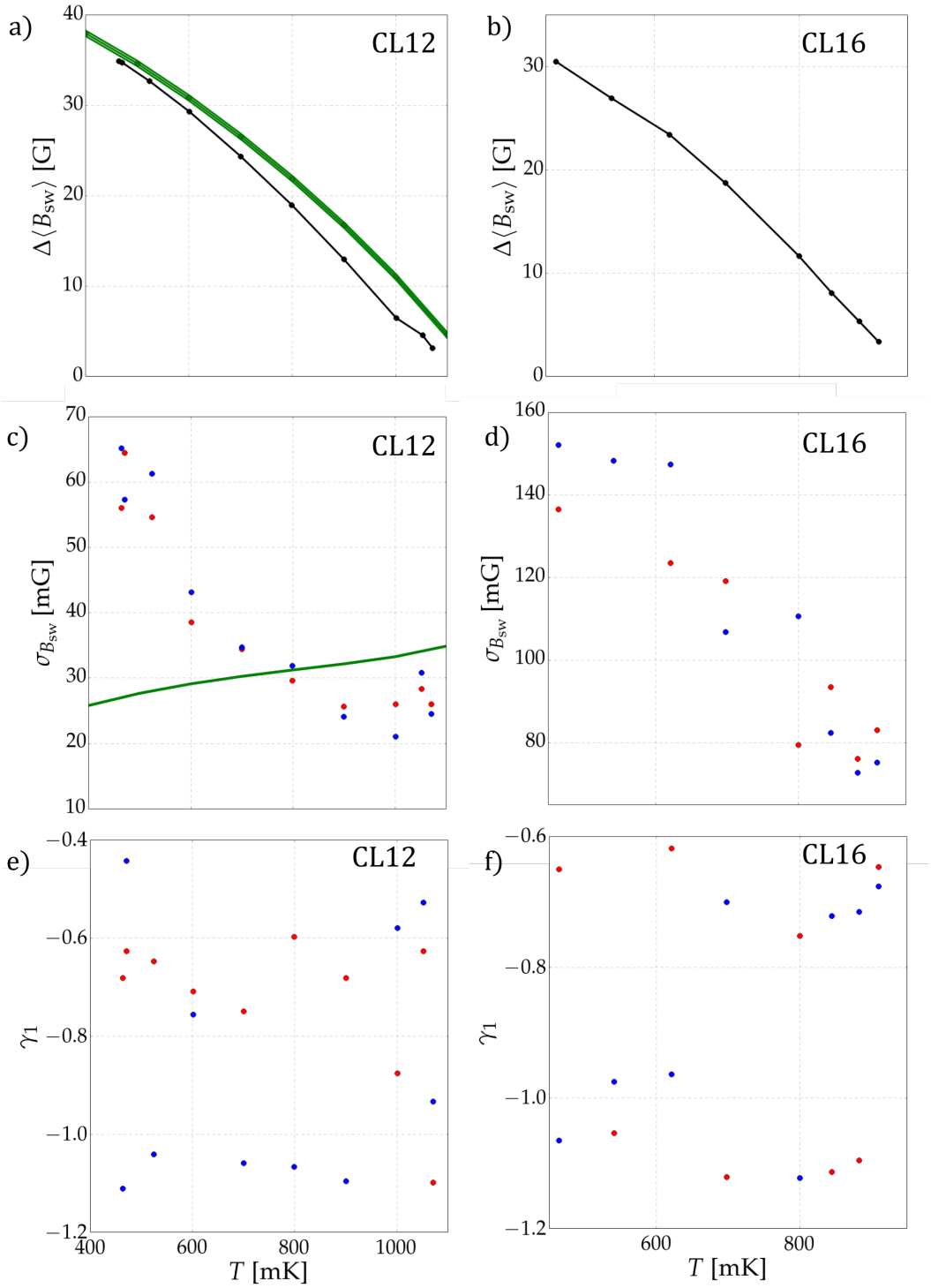

Figure 7.36: (Top row). Applied magnetic field distance between the mean of the two phase slips distributions for $\Delta n = 1$ and $\Delta n = -1$. (Middle row). Standard deviation of the measured $P(B_{sw})$ distributions. Red (blue) is for increasing (decreasing) B. For CL12, where we were able to perform GL fits, we illustrate the theoretical prediction in green. Error on the fit parameters leads to an error in $\Delta\langle B_{sw}\rangle$, though the error on $\sigma_{B_{sw}}$ is within the line thickness. (Bottom row) Skewness. Blue points ($\dot{B} < 0$) were multiplied by -1, so that the skewness is plotted with respect to a ramp that decreases the free energy barrier.

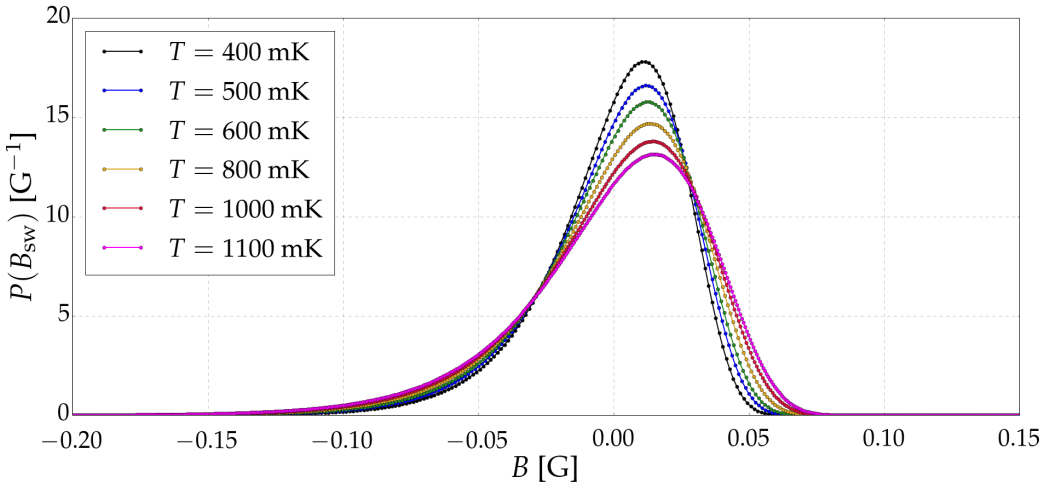

Figure 7.37: Calculated $P(B_{\rm sw})$ distributions for CL12 given the GL fit parameters. We have subtracted the means to illustrate the temperature dependence of the width. These distributions assume $n = 0$ and do not include the finite length correction.

For CL12 we notice that the two highest temperature data points are offset from the trend of the lowest temperature data in $\Delta\langle B_{\rm sw}\rangle$ (Fig. 7.36a). Given that these measurements required a large negative offset on the small coil (that is, from Fig. 7.30 the $T = 1052$ mK measurement occurs at $B = 285.4$ T, while the $T = 1001$ mK measurement occurs at $B = 302$ G), we suspect that the systematic offset of the large solenoid was large enough that for these measurements we were observing different transitions, $\psi_{n=11} \rightarrow \psi_{n=12}$ and $\psi_{n=12} \rightarrow \psi_{n=11}$. Given the n-dependence of Eq. 7.3, there should be a larger difference between the means, which is observed. The skewness is expected to be -1.139 for a general escape rate given by Eq. 2.109; however, as we did not use exactly this form, the skewness of the fits is not confined to this single value.[20] As illustrated in Fig. 7.36e for CL12 we find that the average value of skewness across all temperatures is $\gamma_1 = -0.72$ and $\gamma_1 = +0.86$ for the increasing and decreasing winding number phase slip respectively. For CL16 (Fig. 7.36f) we find $\gamma_1 = -0.88$ and $\gamma_1 = +0.87$ for the increasing and decreasing winding number phase

20. We assumed a constant overall frequency for our escape rate, while the Garg and Murphy *et al.* calculation requires the frequency to be of the form $A\left(1 - \frac{B}{B_c}\right)^{a+b-1}$. With this simplification, we were able to obtain an analytic expression for $P(B_{\rm sw})$

slip respectively.[21] The results for the skewness are consistent with what we found in the case of individual phase slip detection for CL12 (Fig. 7.19)

As we find the opposite trend in $\sigma_{B_{\rm sw}}(T)$ from that predicted by LAMH theory for thermally activated phase slips, we use the final few sections to explore the noise in our system and features of our measurement scheme which may impact $P(B_{\rm sw})$. Ultimately, we conclude that none of these mechanisms are responsible for the increase of $\sigma_{B_{\rm sw}}$ we observe with decreasing temperature.

7.3.3 $\Delta\langle B_{\rm sw}\rangle$ ramp rate dependence

All of the measurements of the previous section were taken with the same applied magnetic field ramp rate for a given sample ($\sim$13.5 mG/s for CL12 and $\sim$50 mG/s for CL16). In this section we will show the results of measurements of $P(B_{\rm sw})$ for CL12 at $T = 900$ mK where we varied $\dot{B}$. As we increase the applied magnetic field ramp rate the mean of the switching distribution should move closer to the critical field. This reflects the fact that when compared to a slower ramp, a faster ramp will need to see a higher escape rate to obtain the same probability for a phase slip to occur. As the escape rate depends exponentially on the applied magnetic field, the effect of ramp rate will only be logarithmic in $\dot{B}$.

For these measurements, we persisted the large magnet once and then took all measurements consecutively. Further as we are only concerned with the mean of the switching distribution, we took shorter measurements that only spanned a few hours. With this simplification, we no longer needed to worry about the drift of $B_{\rm sw}$ with time because it would only result in a few mG of drift over these short measurement times, while the expected change in $\Delta\langle B_{\rm sw}\rangle$ for $\dot{B}$ between 10-1000 mG/s is $\sim$200 mG. To increase the magnetic field ramp rate we simply increased the overall ramp frequency of the magnetic field ramp illustrated in Fig. 7.12. To obtain the same field resolution for a given measurement, we also increased the sampling rate on the HF2 proportionally. The average $\Delta f(B)$ traces of these

21. We plot $-\gamma_1$ for the decreasing winding number transition, so that both the increasing and decreasing winding number transitions have a skewness of -1. This reflects the fact that for the $\Delta n = -1$ transition a decreasing field ramp lowers the free energy barrier, so the distribution should be skewed toward higher fields (positive skewness).

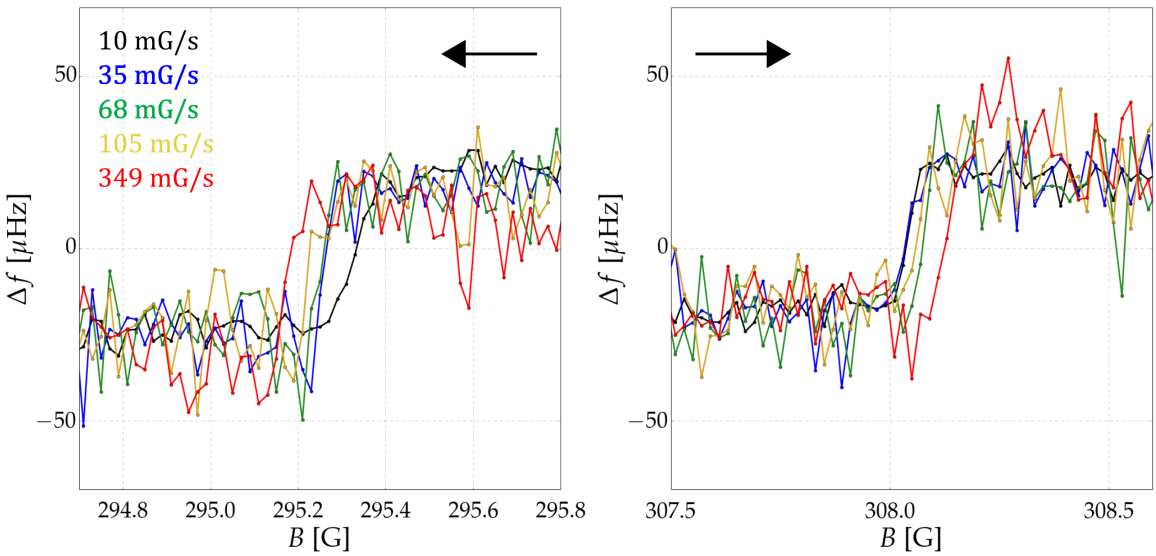

Figure 7.38: Cantilever resonant frequency shift Δf as a function of applied magnetic field for CL12 at $T = 900$ mK at various applied magnetic field ramp rates $\dot{B}$. The bare cantilever resonant frequency has been subtracted from each curve. The arrows indicate the direction of $\dot{B}$. As $|\dot{B}|$ is increased the transitions occur further apart, which is consistent with switching closer to the critical field.

measurements for CL12 at $T = 900$ mK are shown in Fig. 7.38. We have not removed any background other than subtracting the cantilever's resonant frequency from each curve.

We can see that as we increase $|\dot{B}|$, the separation between the $\Delta n = 1$ and $\Delta n = -1$ transition increases, which is consistent with switching closer to the critical field for increased ramp rates. Though the $\Delta f(B)$ curves show a clearly visible step, the probability distributions obtained from numerical differentiation are extremely noisy.[22] To determine the mean of the switching distribution we fit each average $\Delta f(B)$ to a Tanh function given by Eq. 7.4 with 4 fitting parameters: δf, a, $B_{\rm sw}$, and c. We then differentiate the fit to calculate $P(B_{\rm sw})$ (recalling that for $\dot{B} > 0$ $\Delta f(B) \propto 1 - W(B_{\rm sw})$ and for for $\dot{B} < 0$ $\Delta f(B) \propto W(B_{\rm sw})$) and determine the mean from $P(B_{\rm sw})$. In Fig. 7.39 we illustrate a Tanh fit to the average $\Delta f(B)$ curve for the increasing applied magnetic field ramp with $\dot{B} = 10.5$ mG/s and the resulting probability distribution in blue.

The results of all of these measurements are summarized in Fig. 7.40, where we plot

22. Looking at the average $\Delta f(B)$ traces, we can see that the point-to-point difference in $\Delta f(B)$ on the step region is roughly equal to the point-to-point difference far away from the transition, which makes it difficult to distinguish $P(B_{\rm sw})$ from the background noise level.

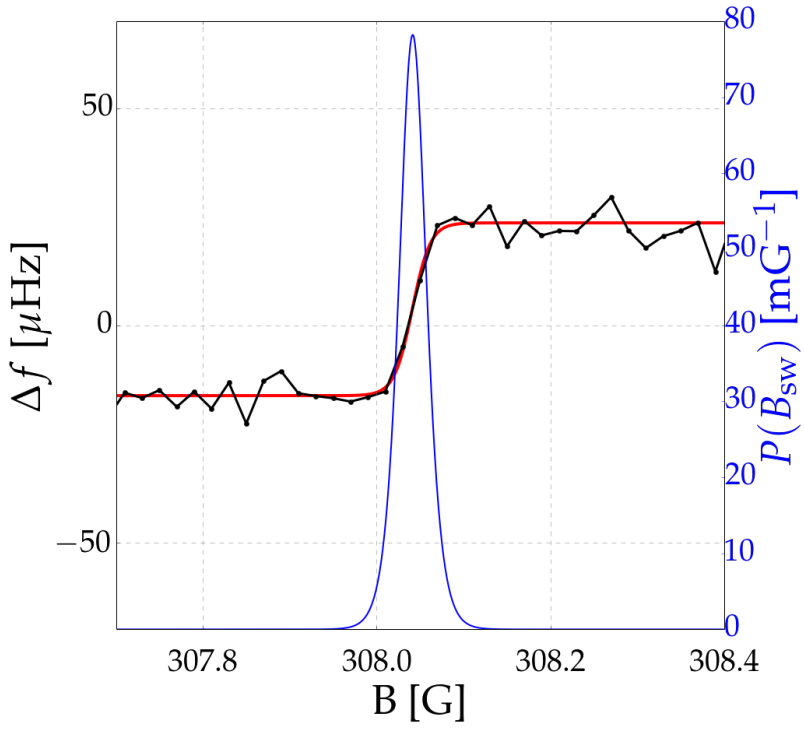

Figure 7.39: Cantilever resonant frequency shift Δf (black) as a function of applied magnetic field for CL12 at $T = 900$ mK with $\dot{B} = 10.5$ mG/s. The red curve indicates a Tanh fit to this trace and the blue curve is the phase slip probability distribution resulting from differentiation of the Tanh fit. From the blue curve, we determine the mean of the phase slip distribution.

the distance between the increasing and decreasing winding number transition $\Delta\langle B_{\rm sw}\rangle$ as a function of applied magnetic field ramp rate $\dot{B}$ as black data points. The solid red curve is the theoretical prediction given the GL fit parameters for CL12 and escape rate we used to create the theoretical predictions for Fig. 7.36.[23] The disparity between the vertical scale is expected as this is the same difference we found in Fig. 7.36a for the $T = 900$ mK measurement with $\dot{B} = 13.5$ mG/s. The dashed red line shifts the theory curve vertically to coincide with the measurement, and we can see that the expected variation in $\Delta\langle B_{\rm sw}\rangle$ with $\dot{B}$ agrees with the measurement.

23. "We used the escape rate given by Eq. 2.97, with the frequency $\frac{\omega}{2\pi}$ given by Eq. 2.103 as we know the switching occurs near the critical current, or equivalently the critical flux. In order to express the critical current in terms of the critical flux through Eq. 2.88 we needed to limit our argument to $n = 0$ and without considering the finite length correction so that $\Phi_{\rm c}$ is given by Eq. 2.84."

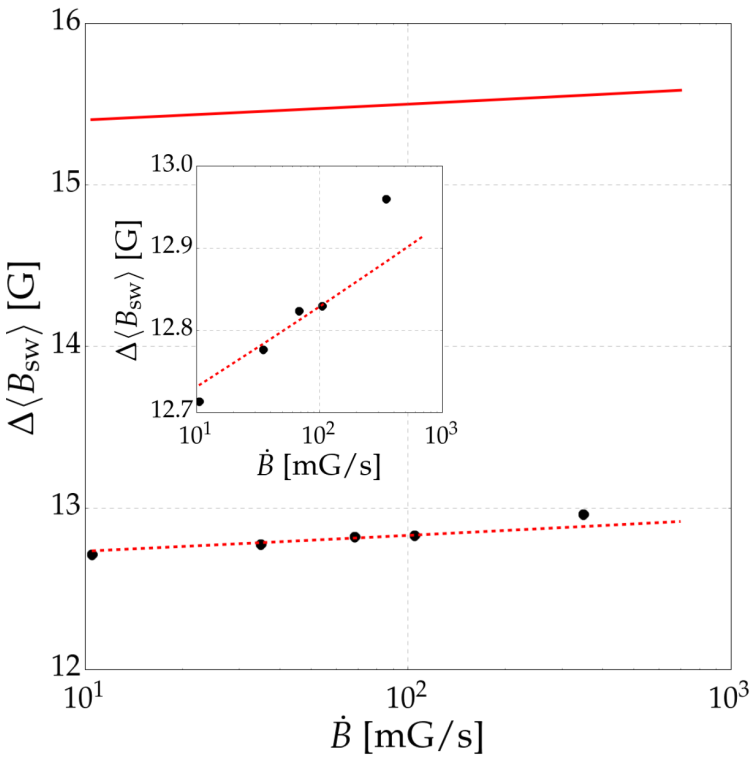

Figure 7.40: Applied magnetic field distance between the means of the $\psi_{n=12} \to \psi_{n=13}$ and $\psi_{n=13} \to \psi_{n=12}$ phase slip probability distributions for CL12 at $T = 900$ mK as a function of applied magnetic field ramp rate $\dot{B}$. The black points are data, while the solid red curve is the theoretical prediction. The dashed red curve is the theory curve shifted vertically, which illustrates that the scaling of $\Delta\langle B_{\rm sw}\rangle$ with $\dot{B}$ follows the theoretical prediction.

7.3.4 Applied magnetic field noise

In this section we will explore the noise on the small magnetic coil. To determine the magnetic field produced by the small coil we use

$$B = B_0 + \kappa \frac{V}{R} \tag{7.18}$$

where B_0 is the large solenoid offset, $\kappa = 550$ G/A is the small coil field to current ratio, and V is the voltage drop across the $R = 10.066\ \Omega$ resistor. Any noise in our record of V will lead to an error in B, so it is important to understand how large of an error on B we can expect given our experimental setup in Fig. 7.10.

We ensured that the increasing and decreasing applied magnetic field ramps had the same $|\dot{B}|$ so $|\frac{\Delta V}{\Delta t}|$ between adjacent measurement points will be directly proportional to the

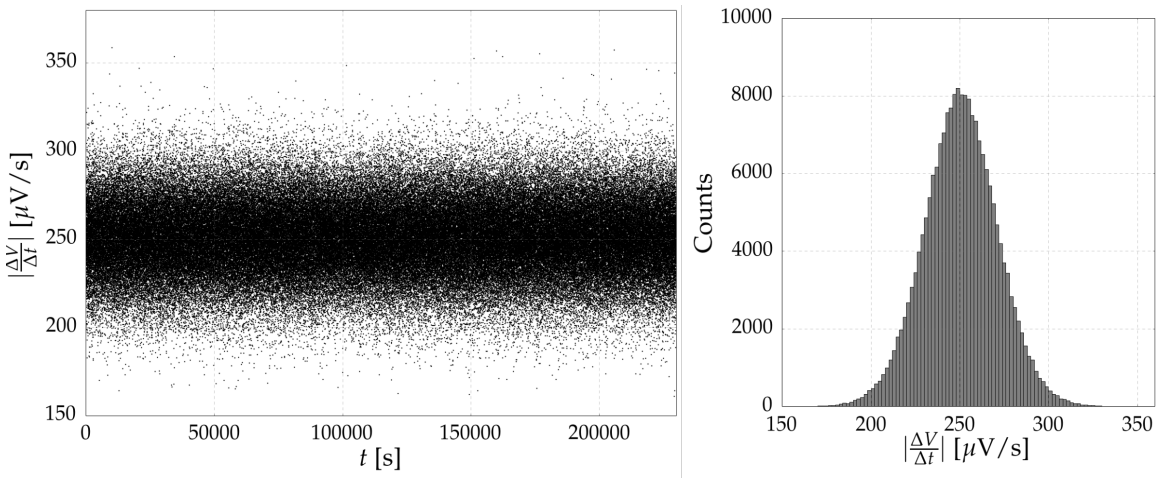

Figure 7.41: (Left panel) Absolute value of the difference in voltage drop across the 10 Ω resistor between adjacent measurement points divided by the measurement time between adjacent measurement points. This value is directly proportional to $|\dot{B}|$. The histogram of this data is shown in the right panel. Given the resistor specification for Johnson noise (0.01 μV_{RMS}/V of applied voltage), this noise is likely due to the voltage source, or input noise of the HF2 voltmeter.

magnitude of the applied magnetic field variation. We have shown this data for a measurement of CL12 taken at $T = 471$ mK in Fig. 7.41. Here we only included data for regions where we varied the applied magnetic field slowly around the phase slip region. The average voltage variation between measurements corresponds to an applied magnetic field variation $|\dot{B}| = 13.6$ mG/s. The distribution of voltage variation has a width that corresponds to $\sigma_{\dot{B}} = 1.12$ mG/s. Performing the analysis for the other measured temperatures of CL12 we find $\sigma_{\dot{B}} = 1.14$, 0.99, 1.40, 1.22, 1.14, and 1.08 mG/s for $T = 524$, 601, 700, 799, 900, 1052 mK respectively. From this, we conclude that applied magnetic field noise displays no major temperature dependence and is always on the order of 1 mG/s for CL12. As our measurements are separated by 1 second, this corresponds to a field error of 1 mG for CL12. Given that our distribution widths vary between 20-70 mG, this cannot be responsible for the trend we see, where the distribution width decreases with increased temperature.

7.3.5 Electron temperature

A possible explanation for our observed trend in the distribution width is that the superconducting electrons are at a different (higher) temperature than that of the sample

thermometer. And if for some reason the electron temperature decreased as we increased the stage and sample temperature, we would in fact find that $P(B_{\rm sw})$ becomes broader with increased electron temperature, which is in agreement with the LAMH theory.

When a phase slip occurs (near the critical current), a portion of the ring with volume $V = ws\xi(T)$ transitions to the normal state and and is heated by an amount of energy $\sim I_{\rm c}h/(2e)$. At lower temperatures, the coherence length is smaller and the supercurrent is larger (as the condensation energy is larger), thus a larger amount of heat is deposited into a smaller physical volume. The heat capacity and heat conductivity both decrease as temperature is decreased [4], so at lower temperatures each phase slip is more effective at heating the ring. If this heat due to a single phase slip was not dissipated before a subsequent phase slip, then these three effects make it plausible to suspect that at the lowest stage temperature, the superconducting electrons are actually the hottest.

When we measure $\Delta f(B)$ we directly measure the supercurrent in each ring, which is due to the superconducting electrons. For a ring of finite width, both the magnitude of the supercurrent (Eq. 2.47) and the applied magnetic field location of the phase slip (Eq. 2.94) depend upon $\xi(T)$. Because of this, a measurement of $\Delta f(B)$ can also serve as a useful thermometry measurement. From the measurements of $\Delta\langle B_{\rm sw}\rangle$ we can see that as the sample thermometer temperature increases, the average of $P(B_{\rm sw})$ occurs closer to $B_{{\rm min},n}$ (the magnetic field which minimizes the free energy $F_n(B)$). For the array measurements we proved that this is consistent with the finite-length stabilized switching flux given by Eq. 2.94. As the only temperature-dependent quantity in that expression is $\xi(T)$, this measurement is consistent with the coherence length increasing as the temperature of the sample thermometer increases, that is, the electron temperature increases as the sample thermometer temperature increases. Further, from the average $\Delta f(B)$ trace we can calculate $I(B)$ from Eq. 6.1 and we find that the magnitude of the current jump during a phase slip decreases as the sample thermometer temperature increases, as illustrated in Fig. 7.42. Again, this is consistent with the electron temperature increasing as the sample thermometer temperature increases.

7.3.6 Effect of cantilever oscillations on $P(B_{\mathrm{sw}})$

Though we apply a linear magnetic field ramp with a small coil to vary the magnetic field through the ring at a constant rate, the rings are attached to a cantilever which oscillates in the middle of a large solenoid. As a result, the true applied field normal to the ring is modulated by the cantilever's oscillation and is of the form

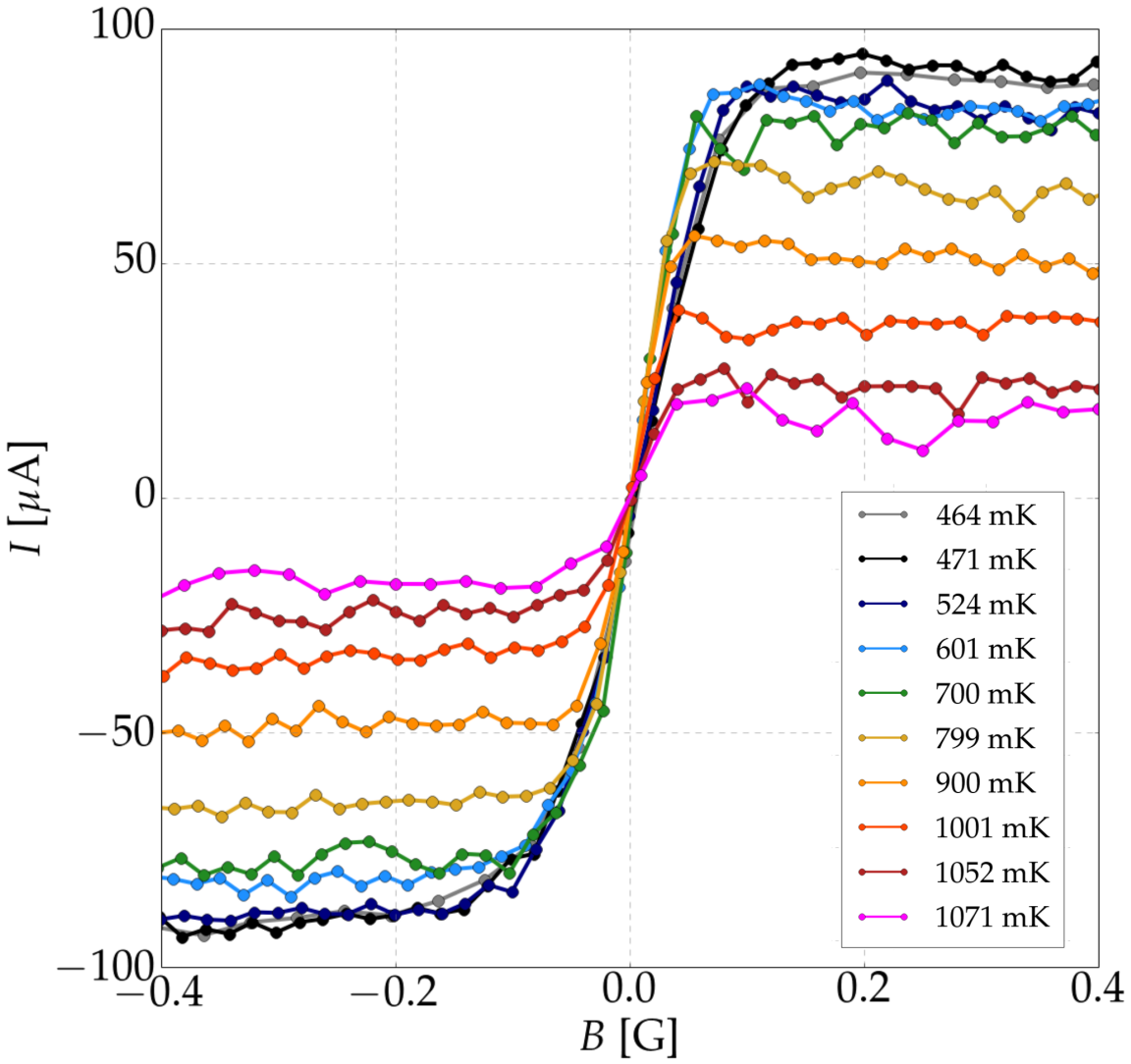

Figure 7.42: Supercurrent as a function of applied magnetic field B for all single ring measurements of CL12 with $\dot{B} > 0$. The average B_{sw} has been subtracted from each trace, and curves have been shifted vertically so they are centered around $I = 0$. As temperature (measured by the sample thermometer) is increased, the magnitude of of the current jump is diminished, indicating that the superconducting electrons are getting hotter.

$$B(t) = \dot{B}t + B_{\rm ac}\sin\Big(2\pi f_0 t + \theta_i\Big) \tag{7.19}$$

In this section, we will explore the effect of this full time dependence on the measured $P(B_{\rm sw})$ distributions.

The single ring phase slip measurements in this dissertation were taken at $B \approx 300$ G. During these measurements we drove the $\sim$470 μm long cantilevers so that they had 400$-$500 nm of tip displacement, so we will take 1 mrad as the maximal angular displacement. Given the orientation of Fig. 4.3 we can calculate amplitude of flux modulation by

$$\Phi_{\rm ac} = |BA - BA\cos\theta| \approx \frac{1}{2}\pi R^2 B\theta^2 \tag{7.20}$$

This corresponds to $2 \times 10^{-4}\Phi_0$ of flux modulation through the ring, which we can think of as an equivalent field modulation with magnitude $B_{\rm ac} = 150$ μG. Instead of working in terms of field, it is more intuitive to study the phase slip behavior as a function of time as each value of applied field is revisited many times given the ac modulation.

We will consider an escape rate of the form

$$\Gamma = \frac{\omega(t)}{2\pi}\exp\Big[-\frac{\delta F(t)}{k_B T}\Big] \tag{7.21}$$

where the frequency $\frac{\omega}{2\pi}$ is given by Eq. 2.104, and the free energy barrier δF is given by Eq. 2.80. The time dependence of these quantities is given through their relationship to $I(t)$ directly or $\Delta(t)$ (from Eq. 2.72 $\Delta(t)$ is related to the bias current divided by the critical current and thus has a time dependence through $I(t)$). As we bias the rings with flux instead of current, we must solve for the current in Eq. 2.47 with the applied flux $\Phi(t) = \pi R^2 B(t)$. Here we will restrict the argument to $n = 0$ and only concentrate on the time dependence, though the frequency and free energy barrier are still T-dependent. For the sake of this argument, we will consider $\dot{B} > 0$ to drive the transition $\psi_n \rightarrow \psi_{n+1}$. $I(t)$ and $\Delta(t)$ are illustrated in Fig. 7.43 for a purely linear applied field ramp. As flux is directly proportional to time, $I(t)$ has the same shape as $I(\Phi)$. For $\Delta(t)$, if we use Eq. 2.81 and Eq. 2.88 to express all terms near the critical current, we find $\Delta(\Phi) \approx 2(1 - \frac{\Phi}{\Phi_{\rm c}})$. Thus,

the linear decrease in $\Delta(t)$ for $\Delta \to 0$ is expected.

The probability distribution is calculated by first calculating the cumulative distribution function for a phase slip to occur at $t = t_{\rm sw}$ through numerical integration and then taking the numerical derivative as described in Section 2.4.2. That is,

$$P(t_{\rm sw}) = \frac{d}{dt}\left(1 - \exp\Big(-\int_0^t \Gamma(t')dt'\Big)\right) \tag{7.22}$$

We have used all of the experimentally relevant parameters determined from the GL fits to CL12 (Table 7.1) to determine δF and $\frac{\omega}{2\pi}$. We assume a linear field ramp of $\dot{B} = 13.4$ mG/s to match our measurements. For the modulation frequency we limit the analysis to 100 Hz. As we will show in Fig. 7.46, the effect of increased frequency is to increase the number of oscillations of $P(t_{\rm sw})$, so limiting the analysis to 100 Hz allows us to determine

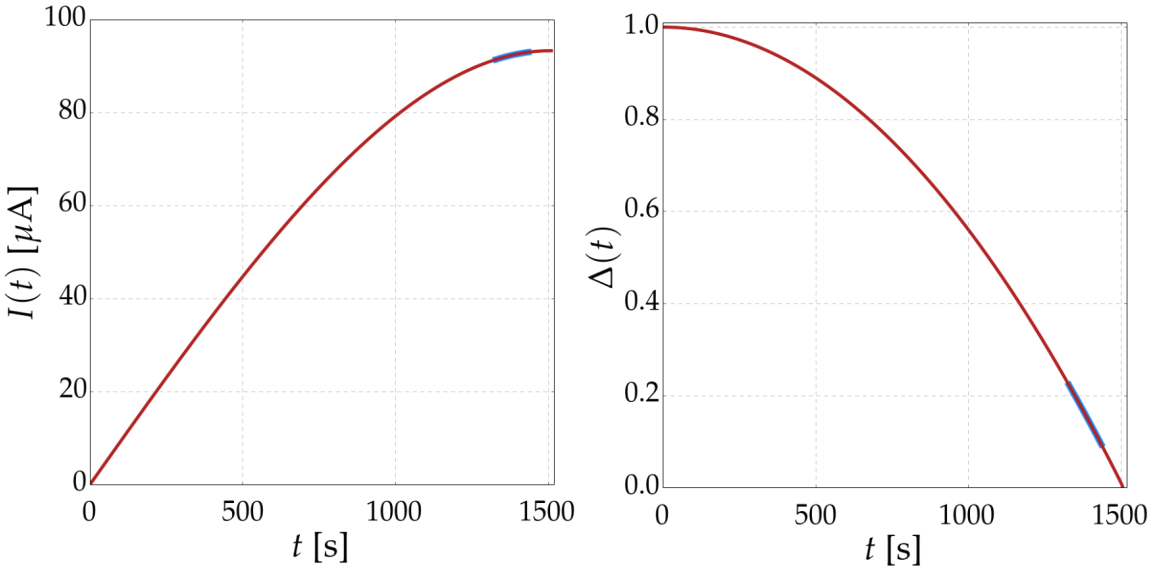

Figure 7.43: Current $I(t)$ and $\Delta(t)$ for a single ring with the parameters of CL12 at $T = 900$ mK. Here we have assumed a linear applied field ramp $B(t) = \dot{B}t$ with $\dot{B} = 13.4$ mG/s, which matches the experiments in this text. In blue we have indicated the region in which $P(t_{\rm sw})$ has an appreciable probability. As this occurs close to $I_{\rm c}$ we can use the approximation for Δ given by Eq. 2.81.

the impact of ac modulation, while keeping the calculating tractable.[24]

For a purely linear applied magnetic field ramp, at some field $B^*, \Gamma(B^*)$ becomes large enough that switching is appreciably probable given the measurement time $\tau_{\rm meas}$ ($\tau_{\rm meas}$ is the measurement time we require to sweep through the underlying probability distribution). For $B < B^*$, switching is extremely improbable given the exponential escape rate. The inclusion of ac modulation does not change this fact, but instead ensures that for portions of the applied magnetic field ramp the ring sees enhanced phase slip probability, and for other portions the ring sees decreased phase slip probability. In the case of large $B_{\rm ac}$ ($B_{\rm ac} \gg \tau_{\rm meas}\dot{B}$) and high frequency ($f_0 \gg 1/\tau_{\rm meas}$), the system will revisit fields at which $\Gamma(B) < \Gamma(B^*)$ many times while sweeping through the entire probability distribution. In these regions, it becomes extremely improbable for a phase slip to occur, compared to earlier times where the escape rate was enhanced due to the ac modulation, and thus $P(t_{\rm sw}) \to 0$.

Given that switching will only be appreciable when $B(t) \geq B^*$ and that $f_0 \gg 1/\tau_{\rm meas}$, this will first occur near a peak of the ac modulation. At this point, the maximum amplitude of the applied field ramp can only increase at a rate given by $\dot{B}$, and thus, even with the inclusion of large ac modulation, the width of $P(t_{\rm sw})$ is largely unaffected.[25] This is illustrated in by the black curve in Fig. 7.44, where the ac oscillation period (0.1 s) is much faster than the $\sim$ 15 seconds it takes to sweep through the probability distribution, thus we observe many oscillations in $P(B_{\rm sw})$. As we modeled $B(t)$ with $\dot{B} = 13.4$ mG/s and $B_{\rm ac} = 150$ mG the ac modulation is large enough for the ring to revisit applied magnetic fields at which escape is very improbable many times during the measurement. From the inset we can see the peaks of the ac modulation are where the phase slip probability is the largest, and near troughs of the ac modulation the probability is essentially zero, given the escape rates exponential dependence on $B(t)$.

24. With a 2 kHz cantilever frequency and magnetic field variation rate that takes 20 seconds to span the probability distribution, we would need to use time resolution of at most 200 μs to properly model the system. Given that this calculation depends upon the exponent of a numerical integral, which is then numerically differentiated, for small time resolution the numerical precision needs to be large ($>$ 100 digits) to obtain a smooth result (one where the derivative isn't dominated by numerical imprecision). The 100 Hz simulation took over 6 hours to run, and given that the effect of increasing the frequency from the inset of Fig. 7.46 is clear, we did not simulate 2 kHz.

25. We find there is a $\sim$ 2% difference in the width due to the fact that the overall ramp rate of the ac modulated $B(t)$ is not equivalent to that of the purely linear ramp at every point.

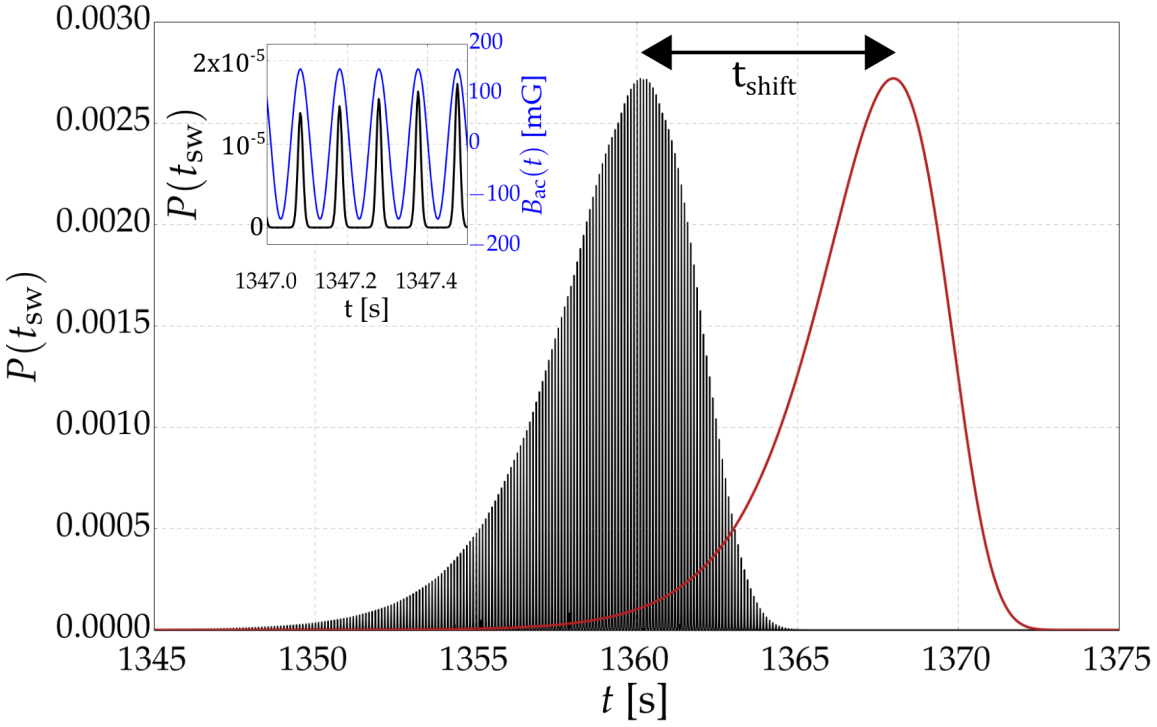

Figure 7.44: $P(t_{sw})$, the probability for a phase slip to occur at time t_{sw}. The black histogram corresponds to a 10 Hz ac modulated $B(t)$ with $\dot{B} = 13.4$ mG/s and $B_{ac} = 150$ mG. The red curve is for a purely linear ramp with the same $\dot{B}$. The parameters used for the escape rate are those of CL12 at $T = 900$ mK. The blue curve represents the ac part of the magnetic field variation. The inset illustrates that the peaks of the ac modulated magnetic field are where $P(t_{sw})$ begins to increase from 0.

Though large ac modulation does not impact the width considerably, it does impact the mean of the distribution. As only the positive peaks of the modulated field play a role in phase slips, the ac modulation can be seen as adding an RMS magnetic field of magnitude $B_{ac}/\sqrt{2}$ to the linear ramp. That is, a ring subject to a large ac modulated $B(t)$ will see larger fields at considerably earlier times when compared to a purely linear ramp. This shifts the ac modulated histogram to earlier times compared to the purely linear ramp, with the time shift given by $t_{shift} = B_{ac}/(\sqrt{2}\dot{B})$. The red curve of of Fig. 7.44 represents a probability distribution assuming a purely linear ramp and we find that to within 3%, $t_{shift} = B_{ac}/(\sqrt{2}\dot{B})$ gives the required time shift to make the mean of the red and black curves equal.

For the case of moderate to small B_{ac} ($B_{ac} \approx \tau_{meas}\dot{B}$) and high frequency, the ac modulation is small enough that the ring will only revisit $B < B^*$ during the first few

oscillations. As a result, $P(t_{\rm sw})$ will not revisit zero on each successive minimum. Instead, the oscillation will simply lead to periods when the ring sees a slightly higher or lower applied magnetic field compared to the linear ramp. This higher magnetic field leads to a lower free energy barrier, which enhances the probability for escape. Conversely, when $\sin\left(2\pi f_0 t+\theta_i\right) < 0$, the ring sees a lower magnetic field and thus a higher free energy barrier and so $P(t_{\rm sw})$ will decrease compared with $P(t_{\rm sw})$ for the purely linear ramp. Ultimately, this will appear as a small oscillation on top of a typical LAMH $P(B_{\rm sw})$ distribution. This

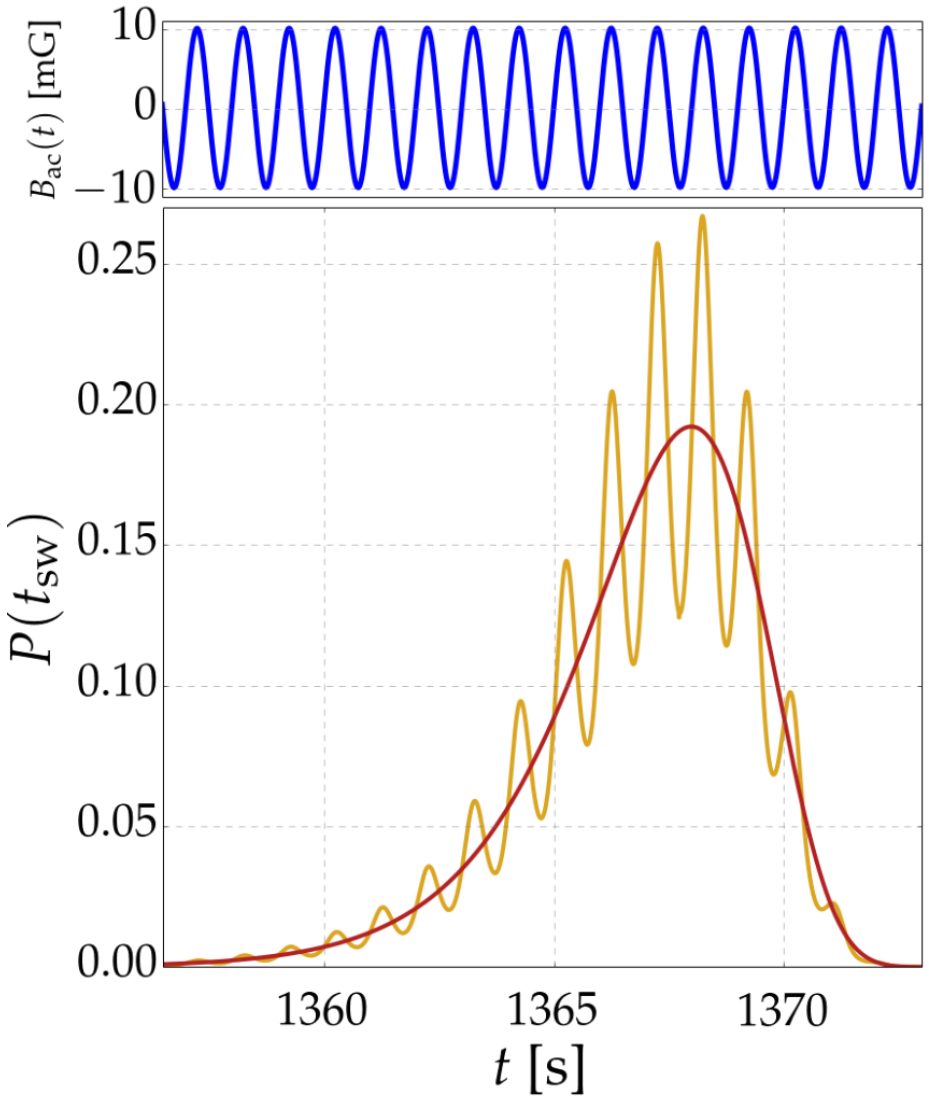

Figure 7.45: $P(t_{\rm sw})$, the normalized probability for a phase slip to occur at time $t_{\rm sw}$ for a single ring with the parameters of CL12. The red curve corresponds to a purely linear applied magnetic field ramp with $\dot{B} = 13.4$ mG/s. The gold curve has $B_{\rm ac} = 10$ mG. The ac oscillation of $B(t)$ is shown in blue as a reference.

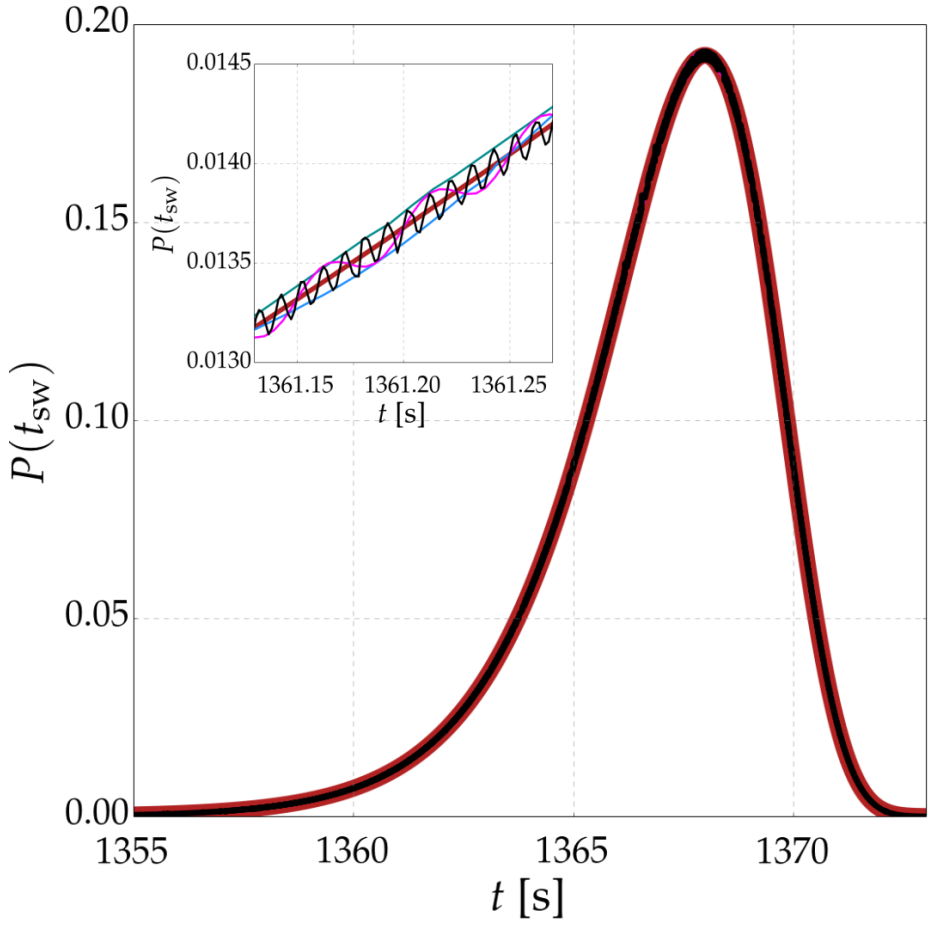

Figure 7.46: $P(t_{sw})$, the normalized probability for a phase slip to occur at time t_{sw} for a single ring with the parameters of CL12 and the expected ac modulation of our experimental setup. The red curve corresponds to a purely linear applied magnetic field ramp with $\dot{B} = 13.4$ mG/s. The black curve correspond to a 100 Hz ac modulated signal with $B_{ac} = 150$ μG. The inset makes the oscillations visible. We have also included a 10 Hz (magenta), 2 Hz (blue) and 1 Hz (green) simulation.

is shown in Fig. 7.45.

As this effect represents an extremely small oscillation on top of the probability distribution, we conclude that it does not impact our measurement of the switching distribution. Further, we would never be able to measure such an oscillation in this experiment. For the measurements reported in this text, we measure the cantilever resonant frequency as an average over 1 second. Thus, we would average over approximately 2000 oscillations in $P(t_{sw})$, and given that the ac modulated $P(t_{sw})$ oscillates with the center given by $P(t_{sw})$ of the purely linear ramp, we should recover the result of the purely linear ramp.

For our experimental parameters ($f_0 \approx 2$ kHz, $\tau_{\rm meas} \approx 20$ s, $B_{\rm ac} = 150$ μG and $\dot{B} = 13.4$ mG), we are safely within the high frequency and small $B_{\rm ac}$ regime. Qualitatively the small $B_{\rm ac}$ is similar to the moderate $B_{\rm ac}$ regime. The only difference is the oscillation on top of $P(t_{\rm sw})$ is extremely small in the small $B_{\rm ac}$ regime. We have illustrated this effect in Fig. 7.46. Here we have used the real experimental parameters, however we only simulated the effect up to $f_0 = 100$ Hz. From the inset we can see that the effect of increased f_0 is only to increase the oscillation frequency on $P(t_{\rm sw})$. The amplitude of modulation remains the same, given the agreement between the amplitude of all oscillatory curves in the inset.

7.3.7 Outlook

Though we have ruled out a few of the most apparent reasons for why the $P(B_{\rm sw})$ histograms could narrow with increased temperature, it is possible that LAMH theory for phase slips in a uniform wire with periodic boundary conditions is not perfectly relevant to the uniform flux-biased rings of these experiments. Given that the expected distribution width, given by Eq. 2.112 and illustrated in Fig. 7.36c, only weakly increases with temperature over the temperature range relevant to these experiments, it is possible that a small correction could reverse this trend. That is, since the width scales as $T^{2/5}\Big(1 - T/T_{\rm c}\Big)^{-1/10}$ it only requires a multiplicative correction on the order of $\Big(1 - T/T_{\rm c}\Big)$ to completely reverse the temperature dependence and obtain histograms that clearly narrow with increased temperature over the temperature range of these experiments..

One thing that may be missing from this discussion is that for a uniform ring the phase slip can occur at any point along the ring. Along the circumference of the ring, there are $L/\xi(T)$ statistically independent regions which can become normal [33], and this is exactly why the escape rate prefactor (Eq. 2.98) has such a term. Though δF already includes the term $\frac{\alpha^2}{2\beta}\sigma\xi(T)$, which takes into account the condensation energy required for a volume of the ring to transition to the normal state, the escape rate exponent does not seem to acknowledge that this section can occur at any point around the ring. At lower temperatures, where $\xi(T)$ is smaller, there are multiple independent regions which may become normal. But at the highest temperatures close to $T_{\rm c}$, where $\xi(T) \approx L/2$, then nearly the entire ring becomes normal and there is only a single path for a phase slip to

occur. Throughout this dissertation I have typically made the analogy to a ball escaping from a 1-dimensional hill, but really the more apt analogy is a ball escaping from a caldera of a volcano.

It is also worth noting that while the rings studied in these experiments are nearly uniform (to within 1% of R), we know that small lithographic imperfections (evinced by Fig. 6.22) ruin perfect homogeneity. At low temperatures, this could cause phase slips to preferentially occur in a particular region of the ring where the condensation energy is the lowest due to lithographic imperfections that decrease the width in a section of the ring. At higher temperatures, these inhomogeneities would become smeared out as $\xi(T)$ becomes approximately 700 nm and small variations on the nm-scale become less important. Thus, though there are more statistically independent regions where a phase slip can occur at lower temperatures, it may be that at the lowest temperatures a phase slip really only ever occurs in a single particular region, and at higher temperatures phase slips can occur over multiple statistically independent regions of the ring.

Chapter 8

Conclusion

In this dissertation we have reported measurements of the supercurrent in isolated mesoscopic superconducting aluminum rings. We measured both arrays of rings and individual rings and found quantitative agreement between our measured supercurrent and that predicted by 1-dimensional Ginzburg-Landau theory for equilibrium states of a uniform ring.

Our measurements of the supercurrent in arrays of rings for $T_c/2 < T < T_c$, $|B| < B_{c,3}$ and various ring dimensions greatly expand the range of parameters over which such quantitative analysis was performed. And as predicted by GL theory, we found that phase slips occurred deterministically at the flux where the free energy barrier confining metastable states of the ring disappears. Given this agreement, we have demonstrated that isolated flux-biased uniform rings are a conceptually simple system in which many of the important physical quantities (ξ and λ) can be determined with accuracy and precision. As GL theory has a simple analytic form in one dimension, this provides us with detailed knowledge of the free energy landscape of these samples, which should enable systematic studies of thermal and quantum phase slips in the future and progress toward the quantitative understanding of coherent quantum phase slips.

Our measurement of the supercurrent in a single isolated superconducting ring is the first step in such a systematic study of phase slip dynamics. Again, we find quantitative agreement between our measured $I(B)$ for a single ring and that predicted by GL theory. However our measurement of phase slip dynamics (measured as the probability distribution of the applied magnetic field at which a phase slip occurs $P(B_{sw})$) is not in complete

agreement with GL theory and LAMH theory for thermally activated phase slips. Given the material parameters we determine from the GL fits, we find qualitative agreement for the trend in the mean of $P(B_{\rm sw})$ with temperature. We find that the skewness of these distributions is temperature independent and is -0.85 ± 0.15, which is slightly smaller than the expected value of -1.139. The most noticeable disagreement is with the measured trend of the distribution width as a function of temperature. We find that as temperature is increased, $P(B_{\rm sw})$ becomes narrower, which is the opposite of the trend predicted by LAMH theory for thermally activated phase slips.

This disagreement indicates that we may still lack a complete understanding of what truly determines the phase slip dynamics in uniform superconducting rings. For example, despite extensive research we are still unable to predict *a priori* into which metastable state a ring will end up when there are multiple metastable states available to the system. While the trend in the literature is that larger and thicker rings undergo phase slips in which $\Delta n > 1$, while smaller and thinner rings always have $\Delta n = 1$, our understanding of this process still remains qualitative.

Appendix A

Mathematical derivations

In this appendix we will go through the necessary mathematics and intermediate calculations for many of the major equations quoted in the main text

A.1 Derivation of the GL differential equations

A.1.1 The calculus of variations

Minimizing the GL free energy requires the variational principle, as the free energy $F[\psi(\mathbf{r})]$ can be written as the integral of a functional L which itself is a function of $\mathbf{r}$, $\psi(\mathbf{r})$, and $\nabla\psi(\mathbf{r})$, that is

$$F[\psi(\mathbf{r})] = \int_V L[\mathbf{r}, \psi(\mathbf{r}), \nabla\psi(\mathbf{r})]dV \tag{A.1}$$

For the function $F[\psi(\mathbf{r})]$ to attain a minimum at $\psi_0(\mathbf{r})$ the following inequality must hold for an arbitrary function $\delta\psi(\mathbf{r})$ which is close to zero and differentiable at least once

$$F[\psi_0(\mathbf{r})] < F[\psi_0(\mathbf{r}) + \delta\psi(\mathbf{r})] \tag{A.2}$$

If we express $F[\psi_0(\mathbf{r}) + \delta\psi(\mathbf{r})]$ as $F[\psi_0(\mathbf{r})] + \delta F[\psi_0(\mathbf{r}), \delta\psi(\mathbf{r})]$ we can say that this minimization condition is equivalent to

$$\delta F[\psi_0(\mathbf{r}), \delta\psi(\mathbf{r})] = 0 \tag{A.3}$$

He we should note that we are only taking the first order variation in $\delta\psi(\mathbf{r})$

A.1.2 The Euler-Lagrange equation

An alternative method to minimize the variation is by applying the Euler-Lagrange equation, which I will derive in this section. Continuing with the setup in the previous section, we will define $\Phi(\epsilon) = F[\psi(\mathbf{r})] = F[\psi_0(\mathbf{r}) + \epsilon\delta\psi(\mathbf{r})]$ and note that $\Phi(\epsilon)$ is minimized at $\epsilon = 0$ as $F[\psi(\mathbf{r})]$ is minimized for $F[\psi_0(\mathbf{r})]$, that is

$$\left.\frac{d\Phi(\epsilon)}{d\epsilon}\right|_{\epsilon=0} = \int_V \left.\frac{dL[\mathbf{r}, \psi_0(\mathbf{r}) + \epsilon\delta\psi(\mathbf{r}), \nabla\psi_0(\mathbf{r}) + \epsilon\nabla\delta\psi(\mathbf{r})]}{d\epsilon}\right|_{\epsilon=0} dV = 0 \tag{A.4}$$

$\mathbf{r}$ is not a function of ϵ so the total derivative of $L[\mathbf{r}, \psi(\mathbf{r}), \nabla\psi(\mathbf{r})]$ is

$$\frac{dL}{d\epsilon} = \frac{\partial L}{\partial\psi(\mathbf{r})}\frac{d\psi(\mathbf{r})}{d\epsilon} + \frac{\partial L}{\partial\nabla\psi(\mathbf{r})} \cdot \frac{d\nabla\psi(\mathbf{r})}{d\epsilon} \tag{A.5}$$

where from our definition of $\psi(\mathbf{r})$ we have $\frac{d\psi(\mathbf{r})}{d\epsilon} = \delta\psi(\mathbf{r})$ and $\frac{d\nabla\psi(\mathbf{r})}{d\epsilon} = \nabla\delta\psi(\mathbf{r})$. Thus,

$$\int_V \left.\frac{dL}{d\epsilon}\right|_{\epsilon=0} dV = \int_V \left(\frac{\partial L}{\partial\psi(\mathbf{r})}\delta\psi(\mathbf{r}) + \frac{\partial L}{\partial\nabla\psi(\mathbf{r})} \cdot \nabla\delta\psi(\mathbf{r})\right) dV \tag{A.6}$$

Integrating the second term by parts we find

$$\int_V \left(\frac{\partial L}{\partial\nabla\psi(\mathbf{r})} \cdot \nabla\delta\psi(\mathbf{r})\right) dV = \left.\frac{\partial L}{\partial\nabla\psi(\mathbf{r})}\delta\psi(\mathbf{r})\right|_V - \int_V \nabla \cdot \frac{\partial L}{\partial\nabla\psi(\mathbf{r})}\delta\psi(\mathbf{r})dV \tag{A.7}$$

We require $\delta\psi(\mathbf{r})$ to vanish on V so we can write

$$0 = \frac{d\Phi(\epsilon)}{d\epsilon} = \int_V \delta\psi(\mathbf{r}) \left(\frac{\partial L}{\partial\psi(\mathbf{r})} - \nabla \cdot \frac{\partial L}{\partial\nabla\psi(\mathbf{r})}\right) dV \tag{A.8}$$

If $\delta\psi(\mathbf{r})$ is an arbitrary function, this equation is satisfied only when the integrand is zero, leading to the well-known Euler-Lagrange equation

$$\frac{\partial L}{\partial\psi(\mathbf{r})} - \nabla \cdot \frac{\partial L}{\partial\nabla\psi(\mathbf{r})} = 0 \tag{A.9}$$

A.1.3 The variation of $F[\psi(\mathbf{r})]$

As is customary, we will calculate the variation of $F[\psi(\mathbf{r})]$ by considering an expansion in $\delta\psi^*(\mathbf{r})$ so our GL equations are in terms of $\psi(\mathbf{r})$ and not $\psi^*(\mathbf{r})$. To simplify notation in this calculation we will no longer explicitly write the $\mathbf{r}$-dependence of $\psi(\mathbf{r})$ or $\delta\psi(\mathbf{r})$. The variation of Eq. 2.15 is

$$\begin{aligned}
&F[\mathbf{r},\psi_0,\nabla\psi_0,\psi_0^*+\delta\psi^*,\nabla\psi_0^*+\nabla\delta\psi^*] = \\
&\quad\int_V\Bigg(\alpha\psi_0(\psi_0^*+\delta\psi^*)+\frac{1}{2}\beta\psi_0^2(\psi_0^*+\delta\psi^*)^2+\frac{1}{2m^*}\Bigg[\hbar^2\nabla\psi_0(\nabla\psi_0^*+\nabla\delta\psi^*) \\
&\qquad+\frac{i\hbar e^*\mathbf{A}}{c}\Big(\nabla\psi_0(\psi_0^*+\delta\psi^*)-(\nabla\psi_0^*+\nabla\delta\psi^*)\psi_0\Big)+\frac{e^{*2}\mathbf{A}^2}{c^2}\psi_0(\psi_0^*+\delta\psi^*)\Bigg] \\
&\qquad+f_{\mathrm{n}}+\frac{\mathbf{B}^2}{8\pi}\Bigg)dV
\end{aligned} \tag{A.10}$$

Keeping only terms to first order in $\delta\psi^*$ and $\nabla\delta\psi^*$

$$\begin{aligned}
&F[\mathbf{r},\psi_0,\nabla\psi_0,\psi_0^*+\delta\psi^*,\nabla\psi_0^*+\nabla\delta\psi^*] = F[\mathbf{r},\psi_0,\nabla\psi_0,\psi_0^*,\nabla\psi_0^*] \\
&\quad+\int_V\Bigg(\alpha\psi_0\delta\psi^*+\beta|\psi_0|^2\psi_0\delta\psi^*+\frac{1}{2m^*}\Bigg[\hbar^2\nabla\psi_0\nabla\delta\psi^*+\frac{e^{*2}\mathbf{A}^2}{c^2}\psi_0\delta\psi^* \\
&\qquad+\frac{i\hbar e^*\mathbf{A}}{c}(\nabla\psi_0\delta\psi^*-\nabla\delta\psi^*\psi_0)\Bigg]\Bigg)dV
\end{aligned} \tag{A.11}$$

Thus,

$$\begin{aligned}
&\delta F\left[\psi_0^*(\mathbf{r}),\delta\psi^*(\mathbf{r})\right] = \\
&\quad\int_V\Bigg(\alpha\psi_0\delta\psi^*+\beta|\psi_0|^2\psi_0\delta\psi^*+\frac{1}{2m^*}\Big(i\hbar\nabla\psi_0+\frac{e^*\mathbf{A}}{c}\psi_0\Big)\Big(-i\hbar\nabla\delta\psi^*+\frac{e^*\mathbf{A}}{c}\delta\psi^*\Big)\Bigg)dV
\end{aligned} \tag{A.12}$$

We can use a corollary of the divergence theorem for a scalar function f and a vector field $\mathbf{c}$, where $\mathbf{S}$ is the surface bounding V

$$\int_V\mathbf{c}\cdot\nabla f dV=\int_S(\mathbf{c}f)\cdot d\mathbf{S}-\int_V f(\nabla\cdot\mathbf{c})dV \tag{A.13}$$

to rewrite the term involving $\nabla\delta\psi^*$ in Eq. A.12 as

$$\int_V \left(i\hbar\nabla\psi_0 + \frac{e^*\mathbf{A}}{c}\psi_0\right)(-i\hbar\nabla\delta\psi^*)dV = \int_S \left(i\hbar\nabla\psi_0 + \frac{e^*\mathbf{A}}{c}\psi_0\right)(-i\hbar\delta\psi^*)\cdot d\mathbf{S} - \int_V (-i\hbar\delta\psi^*)\nabla\cdot\left(i\hbar\nabla\psi_0 + \frac{e^*\mathbf{A}}{c}\psi_0\right)dV \tag{A.14}$$

Including the rest of the terms in Eq. A.12, noting $\nabla\cdot(\nabla\psi) = \nabla^2\psi$

$$\begin{aligned}\delta F\big[\psi_0^*(\mathbf{r}), \delta\psi^*(\mathbf{r})\big] =& \frac{i\hbar}{2m^*}\int_S \delta\psi^*\Big(-i\hbar\nabla - \frac{e^*\mathbf{A}}{c}\Big)\psi_0\cdot d\mathbf{S} \\ &+ \int_V \delta\psi^*\left(\alpha\psi_0 + \beta|\psi_0|^2\psi_0 + \frac{1}{2m^*}\Big(-i\hbar\nabla - \frac{e^*\mathbf{A}}{c}\Big)^2\psi_0\right)dV\end{aligned} \tag{A.15}$$

The variation has two contributions, a bulk term and a surface term. In general, these two terms will not compensate for one another so for the variation to be zero each term must go to zero separately. As this must hold for an arbitrary $\delta\psi^*$, V, and $\mathbf{S}$ the integrands must be zero. With this, the volume integral gives us the first GL differential equation

$$\alpha\psi_0 + \beta|\psi_0|^2\psi_0 + \frac{1}{2m^*}\Big(-i\hbar\nabla - \frac{e^*\mathbf{A}}{c}\Big)^2\psi_0 = 0 \tag{A.16}$$

The surface integral specifies our boundary condition, which states that no current passes through the surface of the superconductor so that the dot product evaluates to zero, that is

$$\left(-i\hbar\nabla - \frac{e^*\mathbf{A}}{c}\right)\psi_0\bigg|_{\mathrm{n}} = 0 \tag{A.17}$$

A.1.4 The variation of $F[\mathbf{A}]$

To derive the second GL equation, we must look at the variation of free energy with respect to the vector potential. Letting $\mathbf{A_0}$ minimize $F[\mathbf{A}]$ and looking for variations with

respect to a small deviation $\delta\mathbf{A}$ we have

$$F[\mathbf{A_0}+\delta\mathbf{A}] = \int_V \Bigg(f_{\rm n} + \alpha|\psi|^2 + \frac{\beta}{2}|\psi|^4 + \frac{\big(\nabla\times(\mathbf{A_0}+\delta\mathbf{A})\big)^2}{8\pi} + \frac{1}{2m^*}\Big(-i\hbar\nabla\psi - \frac{e^*(\mathbf{A_0}+\delta\mathbf{A})}{c}\psi\Big)\Big(i\hbar\nabla\psi^* - \frac{e^*(\mathbf{A_0}+\delta\mathbf{A})}{c}\psi^*\Big)\Bigg)dV \tag{A.18}$$

Keeping terms only to first order in $\delta\mathbf{A}$

$$F[\mathbf{A_0}+\delta\mathbf{A}] = F[\mathbf{A_0}] + \int_V \left(\frac{1}{4\pi}(\nabla\times\mathbf{A_0})\cdot(\nabla\times\delta\mathbf{A}) + \frac{e^*}{2m^*c}\delta\mathbf{A}\Big(i\hbar(\psi^*\nabla\psi - \psi\nabla\psi^*) + \frac{2e^*}{c}\mathbf{A_0}|\psi|^2\Big)\right)dV \tag{A.19}$$

Using the vector identity $\nabla\cdot(\mathbf{a}\times\mathbf{b}) = \mathbf{b}\cdot(\nabla\times\mathbf{a}) - \mathbf{a}\cdot(\nabla\times\mathbf{b})$ with $\mathbf{a} = \nabla\times\mathbf{A_0}$ and $\mathbf{b} = \delta\mathbf{A}$ we can write

$$(\nabla\times\mathbf{A_0})\cdot(\nabla\times\delta\mathbf{A}) = -\nabla\cdot(\nabla\times\mathbf{A_0}\times\delta\mathbf{A}) + \delta\mathbf{A}(\nabla\times\nabla\times\mathbf{A_0}) \tag{A.20}$$

With this

$$\delta F[\mathbf{A_0},\delta\mathbf{A}] = \int_V \Bigg(-\frac{1}{4\pi}\nabla\cdot(\mathbf{B_0}\times\delta\mathbf{A}) + \delta\mathbf{A}\Big(\frac{\nabla\times\mathbf{B_0}}{4\pi} + \frac{i\hbar e^*}{2m^*c}(\psi^*\nabla\psi - \psi\nabla\psi^*) + \frac{e^{*2}}{m^*c^2}|\psi|^2\mathbf{A_0}\Big)\Bigg)dV \tag{A.21}$$

Using the divergence theorem, the first term in Eq. A.21 can be re-written as

$$\int_V \Big(\nabla\cdot(\mathbf{B_0}\times\delta\mathbf{A})\Big)dV = \int_S (\mathbf{B_0}\times\delta\mathbf{A})\cdot d\mathbf{S} \tag{A.22}$$

In the previous section as we were looking at the order parameter we only needed to extend the integration over the volume of the superconducting sample, where $\psi(\mathbf{r})$ is non-zero. In this case, we are minimizing with respect to the vector potential that exists in all space. Thus, the above surface integral is taken over an infinite surface and assuming there are no

currents exenting to $|\mathbf{r}| = \infty$, this term must disappear. Again, setting the variation equal to zero demands that the remaining integrand of Eq. A.21 evaluates to zero, which together with $\mathbf{J} = \frac{c}{4\pi}\nabla \times \mathbf{B}$ leads us to the second GL differential equation

$$\mathbf{J} = \frac{i\hbar e^*}{2m^*}(\psi\nabla\psi^* - \psi^*\nabla\psi) - \frac{e^{*2}}{m^*c}\mathbf{A}|\psi|^2 \tag{A.23}$$

A.2 Calculation of finite width correction to the GL free energy of a ring

To incorporate finite width into our Ginzburg-Landau calculation, we must calculate the following integral of section 2.2.5 for the free energy density of a ring (mean radius R, width w, and thickness s) in a magnetic field given by the vector potential $\mathbf{A} = \frac{1}{2}Br\hat{\theta}$

$$f - f_{\mathrm{n}} = \alpha\psi_0^2 + \frac{1}{2}\beta\psi_0^4 + \frac{1}{2m^*V}\int\left(\left|\left(-i\hbar\nabla - \frac{e^*}{c}\mathbf{A}\right)\psi_0 e^{in\theta}\right|^2\right)dV \tag{A.24}$$

where we have already assumed an order parameter of the form $\psi(\mathbf{r}) = \psi_0 e^{in\theta}$. For a ring, cylindrical coordinates are the most appropriate where $dV = r dr\, d\theta\, dz$ and $\nabla = \hat{\mathbf{r}}\frac{\partial}{\partial r} + \hat{\theta}\frac{1}{r}\frac{\partial}{\partial\theta} + \hat{\mathbf{z}}\frac{\partial}{\partial z}$. With this we can write

$$f - f_{\mathrm{n}} = \alpha\psi_0^2 + \frac{1}{2}\beta\psi_0^4 + \frac{\psi_0^2}{2m^*V}\int\left(\left(\left[-i\hbar\frac{1}{r}\frac{\partial}{\partial\theta} - \frac{e^*rB}{2c}\right]e^{in\theta}\right)\left(\left[i\hbar\frac{1}{r}\frac{\partial}{\partial\theta} - \frac{e^*rB}{2c}\right]e^{-in\theta}\right)\right)dV$$

$$f - f_{\mathrm{n}} = \alpha\psi_0^2 + \frac{1}{2}\beta\psi_0^4 + \frac{\psi_0^2}{2m^*V}\int\left(\frac{n\hbar}{r} - \frac{e^*rB}{2c}\right)^2 r dr\, d\theta\, dz \tag{A.25}$$

As the integrand does not depend on θ nor z those integrals evaluate to $2\pi s$. R is the mean radius so the r integral is evaluated from $R - \frac{w}{2}$ to $R + \frac{w}{2}$

$$f - f_{\mathrm{n}} = \alpha\psi_0^2 + \frac{1}{2}\beta\psi_0^4 + \frac{\psi_0^2 2\pi s}{2m^*V}\int_{R-\frac{w}{2}}^{R+\frac{w}{2}}\left(\frac{n^2\hbar^2}{r} - \frac{e^*n\hbar B}{c}r + \frac{e^{*2}B^2}{4c^2}r^3\right)dr$$

$$f - f_{\mathrm{n}} = \alpha\psi_0^2 + \frac{1}{2}\beta\psi_0^4 + \frac{\psi_0^2 2\pi s}{2m^*V}\left(n^2\hbar^2\ln\left[\frac{R+\frac{w}{2}}{R-\frac{w}{2}}\right] - \frac{e^*n\hbar B}{2c}\left[\left(R+\frac{w}{2}\right)^2 - \left(R-\frac{w}{2}\right)^2\right]\right.$$
$$\left. + \frac{e^{*2}B^2}{16c^2}\left[\left(R+\frac{w}{2}\right)^4 - \left(R-\frac{w}{2}\right)^4\right]\right)$$

$$f - f_{\rm n} = \alpha\psi_0^2 + \frac{1}{2}\beta\psi_0^4 + \frac{\psi_0^2 2\pi s}{2m^* V}\left(n^2\hbar^2 \ln\left[\frac{1+\frac{w}{2R}}{1-\frac{w}{2R}}\right] - \frac{2e^* n\hbar B R^2}{c}\left(\frac{w}{2R}\right) + \frac{e^{*2}B^2R^4}{2c^2}\left(\left(\frac{w}{2R}\right) + \left(\frac{w}{2R}\right)^3\right)\right) \tag{A.26}$$

At this point it is useful to replace the sample volume by $V = 2\pi Rsw$ and use the identity $2\hbar\frac{\Phi}{\Phi_0} = \frac{Be^*R^2}{c}$. With this Eq. A.26 becomes

$$f - f_{\rm n} = \alpha\psi_0^2 + \frac{1}{2}\beta\psi_0^4 + \frac{\psi_0^2\hbar^2}{2m^* Rw}\left(n^2 \ln\left[\frac{1+\frac{w}{2R}}{1-\frac{w}{2R}}\right] - 4n\frac{\Phi}{\Phi_0}\left(\frac{w}{2R}\right) + 2\left(\frac{\Phi}{\Phi_0}\right)^2\left(\left(\frac{w}{2R}\right) + \left(\frac{w}{2R}\right)^3\right)\right) \tag{A.27}$$

Now we need to apply the variational method to find the states $\psi(\mathbf{r}) = \psi_0 e^{in\theta}$ that minimize the free energy, given by this free energy density. Unlike the previous sections, here we assumed a specific form of $\psi(\mathbf{r})$ which allowed us to calculate the gradient terms in f explicitly. This simplifies the variational problem considerably, as minimizing the free energy is the same as minimizing the free energy density with respect to ψ_0, or equivalently ψ_0^2.

$$\begin{aligned} 0 = \frac{df}{d\psi_0^2} &= \alpha + \beta\psi_0^2 + \frac{\hbar^2}{2m^* Rw}\left(n^2 \ln\left[\frac{1+\frac{w}{2R}}{1-\frac{w}{2R}}\right] - 4n\frac{\Phi}{\Phi_0}\left(\frac{w}{2R}\right) + 2\left(\frac{\Phi}{\Phi_0}\right)^2\left(\left(\frac{w}{2R}\right) + \left(\frac{w}{2R}\right)^3\right)\right) \\ \psi_0^2 &= -\frac{\alpha}{\beta} - \frac{\hbar^2}{2m^* Rw\beta}\left(n^2 \ln\left[\frac{1+\frac{w}{2R}}{1-\frac{w}{2R}}\right] - 4n\frac{\Phi}{\Phi_0}\left(\frac{w}{2R}\right) + 2\left(\frac{\Phi}{\Phi_0}\right)^2\left(\left(\frac{w}{2R}\right) + \left(\frac{w}{2R}\right)^3\right)\right) \end{aligned} \tag{A.28}$$

At this point we have succeeded in finding the full form of the order parameter that carries constant current and minimizes the free energy in a ring geometry, including the ring's finite width. However it is useful to make the assumption that $\frac{w}{2R}$ is small and expand the

logarithm in Eq. A.28 to third order in this parameter.[1]

$$\psi_0^2 = -\frac{\alpha}{\beta} - \frac{\hbar^2}{2m^* Rw\beta}\left(n^2\left[2\left(\frac{w}{2R}\right) + \frac{2}{3}\left(\frac{w}{2R}\right)^3 \right] - 4n\frac{\Phi}{\Phi_0}\left(\frac{w}{2R}\right) + 2\left(\frac{\Phi}{\Phi_0}\right)^2\left(\left(\frac{w}{2R}\right) + \left(\frac{w}{2R}\right)^3\right)\right)$$

$$\psi_0^2 = -\frac{\alpha}{\beta} - \frac{\hbar^2}{2m^* Rw\beta}\left(\left(\frac{w}{2R}\right)\left(2n^2 - 4n\frac{\Phi}{\Phi_0} + 2\left(\frac{\Phi}{\Phi_0}\right)^2\right) + \left(\frac{w}{2R}\right)^3\left(\frac{2n^2}{3} + 2\left(\frac{\Phi}{\Phi_0}\right)^2\right)\right)$$

$$\psi_0^2 = -\frac{\alpha}{\beta} - \frac{\hbar^2}{m^* Rw\beta}\left(\left(\frac{w}{2R}\right)\left(n - \frac{\Phi}{\Phi_0}\right)^2 + \left(\frac{w}{2R}\right)^3\left(\frac{n^2}{3} + \left(\frac{\Phi}{\Phi_0}\right)^2\right)\right)$$

$$\psi_0^2 = -\frac{\alpha}{\beta} - \frac{\hbar^2}{2m^* R^2\beta}\left(\left(n - \frac{\Phi}{\Phi_0}\right)^2 + \left(\frac{w}{2R}\right)^2\left(\frac{n^2}{3} + \left(\frac{\Phi}{\Phi_0}\right)^2\right)\right) \tag{A.29}$$

Using our usual definition $|\psi_\infty|^2 = \frac{-\alpha}{\beta}$ this can be re-written in the form

$$\psi_0^2 = |\psi_\infty|^2\left[1 - \frac{\hbar^2}{2m^*|\alpha|R^2}\left(\left(n - \frac{\Phi}{\Phi_0}\right)^2 + \left(\frac{w}{2R}\right)^2\left(\frac{n^2}{3} + \left(\frac{\Phi}{\Phi_0}\right)^2\right)\right)\right] \tag{A.30}$$

A.3 Stability condition for stationary states of $F[\psi(\mathbf{r})]$

In this section we will investigate the properties of solutions that extremize $F[\psi(\mathbf{r})]$, which was calculated by Langer and Ambegaokar [21].[2] However to remain consistent with the notation of the main text, we will not adopt their normalization. In particular we care about those solutions which carry constant current, and from Eq. 2.21 we can see these can have a constant amplitude and a phase that only depends linearly on $\mathbf{r}$. Thus we will write $\psi_k(\mathbf{r}) = f_k e^{i\mathbf{k}\cdot\mathbf{r}}$, where f_k is constant. By looking at small perturbations $\nu(\mathbf{r})$ to these solutions we will derive a stability condition for $\psi_k(\mathbf{r})$ to remain an isolated minimum of $F[\psi(\mathbf{r})]$, that is, we will find a condition for the disappearance of an energy barrier for transitions between different $\psi_k(\mathbf{r})$.

Ignoring the magnetic field term, which can be made arbitrarily small in small samples,

1. Due to the presence of $w^{-1}R^{-1}$ in the prefactor of the logarithm, a third order expansion is required to obtain a solution valid to second order in $\frac{w}{2R}$.

2. Tuckerman is also a useful source for this calculation as this stability condition is exactly that of the Eckhaus Instability [75].

the GL free energy is the usual

$$F[\psi(\mathbf{r})] = \int_V \left(\alpha |\psi(\mathbf{r})|^2 + \frac{1}{2}\beta |\psi(\mathbf{r})|^4 + \frac{\hbar^2}{2m^*} |\nabla \psi(\mathbf{r})|^2 \right) dV \tag{A.31}$$

For states $\psi_k(\mathbf{r}) = f_k e^{i\mathbf{k}\cdot\mathbf{r}}$ we can calculate the gradient terms explicitly which yields

$$F[\psi_k(\mathbf{r})] = \int_V \left(\left(\alpha + \frac{\hbar^2 k^2}{2m^*} \right) f_k^2 + \frac{1}{2}\beta f_k^4 \right) dV \tag{A.32}$$

For these states to be equilibrium states of $F[\psi(\mathbf{r})]$, they must minimize F, which is equivalent to minimizing the integrand. This integrand no longer depends on gradient terms, thus the minimization is given by

$$\begin{aligned} 0 = & \frac{d}{df_k^2} \left(\left(\alpha + \frac{\hbar^2 k^2}{2m^*} \right) f_k^2 + \frac{1}{2}\beta f_k^4 \right) \\ f_k^2 = & -\frac{\alpha + \frac{\hbar^2 k^2}{2m^*}}{\beta} \end{aligned} \tag{A.33}$$

Now we can calculate the free energy given a small perturbation. If we can express this free energy as

$$F[\psi_k(\mathbf{r}) + \nu(\mathbf{r})] = F[\psi_k(\mathbf{r})] + Q[\nu(\mathbf{r})] \tag{A.34}$$

where Q is a quadratic function of $\nu(\mathbf{r})$, then the eigenvalues of Q will give the curvature of $F[\psi_k(\mathbf{r}) + \nu(\mathbf{r})]$ at the point $\psi_k(\mathbf{r})$. Thus, if $\psi_k(\mathbf{r})$ is a local minimum of $F[\psi_k(\mathbf{r}) + \nu(\mathbf{r})]$, all of the eigenvalues of Q must be positive. Writing out the free energy with the perturbation we have

$$\begin{aligned} F[\psi_k(\mathbf{r}) + \nu(\mathbf{r})] = \int_V \Bigg(& \alpha \left| f_k e^{i\mathbf{k}\cdot\mathbf{r}} + \nu(\mathbf{r}) \right|^2 + \frac{1}{2}\beta \left| f_k e^{i\mathbf{k}\cdot\mathbf{r}} + \nu(\mathbf{r}) \right|^4 \\ & + \frac{\hbar^2}{2m^*} \left| \nabla \left(f_k e^{i\mathbf{k}\cdot\mathbf{r}} + \nu(\mathbf{r}) \right) \right|^2 \Bigg) dV \end{aligned} \tag{A.35}$$

We will drop any terms of order $\nu(\mathbf{r})^3$ or higher which leaves us with

$$\begin{aligned}
F[\psi_k(\mathbf{r})+\nu(\mathbf{r})] = &\int_V \left(\left(\alpha + \frac{\hbar^2 k^2}{2m^*} \right) f_k^2 + \frac{1}{2}\beta f_k^4 \right) dV \\
&+ \int_V \Bigg(\alpha|\nu(\mathbf{r})|^2 + \alpha f_k \left(\nu(\mathbf{r}) e^{-i\mathbf{k}\cdot\mathbf{r}} + \nu^*(\mathbf{r}) e^{+i\mathbf{k}\cdot\mathbf{r}} \right) \\
&+ \frac{1}{2}\beta \Bigg(2f_k^2|\nu(\mathbf{r})|^2 + f_k^2 \left(\nu(\mathbf{r}) e^{-i\mathbf{k}\cdot\mathbf{r}} + \nu^*(\mathbf{r}) e^{i\mathbf{k}\cdot\mathbf{r}} \right)^2 + f_k^3 \left(\nu(\mathbf{r}) e^{-i\mathbf{k}\cdot\mathbf{r}} + \nu^*(\mathbf{r}) e^{i\mathbf{k}\cdot\mathbf{r}} \right) \Bigg) \\
&+ \frac{\hbar^2}{2m^*}|\nabla\nu(\mathbf{r})|^2 + \frac{\hbar^2}{2m^*} ik f_k \left(\left[\nabla\nu^*(\mathbf{r})\right] e^{i\mathbf{k}\cdot\mathbf{r}} - \left[\nabla\nu(\mathbf{r})\right] e^{-i\mathbf{k}\cdot\mathbf{r}} \right) \Bigg) dV
\end{aligned} \tag{A.36}$$

Using Eq. A.33 and recognizing the first integral as the free energy of our stationary state we can write

$$\begin{aligned}
F[\psi_k(\mathbf{r}) + \nu(\mathbf{r})] = &F[\psi_k(\mathbf{r})] \\
&+ \int_V f_k \Bigg(\frac{\hbar^2}{2m^*} ik \left(\left[\nabla\nu^*(\mathbf{r})\right] e^{i\mathbf{k}\cdot\mathbf{r}} - \left[\nabla\nu(\mathbf{r})\right] e^{i\mathbf{k}\cdot\mathbf{r}} \right) - k^2 \left(\nu(\mathbf{r}) e^{-i\mathbf{k}\cdot\mathbf{r}} + \nu^*(\mathbf{r}) e^{+i\mathbf{k}\cdot\mathbf{r}} \right) \Bigg) dV \\
&+ \int_V \left(\frac{\hbar^2}{2m^*}|\nabla\nu(\mathbf{r})|^2 - \frac{\hbar^2 k^2}{2m^*}|\nu(\mathbf{r})|^2 - \frac{1}{2}\left(\alpha + \frac{\hbar^2 k^2}{2m^*} \right) \left(\nu(\mathbf{r}) e^{-i\mathbf{k}\cdot\mathbf{r}} + \nu^*(\mathbf{r}) e^{+i\mathbf{k}\cdot\mathbf{r}} \right)^2 \right) dV
\end{aligned} \tag{A.37}$$

The first integral is linear in $\nu(\mathbf{r})$ and must vanish as we are expanding the free energy in a Taylor series about an extremal point. The second integral is quadratic in $\nu(\mathbf{r})$ and by comparison with Eq. A.34, we can write

$$Q[\nu(\mathbf{r})] = \int_V \left(\frac{\hbar^2}{2m^*}|\nabla\nu(\mathbf{r})|^2 - \frac{\hbar^2 k^2}{2m^*}|\nu(\mathbf{r})|^2 - \frac{1}{2}\left(\alpha + \frac{\hbar^2 k^2}{2m^*} \right) \left(\nu(\mathbf{r}) e^{-i\mathbf{k}\cdot\mathbf{r}} + \nu^*(\mathbf{r}) e^{+i\mathbf{k}\cdot\mathbf{r}} \right)^2 \right) \tag{A.38}$$

We will define L as the integrand of $Q[\nu(\mathbf{r})]$, and to find the eigenvalues λ of $Q[\nu(\mathbf{r})]$ we will use the Euler-Lagrange equation given by Eq. A.9.

$$\begin{aligned}
\lambda\nu(\mathbf{r}) &= \frac{\partial L}{\partial \nu^*(\mathbf{r})} - \nabla \cdot \frac{\partial L}{\partial \nabla\nu^*(\mathbf{r})} \\
\lambda\nu(\mathbf{r}) &= -\frac{\hbar^2}{2m^*}\nabla^2\nu(\mathbf{r}) - \frac{\hbar^2 k^2}{2m^*}\nu(\mathbf{r}) - \left(\alpha + \frac{\hbar^2 k^2}{2m^*} \right) \left(\nu(\mathbf{r}) + \nu^*(\mathbf{r}) e^{2i\mathbf{k}\cdot\mathbf{r}} \right)
\end{aligned} \tag{A.39}$$

Eq. A.39 can be solved by writing $\nu(\mathbf{r}) = e^{i\mathbf{k}\cdot\mathbf{r}}\left(u_1(\mathbf{r}) + iu_2(\mathbf{r})\right)$ which leads to

$$\begin{aligned}\lambda\left(u_1(\mathbf{r}) + iu_2(\mathbf{r})\right) = &-\frac{\hbar^2}{2m^*}\Big(\nabla^2 u_1(\mathbf{r}) + i\nabla^2 u_2(\mathbf{r}) - 2k\nabla u_2(\mathbf{r}) + 2ik\nabla u_1(\mathbf{r})\Big) \\ &- 2u_1(\mathbf{r})\left(\alpha + \frac{\hbar^2 k^2}{2m^*}\right)\end{aligned} \tag{A.40}$$

Equating the real and imaginary parts we obtain two equations

$$\lambda u_1(\mathbf{r}) = -\frac{\hbar^2}{2m^*}\nabla^2 u_1(\mathbf{r}) + \frac{\hbar^2}{2m^*}2\mathbf{k}\cdot\nabla u_2(\mathbf{r}) - 2u_1(\mathbf{r})\left(\alpha + \frac{\hbar^2 k^2}{2m^*}\right) \tag{A.41}$$

$$\lambda u_2(\mathbf{r}) = -\frac{\hbar^2}{2m^*}\nabla^2 u_2(\mathbf{r}) - \frac{\hbar^2}{2m^*}2\mathbf{k}\cdot\nabla u_1(\mathbf{r}) \tag{A.42}$$

These two coupled equations have plane wave solutions of the form $u_1(\mathbf{r}) = \mathrm{Re}[a_1 e^{i\mathbf{p}\cdot\mathbf{r}}]$ and $u_2(\mathbf{r}) = \mathrm{Re}[a_2 e^{i\mathbf{p}\cdot\mathbf{r}}]$ which leads to

$$\lambda\mathrm{Re}[a_1 e^{i\mathbf{p}\cdot\mathbf{r}}] = \left(\frac{\hbar^2 p^2}{2m^*} - 2\left(\alpha + \frac{\hbar^2 k^2}{2m^*}\right)\right)\mathrm{Re}[a_1 e^{i\mathbf{p}\cdot\mathbf{r}}] + \frac{\hbar^2}{2m^*}2i\mathbf{k}\cdot\mathbf{p}\mathrm{Re}[a_2 e^{i\mathbf{p}\cdot\mathbf{r}}] \tag{A.43}$$

$$\lambda\mathrm{Re}[a_2 e^{i\mathbf{p}\cdot\mathbf{r}}] = \frac{\hbar^2 p^2}{2m^*}\mathrm{Re}[a_2 e^{i\mathbf{p}\cdot\mathbf{r}}] - \frac{\hbar^2}{2m^*}2i\mathbf{k}\cdot\mathbf{p}\mathrm{Re}[a_1 e^{i\mathbf{p}\cdot\mathbf{r}}] \tag{A.44}$$

Combining these two equations to eliminate the $\mathrm{Re}[a_1 e^{i\mathbf{p}\cdot\mathbf{r}}]$ terms we arrive at the characteristic polynomial

$$\lambda^2 + 2\lambda\left(-\frac{\hbar^2 p^2}{2m^*} + \alpha + \frac{\hbar^2 k^2}{2m^*}\right) + \left(\frac{\hbar^2}{2m^*}\right)^2 p^4 - 2\frac{\hbar^2}{2m^*}p^2\left(\alpha + \frac{\hbar^2 k^2}{2m^*}\right) - \left(\frac{\hbar^2}{2m^*}\right)^2 4(\mathbf{k}\cdot\mathbf{p})^2 = 0 \tag{A.45}$$

which has roots

$$\lambda = \frac{\hbar^2 p^2}{2m^*} - \left(\alpha + \frac{\hbar^2 k^2}{2m^*}\right) \pm \sqrt{\left(\alpha + \frac{\hbar^2 k^2}{2m^*}\right)^2 + \left(\frac{\hbar^2}{2m^*}\right)^2 4(\mathbf{k}\cdot\mathbf{p})^2} \tag{A.46}$$

For $\psi_k(\mathbf{r})$ to remain a minimum of $F[\psi(\mathbf{r})]$, every λ must be positive for all p, and this leads to a restriction between α and k. To determine this restriction, we will determine what needs to happen to make one of these eigenvalues zero. First, we only need to consider the roots with a negative sign before the square root, as these will always be less than or equal to the corresponding root with the plus sign. Second, we only need to worry about small

values of p as for large values of p the p^2 term, which is positive, dominates the behavior. In our notation, α is negative so to avoid confusion in the following expansion of the negative root I will write $-\alpha = |\alpha|$. Eq. A.46 is

$$\begin{aligned}
\lambda &= \frac{\hbar^2 p^2}{2m^*} + \left(|\alpha| - \frac{\hbar^2 k^2}{2m^*}\right) - \sqrt{\left(|\alpha| - \frac{\hbar^2 k^2}{2m^*}\right)^2 + \left(\frac{\hbar^2}{2m^*}\right)^2 4(\mathbf{k}\cdot\mathbf{p})^2} \\
\lambda &= \frac{\hbar^2 p^2}{2m^*} + \left(|\alpha| - \frac{\hbar^2 k^2}{2m^*}\right) - \left(|\alpha| - \frac{\hbar^2 k^2}{2m^*}\right)\sqrt{1 + \frac{\left(\frac{\hbar^2}{2m^*}\right)^2 4(\mathbf{k}\cdot\mathbf{p})^2}{\left(|\alpha| - \frac{\hbar^2 k^2}{2m^*}\right)^2}} \\
\lambda &\approx \frac{\hbar^2 p^2}{2m^*} + \left(|\alpha| - \frac{\hbar^2 k^2}{2m^*}\right) - \left(|\alpha| - \frac{\hbar^2 k^2}{2m^*}\right) - \frac{\left(\frac{\hbar^2}{2m^*}\right)^2 2(\mathbf{k}\cdot\mathbf{p})^2}{|\alpha| - \frac{\hbar^2 k^2}{2m^*}} \\
\lambda &\approx \frac{\hbar^2 p^2}{2m^*} - \frac{\left(\frac{\hbar^2}{2m^*}\right)^2 2(\mathbf{k}\cdot\mathbf{p})^2}{|\alpha| - \frac{\hbar^2 k^2}{2m^*}}
\end{aligned} \tag{A.47}$$

As we are considering the extreme case where this first becomes zero, we take the maximal value of $\mathbf{k}\cdot\mathbf{p} = kp$. With this we have

$$\begin{aligned}
\lambda = 0 &= \frac{\hbar^2 p^2}{2m^*} - \frac{\left(\frac{\hbar^2}{2m^*}\right)^2 2k^2 p^2}{|\alpha| - \frac{\hbar^2 k^2}{2m^*}} \\
|\alpha| &= 3\frac{\hbar^2 k^2}{2m^*}
\end{aligned} \tag{A.48}$$

Thus, for $\psi_k(\mathbf{r})$ to remain a minimum of $F[\psi(\mathbf{r})]$, we require $\frac{\hbar^2 k^2}{2m^*} \leq \frac{1}{3}|\alpha|$. To make this condition more transparent, we can use Eq. 2.22 to write $m^*\mathbf{v}_s = \hbar k$ for our constant current carrying order parameter in the presence of no magnetic field. Thus, this condition is equivalent to

$$\begin{aligned}
\frac{m^{*2}\mathbf{v}_s^2}{2m^*} &\leq \frac{1}{3}|\alpha| \\
\mathbf{v}_s &\leq \sqrt{\frac{2|\alpha|}{3m^*}}
\end{aligned} \tag{A.49}$$

This familiar velocity is the same velocity that maximized the current density and led to the critical current of Eq. 2.26. Thus, there is an intuitive physical interpretation of this mathematical relationship: for any current below the critical current, there exists an energy

barrier for transitions between constant current carrying states of different winding numbers and at the critical current, this barrier disappears. Or, stated differently: below I_c all of the eigenvalues are positive, so any Fourier component of the perturbation increases the energy quadratically in its magnitude, so the system is confined to the case where the perturbation equals zero. Above I_c there is at least one mode with a negative eigenvalue ("negative spring constant"), so its magnitude will grow exponentially in time, and so the system is no longer confined to its initial state.

Appendix B

Sample photos

This appendix contains optical and Scanning Electron Microscope (SEM) photos of the sample measured in this dissertation. The sample used in this work was created by William Shanks and Ania Bleszynski-Jayich. For a detailed step-by-step list of all steps in the fabrication process see Appendix D of Shanks [3].

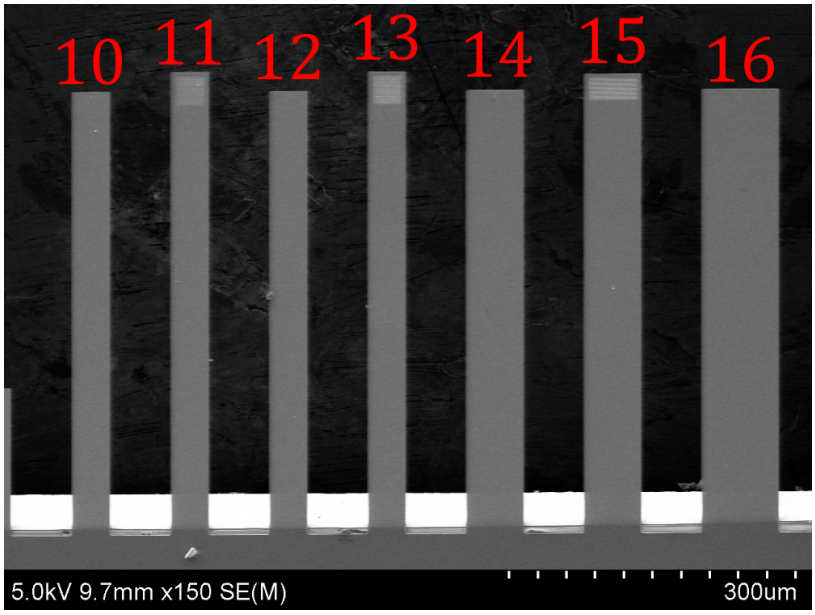

Figure B.1: SEM image of the cantilevers measured in this work. All cantilevers were made of silicon and were $\sim 400\,\mu$m long, 340 nm thick and $\sim 60\,\mu$m wide. The numbering begins at 10 as there were 9 shorter cantilevers to the left (not shown) which were not measured in this work. There was a single ring at the end of even numbered cantilevers and an array of rings at the end of odd numbered cantilevers. Pairs of cantilevers (10 and 11, 12 and 13, 14 and 15, 16 and 17) had identical lithographic dimensions for the aluminum rings.

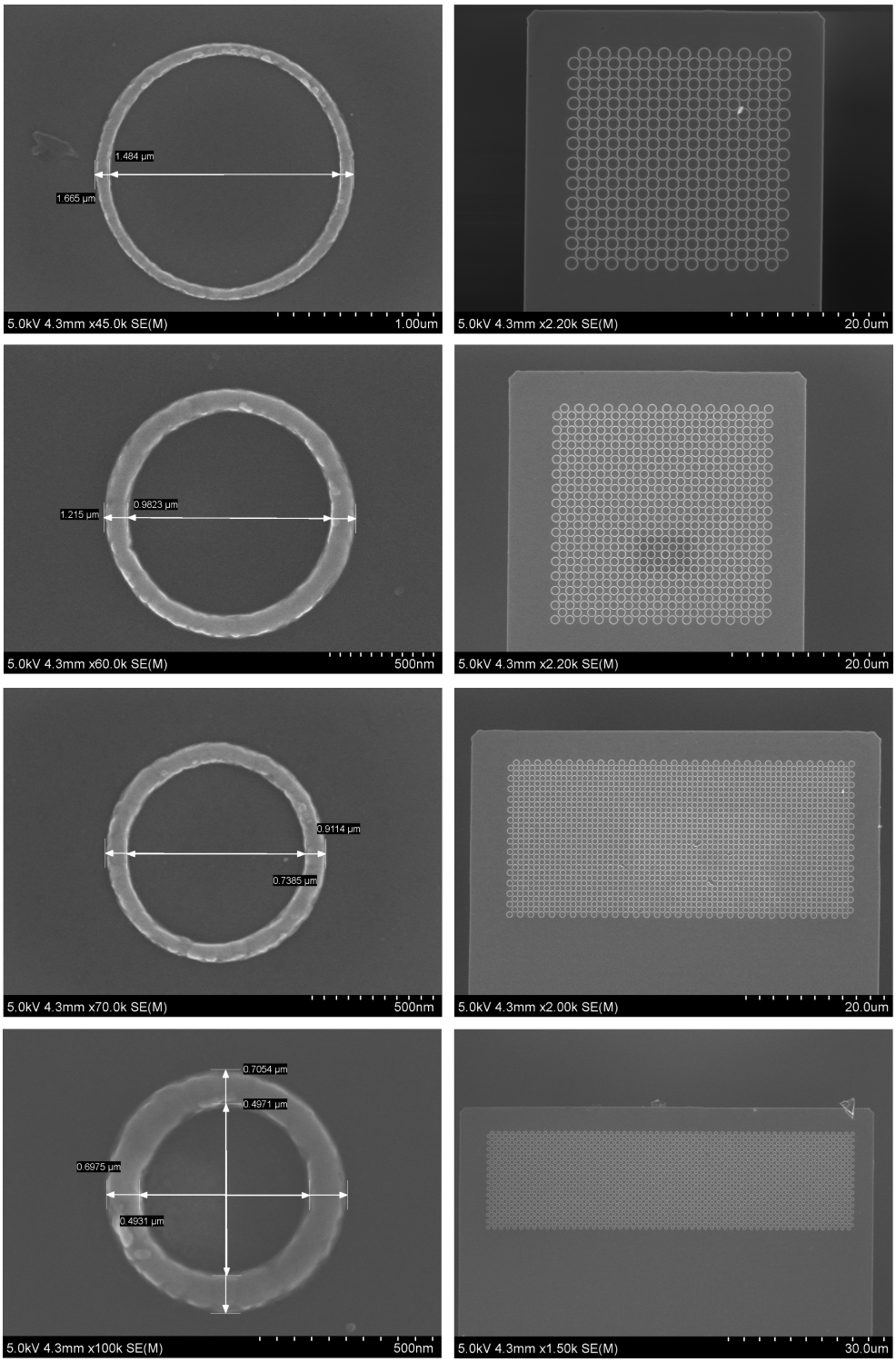

Figure B.2: SEM image of the aluminum rings measured in this work. The left column shows the single rings at the end of CL 10, CL 12, CL 14, and CL 16 from top to bottom. The right column shows the arrays of rings at the end of CL 11, CL 13, CL 15, and CL 17 from top to bottom. For the single rings a representative measurement of the inner and outer radius is shown.

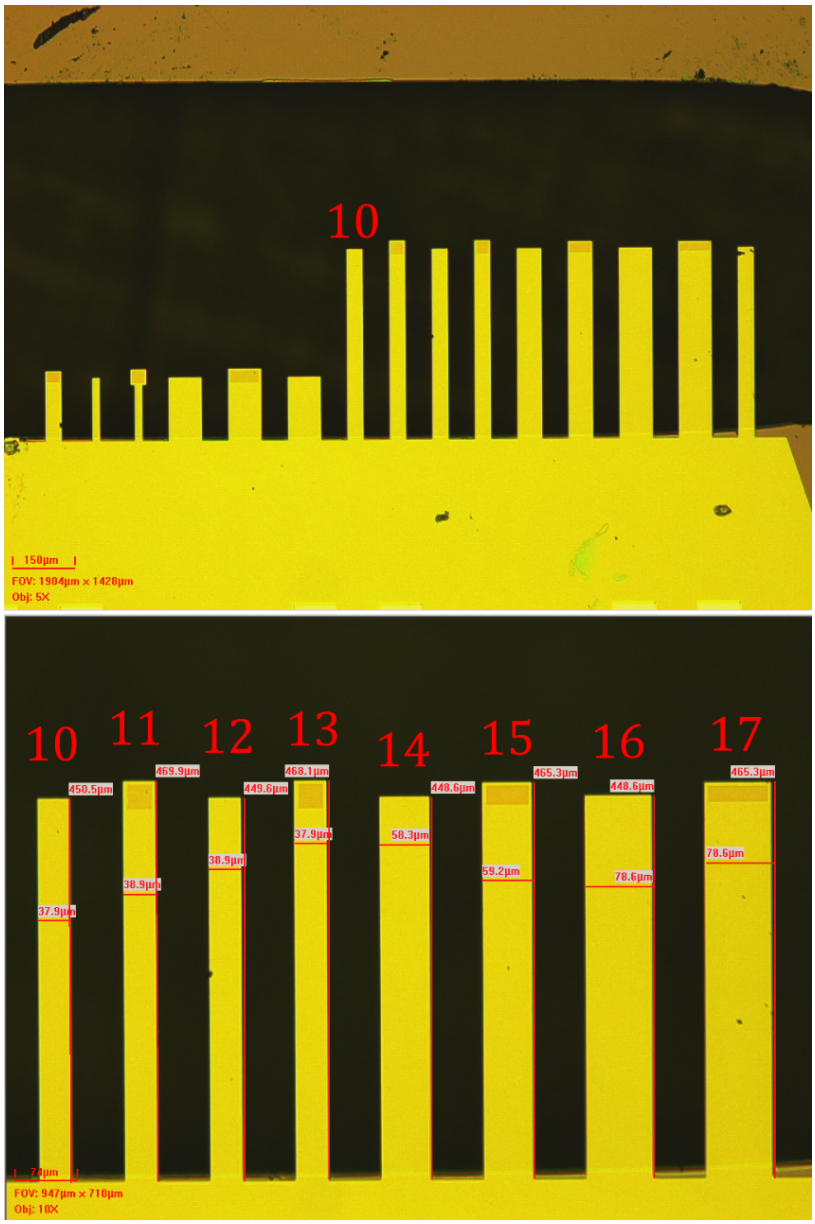

Figure B.3: Optical images of the cantilevers measured in this work. The top image shows a larger view of the window of cantilevers while the bottom image zooms in on the 8 cantilevers we measured. The silicon cantilevers are yellow in this photo and arrays of rings are clearly visible at the end of odd numbered cantilevers. The cantilever dimensions were estimated from the bottom panel.

Appendix C

Switching distributions for individual phase slip detection (CL12)

In this appendix we display the distributions of magnetic fields at which a phase slip occurs, $P(B_{\rm sw})$, obtained by the individual phase slip detection analysis of Section 7.3.1. For each temperature we show two typical $f_0(B)$ traces (with one curve offset for clarity) and the corresponding Tanh fits. The R^2 for each curve is calculated over a 0.7 G window centered on the phase slip (i.e., the extent of the black curve). We only consider events with an $R^2 > 0.55$ when we determine $P(B_{\rm sw})$. Red and blue are for the $\psi_{n=12} \rightarrow \psi_{n=13}$ and $\psi_{n=13} \rightarrow \psi_{n=12}$ transition respectively. From these distributions and the the $T = 471$ mK data of Section 7.3.1 we generated Fig. 7.19. For $T = 464$, 524, 601, 700, and 799 mK the total continuous measurement time was 68, 90, 65, 30 and 49 hours respectively, which resulted in approximately 320, 370, 400, 135 and 190 events with $R^2 > 0.55$ for each transition.

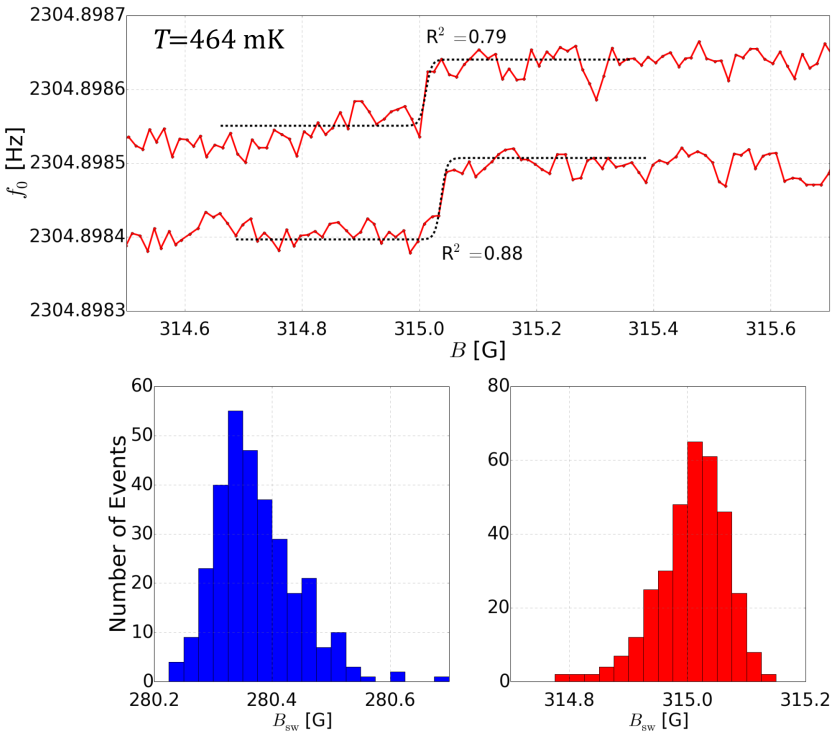

Figure C.1: (Top panel) Example $f_0(B)$ measurements for $\dot{B} > 0$ with the corresponding Tanh fit to the phase slip. (Bottom panels) Unnormalized $P(B_{\rm sw})$.

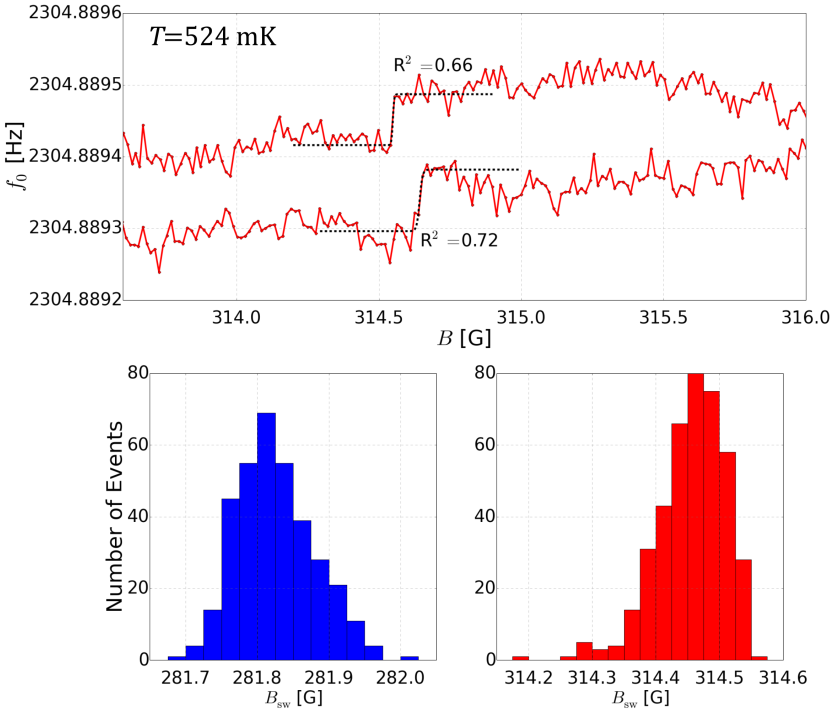

Figure C.2: (Top panel) Example $f_0(B)$ measurements for $\dot{B} > 0$ with the corresponding Tanh fit to the phase slip. (Bottom panels) Unnormalized $P(B_{\rm sw})$.

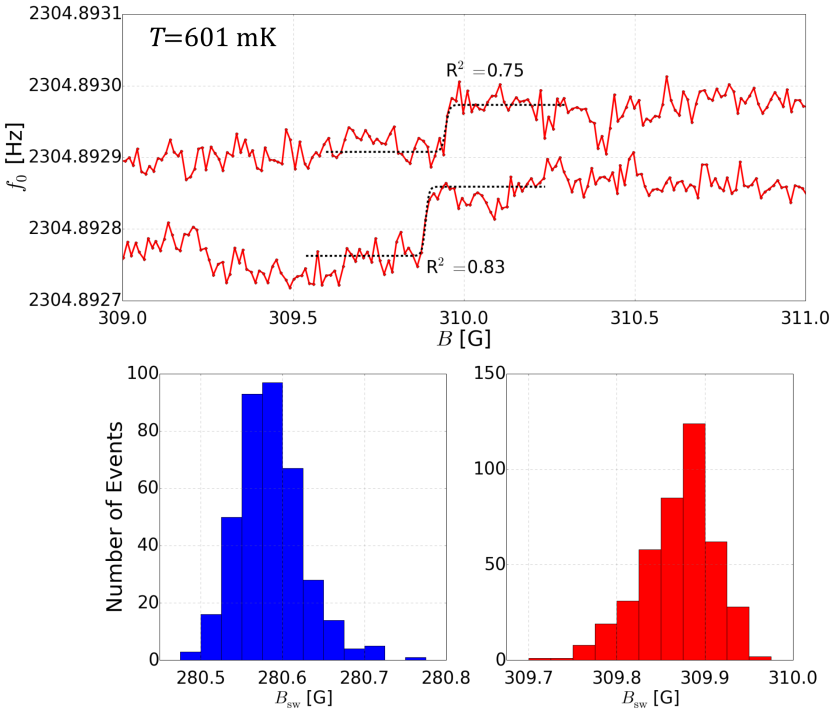

Figure C.3: (Top panel) Example $f_0(B)$ measurements for $\dot{B} > 0$ with the corresponding Tanh fit to the phase slip. (Bottom panels) Unnormalized $P(B_{\rm sw})$.

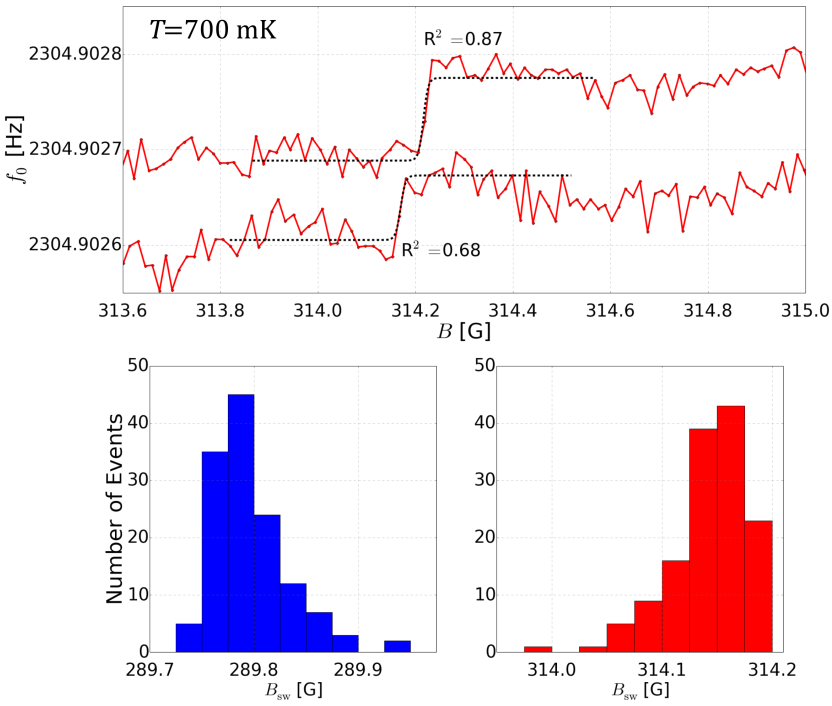

Figure C.4: (Top panel) Example $f_0(B)$ measurements for $\dot{B} > 0$ with the corresponding Tanh fit to the phase slip. (Bottom panels) Unnormalized $P(B_{\rm sw})$.

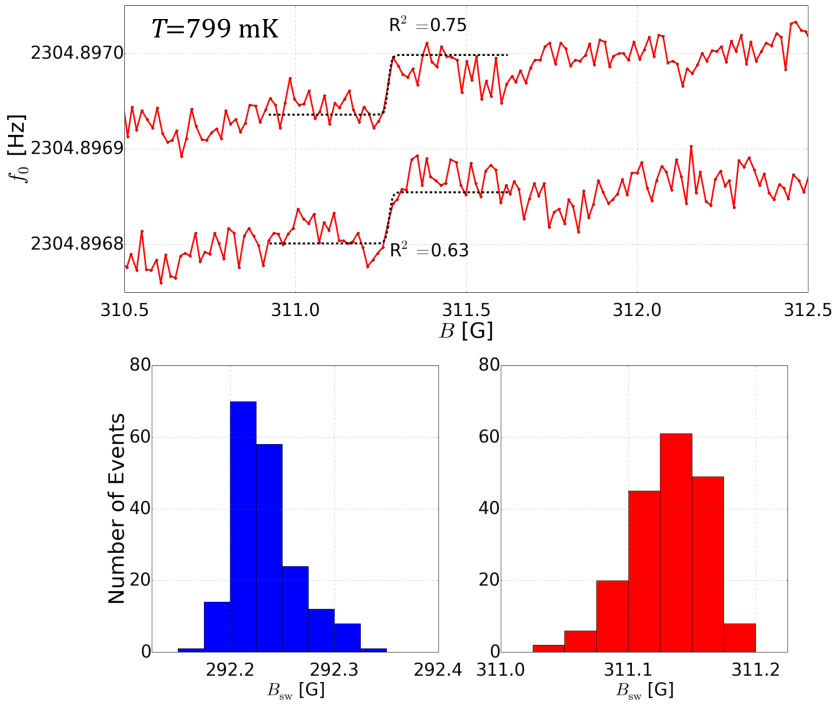

Figure C.5: (Top panel) Example $f_0(B)$ measurements for $\dot{B} > 0$ with the corresponding Tanh fit to the phase slip. (Bottom panels) Unnormalized $P(B_{\rm sw})$.

Appendix D

Individual phase slip detection on null data (CL12)

In this appendix we present our individual phase slip detection analysis for the $\psi_{n=13} \rightarrow \psi_{n=12}$ transition of CL12 at $T = 460$ mK between $273 < B < 276$ G. For this temperature, we know the the phase slip occurs between 280.2 and 280.6 G (Fig. C.1). Thus, there should be no phase slips within this region. An example of two of these frequency traces is shown in Fig. D.1. We perform the same analysis of Section 7.3.1 and begin by fitting each of these traces to Eq. 7.4 with $a = 110$ G^{-1}.[1] To ensure that our fit does not get stuck in a local maximum of R^2 (which is likely in this case where we are fitting a step to the noise) we perform multiple iterations of the Tanh fit where we seed the initial jump location to successive values between 274.2 and 275.2 G in 0.1 G steps. This ensures that we locate the fit which returns the absolute maximum for R^2 and that our results for the switching field is insensitive to our initial estimate for $B_{\rm sw}$.

From the top row of Fig. D.2 we can see that our determined switching field is distributed uniformly over the field range in which we looked for phase slips. Further, the phase slip location shows no correlation with the magnitude of frequency shift or the goodness of fit, with $r_{B_{\rm sw},\delta f} = 0.02$ and $r_{B_{\rm sw},R^2} = -0.06$. A real phase slip would result in $\delta f > 0$;

1. For these fits, we fix a to the average value obtained from from fits to real phase slip data for CL12 at $T = 460$ mK with $R^2 > 0.55$. Without this restriction, the best Tanh fits typically have $a \approx 1 - 5$ G^{-1}, which results in a step that spans 200-1000 mG and does not physically represent a phase slip, which should be an instantaneous jump in our $f_0(B)$ traces.

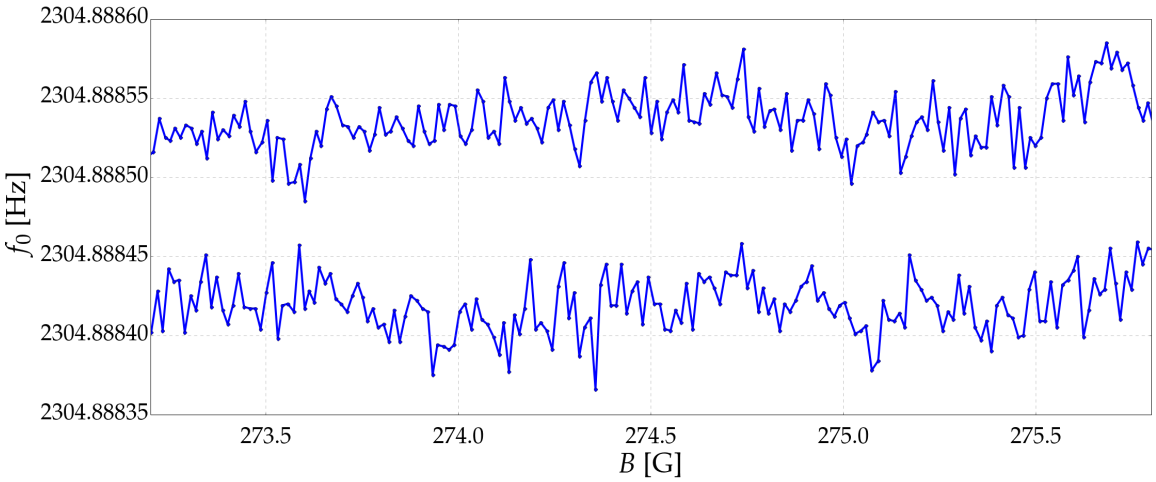

Figure D.1: Cantilever resonant frequency of CL12 as a function of applied magnetic field for $\dot{B} < 0$ and $T = 460$ mK. Over this region there are no phase slips, so $f_0(B)$ should not display a discontinuous jump.

however, we see that for the null dataset δf is equally distributed between positive and negative values, with the most common amplitude ~ 25 μHz. That is, the most common step height is the expected standard deviation of our frequency noise given our measurement time. These differences can be visualized by comparing the corresponding panels of Fig. D.2 against Fig. 7.16 and Fig. 7.18.

From this, we conclude that our analysis of Section 7.3.1 is not systematically flawed. In the presence of a real phase slip, the fits return B_{sw} values that are clearly clustered around a mean, instead of being uniformly distributed over the ~ 1 G region in which we look for phase slips. Further, in the presence of a real phase slip, every fit returns $\delta f > 0$, which is in stark contrast to the null dataset where δf has an nearly equal probability to be positive or negative. Further, the increase in the mean fit value for δf in the presence of a real phase slip indicates that we are detecting the phase slip and not simply fitting the noise.

At higher temperatures ($T > 800$ mK) our phase slip analysis begins to resemble that of the null dataset. That is, as the expected value of δf due to a phase slip approaches the frequency noise due to thermal fluctuations, we begin to have a larger number of false detection events. At these temperatures we find that some fits with the largest R^2 have $\delta f < 0$. For this reason, we limit this analysis to $T \leq 800$ mK where every phase slip

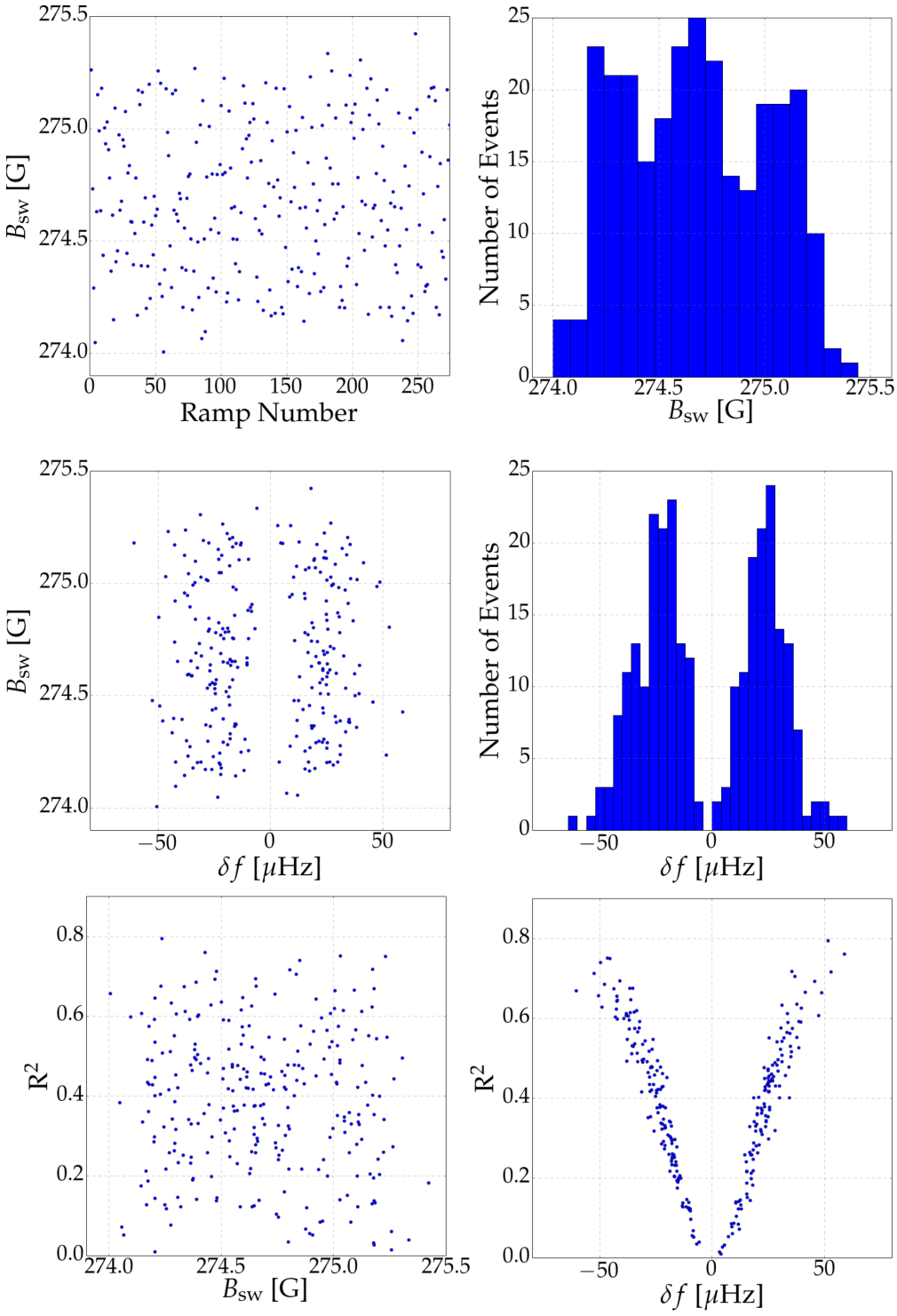

Figure D.2: (Top left) Fit phase slip location B_{sw} as a function of ramp number for CL12 at $T = 460$ mK with $\dot{B} < 0$ over a field range where we do not expect a phase slip. The corresponding unnormalized probability distribution (top right). The other four panels illustrate the correlations between the phase slip location and phase slip frequency shift, δf, and the goodness of fit, R^2.

detection has $\delta f > 0$ and we are confident that fits with $R^2 > 0.55$ are fits to physical phase slips and not occasional noise spikes.

Bibliography

[1] William A. Little. Decay of persistent currents in small superconductors. *Phys. Rev.*, 156:396–403, Apr 1967.

[2] W. A. Little and R. D. Parks. Observation of quantum periodicity in the transition temperature of a superconducting cylinder. *Phys. Rev. Lett.*, 9:9–12, Jul 1962.

[3] W. E. Shanks. Persistent currents in normal metal rings. 2011.

[4] M. Tinkham. Introduction to superconductivity. 2004.

[5] H. Kamerlingh Onnes. *Leiden Communications*, 120b, 122b, 124c, 1911.

[6] W. Meissner and R. Ochsenfeld. Kurze originalmitteilungen. *Naturwissenschaften*, 21:787, 1933.

[7] F. London and H. London. The electromagnetic equations of the supraconductor. *Proceedings of the Royal Society of London A: Mathematical, Physical and Engineering Sciences*, 149(866):71–88, 1935.

[8] F. London. *Superfluids*, 1, 1950.

[9] V. L. Ginzburg and L. D. Landau. *Zh. Eksperim. i Teor. Fiz.*, 20:866, 1950.

[10] L. P. Gor'kov. *Zh. Eksperim. i Teor. Fiz.*, 36:1918, 1959.

[11] W.H Keesom and J.A Kok. Measurements of the specific heat of thallium at liquid helium temperatures. *Physica*, 1(1):175 – 181, 1934.

[12] J. R. Clement and E. H. Quinnell. The atomic heat of lead in the region of its transition to superconductivity. *Phys. Rev.*, 85:502–503, Feb 1952.

[13] B. T. Matthias, T. H. Geballe, S. Geller, and E. Corenzwit. Superconductivity of nb_3sn. *Phys. Rev.*, 95:1435–1435, Sep 1954.

[14] J. E. Kunzler, E. Buehler, F. S. L. Hsu, and J. H. Wernick. Superconductivity in nb_3sn at high current density in a magnetic field of 88 kgauss. *Phys. Rev. Lett.*, 6:89–91, Feb 1961.

[15] J. G. Bednorz and K. A. Müller. Possible hightc superconductivity in the balacuo system. *Zeitschrift für Physik B Condensed Matter*, 64(2):189–193, Jun 1986.

[16] M. K. Wu, J. R. Ashburn, C. J. Torng, P. H. Hor, R. L. Meng, L. Gao, Z. J. Huang, Y. Q. Wang, and C. W. Chu. Superconductivity at 93 k in a new mixed-phase y-ba-cu-o compound system at ambient pressure. *Phys. Rev. Lett.*, 58:908–910, Mar 1987.

[17] A. Schilling, M. Cantoni, J. D. Guo, and H. R. Ott. Superconductivity above 130 k in the hg-ba-ca-cu-o system. *Nature*, 363(6424):56–58, 05 1993.

[18] A. P. Drozdov, M. I. Eremets, I. A. Troyan, V. Ksenofontov, and S. I. Shylin. Conventional superconductivity at 203 kelvin at high pressures in the sulfur hydride system. *Nature*, 525(7567):73–76, 09 2015.

[19] A.B. Pipard. *Proc. Roy. Soc.*, A216, 1953.

[20] H. Kamerlingh Onnes. *Leiden Communications*, 133a, 1913.

[21] J. S. Langer and Vinay Ambegaokar. Intrinsic resistive transition in narrow superconducting channels. *Phys. Rev.*, 164:498–510, Dec 1967.

[22] H. Polshyn, T. R. Naibert, and R. Budakian. Imaging phase slip dynamics in micron-size superconducting rings. *ArXiv:1703.08184*, 2017.

[23] W. Hecht and M. Conrad. *Z. Phys. Chem.*, 3(450), 1889.

[24] S. Arrhenius. *Z. Phys. Chem.*, 4(226), 1889.

[25] C. Wert and C. Zener. Interstitial atomic diffusion coefficients. *Phys. Rev.*, 76:1169–1175, Oct 1949.

[26] K. J. Laidter S. Glasstone and H. Eyring. The theory of rate processes. *J. Chem. Phys.*, 3, 1935.

[27] P. Hanggi. Escape from a metastable state. *J. Stat. Phys.*, 42:105–148, 07 1986.

[28] A. C. Bleszynski-Jayich, W. E. Shanks, P. Peaudecerf, E. Ginossar, F. von Oppen, L. Glazman, and J. G. E Harris. Persistent currents in normal metal rings. *Science*, 326(5950):272–275, 2009.

[29] M. A. Castellanos-Beltran, D. Q. Ngo, W. E. Shanks, A. B. Jayich, and J. G. E. Harris. Measurement of the full distribution of persistent current in normal-metal rings. *Phys. Rev. Lett.*, 110:156801, Apr 2013.

[30] A. C. Bleszynski-Jayich, W. E. Shanks, and J. G. E. Harris. Noise thermometry and electron thermometry of a sample-on-cantilever system below 1kelvin. *Applied Physics Letters*, 92(1):013123, 2008.

[31] T. A. Fulton and L. N. Dunkleberger. Lifetime of the zero-voltage state in josephson tunnel junctions. *Phys. Rev. B*, 9:4760–4768, Jun 1974.

[32] A. Garg. Escape-field distribution for escape from a metastable potential well subject to a steadily increasing bias field. *Phys. Rev. B*, 51:15592–15595, Jun 1995.

[33] D. E. McCumber and B. I. Halperin. Time scale of intrinsic resistive fluctuations in thin superconducting wires. *Phys. Rev. B*, 1:1054–1070, Feb 1970.

[34] A. Murphy, P. Weinberg, T. Aref, U. C. Coskun, V. Vakaryuk, A. Levchenko, and A. Bezryadin. Universal features of counting statistics of thermal and quantum phase slips in nanosize superconducting circuits. *Phys. Rev. Lett.*, 110:247001, Jun 2013.

[35] B. S. Deaver and W. M. Fairbank. Experimental evidence for quantized flux in superconducting cylinders. *Phys. Rev. Lett.*, 7:43–46, Jul 1961.

[36] L. D. Jackel, W. W. Webb, J. E. Lukens, and S. S. Pei. Measurement of the probability distribution of thermally excited fluxoid quantum transitions in a superconducting ring closed by a josephson junction. *Phys. Rev. B*, 9:115–118, Jan 1974.

[37] Xiaxian Zhang and John C. Price. Susceptibility of a mesoscopic superconducting ring. *Phys. Rev. B*, 55:3128–3140, Feb 1997.

[38] D. Y. Vodolazov, F. M. Peeters, S. V. Dubonos, and A. K. Geim. Multiple flux jumps and irreversible behavior of thin al superconducting rings. *Phys. Rev. B*, 67:054506, Feb 2003.

[39] N. C. Koshnick, H. Bluhm, M. E. Huber, and K. A. Moler. Fluctuation superconductivity in mesoscopic aluminum rings. *Science*, 318(5855):1440–1443, 2007.

[40] J. A. Bert, N. C. Koshnick, H. Bluhm, and K. A. Moler. Fluxoid fluctuations in mesoscopic superconducting rings. *Phys. Rev. B*, 84:134523, Oct 2011.

[41] Konstantin Yu. Arutyunov, Terhi T. Hongisto, Janne S. Lehtinen, Leena I. Leino, and Alexander L. Vasiliev. Quantum phase slip phenomenon in ultra-narrow superconducting nanorings. *Scientific Reports*, 2:293, 2012.

[42] N. Giordano. Evidence for macroscopic quantum tunneling in one-dimensional superconductors. *Phys. Rev. Lett.*, 61:2137–2140, Oct 1988.

[43] A. Bezryadin, C. N. Lau, and M. Tinkham. Quantum suppression of superconductivity in ultrathin nanowires. *Nature*, (6781):971–974, 04.

[44] C. N. Lau, N. Markovic, M. Bockrath, A. Bezryadin, and M. Tinkham. Quantum phase slips in superconducting nanowires. *Phys. Rev. Lett.*, 87:217003, Nov 2001.

[45] Fabio Altomare, A. M. Chang, Michael R. Melloch, Yuguang Hong, and Charles W. Tu. Evidence for macroscopic quantum tunneling of phase slips in long one-dimensional superconducting al wires. *Phys. Rev. Lett.*, 97:017001, Jul 2006.

[46] Mitrabhanu Sahu, Myung-Ho Bae, Andrey Rogachev, David Pekker, Tzu-Chieh Wei, Nayana Shah, Paul M. Goldbart, and Alexey Bezryadin. Individual topological tunnelling events of a quantum field probed through their macroscopic consequences. *Nat Phys*, 5(7):503–508, 07 2009.

[47] T. Aref, A. Levchenko, V. Vakaryuk, and A. Bezryadin. Quantitative analysis of quantum phase slips in superconducting $mo_{76}ge_{24}$ nanowires revealed by switching-current statistics. *Phys. Rev. B*, 86:024507, Jul 2012.

[48] A. Belkin, M. Belkin, V. Vakaryuk, S. Khlebnikov, and A. Bezryadin. Formation of quantum phase slip pairs in superconducting nanowires. *Phys. Rev. X*, 5:021023, Jun 2015.

[49] N. Byers and C. N. Yang. Theoretical considerations concerning quantized magnetic flux in superconducting cylinders. *Phys. Rev. Lett.*, 7:46–49, Jul 1961.

[50] J. T. Anderson and A. M. Goldman. Thermal fluctuations and the josephson supercurrent. *Phys. Rev. Lett.*, 23:128–131, Jul 1969.

[51] Vinay Ambegaokar and B. I. Halperin. Voltage due to thermal noise in the dc josephson effect. *Phys. Rev. Lett.*, 22:1364–1366, Jun 1969.

[52] M. Simmonds and W. H. Parker. Thermal fluctuations in superconducting weak links. *Phys. Rev. Lett.*, 24:876–879, Apr 1970.

[53] Juhani Kurkijärvi. Intrinsic fluctuations in a superconducting ring closed with a josephson junction. *Phys. Rev. B*, 6:832–835, Aug 1972.

[54] Hermann Grabert and Ulrich Weiss. Crossover from thermal hopping to quantum tunneling. *Phys. Rev. Lett.*, 53:1787–1790, Nov 1984.

[55] Andrew N. Cleland, John M. Martinis, and John Clarke. Measurement of the effect of moderate dissipation on macroscopic quantum tunneling. *Phys. Rev. B*, 37:5950–5953, Apr 1988.

[56] Michel H. Devoret, John M. Martinis, and John Clarke. Measurements of macroscopic quantum tunneling out of the zero-voltage state of a current-biased josephson junction. *Phys. Rev. Lett.*, 55:1908–1911, Oct 1985.

[57] Michel H. Devoret, John M. Martinis, and John Clarke. Devoret, martinis, and clarke reply. *Phys. Rev. Lett.*, 63:212–212, Jul 1989.

[58] John M. Martinis, Michel H. Devoret, and John Clarke. Experimental tests for the quantum behavior of a macroscopic degree of freedom: The phase difference across a josephson junction. *Phys. Rev. B*, 35:4682–4698, Apr 1987.

[59] V. M. Krasnov, T. Bauch, S. Intiso, E. Hürfeld, T. Akazaki, H. Takayanagi, and P. Delsing. Collapse of thermal activation in moderately damped josephson junctions. *Phys. Rev. Lett.*, 95:157002, Oct 2005.

[60] H. F. Yu, X. B. Zhu, Z. H. Peng, Ye Tian, D. J. Cui, G. H. Chen, D. N. Zheng, X. N. Jing, Li Lu, S. P. Zhao, and Siyuan Han. Quantum phase diffusion in a small underdamped josephson junction. *Phys. Rev. Lett.*, 107:067004, Aug 2011.

[61] R. L. Kautz and John M. Martinis. Noise-affected i-v curves in small hysteretic josephson junctions. *Phys. Rev. B*, 42:9903–9937, Dec 1990.

[62] D. Vion, M. Götz, P. Joyez, D. Esteve, and M. H. Devoret. Thermal activation above a dissipation barrier: Switching of a small josephson junction. *Phys. Rev. Lett.*, 77:3435–3438, Oct 1996.

[63] A. K. Geim, I. V. Grigorieva, S. V. Dubonos, J. G. S. Lok, J. C. Maan, A. E. Filippov, and F. M. Peeters. Phase transitions in individual sub-micrometre superconductors. *Nature*, 390:259–262, Nov 1997.

[64] D. Y. Vodolazov, F. M. Peeters, S. V. Dubonos, and A. K. Geim. Multiple flux jumps and irreversible behavior of thin al superconducting rings. *Phys. Rev. B*, 67:054506, Feb 2003.

[65] A.N. Cleland. Foundations of nanomechanics. 2003.

[66] Janis Research. He-3 SSV insert. https://www.janis.com/Products/productsoverview/He-3Systems/HE-3-SSVUltraLowTemperatureCryostat.aspx.

[67] Masahiro Ojima, Akira Arimoto, Naoki Chinone, Toshihiko Gotoh, and Kunio Aiki. Diode laser noise at video frequencies in optical videodisc players. *Appl. Opt.*, 25(9):1404–1410, May 1986.

[68] A. C. Bleszynski-Jayich, W. E. Shanks, B. R. Ilic, and J. G. E. Harris. High sensitivity cantilevers for measuring persistent currents in normal metal rings. *Journal of Vacuum Science & Technology B: Microelectronics and Nanometer Structures Processing, Measurement, and Phenomena*, 26(4):1412–1416, 2008.

[69] D. H. Douglass. Magnetic field dependence of the superconducting penetration depth in thin specimens. *Phys. Rev.*, 124:735–739, Nov 1961.

[70] J. Pearl. Current distribution in superconducting films carrying quantized fluxoids. *Appl. Phys. Lett.*, 5:64–659, 1964.

[71] H. J. Fink and V. Grünfeld. Flux periodicity in superconducting rings: Comparison to loops with josephson junctions. *Phys. Rev. B*, 33:6088–6093, May 1986.

[72] P. M. Tedrow and R. Meservey. Spin-paramagnetic effects in superconducting aluminum films. *Phys. Rev. B*, 8:5098–5108, Dec 1973.

[73] M. David Maloney, Francisco de la Cruz, and Manuel Cardona. Superconducting parameters and size effects of aluminum films and foils. *Phys. Rev. B*, 5:3558–3572, May 1972.

[74] J. F. Kenney and E. S. Keeping. Mathematics of statistics. 1962.

[75] Laurette S. Tuckerman and Dwight Barkley. Bifurcation analysis of the eckhaus instability. *Physica D: Nonlinear Phenomena*, 46(1):57 – 86, 1990.